University of Buenos Aires
Department of Physics

Supersymmetry search in final states with missing energy and at least three b-jets

CERN-THESIS-2012-228
21/12/2012

Thesis submitted in partial fulfilment of the
requirements for the degree of Doctor of Philosophy by

Gastón Leonardo Romeo

Thesis supervisor: Prof. Ricardo Néstor Piegaia

Buenos Aires, Argentina
October 15, 2012

Abstract

Supersymmetry search in final states with missing energy and at least three b-jets

Supersymmetry (SUSY) is a leading candidate theory for describing physics beyond the Standard Model (SM) as it has the potential for providing a consistent and natural embedding of the SM in a more general theory whose natural scale is the Planck scale (M_P). The Large Hadron Collider (LHC) and the ATLAS experiment have been designed with the capability to determine whether SUSY is a correct description of Nature. This thesis presents the results of the first search for top and bottom squarks from gluino pair production in events with large missing transverse momentum and at least three jets identified as originating from a b-quark. The analysis is performed with a total integrated luminosity corresponding to 4.7 fb^{-1} of proton-proton collisions at center-of-mass energy $\sqrt{s} = 7$ TeV. An exhaustive optimization has been done targeting different topologies involving SUSY particles, from which five enriched signal regions (SR) have been chosen to identify possible SUSY-like event candidates with at least three b-jets and missing transverse energy. The results obtained in each of the five SR have been found to be in good agreement with the SM predictions. Therefore, exclusion limits at 95% confidence level are presented for a variety of gluino-mediated models with gluino masses up to 1.02 TeV excluded. These are the most stringent limits obtained up to now by collider experiments, and impose harsh constraints in several supersymmetric models.

Keywords: Supersymmetry, LHC, ATLAS, stop, sbottom, gluino, b-jets, missing transverse energy.

Acknowledgments

My experience at CERN has been wonderful and inspiring. I will be always indebted to my advisor Ricardo Piegaia. It has been a pleasure to work under his tutelage and profit from his instructional qualities in different aspects of my formation. He has guided me through several lines of work, and he has spent countless hours helping me develop into a good scientist and researcher. He managed to capture my strenghts and spot my weaknesses, and addressed them irrespective of the time or effort required. His critical reasoning and encouragement towards meticulous execution has been enormously fruitful for me. I am proud to express my gratitude to Ariel Schwartzman. I certainly would not be the scientist who I have become today if it was not for his influence, mentoring, instructive capabilities and for being a compelling force for progress. I would like to thank the confidence Tancredi Carli had in me for the major task of measuring the jet energy resolution in ATLAS. I would also like to express my gratitude to Bart Butler, David López, Zach Marshall and David Miller for the meaningful discussions, and especially for sharing their impressive technical expertise with me during all these years. I would like to appreciate the members of the SUSY analysis group with b-jets in ATLAS: Antoine Marzin, Monica D'Onofrio, Davide Costanzo, Iacopo Vivarelli, Xavier Portell Bueso, Alan Tua, Per Hansson, Takashi Yamanaka, and all other members... thanks a lot for the nice working atmosphere, the endless meaningful discussions and enormous patience. It has been a pleasure working with all you!

Estoy infinitamente agradecido a mi familia, a ustedes les dedico este trabajo. A mis viejos Guillermo y Francisca, a mi hermana Leticia y a mi hermano Ariel, quienes han forjado la persona detrás de estas palabras. Muchísimas gracias por ser como son, por su incondicional amor y apoyo durante todos estos años de esfuerzo, por haberse brindado desde siempre en todos los aspectos para que pueda alcanzar mis objetivos. A mis tíos y primos, y en especial a Tincho.

A mis amigos de hoy y siempre, de este y del otro lado del océano... gracias por estar durante todos estos años de muchísimo sacrificio y esfuerzo, por compartir el fútbol, la música, el café, el asado, la arena y la nieve, las noches de espadachines y los días de cabra.

Estoy convencido que no podría haber llegado a esta instancia de no haber sido por tener la suerte de encontrar en mi camino a Xabier Anduaga y a Martín Tripiana. Baskito, Tinchito... siempre les estaré agradecido. A Laurita, mi compañera de aventuras. No tengo palabras para agradecerte todos estos años de amistad... gracias genia! A Monti, no me puedo olvidar del 0-800. A Susy y a Javi, por su hermosa amistad.

A toda la gente de la oficina: Hernán, Javi, Yann, Sabrina, Pablito, Orel y Gustavo. Muchas gracias por la buena onda y su sonrisa día a día.

A Sabri, mi amor. Gracias por darme todo sin pedir nada, por compartir deseos y esperanzas, y por llevarme de la mano en este hermoso camino que transitamos juntos.

Contents

Abstract iii

Acknowledgments v

Introduction 1

1 The Standard Model framework 5
- 1.1 Particle content and interactions . . . 6
- 1.2 Higgs mechanism . . . 8
- 1.3 Quantum Chromodynamics . . . 9
  - 1.3.1 Asymptotic freedom and confinement . . . 10
- 1.4 Jet physics and phenomenology . . . 11
  - 1.4.1 Hard interaction and parton shower . . . 13
  - 1.4.2 Parton distribution function and factorization . . . 14
  - 1.4.3 Hadronization . . . 16
  - 1.4.4 Underlying event . . . 17

2 The Supersymmetric extension of the Standard Model 19
- 2.1 The limitations of the Standard Model . . . 19
  - 2.1.1 Fine-tuning, naturalness and hierarchy problems . . . 20
  - 2.1.2 The vanishing of quadratic divergencies . . . 21
- 2.2 The supersymmetric extension of the Standard Model . . . 23
- 2.3 Benefits from introducing SUSY . . . 24
  - 2.3.1 Solution of the hierarchy and naturalness problem . . . 24
  - 2.3.2 Unification of interactions . . . 25
  - 2.3.3 Dark Matter candidate . . . 25
  - 2.3.4 Incorporation of gravity . . . 25
- 2.4 Minimal Supersymmetric Standard Model . . . 26
  - 2.4.1 Particle content . . . 26
  - 2.4.2 R-parity . . . 28

2.4.3 Supersymmetry breaking . . . 30
2.4.4 The mass spectrum . . . 31
2.4.5 Sparticles decays . . . 33
2.4.6 Benchmark models and Phenomenological MSSM . . . 34
2.5 Simplified Models . . . 36
2.6 Characterization of heavy flavour topologies . . . 39
2.6.1 Production . . . 39
2.6.2 Stop and sbottom signatures . . . 40
2.7 Simplified Models for heavy-flavour jets and $E_{\mathrm{T}}^{\mathrm{miss}}$ topologies . . . 42
2.8 Previous experimental results . . . 43

3 Statistical methods for exclusion limits and discovery 47
3.1 Hypothesis testing . . . 47
3.2 Statistical significance . . . 48
3.3 Frequentist significance test . . . 49
3.4 Profile likelihood-ratio . . . 50
3.5 Profile likelihood asymptotic approximation . . . 51
3.6 CL_s method . . . 53
3.7 Quantifying an excess of events . . . 54

4 The ATLAS experiment 55
4.1 The Large Hadron Collider . . . 55
4.1.1 Machine design . . . 55
4.1.2 Luminosity and pile-up . . . 58
4.1.3 LHC operation during 2011 . . . 60
4.2 The ATLAS detector system . . . 60
4.2.1 Coordinate system . . . 61
4.2.2 The solenoidal and toroidal magnet systems . . . 62
4.2.3 Inner Detector . . . 63
4.2.4 Calorimeter . . . 68
4.2.5 The Muon Spectrometer . . . 74
4.2.6 Luminosity detectors . . . 78
4.2.7 Trigger and data acquisition . . . 79
4.2.8 ATLAS operation during 2011 . . . 81
4.2.9 Luminosity measurement . . . 82
4.3 Monte Carlo simulation . . . 84
4.3.1 Standard Model processes . . . 84
4.3.2 SUSY signals . . . 86

5 Event reconstruction **89**
5.1 Track reconstruction . . . 89
5.2 Vertex reconstruction . . . 90
5.3 Electrons . . . 91
5.3.1 Reconstruction . . . 91
5.3.2 Identification . . . 92
5.3.3 Isolation . . . 93
5.3.4 Performance . . . 93
5.4 Muons . . . 94
5.4.1 Reconstruction . . . 94
5.4.2 Identification . . . 95
5.4.3 Isolation . . . 95
5.4.4 Performance . . . 96
5.5 Jets . . . 96
5.5.1 Inputs to jet reconstruction . . . 97
5.5.2 Jet algorithm . . . 97
5.5.3 Jet energy calibration . . . 98
5.6 *b*-tagging . . . 102
5.6.1 Track selection and properties . . . 102
5.6.2 High-performance spatial *b*-tagging algorithms . . . 103
5.6.3 Combination of algorithms . . . 104
5.6.4 Expected performance and operating points . . . 105
5.6.5 Calibration . . . 106
5.7 Missing transverse momentum . . . 108
5.7.1 Reconstruction and calibration . . . 109
5.7.2 Performance . . . 110

6 Jet energy resolution **111**
6.1 QCD Monte Carlo samples . . . 112
6.2 Event and jet selection . . . 113
6.3 Jet energy calibration . . . 114
6.3.1 The Local Cluster Weighting (LCW) calibration . . . 115
6.3.2 The Global Cell Weighting (GCW) calibration . . . 115
6.3.3 The Global Sequential (GS) calibration . . . 115
6.3.4 Track-based correction to the jet calibration . . . 116
6.4 In situ jet resolution measurement . . . 116
6.4.1 The dijet balance method . . . 116
6.4.2 The bisector technique . . . 120
6.5 Performance for the EM+JES calibration . . . 123
6.6 Closure test . . . 125
6.7 Jet energy resolution uncertainties . . . 126

6.7.1 Experimental uncertainties . . . 126
6.7.2 Uncertainties due to the event modelling in the Monte Carlo generators . . . 128
6.7.3 Uncertainties of the measured resolutions . . . 128
6.8 Results for other calibration schemes . . . 130
6.9 Improvement in jet energy resolution using tracks . . . 132
6.10 Summary of results with 2010 data . . . 132
6.11 JER performance with 2011 data . . . 133
6.11.1 Impact of pile-up on jet energy resolution . . . 134
6.11.2 Forward regions . . . 136
6.12 Final remarks and future prospects . . . 136

7 Analysis strategy **139**
7.1 Event Selection . . . 140
7.2 Final state object definition . . . 141
7.3 Event preselection . . . 144
7.3.1 Data quality . . . 144
7.3.2 Trigger selection and efficiency . . . 144
7.3.3 Vertex selection . . . 147
7.3.4 LAr hole veto . . . 147
7.3.5 Jet cleaning . . . 148
7.3.6 Cosmic cleaning . . . 148
7.3.7 Bad muons cleaning . . . 148
7.3.8 Lepton selection . . . 148
7.4 Systematic uncertainties on the background . . . 149
7.4.1 Experimental uncertainties . . . 149
7.4.2 Theoretical uncertainties . . . 151
7.5 Systematic uncertainties on the signal . . . 153
7.6 Optimization of event selection . . . 154
7.6.1 Kinematic studies with heavy flavor Simplified Models . . . 155
7.6.2 Optimization procedure . . . 156
7.6.3 Optimization for Gbb topologies . . . 158
7.6.4 Optimization for Gtt topologies . . . 163
7.6.5 Other trigger strategies . . . 169
7.6.6 Summary of most promising 0-lepton signal regions . . . 171
7.7 Final event selection . . . 173

8 Background estimation **175**
8.1 Multi-jet background estimation . . . 176
8.1.1 Seed selection . . . 176
8.1.2 The smearing function . . . 178

8.1.3 Normalization and validation . . . 180
8.1.4 Systematic uncertainties in the multi-jet background . . . 181
8.1.5 Final multi-jet estimate . . . 183
8.2 Non multi-jet background estimate . . . 183
8.2.1 Prediction of the $t\bar{t}$ background . . . 184
8.2.2 Estimation of other background processes . . . 193
8.2.3 Semi data-driven $t\bar{t}$ background results . . . 195
8.3 Validation of the transfer factors in the 1-lepton channel . . . 195

9 Results and interpretation **199**
9.1 Experimental results . . . 199
9.2 Interpretation of the results . . . 200
9.2.1 Exclusion limits for the Gbb simplified model . . . 205
9.2.2 Exclusion limits for the Gtt simplified model . . . 209
9.2.3 Exclusion limits for the Gtb simplified model . . . 211
9.2.4 Exclusion limits for the gluino-stop pMSSM model . . . 214
9.2.5 Exclusion limits for the gluino-sbottom pMSSM model . . . 215
9.3 Discussion . . . 216

10 Conclusions **219**

List of Tables

1.1 Fermionic sector of the Standard Model. 7
1.2 Standard Model gauge bosons and the corresponding interactions. . . 8

2.1 Chiral supermultiplets in the Minimal Supersymmetric Standard Model. 28
2.2 Gauge supermultiplets in the Minimal Supersymmetric Standard Model. 29
2.3 Summary of the heavy flavor simplified models with the corresponding MSSM process and the expected final states. 44

4.1 Values of LHC parameters at the ATLAS interaction point, for the 2009, 2010 and 2011 LHC operation, and the design parameters. . . . 60
4.2 General performance goals of the ATLAS detector. 61
4.3 The most important SM background processes and their production cross sections, multiplied by the relevant branching ratios (BR). . . . 85

6.1 The total systematic uncertainties for different p_{T} ranges, for the four rapidity regions and the two jet radii studied. 129

7.1 Nominal b-tagging efficiency for jets with $p_T > 15$ GeV and $|\eta| < 2.5$ as well as the light quarks, c-quarks and τ leptons rejection factor (RF) for different opertaing points. 143
7.2 Trigger chains used for each data period. 146
7.3 The set of cuts that have been examined for the optimization study for zero-lepton selection candidates. 159
7.4 Reduced set of nine selection cuts aimed at Gbb topologies. 163
7.5 The set of cuts that has been examined for the optimization study of 1-lepton selection candidates. 166
7.6 Most promising reduced set of signal regions for the 0-lepton channel targeting Gtt topologies. 167
7.7 Most promising reduced set of signal regions for the 1-lepton channel targeting Gtt topologies. 167
7.8 Reduced set of eight selection cuts using a multi-jet trigger strategy. . 170

7.9 Reduced set of eight selection cuts using a b-jet trigger strategy. . . . 170
7.10 Summary of the most promising b-jets + $E_{\mathrm{T}}^{\mathrm{miss}}$ signal regions targeting Gbb and Gtt topologies after the optimization procedure. 173
7.11 Summary of the event selection in each signal region. 174

8.1 The 2011 single-jet trigger chains used to select seed events in the Jet Smearing method. 177
8.2 Estimate of the multi-jet background and its systematic uncertainties for each of the five signal regions. 183
8.3 Estimate of the multi-jet background for 4.7 fb^{-1} from the jet smearing method in the various signal regions. 184
8.4 Definition of the four control regions used to estimate the $t\bar{t}$+jets background. 185
8.5 Expected numbers of SM events and observed data events in the four $t\bar{t}$ control regions. 191
8.6 Monte Carlo based $t\bar{t}$ background estimation in the control regions and associated systematic uncertainties. 191
8.7 Theoretical uncertainties on the number of $t\bar{t}$ events in each control region as predicted by the Monte Carlo simulations. 192
8.8 Estimation of the transfer factor T_f for the five signal regions of the 0-lepton analysis. 192
8.9 Theoretical uncertainties on the $t\bar{t}$ transfer factors. 193
8.10 Monte Carlo based top background estimation in the signal regions and associated systematic uncertainties. 193
8.11 Theoretical uncertainties on the number of $t\bar{t}$ events in each signal region as predicted by the Monte Carlo simulations. 193
8.12 Monte Carlo based backgrounds estimation and associated systematic uncertainties for W/Z boson and $t\bar{t}$ production in association with heavy flavour jets, single top, associate production of a $t\bar{t}$ pair with a vector boson ($t\bar{t}$+W/Z), for each of the five signal regions. 194
8.13 Estimation of the $t\bar{t}$ background for the five signal regions, as determined by a pure MC estimate and the semi data-driven method. . . . 195
8.14 Validation of $t\bar{t}$ background estimation and associated systematic uncertainties using the 1-lepton selection. 198

9.1 Comparison between the results for the SM prediction and the numbers of observed events in the five signal regions. 200
9.2 Observed (expected) 95% CL upper limits on the non-SM contributions to all signal regions. 204
9.3 Gluino pair production cross-section and its theoretical uncertainty as a function of the gluino mass. 205

List of Figures

1.1 The QCD coupling as measured in physics processes at different scales Q and first evidence for hadronic jet production at the CERN $Sp\bar{p}S$ collider. . . . 12
1.2 Most common phenomenological models for describing the parton shower in Monte Carlo simulations. . . . 17
1.3 Illustration of the complex picture of a hadron-hadron collision. . . . 18

2.1 One-loop quantum correction to different mass parameters. . . . 22
2.2 Distributions of inclusive transverse momentum and rapidity of the partonic gluino for the SUSY $\tilde{g}\tilde{g}$ pair production compared with a flat matrix element $|\mathcal{M}|^2 \propto 1$. . . . 37
2.3 Distribution of inclusive transverse momentum for the partonic gluino for the SUSY $\tilde{\chi}_2^0\tilde{g}$ associated production process compared with a flat matrix element $|\mathcal{M}|^2 \propto 1$ and a threshold-corrected matrix element $|\mathcal{M}|^2 \propto 1 - 1/X$. . . . 38
2.4 Cross-sections for SUSY sparticles production, as a function of their masses calculated to NLO using PROSPINO. . . . 39
2.5 The tree-level Feynman diagrams for two cases of $\tilde{t}_1$ and $\tilde{g}$ three body decay. . . . 42
2.6 Diagrams of the production and schematics depicting the particle mass spectrum for Gbb, Gtt and Gtb topologies, with 4 b-jets and $E_{\mathrm{T}}^{\mathrm{miss}}$ expected in each of the final states. . . . 44

4.1 The CERN accelerator facility. . . . 57
4.2 Cross-sections for various processes as a function of the center-of-mass energy ($\sqrt{s}$). . . . 59
4.3 Cut-away view of the ATLAS detector. . . . 62
4.4 Magnet system arrangement of the ATLAS detector. . . . 63
4.5 Scheme of the ATLAS Inner Detector layout. . . . 64

4.6 Diagram with an indication of a partially reconstructed track in the TRT detector. . . . 67
4.7 Cut-away view of the ATLAS calorimeter system. . . . 69
4.8 Photograph showing a side view of a lead/LAr EM calorimeter module and sketch of a barrel module. . . . 70
4.9 Mechanical assembly of the steel-scintillator structure and the optical readout of the tile calorimeter. . . . 72
4.10 Electrode structure of one forward calorimeter (FCal1). . . . 73
4.11 Cross-section of the ATLAS Muon Spectrometer. . . . 74
4.12 Mechanical structure of a MDT chamber. . . . 76
4.13 Structure of the CSC layout. . . . 77
4.14 Cumulative luminosity versus day delivered and recorded by ATLAS during stable beams and for pp collisions at $\sqrt{s} = 7$ TeV in 2011 and luminosity-weighted distribution of the mean number of interactions per crossing ($\langle\mu\rangle$) for 2011. . . . 82

5.1 The electron energy-scale correction factor as a function of its energy as determined using different SM decays and efficiencies measured from $Z \to ee$ events for medium identification criterion. . . . 94
5.2 Efficiencies for CB plus ST muons, obtained from data and Monte Carlo simulation as function of muon η and integrated over a p_{T} range of 20 GeV - 100 GeV, using STACO-family algorithms and muon momentum resolution curve in collision data and simulation as a function of the muon p_{T}, for the pseudo-rapidity region $|\eta| < 1.05$. . 97
5.3 The average simulated jet energy response at the electromagnetic scale in bins of EM+JES calibrated jet energy and as a function of the detector pseudorapidity. . . . 100
5.4 Fractional jet energy scale systematic uncertainty as a function of p_{T} for jets for different pseudorapidity regions in the calorimeter system. 101
5.5 The expected performance of the light-jet and c-jet rejection as a function of the b-tag efficiency for different b-tagging algorithms, based on simulated $t\bar{t}$ events. . . . 106
5.6 The b-tag efficiency in data and simulation with the resulting scale factors for the MV1 tagging algorithm at OP = 70% efficiency as a function of the jet p_{T}, obtained with the $p_{\mathrm{T}}^{\mathrm{rel}}$ and $System8$ methods. . 108
5.7 The c-tag efficiency in data and simulation, and the corresponding scale factors as a function of the jet p_{T}, as measured for the MV1 b-tagging algorithm at OP = 70 % efficiency. . . . 109

6.1 Asymmetry distribution as defined in Equation (6.1) for $\bar{p}_{\mathrm{T}} = 60 - 80$ GeV and $|y| < 0.8$ for data and Monte Carlo simulation. . . . 118

6.2 Relative jet p_{T} resolutions, from Equation 6.2, measured in events with $60 \leq \bar{p}_{\mathrm{T}} < 80$ GeV. 119
6.3 Particle-level imbalance (PI) correction to the measured resolutions. . 120
6.4 Definition of the variables used in the bisector technique. 121
6.5 Distributions of the $P_{\mathrm{T},\psi}$ and $P_{\mathrm{T},\eta}$ components of the imbalance vector $\vec{P}_{\mathrm{T}}$, for $\bar{p}_{\mathrm{T}} = 60 - 80$ GeV for data and Monte Carlo simulation. . . . 122
6.6 Standard deviations of $P_{\mathrm{T},\psi}$ and $P_{\mathrm{T},\eta}$, the components of the imbalance vector, as a function of $\bar{p}_{\mathrm{T}}$. 122
6.7 Standard deviations involved in the bisector method as a function of the upper $p_{\mathrm{T},3}^{\mathrm{EM-scale}}$ cut, for $R = 0.6$ anti-k_t jets. 123
6.8 Relative jet p_{T} resolution for the dijet balance and bisector techniques as a function of $\bar{p}_{\mathrm{T}}$. 124
6.9 Fractional jet p_{T} resolution as a function of $\bar{p}_{\mathrm{T}}$ for anti-k_t with $R = 0.6$ jets in the Extended Tile Barrel, Transition and End-Cap regions using the bisector technique. 125
6.10 Comparison between the Monte Carlo simulation truth jet p_{T} resolution and the final results obtained from the bisector and dijet balance in situ techniques (applied to Monte Carlo simulation) for the EM+JES calibration, as a function of $\bar{p}_{\mathrm{T}}$. 126
6.11 The experimental systematic uncertainty in the dijet balance and bisector methods as a function of $\bar{p}_{\mathrm{T}}$. 127
6.12 Dependence of the resolution on the event modelling in the Monte Carlo generators, taking Pythia MC10 as reference. 128
6.13 Fractional jet p_{T} resolution as a function of $\bar{p}_{\mathrm{T}}$ for anti-k_t jets with $R = 0.6$ in different rapidity regions for four jet calibration schemes. . 130
6.14 Fractional jet p_{T} resolutions as a function of $\bar{p}_{\mathrm{T}}$ for anti-k_t jets with $R = 0.6$ for the Local Cluster Weighting (LCW+JES), Global Cell Weighting (GCW+JES) and Global Sequential (GS) calibrations. . . 131
6.15 Fractional jet p_{T} resolution as a function of $\bar{p}_{\mathrm{T}}$, measured in data for anti-k_t jets with $R = 0.6$ and $R = 0.4$ for four jet calibration schemes: EM+JES, EM+JES+TBJC, LCW+JES and LCW+JES+TBJC. . . 132
6.16 Fractional jet momentum resolution as a function of the average jet transverse momenta for two-jet events, using Track-based jet corrections (TBJC) applied on top of Local Cluster Weighting (LCW) anti-k_t jets with $R = 0.6$ and $R = 0.4$ in ATLAS and Particle flow anti-k_t 0.5 jets in CMS. 133
6.17 Comparison of the fractional jet momentum resolution as a function of the average jet transverse momenta with GCW calibrated jets as determined using 2010 data, with respect to the truth resolution expected from Monte Carlo simulation before data-taking begins. 134

6.18 Fractional jet energy resolution as a function of the average jet transverse momenta measured with the bisector in-situ technique for events with two jet in the same rapidity bin for EM+JES and Local Cluster Weighting (LCW) calibrations with 2011 data. 135
6.19 Fractional jet energy resolution as a function of the average jet transverse momenta measured with the bisector in-situ technique for events with two jet in the same rapidity bin for EM+JES calibration with 2011 and 2010 data. 135
6.20 The dependence of the determined jet p_{T} resolution on the presence of a third jet for a $\bar{p}_{\mathrm{T}}$ bin of $60 \leq \bar{p}_{\mathrm{T}} < 80$ GeV, for $2.8 \leq |y| < 3.6$ and $3.6 \leq |y| < 4.4$, using anti-k_t 0.4 jets calibrated at the EM+JES. 137
6.21 The jet energy resolution and its uncertainty for anti-k_t with R= 0.6 jets calibrated with the EM+JES and LCW calibration schemes using 2011 data. 137

7.1 The zero-lepton trigger `EF_j75_a4tc_EFFS_xe45_loose_noMu` turn-on curve shown for data and $t\bar{t}$ Monte Carlo simulation. 146
7.2 Distributions of first- and second-leading jet p_{T} for the Gbb topology for different masses of the pair produced gluino and the LSP. 157
7.3 Distributions of $E_{\mathrm{T}}^{\mathrm{miss}}$ and overall energy sum in the event $\mathrm{m_{eff}}$ for the Gbb topology for different masses of the pair produced gluino and the LSP. 158
7.4 Distribution of $\Delta\phi_{min}$ and $E_{\mathrm{T}}^{\mathrm{miss}}/\mathrm{m_{eff}}$, after requiring the event to have the leading jet with $p_{\mathrm{T}}>$ 130 GeV, $E_{\mathrm{T}}^{\mathrm{miss}} >$ 130 GeV and at least three jets with $p_{\mathrm{T}}>$ 30 GeV, in the zero-lepton selection. 160
7.5 Distribution of $E_{\mathrm{T}}^{\mathrm{miss}}$ and $\mathrm{m_{eff}}$ in the zero-lepton selection, after applying both a $\Delta\phi_{min} > 0.4$ cut and a $E_{\mathrm{T}}^{\mathrm{miss}}/\mathrm{m_{eff}} > 0.25$ cut (QCD rejection). 161
7.6 Relative improvement in significance with respect to previous analyses, best set of cuts and significances for the Gbb topology. 162
7.7 Impact on the significance after removing the $E_{\mathrm{T}}^{\mathrm{miss}}/\mathrm{m_{eff}}$ cut and the $\Delta\phi_{min} > 0.4$ cut for Gbb topologies. 164
7.8 Distributions of $\mathrm{m_T}$ and $E_{\mathrm{T}}^{\mathrm{miss}}$, after requiring the event to have either an electron or a muon. 166
7.9 Comparison of significances in the zero- and one-lepton selection for the Gtt topology. 168
7.10 Best set of cuts and the corresponding significances using a multi-jet trigger strategy for a given point in the gluino/LSP mass plane. . . . 171
7.11 Best set of cuts and the corresponding significances using a multi-jet trigger strategy for a given point in the gluino/LSP mass plane. . . . 172

8.1 The respose function binned in true p_{T} as calculated using PYTHIA QCD samples. . . . 178
8.2 The response function for b-tagged jets, true b-jets and un-tagged jets, as calculated using MC samples in two different truth p_{T} ranges. . . . 179
8.3 Event display of a Mercedes event. . . . 180
8.4 Distributions of the p_{T} of the two leading jets, $E_{\mathrm{T}}^{\mathrm{miss}}$, and $\mathrm{m_{eff}}$ for a multi-jet enriched control region, after requiring $\Delta\phi_{min} < 0.4$, at least 4-jets above 50 GeV, 3 b-tagged selection (with OP = 60 %), and $\mathrm{m_{eff}} > 500$ GeV. . . . 182
8.5 The jet multiplicity after applying the cuts $\#1 - 13$ (for the 4-jet selection and $E_{\mathrm{T}}^{\mathrm{miss}} > 160$ GeV) as introduced in Table 7.11. . . . 186
8.6 The distributions of the leading jet p_{T}, the second leading jet p_{T}, the leading jet MV1 b-tagger weight and $\mathrm{m_{eff}}$ after applying the cuts $\#1 - 13$ as introduced in Table 7.11. . . . 186
8.7 The $E_{\mathrm{T}}^{\mathrm{miss}}$ distribution for the 4-jet and 6-jet selections, after applying the cuts $\#1 - 13$ as introduced in Table 7.11. . . . 187
8.8 The b-jet multiplicity after requiring at least 1 b-tagged jet, for the three MV1 b-tagger operating points used in this analysis. . . . 187
8.9 The $E_{\mathrm{T}}^{\mathrm{miss}}$ distribution after requiring at least 1 b-tagged jet, using the 60% and 70% MV1 b-tagger operating points. . . . 188
8.10 The $E_{\mathrm{T}}^{\mathrm{miss}}$ distribution after requiring at least 1 b-tagged jet, using the 70% and 75% MV1 b-tagger operating points. . . . 188
8.11 The first-, second-, third-leading jet p_{T} and their MV1 b-tagger weights, $E_{\mathrm{T}}^{\mathrm{miss}}$ and $\mathrm{m_{eff}}$ distributions in CR4-60. . . . 189
8.12 The first-, second-, third-leading jet p_{T} and their MV1 b-tagger weights, $E_{\mathrm{T}}^{\mathrm{miss}}$ and $\mathrm{m_{eff}}$ distributions in CR6-70. . . . 190
8.13 Distributions of $E_{\mathrm{T}}^{\mathrm{miss}}$ and $\mathrm{m_{eff}}$ in VR1-2b-OP60 and VR1-3b-OP60 for the electron channel. . . . 197
8.14 Distributions of $E_{\mathrm{T}}^{\mathrm{miss}}$ and $\mathrm{m_{eff}}$ in VR1-2b-OP60 and VR1-3b-OP60 for the muon channel. . . . 197

9.1 Distributions of the first- and second-leading jet p_{T}, the b-jet multiplicity, the leading jet MV1 b-tagger weight, the $E_{\mathrm{T}}^{\mathrm{miss}}$ and the $\mathrm{m_{eff}}$ in the SR4-L signal region. . . . 201
9.2 Distributions of the first- and second-leading jet p_{T}, the b-jet multiplicity, the leading jet MV1 b-tagger weight, the $E_{\mathrm{T}}^{\mathrm{miss}}$ and the $\mathrm{m_{eff}}$ in the SR6-T signal region. . . . 202
9.3 Plots of CL_s^{obs} and CL_s^{exp} as a function of the signal strength μ for an excluded and a non-excluded simplified model. . . . 203
9.4 Total theoretical uncertainty for the Gbb model. . . . 206
9.5 Acceptance for the Gbb model in the SR4-T signal region. . . . 206

9.6 Detector efficiency for the Gbb model in the SR4-T signal region. . . 207
9.7 Impact of the experimental uncertainty for the Gbb model in the SR4-T signal region. 208
9.8 Exclusion limits in the $(m_{\tilde{g}}, m_{\tilde{\chi}_1^0})$ plane for the Gbb model. 208
9.9 95 % CL excluded signal model cross-section and the signal region which leads to the best expected upper limit on the visible cross-section for the Gbb model. 209
9.10 Acceptance for the Gtt model in the SR6-L signal region. 210
9.11 Detector efficiency for the Gtt model in the SR6-L signal region. . . . 210
9.12 Relative experimental uncertainty for the Gtt model in the SR6-L signal region. 211
9.13 Exclusion limits in the $(m_{\tilde{g}}, m_{\tilde{\chi}_1^0})$ plane for the Gtt model. 212
9.14 95 % CL excluded signal model cross-section and the signal region which leads to the best expected upper limit on the visible cross-section for the Gtt model. 212
9.15 Exclusion limits in the $(m_{\tilde{g}}, m_{\tilde{\chi}_1^0})$ plane for the Gtb model. 213
9.16 The signal efficiency for gluino mediated stop pair production in the $(m_{\tilde{g}}, m_{\tilde{t}_1})$ plane for the pMSSM gluino-stop model, for the signal region SR6-T. 215
9.17 Impact of the b-tagging and JES uncertainties for gluino mediated stop pair production in the $(m_{\tilde{g}}, m_{\tilde{t}_1})$ plane in the pMSSM gluino-stop model, for the signal region SR6-T. 215
9.18 The exclusion limits in the $(m_{\tilde{g}}, m_{\tilde{t}_1})$ plane for the gluino-stop model. 216
9.19 The exclusion limits in the $(m_{\tilde{g}}, m_{\tilde{b}_1})$ plane for the gluino-sbottom model. 217

Introduction

The Large Hadron Collider (LHC) [1] is the largest and highest-energy particle accelerator world-wide, and will extend the frontiers of particle physics with its unprecedented high energy and luminosity, where bunches of $\mathcal{O}(10^{11})$ protons will collide 40 millions times per second to provide 14 TeV proton-proton collisions at a design luminosity of $10^{34}\text{cm}^{-2}\text{s}^{-1}$. The LHC and the experiments therein constitute the most complex scientific instruments ever built in human history, with enormous potential to shed light on fundamental physics, and it is expected to take scientists into the deepest understanding of Nature. After decades of preparation, the experiments at the LHC are taking the first steps toward resolving many long-standing puzzles about fundamental physics at the weak scale and their results are eagerly waited by the scientific community. One of the key experiments at the LHC is ATLAS ("A Toroidal LHC ApparatuS") [2], a general-purpose detector designed to fulfil precision measurements within the Standard Model [3–9] and to characterize a wide set of processes covering much of the new phenomena sought to be observed at the TeV scale. Spanned over 44 m in length and 25 m in height, ATLAS represents the biggest multi-purpose particle detector ever built in all mankind history.

Particle physics entered the era of electroweak symmetry breaking after the discovery of the W and Z gauge bosons in the early 1980s. Nevertheless, the fundamental origin of such breaking is still unknown. Theoretical arguments have made a convincing case that the dynamics underlying electroweak symmetry breaking must be associated with physics at the TeV scale. Supersymmetry (SUSY) [10] is a leading candidate for these dynamics, providing a consistent and natural embedding of the Standard Model of particle physics in a more fundamental theory whose natural scale is the Planck scale (M_P). The supersymmetric framework is a very ambitious one, as it attempts to connect physics at low energies (the TeV scale and below) with the ultimate energy scale of fundamental physics (the Planck scale). The unification of coupling constants [11] provides perhaps the strongest hint that an extrapolation from the TeV scale all the way up to energies near M_P may be achieved.

The LHC and the ATLAS experiment have been designed with the capability to discover supersymmetric particles. If the squarks and gluinos are sufficiently light,

these particles can be pair-produced at the LHC from gluon-gluon and gluon-quark collisions with cross sections of the order of 1 pb [12]. SUSY predicts light supersymmetric partners of the top and bottom quarks [13], of several hundreds GeV (even if other coloured supersymmetric particles are much heavier) due to the mixing of the right- and left-handed supersymmetric quarks, and the strong Yukawa coupling. Thus, these two particles and the gluinos provide a gateway into the SUSY world, with other supersymmetric particles likely to be found in the subsequent decays of these particles. In R-parity conserving SUSY [14], the production of supersymmetric partners of the top and bottom quarks results in a final state with several jets identified as originating from a b-quark (b-jets), possible leptons, and missing transverse energy originated from the so-called lightest supersymmetric particle (LSP).

The first 1 fb^{-1} of data delivered by the LHC has shown no evidence for new physics beyond the Standard Model, where hundreds of theory papers have been tossed into the furnace [15], including some widely known benchmark models. As a consequence of the limits imposed, the heavy flavor final states are suggested as one of the most favored scenarios for physics beyond the SM to be observed at the LHC. Thus, the searches involving missing transverse energy in association with b-jets are eagerly waited by the physics community, and they are expected to be very promising for these final states given the total amount of recorded data by the ATLAS experiment during 2011.

In this thesis, the search for top and bottom squarks from gluino pair production in final states with missing transverse energy and at least three b-jets is presented, using 4.7 fb^{-1} proton-proton collisions at $\sqrt{s} = 7$ TeV of recorded data by the ATLAS detector during 2011. This analysis has never been done before in ATLAS.

The description of the work presented in this thesis is organized as follows. Chapter 1 begins with an introduction of the Standard Model of Particle Physics, with a special emphasis in QCD physics and its phenomenology. The formulation of Supersymmetric theories is introduced in Chapter 2 along with a description of the Minimal Supersymetric Standard Model (MSSM). In addition, a new strategy to characterize the first robust evidence for new physics likely to be seen at the LHC is also presented in this chapter, by means of the so-called *simplified models*.

The basic concepts needed for the understanding of the statistical treatment of the data is introduced in Chapter 3. It is focused primarily on searching for new signals in high energy physics, aiming at stating the precise definition and notation of the key components for setting exclusion limits or claiming a discovery.

Chapter 4 describes the LHC proton-proton collider and the ATLAS experiment. The acceleration chain the protons undergo prior to being injected into the LHC, which successively increase their energy, and imprint on the resulting beam structure and stability, is also discussed. Each of the ATLAS sub-systems is presented, with special emphasis in those relevant for this work. The trigger system is also described, along with a brief overview of the accelerator and detector performance during 2011

data-taking.

The experimental objects resulting from particles originated in the proton-proton collision (i.e., *signatures*) are reconstructed from the enormous variety of signals that the detector systems of the ATLAS experiment provide. These signatures are used in the analysis in order to provide a complete characterization of the event through the kinematics and dynamics of the particles involved. The experimental objects of importance for the analysis presented in this thesis are introduced in Chapter 5.

The contribution of the calorimeter information to the data analysis in ATLAS is of key importance to provide solid and common foundations for understanding the jet physics and missing transverse energy. A major task of the ATLAS jet calibration program is the precise determination of the jet energy resolution (JER), of key importance for the measurement of the cross-sections of inclusive jets, dijets or multijets, vector bosons accompanied by jets and top-quark measurements. Moreover, it has a direct impact on the determination of the missing transverse energy, which plays an important role in many searches for new physics with jets in the final state. Chapter 6 presents a major contribution of this thesis: the first determination of the jet energy resolution and its uncertainty with the `ATLAS` detector in proton-proton collisions at a centre-of-mass energy of $\sqrt{s} = 7$ TeV. The jet energy resolution is determined by exploiting the transverse momentum balance in events with jets at high transverse momenta (p_{T}). The techniques used to estimate the jet energy resolution from calorimeter observables are discussed in detail.

The SUSY physics analysis itself is covered from Chapter 7 to Chapter 9. The search strategy is presented in Chapter 7. Monte Carlo simulated event samples are used in order to aid in the description of the Standard Model background processes and to model the SUSY signals. The final state object definition and the event selection used, along with a complete overview of the optimization procedure implemented to determine the enriched signal regions (SR) are discussed in detail, as these allow to identify possible SUSY-like event candidates with b-jets and missing transverse energy. The description of the procedures to evaluate the systematic uncertainties for SM background and SUSY signal processes is presented. It includes the systematic uncertainties depending on the luminosity and pile-up running conditions, detector effects, objects reconstruction and identification, among others (*experimental uncertainties*), and the uncertainties in the generation model (*theoretical uncertainties*).

The Standard Model background estimation is presented in Chapter 8. For each of the SM backgrounds, the corresponding technique implemented to estimate their contribution to the signal region yields and the different sources of systematic uncertainties are discussed in detail. The background predictions, normalised to theoretical cross sections, including higher-order QCD corrections when available, are also compared to data in the so-called background-enriched control regions (CR).

Chapter 9 presents the final results of the search, obtained using the data col-

lected during 2011 corresponding to a total integrated luminosity of 4.7 fb^{-1}. The observed event yields are compared to the SM background prediction as determined in Chapter 8. An interpretation of the results in terms of a variety of models is also discussed in detail. Finally, the conclusions of this thesis are presented in Chapter 10.

1

The Standard Model framework

The first formulation of a quantum theory describing radiation and matter interaction was introduced in 1920s by Dirac [16]. During the late 1940s and early 1950s, Tomonaga [17], Schwinger [18] and Feynman [19] developed the Quantum Electrodynamics (QED) theory to describe the electromagnetic interactions of electrons and photons. The weak theory was initially proposed by Enrico Fermi in 1934 to explain the proton β-decay [20]. In 1967, the electromagnetic and weak interactions were successfully unified by Glashow, Weinberg and Salam [3–5], where both interactions were combined into one single theoretical framework in which they appear as two manifestations of the same fundamental interactions. This unification constitutes the core of the Standard Model of particle physics (SM).

The SM is the most compelling, consistent, finite, computable and precise theoretical framework to understand the fundamental microscopic interactions, and provides a remarkably successful description for nearly all electroweak and strong interaction phenomena. The SM includes e.g., the forces that hold together the protons and the neutrons in the atomic nuclei, associated to strong interactions, the binding of electrons to nuclei in atoms or of atoms in molecules, caused by electromagnetism and the energy production in the sun and the other stars which occurs through nuclear reactions, induced by weak interactions. In principle gravitational forces should also be included in the list of fundamental interactions but their impact on fundamental particle processes at accessible energies is totally negligible.

In the SM framework, the fundamental constituents of matter are *fermions*, and their interactions are mediated by integer spin particles called *gauge bosons*. The SM encompasses quantum electroweak and chromodynamic theories into an internally consistent framework that describes the interactions between all known particles in terms of quantum field theory. The description of electroweak and strong interactions is introduced in terms of symmetries, using the formalism of gauge theories,

which play a fundamental role in particle physics. The SM is a renormalizable field theory based on a local symmetry (i.e., separately valid at each space-time point x) with a set of conserved currents and charges. The commutators of the color and electro-weak charges form the $SU(3)_C \times SU(2)_L \times U(1)_Y$ algebra, which the SM gauge theory is based on. The hypercharge Y, the left chirality L[1], and the colour charge C, correspond to the conserved quantities of the symmetry group [21]. The subgroups $SU(2)_L \times U(1)_Y$ and $SU(3)_C$ represent the quantum electroweak and the quantum chromodynamic sectors, respectively. The conserved charged of $SU(2)$ is the weak isospin T, from which the electric charge Q is defined through the Gell-Mann-Nishijima formula $Q = T_3 + \frac{Y}{2}$ [22, 23], with the third component of weak isospin written as T_3. A complete discussion of the SM is broadly available in the literature [24, 25].

1.1 Particle content and interactions

The Standard Model includes twelve elementary particles of spin one-half that obey the Fermi-Dirac statistic: the fermions. These are classified according to how they interact (i.e., charges they carry) and they are divided in two families: *quarks* and *leptons*. There are six flavours of quarks; *up* (u), *down* (d), *charm* (c), *strange* (s), *top* (t) and *bottom* (b). The quarks interact via the strong interaction and they carry an internal quantum number denoted as color charge (C), which represents the charge associated to the strong interaction. The color charge is of three types: red (r), green (g) and blue (b). Quarks are bound to one another, forming color-neutral composite particles (hadrons) containing either a quarks and antiquark (mesons) or three quarks (baryons). They also carry fractionary electric charge (2/3 or $-1/3$) and weak isospin, hence, quarks interact with other fermions both electromagnetically and via the weak interaction. Therefore, quarks experiment the four fundamental forces. Fermions that do not carry colour charge are called leptons, and there are six flavours of them; *electron* (e^-), *muon* (μ^-), *tau* (τ^-) and their corresponding neutrinos, denoted by ν_e, ν_μ and ν_τ, respectively. The neutrino does not carry electric charge either, so its dynamics is driven by the weak nuclear force only. The electron, muon, and tau leptons interact both electromagnetically and weakly. Pairs from each classification are grouped together to form a generation, with corresponding particles exhibiting similar physical behaviour. The pattern is as follows:

$$\begin{pmatrix} \nu_e \\ e^- \end{pmatrix}_L \begin{pmatrix} \nu_\mu \\ \mu^- \end{pmatrix}_L \begin{pmatrix} \nu_\tau \\ \tau^- \end{pmatrix}_L \quad \text{and} \quad \begin{pmatrix} u \\ d' \end{pmatrix}_L \begin{pmatrix} c \\ s' \end{pmatrix}_L \begin{pmatrix} t \\ b' \end{pmatrix}_L . \tag{1.1}$$

[1]The particle chirality is the projection of its spin in the direction of its momentum. Thus, a particle with the spin parallel to its momentum has positive chirality, and the opposite is defined as negative chirality.

Each family contains a weakly charged doublet of quarks (in three color replicas), and a colorless weakly charged doublet with charged lepton and its associated neutrino. In addition, each generation contains two flavours of quarks with baryon number B = 1/3 and lepton number L = 0, and two leptons with B = 0 and L = 1. The left-handed (i.e., negative chirality) leptons and quarks, denoted with subscript L, are arranged into three generations of $SU(2)_L$ doublets, with the corresponding right-handed (i.e., positive chirality) fields transforming as singlets under $SU(2)_L$. Each particle has also a corresponding antiparticle with the same mass and opposite quantum numbers. The primed quarks in Eq. 1.1 are weak eigenstates related to mass eigenstates by the so-called Cabibbo-Kobayashi-Maskawa (CKM) matrix [26, 27]. The fermionic sector of the Standard Model is summarized in Table 1.1.

QUARKS (spin = $\frac{1}{2}$)								
1^{st} Generation			2^{nd} Generation			3^{rd} Generation		
Particle	mc^2	Q[e]	Particle	mc^2	Q[e]	Particle	mc^2	Q[e]
u	2.4 MeV	$\frac{2}{3}$	**c**	1.27 GeV	$\frac{2}{3}$	**t**	171.2 GeV	$\frac{2}{3}$
d	4.8 MeV	$-\frac{1}{3}$	**s**	104 MeV	$-\frac{1}{3}$	**b**	4.2 GeV	$-\frac{1}{3}$
LEPTONS (spin = $\frac{1}{2}$)								
1^{st} Generation			2^{nd} Generation			3^{rd} Generation		
Particle	mc^2	Q[e]	Particle	mc^2	Q[e]	Particle	mc^2	Q[e]
ν_e	<2.2 eV	0	ν_μ	<0.17 MeV	0	ν_τ	<15.5 MeV	0
e	0.511 MeV	−1	μ	105.7 MeV	−1	τ	1768 MeV	−1

Table 1.1 Fermionic sector of the Standard Model. Masses are taken from the Particle Data Group (PDG) [28].

In the Standard Model framework, gauge bosons are defined as force carries that mediate the strong, weak and electromagnetic fundamental interactions. The SM explains such forces through quantum perturbation theory as resulting from matter particles exchanging other particles, known as force mediating particles. At macroscopic level, the effect is equivalent to a force influencing both of them, and the particle is said to have mediated that force. The gauge bosons of the Standard Model all have integer spin, of value one. Thus, they obey a Bose-Einstein statistic. The electromagnetic force between electrically charged particles is mediated by the photon, denoted by γ, which is massless and well-described by the QED theory. The

weak interactions between particles of different flavours (all quarks and leptons) are mediated by the W^+, W^- and Z gauge bosons, which are all massive. The $W^\pm$ carries an electric charge of ± 1, and couples to the electromagnetic interaction. The weak interactions involving the $W^\pm$ exclusively act on left-handed particles and right-handed anti-particles only. The electrically neutral Z boson interacts with both left-handed particles and antiparticles. The W bosons may also interact among themselves, and with Z and γ, as the W^+ and W^- are both weakly and electrically charged. The three weak gauge bosons along with the photon are grouped together, as collectively mediating the electroweak interaction. The remaining bosons are called gluons (g), and there are eight in total. They are massless and mediate the strong interaction between color charged particles. Since gluons have an effective color charge they can also interact among themselves. Quarks, gluons and their interactions are described by the theory of Quantum Chromodynamics (QCD), and it is further discussed in Section 1.3. The SM gauge bosons are summarized in Table 1.2.

Gauge Bosons (spin = 1)			
Particle	mc^2	Interaction	Q[e]
g	0	strong/colour $SU(3)_C$	0
$W^\pm$	80.403 GeV	weak charged	± 1
Z	91.1876 GeV	weak neutral	0
γ	0	electromagnetic $U(1)_{\text{em}}$	0

Table 1.2 Standard Model gauge bosons and the corresponding interactions. Masses are taken from the Particle Data Group (PDG) [28].

1.2 Higgs mechanism

The photon and the gluons have zero masses as a consequence of the exact conservation of the corresponding symmetry generators: the electric charge and the eight color charges, respectively. On the other hand, the weak bosons have large masses signalling that the corresponding symmetries are largely broken. The Standard Model predicts in principle massless fermions and gauge bosons, in contradiction with the observations. The idea behind the underlying mechanism for generating non-zero masses while preserving the renormalisability of the theory was initially studied by Nambu, Goldstone [29, 30] and Anderson [31], and developed into a full relativistic model in 1964 independently and almost simultaneously by

three groups of physicists: Higgs [32,33], Englert and Brout [34], and Guralnik, Hagen and Kibble [35]. Furthermore, Higgs proposed the existence of a hypothetical massive scalar elementary particle as a proof for this idea [36]. This particle has no intrinsic spin, and therefore is classified as boson. A spontaneous breaking of the electroweak gauge symmetry in the SM is induced:

$$SU(3)_C \times SU(2)_L \times U(1)_Y \rightarrow SU(3)_C \times U(1)_Q \ , \tag{1.2}$$

and it results in the generation of the massive $W^{\pm}$ and Z gauge bosons via the so-called Higgs mechanism, predicting also the presence in the physical spectrum of one spin-0 particle, *the Higgs boson* [24,25]. Weinberg and Salam were the first to apply the Higgs mechanism to the breaking of the electroweak symmetry [4,5] and showed how a Higgs mechanism could be incorporated into Glashow's electroweak theory [3], setting thus the foundations of the Standard Model of particle physics.

The relationship between the masses of $W^{\pm}$ and Z gauge bosons predicted by the SM is given by:

$$m_W = m_Z \cos\theta_W \ , \qquad \text{with } \tan\theta_W = g^{'}/g \ , \tag{1.3}$$

where the weak mixing angle θ_W relates the electromagnetic and weak coupling constant, denoted by g and $g^{'}$, respectively. The $W^{\pm}$ and Z vector bosons were discovered in 1982 by the UA1 and UA2 collaborations at the CERN S$p\bar{p}$S [37,38], where the prediction given by Eq. 1.3 was successfully verified. Furthermore, not only the bosons acquire mass through the Higgs mechanism but also the fermions. The masses are not predicted by the SM so they are just parameters of this framework. After the discovery of the top quark in 1995 by DZero and CDF Collaborations [39,40], the masses of the fermions have been all measured experimentally[2].

On 4^{th} July 2012, the ATLAS [2] and the CMS [41] experiments at the LHC independently announced that they each confirmed the formal discovery of a previously unknown boson of mass between 125 and 127 GeV/c^2, whose behaviour has been found (so far) to be consistent with a Standard Model Higgs boson [42,43]. Currently, a tremendous experimental effort is underway aimed at understanding the Higgs sector of the SM.

1.3 Quantum Chromodynamics

The study of the strong interactions was transformed with the advent of accelerators in the multi-GeV energy range in the mid 20^{th} century. The huge effort to describe the rich spectrum of mesons and hadron resonances that were discovered during the 1950s, prompted Gell-Mann and Zweig [44–46] to propose in 1964

[2] In the SM framework, the neutrinos are massless.

the quark model. This framework could rationalize the vast hadron spectroscopy already observed in terms of smaller particles; the quarks, in the fundamental representation of $SU(3)$. Mesons and hadrons were interpreted as excited bound states of these point-like constituents. The idea that quarks have an additional quantum $SU(3)$ degree of freedom, the color charge, was introduced later, with the possibility that these particles might interact via an octet of vector gauge bosons; the gluons [47–49]. The famous high-energy inelastic electron-proton scattering experiments at SLAC during the 1960s and 1970s were the first to spectacularly verify the point-like substructure of hadrons [50,51], which confirmed the scale invariance phenomenon anticipated by Bjorken, i.e, that scattering of high-energy electrons on the proton where independent of four-momentum transferred [52]. The parton model, introduced within those days by Feynman, showed that elementary constituents interacting weakly, that he referred to as "partons", could also convincingly explain the central experimental results in deep inelastic scattering experiments [53]. In the early 1970s, the newfound ability to quantize gauge theories in a manner that was at once unitary and renormalizable prompted naturally the idea of extending a global color model to a $SU(3)$ Yang-Mills gauge theory [54] of color-charged quarks and gluons. Such theoretical framework was successfully achieved in 1973, and it is referred to as Quantum Chromodynamics (QCD) [6–9]. The most prominent properties of QCD are *asymptotic freedom* and *confinement*, and they are introduced next.

1.3.1 Asymptotic freedom and confinement

One of the approaches to solving QCD is referred to as Perturbative QCD (pQCD) [55], which essentially relies on the idea of an order-by-order expansion of a given observable in terms of a small coupling $\alpha_s \equiv g_s^2/4\pi \ll 1$, where g_s denotes the QCD coupling constant. By early 1970s, it was clear that any field theory of the strong interactions would have to have an energy-dependent coupling strength, to harmonize the low-energy nature of the strong interaction with their weakness at high energy. In field theory the effective coupling of a given interaction vertex is modified by the interaction. As a result, the measured intensity of the force depends on the transferred four-momentum squared Q^2, among the particles participants. On the other hand, quantum field theory integrates out the physics at high scales using the renormalization procedure [56], necessary in order to allow the theory to give meaningful (i.e. non-infinite) results that can be compared to the experimental measurements. This procedure introduces a correction to the renormalised parameter, which depends on the physical scale at which the measurement is made (Q^2) and the so-called renormalisation scale, denoted by μ_R. The QCD coupling dependence on the scale μ_R is expressed in terms of the QCD renormalization group equation [55]. The amplitude of the strong interaction process at a given momentum transfer Q^2

can be parameterized in terms of the running coupling constant $\alpha_s(\mu_R)$ as [55]:

$$\alpha_s(Q^2) = \frac{1}{b_0 \ln \frac{Q^2}{\Lambda^2_{\mathrm{QCD}}}} , \quad \text{with } \mu_R \approx Q^2 , \tag{1.4}$$

where b_0 denotes a known constant and Λ_{QCD} refers to the scale at which the coupling diverges, of order 200 MeV/c. Thus, only for scales $\Lambda_{\mathrm{QCD}} \ll Q$, corresponding to $\alpha_s \ll 1$, the pQCD theory is valid. The coupling $\alpha_s(Q^2)$ decreases for increasing Q^2 (i.e., small distances) and vanishes asymptotically. Figure 1.1 (left) shows the running of α_s at various scales, illustrating the good consistency of the measurements with the expected behaviour from theory [57]. The QCD interaction becomes very weak in processes with large Q^2, therefore the quarks and gluons behave as essentially free in such limit. This phenomenon is referred to as asymptotic freedom, and it was discovered by Gross, Politzer and Wilczek [58, 59] in 1973. On the contrary, the interaction strength becomes large at small transferred momenta (i.e. large distances), of order $Q \lesssim \Lambda_{\mathrm{QCD}}$. The increasing force either binds the quarks together or it breaks when the energy density of the colour field between the quarks is great enough to create from the vacuum quark-antiquark pairs. As consequence, quarks do not exist in isolation, but rather hadronize to form tightly bound composite states of quarks, with compensating color charges so that they are overall neutral in color (hadrons). The impossibility of separating color charges as individual quarks and gluons is known as confinement [60]. Consequently, the experimental signatures of quarks and gluons are the final state hadrons into which they eventually coalesce. The bundle of particles produced tends to travel collinearly with the direction of the initiator quark or gluon. This results in a spray of hadrons entering the detector in place of the original parton, referred to as a *jet*. The first evidences of jets were observed in electron-positron collisions at SLAC in 1975 [61] and at CERN $Sp\bar{p}S$ collider in 1982 [62] (Figure 1.1, right).

1.4 Jet physics and phenomenology

The knowledge of the different phenomena that take place in a proton-proton (pp hereafter) collision is of key importance for understanding the resulting event correctly. The collimated shower of particles mentioned at the end of the previous section are the product of many different steps associated to various physics processes, and they are highlighted next in an inwards-outwards flow (i.e., from short-distance processes to long-distance ones).

1. Initially two hadrons are coming in on a collision course, where each hadron can be viewed as a group of partons. Each particle is characterized by a set of parton distributions, defining the partonic substructure of the incoming

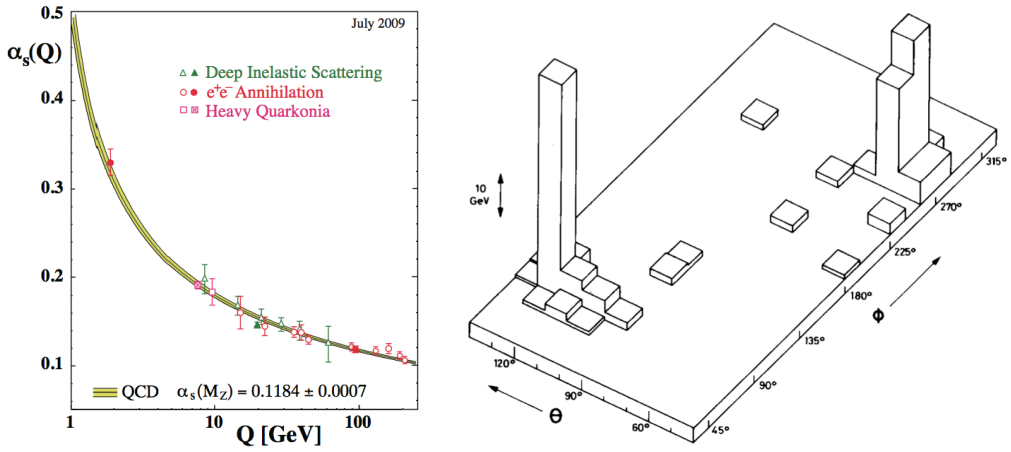

Figure 1.1 The QCD coupling as measured in physics processes at different scales Q, together with the band obtained by running the world average for α_s within its uncertainties (left). First evidence for hadronic jet production as observed by the UA2 experiment at the CERN $Sp\bar{p}S$ collider (1982). The cell energy distribution is shown as a function of the polar and azimuthal angles θ and ϕ, respectively (right).

hadrons.

2. In a collision-scenario with accelerated particles carrying electromagnetic and colour charges, bremsstrahlung can occur, e.g, as gluon radiation such as $q \to qg$. Emission that are started off from the two incoming colliding partons are called Initial-State Radiation (ISR).

3. A collision between two partons, one from each side, takes place and gives the hard process of interest, that can be calculated by a perturbative approach to some order in α_s.

4. After the collision, outgoing partons can also radiate. Emission that can be associated with the outgoing partons are instead called Final-State Radiation (FSR).

5. Colour field strength increases as partons recede, and they can break up by the production of new quark-antiquark pair. Thus, quarks and antiquarks may combine to produce a primary hadron. The creation of hadrons as a consequence of the confimenent phenomenon is referred to as *hadronization*.

6. Each of the incoming hadrons is made up of a multitude of further partons, which may also collide within one single hadron-hadron collision. These semi-hard secondary collisions are referred to as multiple parton interactions (MPI)[3]. Each of these further collisions also may be associated with its ra-

[3]These are different from pile-up events, when several hadron pairs collide during a bunch-bunch crossing.

diation. The remnants form a net colour charge generating further hadrons. The additional products of the collision that are not explicitely related to the hard process of the collision (radiation, hadron remnants, products of multiple parton interactions, etc.), are generally grouped altogether and referred to as *the underlying event*.

The processes that take place during a pp collision cannot completely be calculated through pQCD. Currently, there are different Monte Carlo (MC) tools available, involving various suitable approximations, that have been developed to address some of the phenomena mentioned above (see [63, 64] and references therein). The key features of the MC tools required for the understanding of the analysis presented in this thesis are discussed next.

1.4.1 Hard interaction and parton shower

In order to describe a $2 \to n$ process from the Lagrangian of the theory (where n represents a large number of partons in the final state), a set of Feynman rules are initially derived and *matrix elements* (ME) can then be calculated in powers of the strong coupling constant α_s. The leading-order (LO) $2 \to 2$ processes, of $\mathcal{O}(\alpha_s^2)$, are the simplest one can imagine at a hadron collider, but in reality one needs to go on to higher orders for a reliable description of most phenomena. For instance, in next-to-leading order (NLO) $2 \to 3$ calculations, of $\mathcal{O}(\alpha_s^3)$, two kind of Feynman diagrams generally enter. First, when one additional parton is present in the final state. The cross section for such processes is almost always divergent if one of the parton energies vanish (soft singularities) or two partons become collinear (collinear singularities). The other kind is associated to loop graphs, with an additional intermediate parton not present in the final state (i.e., a correction to the $2 \to 2$ processes). For inclusive event properties, these NLO calculations lead to an improved accuracy of predictions. The procedure of calculating a given observable at a fixed-order in α_s is implemented in matrix-element-centered Monte Carlo programs for each relevant partonic process. A wide spectrum of these are available, each with calculations available for many processes at different orders. For the analysis presented in this thesis, these include `ALPGEN` [65] and `MADGRAPH` [66], with tree-level matrix element calculations (the former with up to $n \leq 6$ partons), and `MC@NLO` [67], with exact matrix element calculations up to one-loop.

The factorially increase of Feynman diagrams with the number of outgoing partons allows only a few QCD processes to be calculated beyond leading order (LO). Therefore, other approaches involving the sampling of the phase-space available for gluon emission with additional approximations need to be implemented. A complex $2 \to n$ process can be factorized into a simple core process, e.g., $2 \to 2$, convoluted with a set of probabilities of partons to split. Simulation programs implementing

this approach include PYTHIA [68] and HERWIG++ [69–71]. These use LO perturbative calculations of matrix elements for 2 →2 processes and implement higher-order QCD processes approximately via the so-called initial- and final-state *parton showers* (PS) [64, 72] to produce the equivalent of multi-parton final states.

In a hard process with virtuality Q^2 (i.e., hardeness), the incoming (outgoing) partons are expected to radiate a succession of harder (softer) gluons while approaching the collision. The emission ratio for a branching such as $q \to qg$ diverges when the gluon either becomes collinear with the quark or when the gluon energy vanished. Furthermore, the non-Abelian character of QCD leads to $g \to gg$ branchings with similar divergences. The third main branching $g \to q\bar{q}$ does not have the soft divergent feature and therefore has a lesser effect. The parton shower needs to be matched to the ME calculation to avoid double counting of radiation generated by both the hard scattering and by the PS. Initial-state radiation is generally modelled by a sequence of emissions that, starting from the scale where confinement becomes important, increase the virtuality in each emission until it matches the Q^2 of the hard process. Similarly, the final-state radiation is constituted by a sequence of emissions that decrease the virtuality of the partons until a lower cut-off is reached; $Q_0^2 \approx \Lambda_{\mathrm{QCD}} \lesssim 1$ GeV. Thus, the whole phase space is expected to be covered with a smooth transition from ME to PS. Below Q_0^2, no further branchings are simulated. Perturbation theory cease to be meaningful, and confimenent effects and hadronization phenomena take over. Different MC programs control the coherence of these emissions by ordering successive emissions in terms of their transverse momenta (p_{T}) or angle with respect to the parton direction. PYTHIA and HERWIG++ generally provide shower models that are p_{T}^2- and angular-ordered, respectively. Matrix-element programs are usually interfaced with some of these programs to provide the parton shower and the hadronization model (e.g., ALPGEN is commonly interfaced with HERWIG). Matrix elements and parton showers are complementary descriptions of parton production, with ME generally needed to describe hard and widely separated jets and PS commonly needed for describing very high jet multiplicities along with the evolution to the hadronization scale. However, for a realistic description of multijet backgrounds, it is necessary to combine both descriptions. Thus, the interfacing of LO matrix element calculations to PS is generally done using a matching procedure (MLM [73] or CKKW [74, 75]), that essentially rely on a slicing of the phase space where some region is constrained to be generated by the parton shower (if it is most accurate), whereas the rest is covered by the ME calculation (i.e., where the PS approximation has limitations).

1.4.2 Parton distribution function and factorization

The modelling of initial-state radiation has an additional feature, due to the non-trivial structure of the incoming hadrons. A proton is made up out of three quarks,

uud, plus the gluons that bind them together. However, gluons are continuously emitted and absorbed by the quarks, and each gluon may in its way temporarily split into two gluons or into a $q\bar{q}$ pair. Thus, the proton is teeming with activity, most taking place in a non-perturbative regime. Partons within a hadron are conventionally divided between gluons, valence quarks and sea quarks. Valence quarks are responsible for the hadron's quantum numbers, whereas sea quarks are generated quark/antiquark pairs from quantum fluctuations. In the description of the parton kinematics inside the hadrons, the concept of a parton distribution function $f_i(x, Q^2)$ (PDF) is introduced [55], describing the probability to find a parton of species i in a hadron, with a fraction x of the hadron energy-momentum when the hadron is probed at a resolution scale Q^2.

One of the reasons of the success of QCD as a predictive theory is that the short-distance component of the scattering process described by perturbative QCD can be separated from the non-perturbative long-distance component. This result is known as the factorisation theorems [76], which essentially imply that perturbation theory can be used to calculate the hard scattering cross section, while universal functions such as the PDFs can be included a posteriori to obtain the full theoretical prediction. The cross-section for a hard scattering process $pp \to X$, initiated by two hadrons with four-momenta p_a and p_b can be written as:

$$\sigma_{p_a,p_b\to X} = \sum_{i,j} \int_0^1 dx_a \int_0^1 dx_b \; f_{i/a}(x_a, \mu_F^2) f_{j/b}(x_b, \mu_F^2) \times \hat{\sigma}_{i,j}(p_a, p_b, \alpha_s(\mu_R^2), Q^2/\mu_R^2, Q^2/\mu_F^2) \; , \tag{1.5}$$

where $f_{i/a}$ and $f_{j/b}$ are the parton momentum distributions for the two interaction partons i, j with respect to hadrons a, b. These are defined at the factorization scale μ_F, introduced to separate the soft and the hard processes. The main idea behind using such scale is that any emissions that ocurr with a transverse momentum less than μ_F are absorbed (i.e., factorized) into the PDF itself. The parton-parton cross-section is denoted as $\hat{\sigma}_{i,j}$. This quantity is, in addition, defined at the renormalization scale μ_R. Often, these scales can be identified with one another and written as $\mu_R = \mu_F = \mu$.

Perturbative QCD does not predict the dependence of the PDFs on the fraction x. Data from different experiments is used to parameterize the PDFs at different starting scales Q_0^2. The predictions for each parton distribution at a different Q^2 are obtained using the DGLAP evolution equations [77], which describe the change with Q^2 of the quark densities due to gluon radiation and gluon splitting, and of the gluon density due to radiation from quarks and gluons. The understanding of the PDFs plays a key role on interpreting the data at hadron colliders in terms of the SM predictions and possible deviations. Dedicated groups perform the parameterisation of PDFs using data from different experiments and processes. The analysis presented

in this thesis uses the LO, LO* (i.e., hybrid LO-NLO), NLO, and NNLO PDFs obtained by the CTEQ [78,79] and MRST/MSTW [80,81] Collaborations.

In principle any observable must be independent of the particular arbitrary renormalization and factorization scales chosen. Nevertheless, in most cases the observables are calculated to a certain order in pQCD. Thus, the dependence on μ_R and μ_F is still present when truncating the theoretical calculation at a given order and therefore it introduces an uncertainty on the theory predictions. The uncertainties associated to the chosen scales and their treatment for the analysis presented in this thesis are discussed in Section 7.4.

1.4.3 Hadronization

As the evolution reaches $Q_0^2 \approx \Lambda_{\mathrm{QCD}}$, the parton shower phase is truncated since the coupling forces become significant and confinement takes place. This phenomenon cannot still be described from first principles, and therefore, it involves some modelling to transform all the outgoing coloured partons into colourless hadrons of a typical 1 GeV mass scale. This process of creating hadrons is referred to as *hadronization*. The dynamics of this evolution is generally absorbed in fragmentation functions that represents the probability of a parton to fragment into a certain hadron of the final state. Many of these primary hadrons are unstable and decay further at various timescales. Those that are sufficiently long-lived have their decays visible in the detector, or they are stable. There are several models of the hadronization process, that attempt to connect the results of the parton shower and the final particle spectrum observed. These models can be complemented and tuned using experimental observations. The hadronization is commonly described by either the string fragmentation model [82,83] (as implemented in `PYTHIA`), or the cluster fragmentation model [84] (as implemented in `HERWIG`). Essentially, the string fragmentation model asummes a linear confinement, where the energy stored in the colour field between quarks and antiquarks is assumed to increase linearly with the separation of colour charges. Thus, it depicts the color force by means of a lineary rising potencial as charges separate. The potential energy stored increases as partons recede, so it may break up by the production of new quark-antiquark pairs that screen the endpoint colours. Then, quarks and antiquarks may combine to produce hadrons. Figure 1.2 (left) shows a schematic diagram of string fragmentation. The cluster fragmentation model is essentially based on the colour preconfinement property of the branching processes, which assumes that the separation of the colour charges forming a singlet are inhibited. After the perturbative parton branching process, the remaining gluons are splitted into light $q\bar{q}$ pairs, and then neighbouring quarks and antiquarks can be combined into colour singlets, with masses distributions peaking at low values and asymptotically independent of the hard subprocess scale. Figure 1.2 (right) shows a schematic diagram of cluster fragmentation.

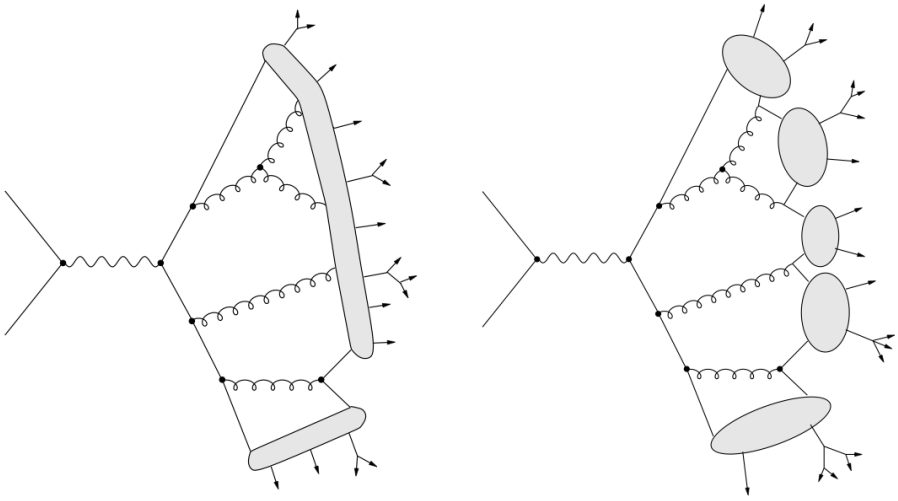

Figure 1.2 Most common phenomenological models for describing the parton shower in Monte Carlo simulations. Left: the string model, or the "Lund model" as implemented in `PYTHIA` leading order Monte Carlo program. Right: the cluster fragmentation model as in the `HERWIG` event generator.

1.4.4 Underlying event

The understanding of hadronic collisions also depends on the knowledge of the interactions between the partons that do not get involved in the hard scatter. Each of the incoming hadrons is made up of a multitude of further partons, which may also collide within one single hadron-hadron collision. Several non-perturbative effects take place, as multiple parton-parton interactions. In addition, these can produce softer partons that may interact (by color connections and reconnections) with others from the parton shower originated by the hard scatter. Thus, the colour flow is tied up with the structure of beam remnants. The additional products of the collision that are not explicitely related to the hard process of the collision, as radiation, hadron remnants, products of multiple parton interactions, are referred to as *the underlying event* (UE). Generally, the UE occurs softly and their cross-sections and properties can not be calculated in the perturbative regime. Moreover, the UE does not only impact on how the hard scatter showers and hadronizes, but also it may place for instance additional energy in the direction of a jet initiated from the hard scatter. Therefore an understanding of the UE is of key importance to properly link the jet measurements to the hard scatter properties. Several models for UE and its components have been implemented in different Monte Carlo generators, usually tuned to fit a specific set of collider data. For the analysis presented in this thesis, the ATLAS tunes to Monte Carlo generators referred to as AMBT1/AUET1 have been used [85, 86]. Overall, the complex picture of a hadron-hadron collision introduced in this section is illustrated in Figure 1.3.

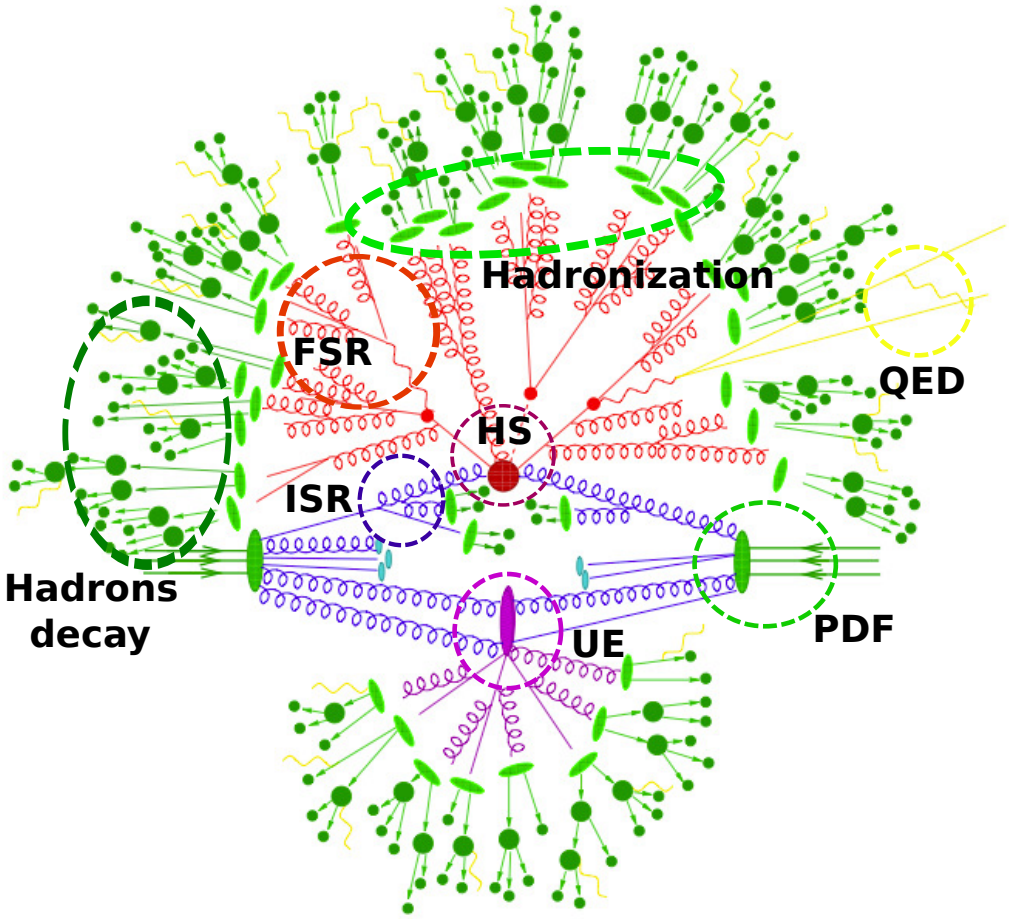

Figure 1.3 Illustration of the complex picture of a hadron-hadron collision introduced in this chapter. The different stages of the Monte Carlo simulation are shown: the hard interaction (HS) that depends on the parton density function (PDF), the initial- and final-state radiation (ISR and FSR, respectively), the hadronization, the subsequent hadron decays, and the underlying event (UE). Furthermore, photon radiation may occurs at any stage (QED).

2

The Supersymmetric extension of the Standard Model

2.1 The limitations of the Standard Model

The Standard Model has been a pillar of fundamental physics during the last 40 years. For decades, the SM has been subjected to thorough experimental scrutiny and has been found to be in stupendous agreement with experimental measurements, tested in some cases to a precision greater than 0.1 %. Nevertheless, there are a wide range of reasons to believe that the Standard Model is incomplete, associated with a variety of nagging theoretically motivated problems which cannot be solved without the introduction of some new physics. The SM is somehow unsatisfactory, as it does not explain the particle quantum numbers, such as the electric charge, the weak isospin, hypercharge and colour. Related aesthetic or philosophical questions arise too: why are left-handed fermions in SU(2) doublets and right-handed ones in SU(2) singlets? Why are there three colors? Why is electric charge quantized? How many generations are there? Why do the Cabibbo-Kobayashi-Maskawa (CKM) angles and the mixing angle have the values they do?

Even if one accepts the peculiar set of group representations and hypercharges that the SM requires, it contains at least 19 arbitrary parameters (three independent gauge couplings, and a possible CP-violating strong-interaction parameter, six quark and three charged-lepton masses, three generalized Cabibbo weak mixing angles and the CP-violationg Kobayashi-Maskawa phase, as well as two independent masses for weak bosons). The Standard Model requires a mechanism to give masses to the W and Z bosons and to the fermions. The Higgs Mechanism provides an explanation, which in-turn implies a fundamental scalar, the Higgs boson. However, it is widely thought that deeper problems exist, connected with the Higgs boson, which suggest

that is is necessary to look beyond the Standard Model to understand the Higgs sector of the theory. These are closely related to a required additional symmetry to protect the Higgs from radiative corrections and stabilize the electroweak scale (see Section 2.1.2). Without such an additional symmetry, the Standard Model remains incomplete.

Moreover, additional parameters must be introduced to accommodate neutrino oscilations and even more would be needed to accommodate other non-accelerator observations [87]. Furthermore, cosmological examples include Dark Matter (DM). A successful DM candidate must be stable, electrically neutral, weakly interacting and massive (non-relativistic) [28,88–91]. This excludes any known Standard Model particle.

The questions raised above, i.e., the big issues that any new model associated to physics beyond the Standard Model should try to address, can be conveniently grouped into three broad categories of [92]:

- **Mass**: what is the origin of particle masses, are they really due to a Higgs boson, and if so, why are the masses so small compared to the Plack mass?
- **Unification**: is there a simple group framework for unifying all the particle interactions, a so-called Grand Unified Theory (GUT)? Does it predict observable new phenomena and relations between parameters of the SM?
- **Flavour**: what is the origin of the six flavours of quarks and leptons and why do their weak interactions mix in the peculiar way observed?

Finally, the difficulty of accomodating gravity within the SM framework may suggest that in principle the SM is the low energy effective theory of a more fundamental one at some high energy scale. However, physicists have not yet been able to construct a consistent quantum theory of gravity that makes clear experimental predictions.

2.1.1 Fine-tuning, naturalness and hierarchy problems

The Higgs boson mass could not have been too heavy [42,43], since for a Higgs mass of the order of a few TeV, the Higgs self-coupling gets too strong, contradicting the succesful perturbation theory at low energies observed [93]. If one denotes μ_2 the scale at which $SU(2) \times U(1)$ breaking takes place, and assumes there is a more fundamental theory which becomes relevant at a higher scale, denoted μ_1 (e.g., a grand unification scale $M_{GUT} \approx 10^{15} - 10^{17}$ GeV or the Planck scale $M_P \approx 10^{19}$ GeV, where gravitational effects become significant on a microscopic level), three interesting features are observed:

- Why is $\mu_2 \ll \mu_1$? This is referred to as the *hierarchy problem* [94–96]. Even in the absence of grand unification of strong and electroweak forces at high

energy scales, it is clear the Standard Model must be modified to incorporate the effects of gravity at the Planck scale ($M_P \simeq 10^{19}$ GeV). In this context, it is a mystery why the ratio $m_W/M_P \simeq 10^{-17}$ GeV is so small. Thus, the mere fact that M_P/m_W is so huge provides a powerful clue to strongly believe that new physics should in principle exist in the $\mathcal{O}(17)$ of magnitude in energy between the presently explored territory near the electroweak scale (m_W) and the Planck scale (M_P).

- In order that $m_H^2(\mu_2) \ll \mu_1^2$, the parameter $m_H^2(\mu_1)$ must be tuned extremely accurately at each order in perturbation theory[1]. Given the large (negative) size of the radiative corrections, a Higgs mass of order the electroweak scale can only be obtained if $m_H^2(\mu_1)$ is of order μ_1^2, in such a way that when this is added to the squared mass shift arising from the radiative corrections, $m_H^2(\mu_2)$ is approximately $\mathcal{O}(17)$ magnitude smaller than the μ_1^2 scale. Hence, this feature is usually referred to as the *fine-tuning problem* [97].

- The requirement on the observable properties of a theory to be stable against minute variations of its fundamental parameters is known as the concept of naturalness. From the discussion above, the natural value for $m_H^2(\mu_2)$ cleary seems to be more like a number of order μ_1^2. The fact that the Higgs mass cannot be equal to its natural value of μ_1^2 is called the *naturalness problem* [98, 99].

2.1.2 The vanishing of quadratic divergencies

The vanishing of quadratic divergences is perhaps one of the primary motivations for pursuing an extension of the Standard Model, and it is discussed in this section. The fermion f couples to the Higgs H with a Lagrangian term $-\lambda_f H \bar{f} f$, and the variation of the fermion mass m_f due to the scalar loop quantum correction (Figure 2.1, left) can be proven to be

$$\Delta m_f = -\frac{3\lambda_f^2 m_f}{64\pi^2} \log \frac{\Lambda_{UV}^2}{m_f^2} + \dots \,, \tag{2.1}$$

where Λ_{UV}^2 is the ultraviolet momentum cut-off used to regulate the loop integral, corresponding to the scale beyond which the low energy theory no longer applies and new physics enters to alter the high-energy behaviour of the theory. The ellipses indicate terms independent of the cut-off. This correction clearly corresponds to a well-defined expansion for m_f, since by taking $\Lambda_{UV} \approx M_P$, it will lead to a 10% correction factor, approximately. Therefore, fermion masses are said to be natural.

[1] If one calculates the SM Higgs mass using the fundamental theory, the relevant quantity for the low energy theory is the running mass evaluated at the scale μ_2.

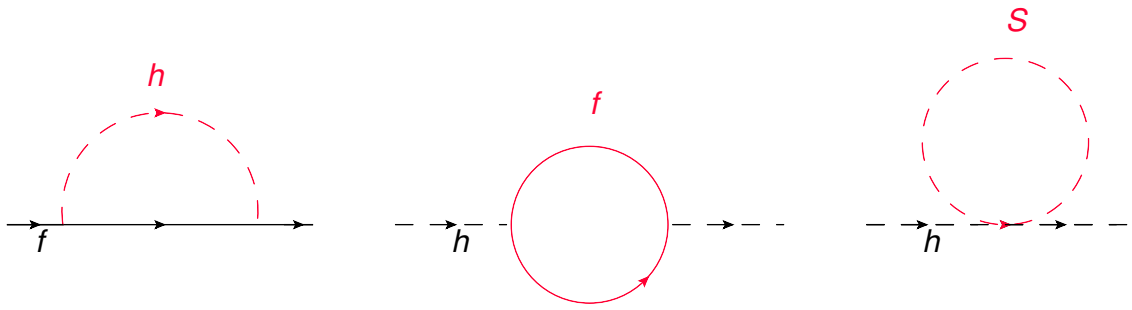

Figure 2.1 One-loop quantum correction to the fermion mass parameter m_f due to a scalar Higgs boson h (left). One-loop quantum correction to the Higgs squared mass parameter m_H^2, due to a Dirac fermion f (middle) and a scalar S (right).

The picture is quite different when one considers the variation of a scalar mass from a fermion loop (Figure 2.1, middle). For example, the radiative corrections to the mass of the Higgs boson of the Standard Model give

$$\Delta m_H^2 = -\frac{|\lambda_f^2|}{8\pi^2}\Lambda_{UV}^2 + \dots \ , \tag{2.2}$$

and therefore the Higgs boson mass diverges quadratically in Λ_{UV}. The ellipses represent terms proportional to m_f^2, which grow at most logaritmically with Λ_{UV}/m_f, and m_f can be any of the leptons and quarks of the Standard Model. Thus, there is nothing that protects[2] the Higgs mass from these quadratic divergences.

If one assumes there exists a heavy complex scalar particle S with mass m_S that couples to the Higgs with a Lagrangian term $-\lambda_S|H|^2|S|^2$, the scalar loop corrections (Figure 2.1, right) would give a contribution to the Higgs mass of

$$\Delta m_H^2 = \frac{\lambda_S}{8\pi^2}\Lambda_{UV}^2 + \dots \ , \tag{2.3}$$

where the first term diverges quadratically in Λ_{UV} and the ellipses correspond to terms proportional to m_S^2, which grow at most logaritmically with Λ_{UV}/m_S.

If a new theory at a given arbitrarily high scale much above the TeV range contains similar corrections from coupling to objects at such a heavy scale, radiative corrections to Higgs mass and vacuum expectation value ($\langle H \rangle$) would be too large unless there is a mechanism to prevent them[3]. Quantum corrections to fermion and gauge boson masses do not have the direct quadratic sensitivity to Λ_{UV}^2, as a consequence of gauge invariance and helicity conservation [24]. However, fermions

[2]Since the Yukawa coupling (proportional to the fermion mass term) breaks the chiral symmetry, the corrections to the mass must be proportional to m_f. On the other hand, the correction given by Eq. 2.2 is not proportional to M_H, because setting $M_H = 0$ does not increase the chiral symmetry of the Lagrangian.

[3]This situation has also an analogy with the self-energy corrections on the electron, which is solved by the presence of the positron.

and the electroweak gauge bosons $Z^0, W^\pm$ of the Standard Model all obtain masses from $\langle H \rangle$ [24], so the entire mass spectrum of the Standard Model is directly or indirectly sensitive to the cut-off Λ_{UV}^2.

Theorists have attempted to circumvent the problems raised above. The proposed solutions involve removing the quadratic divergences from the theory that are the root cause of the naturalness and fine-tuning problems. If one assumes the Higgs boson to be a fundamental particle[4] some striking cancellation is needed between the various contributions to Δm_H^2. By inspection of Eq. 2.2 and Eq. 2.3, if $\lambda_S = |\lambda_f|^2$, the quadratic divergences coming from these two terms would cancel each other, independently of the masses (m_f and m_S) and of the magnitude of the couplings (λ_S and λ_f). The similarity of the dangerous terms to Δm_H^2 in Eq. 2.2 and Eq. 2.3 strongly suggest that a new symmetry ought to relate fermions and bosons (with $\lambda_S = |\lambda_f|^2$) because of the relative minus sign between the fermion loop and the boson loop contributions to Δm_H^2. Because fermion self energies have no quadratic divergences, it is possible in a theory with a symmetry that relates fermions to bosons to guarantee that no quadratic divergences arise in scalar self-energies. Fortunately, a neat cancelation to all orders of all such contributions to scalar masses is unavoidable [14,100,101] once it is assumed there exists a symmetry relating fermions and bosons, referred to as Supersymmetry.

2.2 The supersymmetric extension of the Standard Model

Supersymmetry (SUSY) [10] is a symmetry which relates the masses and couplings of particles of differing spin. In the late 1970s, Fayet was the first to seriously pursue supersymmetric field theoretic models of elementary particles at low energies [102]. A supersymmetry transformation turns a bosonic state into a fermionic state, and vice versa. The operator Q that generates such transformations obeys

$$Q|\text{Boson}\rangle = |\text{Fermion}\rangle \ , \qquad Q|\text{Fermion}\rangle = |\text{Boson}\rangle \ , \tag{2.4}$$

therefore Q is a complex anticommuting spinor and its hermitian conjugate $Q^\dagger$ is also a symmetry generator, both with spin 1/2 (i.e fermionic in nature).

The possible forms for such symmetries in an interacting quantum field theory are highly restricted by the Haag-Lopuszanski-Sohnius extension of the Coleman-Mandula theorem, which demostrates that Supersymmetry is the only way space-time and internal symmetries can be consistently combined [103]. The operators Q and $Q^\dagger$, together with the generators of translations (P^μ) and Lorentz trans-

[4] Other approaches, as including technicolor, composite models, models based on effective four-fermi Lagrangians (e.g., top-mode condensate models), are not considered in this work.

formations ($M^{\mu\nu}$) form a supersymmetry algebra. The single-particle states of a supersymmetric theory fall into irreducible representations of the supersymmetric algebra, called supermultiples. Each supermultiplet contains both fermion and boson states, which are commonly known as superpartners of each other. Particles inhabiting the same irreducible supermultiplet must have equal masses, the same electric charges, weak isospin and color degrees of freedom. In addition, each supermultiplet contains an equal number of fermion and boson degrees of freedom. None of the superpartners of the Standard Model have been discovered as of this writing, therefore Supersymmetry is a broken symmetry in the vacuum state chosen by Nature.

2.3 Benefits from introducing SUSY

The twentieth century has seen the triumph of gauge symmetries as the underlying structure of all theories of fundamental forces and particles. Supersymmetry is a beautiful generalization of the concept of continuous symmetries, reason why many theorists think it would be surprising if Nature did not make use of it. The reasons for pursuing SUSY contain both theoretical arguments as well as phenomenological hints and experimental consequences, as described next.

2.3.1 Solution of the hierarchy and naturalness problem

The Standard Model hierarchy problem presented in Section 2.1.2 is elegantly and neatly solved when considering the supersymmetric theory. The reason is that every Standard Model fermion f has two scalar SUSY partners, S, that also couple to the Higgs, contributing with a mass correction given by Eq. 2.3. If Supersymmetry introduces scalar particles with coupling constants satisfying $\lambda_f^2 = \lambda_S$, the huge Λ_{UV}^2 corrections are canceled [100, 101, 104].

Higher order interactions also contribute to the Higgs mass renormalization (although they are not quadratically divergent), which depends on the mass splitting between the fermion and the scalar. The terms that do not cancel are of the form:

$$(\Delta m_H^2)_{total} \approx \frac{\lambda^2}{16\pi^2}\mathcal{O}(m_f^2 \log(\frac{\Lambda_{UV}}{m_f}) - m_S^2 \log(\frac{\Lambda_{UV}}{m_S})) \tag{2.5}$$

where λ is schematic for various dimensionless couplings, and other smaller contributions have been omitted. In order to avoid considerable fine tuning and keep naturalness, these corrections must not be much greater than the mass of the Standard Model Higgs. Using $\Lambda_{UV} \approx M_P$ and $\lambda \approx 1$ one finds that the masses of at least the lightest few superpartners should be about 1 TeV, in order to provide a Higgs VEV resulting in $m_W \approx 80$ GeV and $m_Z \approx 91$ GeV without any miraculous

cancelation within the SUSY framework. Thus, one associates

$$\mathcal{O}(|m_S^2 - m_f^2|) \lesssim \mathcal{O}((1\text{TeV})^2) \tag{2.6}$$

as the scale where the SM is no longer valid and must be substituted by its supersymmetric extension. Therefore, as long as the mass splitting between scalars and fermions is "small", no unnatural cancellations will be required and the theory can be considered "natural" [105]. In this manner, a theory with nearly degenerate fermions and scalars and carefully adjusted couplings solves the hierarchy problem.

2.3.2 Unification of interactions

Grand unified theories (GUT) [60, 106] provide an attractive framework for understanding the origin of the diverse strengths of the various forces observed in Nature. Essentially, the idea is to have a single force associated with a grand unified local symmetry at a high scale, which below the scale of the symmetry breaking evolves into three different strengths corresponding to the observed weak, electromagnetic and strong interactions. The challenge is to have a theory where the three couplings evolved down to the m_Z scale match their experimentally observed values. A concrete realization of the unification of gauge couplings is provided within the framework of supersymmetric models, where the unification scale is $M_U \approx 2 \times 10^{16}$ GeV [11], when assuming the existence of SUSY particles with masses $M_{SUSY} \approx 1$ TeV. Such unification is a strong hint for grand unification at scales near M_P. The failure of coupling constant unification in the Standard Model may indicate that there is no desert between M_Z and M_U, therefore new physics at some intermediate scale must exist.

2.3.3 Dark Matter candidate

One of the most compelling hints for physics beyond the Standard Model is the cosmological observation that nearly a quarter of our universe consists of Dark (i.e., non-relativistic, non-luminous and non-absorbing) Matter (DM) [28,88–91]. Weakly interacting massive particles (WIMPs), with masses roughly between $10 - 10^4$ GeV and cross sections of approximately weak strength are attractive DM candidates. The currently best motivated WIMP candidate for cold dark matter is the *lightest supersymmetric particle* (LSP) in SUSY models with exact R-parity (see Section 2.4.2).

2.3.4 Incorporation of gravity

Supersymmetry may also be the link between theories of elementary particles and a more fundamental theory that includes gravity. The object which parametrizes

the supersymmetric transformation (Eq. 2.4) is constant space-time. In order to take into account gravity, SUSY must be promoted to a local symmetry. Thus, the parameterization of the SUSY transformation is no longer constant, but can vary from point to point in space-time. The resulting locally supersymmetric theory is called *Supergravity* [107], and unifies the space-time symmetries of ordinary general relativity with local supersymmetry transformations. Therefore SUSY is considered to be a key in the search for a theory that describes the four interactions, playing an important role, as consistent quantum theories that incorporate gravity possesses supersymmetry at some stage in the theory.

2.4 Minimal Supersymmetric Standard Model

The minimal supersymmetric extension of the Standard Model is referred to as the Minimal Supersymmetric Standard Model (MSSM) [102], with one supersymmetry transformation as introduced in Section 2.2. The key features of the MSSM framework required for the understanding of the analysis presented in this thesis are discussed next.

2.4.1 Particle content

There are no candidates for supersymmetric partners within the already observed particles, therefore one must double the entire spectrum, placing the observed particles and the new postulated superpartners within supermultiplets. The simplest supermultiplets consistent with equal bosonic and fermonic degrees of freedom (i.e. $n_f = n_B$) are:

- Chiral (or scalar) supermultiplets: a massless spin-1/2 Weyl fermion with two spin helicity states ($n_f = 2$) and two real scalar fields (each with $n_B = 1$), assembled into a complex scalar field.

- Gauge (or vector) supermultiplets: a massless real spin-1 vector boson ($n_B = 2$) and a massless spin-1/2 Weyl fermion ($n_f = 2$).

In the MSSM, each of the known fundamental particles is included in either a chiral or gauge supermultiplet, and must have a superpartner with the spin differing by 1/2 unit. Thus, Supersymmetry connects particles of differing spin, but all other characteristics, e.g., quantum numbers and masses, are the same. The particle content of the MSSM is introduced next.

- **Squarks and Sleptons**: the names for the spin-0 partners of the quarks and leptons are constructed by prepending an "s" for scalar, so generically they are called squarks and sleptons. The left-handed and right-handed pieces of the

quarks and leptons are separated two-component Weyl fermions with different gauge transformation properties in the Standard Model, so each must have its own complex scalar partners. The symbols for the squarks and sleptons are the same as for the corresponding fermion, but with a tilde used to denote the superpartner of a Standard Model particle. The superpartners of the left-handed and right-handed quarks are denoted as $\tilde{q}_{\rm L}$ and $\tilde{q}_{\rm R}$, respectively ($q = u, d, s, c, b, t$), where the handedness here does not refer to the helicity of the squarks (they are spin-0 particles) but to that of their superpartners. The superpartners of the left-handed and right-handed leptons are denoted as $\tilde{\ell}_{\rm L}$ and $\tilde{\ell}_{\rm R}$, respectively ($\tilde{e}_{\rm L}$, $\tilde{e}_{\rm R}$, $\tilde{\mu}_{\rm L}$, $\tilde{\mu}_{\rm R}$, $\tilde{\tau}_{\rm L}$, $\tilde{\tau}_{\rm R}$). The Standard Model neutrinos (neglecting their very small masses) are always left-handed, so the sneutrinos are denoted generically as $\tilde{\nu}$ (with a possible subscript indicating which lepton flavour they carry). The gauge interactions of each of these squark and slepton fields are the same as for the corresponding Standard Model fermions. Thus, e.g., the left-handed squarks $\tilde{u}_{\rm L}$ and $\tilde{d}_{\rm L}$ couple to the W boson, while $\tilde{u}_{\rm R}$ and $\tilde{d}_{\rm R}$ do not.

- **Gauginos**: the generic nomenclature for a spin$-1/2$ superpartner is to append "-ino" to the name of the Standard Model particles. Since the vector bosons of the SM reside in gauge supermultiplets, their fermionic superpartners are generically referred to as gauginos. The $\mathrm{SU}(3)_C$ color gauge interactions of QCD are mediated by the gluon (g), whose spin-1/2 color-octet supersymmetric partner is the gluino ($\tilde{g}$). The electroweak gauge symmetry $SU(2)_L \times U(1)_Y$ with spin-1 gauge bosons W^+, W^-, W^0 and B^0, is associated with spin$-1/2$ superpartners $\tilde{W}^+, \tilde{W}^-, \tilde{W}^0$ and $\tilde{B}^0$, called winos and bino, respectively.

- **Higgses and Higgsinos**: Since the fermions of the Standard Model have exactly the right quantum numbers to cancel the so-called triangle $\mathrm{SU}(2)_L$ and $\mathrm{U}(1)_Y$ gauge anomalies, it follows that the contribution from the fermionic partner of the Higgs doublet remains uncancelled [108]. Since gauge theories cannot have anomalies, the simplest way to cancel such a contribution is to add a second Higgs doublet, which also have a fermionic partner. Thus, the contributions of the fermion partners of the two Higgs doublets will precisely cancel each other, leaving an anomaly free theory.
  Furthermore, it can be proven that two Higgs doublets are needed in order to generate both up-like and down-like quark masses [109] in a supersymmetric theory. Moreover, given the structure of this theory, only a $Y = 1/2$ Higgs chiral supermultiplet can have the Yukawa couplings necessary to give masses to charge $+2/3$ up-type quarks (up, charm, top), and only a $Y = -1/2$ Higgs gives masses to charge $-1/3$ down-type quarks (down, strange, bottom) and to the charged leptons. The $\mathrm{SU}(2)_L$-doublet complex scalar fields with $Y = 1/2$ and $Y = -1/2$ are denoted as H_u and H_d, respectively. The weak isospin

components of H_u with $T_3 = (1/2, -1/2)$ have electric charges (1,0) respectively, and are denoted as (H_u^+, H_u^0). Similarly, the SU(2)$_L$-doublet complex scalar H_d with $T_3 = (1/2, -1/2)$ components and electric charges (0,-1) are denoted as (H_d^0, H_d^-). The neutral scalar that corresponds to the physical Standard Model Higgs boson is a linear combination of H_u^0 and H_d^0. Following the nomenclature mentioned above, the fermionic partners of the Higgs scalars are called Higgsinos. These are denoted by $\tilde{H}_u^+, \tilde{H}_u^0$ and $\tilde{H}_d^0, \tilde{H}_d^-$.

Overall, the chiral and gauge supermultiplets in Tables 2.1 and 2.2 summarize the particle content of the MSSM. The most obvious and interesting feature of this theory is that none of the superpartners of the Standard Model particles have been discovered so far. Therefore supersymmetry is clearly broken in the vacuum state chosen by Nature.

Chiral supermultiplets				
Names	Symbol	spin-0	spin-1/2	$SU(3)_C, SU(2)_L, U(1)_Y$
squarks and quarks	Q	$(\tilde{u}_\mathrm{L}\ \tilde{d}_\mathrm{L})$	$(u_\mathrm{L}\ d_\mathrm{L})$	$(\mathbf{3}, \mathbf{2}, \frac{1}{6})$
(x3 generations)	$\bar{u}$	$\tilde{u}_\mathrm{R}^*$	$u_\mathrm{R}^\dagger$	$(\bar{\mathbf{3}}, \mathbf{1}, -\frac{2}{3})$
	$\bar{d}$	$\tilde{d}_\mathrm{R}^*$	$d_\mathrm{R}^\dagger$	$(\bar{\mathbf{3}}, \mathbf{1}, \frac{1}{3})$
sleptons and leptons	L	$(\tilde{\nu}\ \tilde{e}_\mathrm{L})$	$(\nu\ e_L)$	$(\mathbf{1}, \mathbf{2}, -\frac{1}{2})$
(x3 generations)	$\bar{e}$	$\tilde{e}_\mathrm{R}^*$	$e_\mathrm{R}^\dagger$	$(\mathbf{1}, \mathbf{1}, 1)$
Higgs and Higgsinos	H_u	$(H_u^+\ H_u^0)$	$(\tilde{H}_u^+\ \tilde{H}_u^0)$	$(\mathbf{1}, \mathbf{2}, \frac{1}{2})$
	H_d	$(H_d^0\ H_d^-)$	$(\tilde{H}_d^0\ \tilde{H}_d^-)$	$(\mathbf{1}, \mathbf{2}, -\frac{1}{2})$

Table 2.1 Chiral supermultiplets in the Minimal Supersymmetric Standard Model. The spin-0 are complex scalars, and the spin-1/2 are left handed two-component Weyl fermions.

2.4.2 R-parity

The interactions and masses of all particles within a renormalizable supersymmetric field theory are determined by their gauge transformation properties and by the so-called superpotential [13, 110]. Given the supermultiplet content of the theory, the Lagrangian for a renormalizable supersymmetry theory with interacting chiral and gauge supermultiplets components must be invariant under both the supersymmetry and gauge transformations, which restrict the form of the superpotential [13, 110]. Although the resulting superpotential for the MSSM is generally

Gauge supermultiplets			
Names	spin-1/2	spin-1	$SU(3)_C, SU(2)_L, U(1)_Y$
gluino and gluon	$\tilde{g}$	g	(**8**, **1**, 0)
winos, W bosons	$\tilde{W}^{\pm}\ \tilde{W}^0$	$W^{\pm}\ W^0$	(**1**, **3**, 0)
bino, B boson	$\tilde{B}^0$	B^0	(**1**, **1**, 0)

Table 2.2 Gauge supermultiplets in the Minimal Supersymmetric Standard Model.

said to be *minimal*, in the sense that it is sufficient to produce a phenomenological viable model, the most general gauge-invariant and renormalizable superpotential might also include terms that violate total baryon and lepton numbers (as well as the individual lepton flavours). The possible existence of these terms is somehow disturbing since corresponding B- and L-violating processes have not been seen experimentally. The most obvious experimental constraint is the non-observation of proton decay, which would violate both B and L by 1 unit. The fact that the proton itself is stable, up to lifetimes of $\mathcal{O}(10^{33})$ years [111], is yet still a postulate based on the fact that we have not seen otherwise. Therefore, a new symmetry is added within the MSSM framework, which has the effect of eliminating the possibility of having baryon and lepton violating terms in the superpotential. This new discrete symmetry is referred to as *R-parity* [14, 102], defined for each particle as

$$P_R = (-1)^{3(B-L)+2s} \ . \tag{2.7}$$

The chiral supermultiplets carry baryon (B) and lepton (L) number assignments as follows: $\mathrm{B}(Q_i) = +1/3$, $\mathrm{B}(\bar{u}_i) = -1/3$, $\mathrm{B}(\bar{d}_i) = -1/3$, $\mathrm{L}(L_i) = +1$, $\mathrm{L}(\bar{e}_i) = -1$ and $\mathrm{B} = \mathrm{L} = 0$ for all others. The spin of the particle is denoted by s. Particles within the same supermultiplet do not have the same R-parity. This assignment is extremely useful for phenomenology, since all of the SM particles and the Higgs bosons have even R-parity ($P_R = +1$), whereas all of the squark, sleptons, gauginos, and higgsinos have odd R-parity ($P_R = -1$).

The MSSM is *defined* to conserve R-parity and therefore there can be no mixing between particles and sparticles. Furthermore, every interaction vertex in the theory contains an even number of sparticles. These features bring about three extremely important phenomenological consequences [13, 110]:

1. The lightest sparticle with $P_R = -1$, referred to as the *lightest supersymmetric particle* (LSP) must be absolutely stable. Moreover, if the LSP is electrically neutral, it interacts only weakly with ordinary matter, so it makes an attractive candidate for the non-baryonic dark matter required by cosmology [112].

2. Each sparticle other than the LSP must eventually decay into a state that contains an odd number of LSPs (usually just one).

3. In collider experiments, sparticles can only be produced in even numbers (usually two-at-a-time).

2.4.3 Supersymmetry breaking

In a theory with exact supersymmetry, fermions and their bosonic superpartners must be degenerate in mass. The Standard Model spectrum clearly does not satisfy this requirement. Thus, if SUSY is realized in Nature, it must be broken and therefore, a realistic phenomenological model must contain supersymmetry breaking. The underlying model should have a Lagrangian density that is invariant under supersymmetry, but a vacuum state that is not. In this way, Supersymmetry is hidden at low energies in a manner analogous to the fate of the electroweak symmetry in the Standard Model. If SUSY is still to provide a solution to the hierarchy problem even in the presence of supersymmetry breaking, then the relationships between dimensionless couplings that hold in an unbroken supersymmetric theory must be maintained to avoid terms of the form $(\lambda_S - |\lambda_f^2|)\Lambda_{UV}^2$.

Supersymmetry-breaking can be implemented by introducing soft breaking terms in order to be able to naturally maintain a hierarchy between the electroweak scale and any other very large mass scale [13, 110]. Thus, if the largest mass scale associated with the soft terms is denoted m_{soft}, then the additional non-supersymmetric corrections to the Higgs scalar squared mass must vanish in the $m_{soft} \to 0$ limit. If the characteristic mass scale $m_{\text{soft}} \lesssim \mathcal{O}$ (1 TeV), a solution to the hierachy problems is still provided in the MSSM framework, no unnatural cancellations are required and the new theory can be considered natural.

Unlike the supersymmetry-preserving part of the Lagrangian, many new parameters, that were not present in the Standard Model, are introduced in the MSSM by the soft supersymmetry-breaking terms (compatible with gauge invariance and R-parity conservation). A careful count [113] reveals that there are 105 masses, phases and mixing angles in the MSSM that cannot be rotated away by redefining the phases and flavour basis from the quark and lepton supermultiplets.

This large number of free parameters makes any phenomenological analysis in the general MSSM very complicated. However, many of these parameters are severely restricted by experiments [13, 114]. As consequence, a phenomenologically viable MSSM can be defined by making the following three assumptions:

- All the soft SUSY–breaking parameters are real and therefore there is no new source of CP–violation generated, in addition to the one from the CKM matrix.

- The matrices for the sfermion masses and for the trilinear couplings are all

diagonal, implying the absence of flavour-changing neutral current processes at the tree–level.

- First and second sfermion generation universality at low energy from constraints on experimental particle masses.

These three assumptions lead to 22 input parameters only: the ratio of the VEVs of the two-Higgs doublet fields, two Higgs mass parameters squared, three gaugino mass parameters, five first/second generation sfermion mass parameters, five third generation sfermion mass parameters, three first/second generation trilinear couplings, and three third generation trilinear couplings. Interestingly, if the soft SUSY–breaking parameters obey a set of universal boundary conditions at the GUT scale, as the unification of the gaugino masses, universal scalar masses and trilinear couplings, it can be proven one is left with only five free parameters, as for the case of the widely known minimal Supergravity (mSUGRA) model [115].

2.4.4 The mass spectrum

The superpartners listed in Tables 2.1 and 2.2 are not necessarily the mass eigenstates of the MSSM. After electroweak symmetry breaking and supersymmetry breaking effects are included, there can be mixing between the electroweak gauginos and the higgsinos, within the various sets of squarks and sleptons and between the Higgs scalars that have the same electric charge. The lone exception is the gluino, which is a color octet fermion and therefore does not have the appropiate quantum numbers to mix with any other particle. The masses and mixings of the superpartners are obviously of paramount importance for experimentalists, and the different possibilities are presented next.

2.4.4.1 Higgs sector

The Higgs scalar fields in the MSSM consist of two complex $\mathrm{SU}(2)_L$-doublets, H_u and H_d, or eight real, scalar degrees of freedom. After the electroweak symmetry is broken, three of them are the Nambu-Goldstone bosons, which become the longitudinal modes of the Z and $W^\pm$ massive vector bosons [25]. The remaining five degrees of freedom yield the physical Higgs bosons of the model. The following nomenclature is used:

$$\begin{aligned} H^\pm &: \quad \text{charged Higgs boson pair} , \\ A^0 &: \quad \mathrm{CP}-\text{odd neutral Higgs boson} , \\ H^0, h^0 &: \quad \mathrm{CP}-\text{even neutral Higgs bosons} , \end{aligned} \tag{2.8}$$

where by convention h^0 is lighter than H^0. In the case $m_{A^0} \gg m_Z$ (referred to as decoupling limit), the particles A^0, H^0 and $H^\pm$ are much heavier than h^0, and

nearly degenerated and decoupled from low-energy experiments. In contrast, the mass of h^0 is upper bounded. Including all corrections (mainly large positive one-loop radiative correction from stop loops) and assuming that all of the sparticles that can contribute to $m_{h^0}^2$ in loops have masses that do not exceed 1 TeV, one obtains $m_{h^0} \lesssim 135$ GeV, consistent with the experimental observation. A weaker bound is obtained if one considers that all of the couplings in the theory remain perturbative up to the unification scale, of $m_{h^0} \lesssim 150$ GeV [116]. Finally, this bound may also be further weakened if the top squarks are heavier that ≈ 1 TeV, but the upper bound rises only logarithmically with the soft masses in the loop corrections. Thus it is a fairly robust prediction of supersymmetry at the electroweak scale that at least one of the Higgs scalar bosons must be light.

2.4.4.2 Neutralinos and charginos

The higgsinos and electroweak gauginos can mix because of the effects of electroweak symmetry breaking. The neutral higgsinos ($\tilde{H}_u^0$ and $\tilde{H}_d^0$) and the neutral gauginos ($\tilde{B}$ and $\tilde{W}^3$) combine to form four mass eigenstates called **neutralinos**, denoted by $\tilde{\chi}_1^0$,$\tilde{\chi}_2^0$,$\tilde{\chi}_3^0$,$\tilde{\chi}_4^0$, with masses $M_{\tilde{\chi}_1^0}$,$M_{\tilde{\chi}_2^0}$,$M_{\tilde{\chi}_3^0}$,$M_{\tilde{\chi}_4^0}$ in ascending order. The lightest neutralino, $\tilde{\chi}_1^0$, is usually assumed to be the LSP (since it is the only MSSM particle that can make a good dark matter candidate). Generally, the mass eigenstates and their corresponding eigenvalues are complicated mixtures of the gauge interaction-eigenstates.

The charged higgsinos ($\tilde{H_u^+}$ and $\tilde{H_d^-}$) and winos ($\tilde{W^+}$ and $\tilde{W^-}$) mix to form two mass eigenstates with charge ± 1, called **charginos** and denoted by $\tilde{\chi}_1^\pm$ $\tilde{\chi}_2^\pm$. The mass eigenstates are denoted by $M_{\tilde{\chi}^\pm{}_{1,2}}$, where by convention $m_{\tilde{\chi}_1^\pm} \leq m_{\tilde{\chi}_2^\pm}$.

2.4.4.3 The gluino

The gluino is a color octet fermion, so it cannot mix with any other particle in the MSSM (even if R-parity is violated). The gluino mass parameter (M_3) is related to the bino and wino mass parameters (M_1 and M_2, respectively), by a rough prediction [13]:

$$M_3 \colon M_2 \colon M_1 \approx 6 \colon 2 \colon 1 \ , \tag{2.9}$$

near the TeV scale (if they have a common mass value at the GUT scale). Therefore, it is reasonable to suspect that the gluino may be considerably heavier that the lighter neutralinos and charginos.

2.4.4.4 The squarks and sleptons

Any pair of scalars with the same electric charge, R-parity, and color quantum numbers can mix with each other. After the addition of the MSSM soft supersymmetry-breaking terms, the mass eigenstates of the squarks and sleptons

of the MSSM can be obtained by diagonalizing three 6×6 matrices for up-type squarks, down-type squarks and charged sleptons, and one additional 3×3 matrix for sneutrinos. The first- and second-family of squarks and sleptons generally end up in 7 nearly degenerate unmixed pairs. In contrast, the third-family squarks and sleptons can have very different masses and substantial mixing in pairs $(\tilde{t}_{\mathrm{L}}, \tilde{t}_{\mathrm{R}})$, $(\tilde{b}_{\mathrm{L}}, \tilde{b}_{\mathrm{R}})$ and $(\tilde{\tau}_{\mathrm{L}}, \tilde{\tau}_{\mathrm{R}})$. For a certain sfermion f of the third generation (with $f = \tilde{t}$, $\tilde{b}$ or $\tilde{\tau}$), the hermitian mass matrices in the gauge-eigenstate basis $(\tilde{f}_{\mathrm{L}}, \tilde{f}_{\mathrm{R}})$ can be diagonalized by an unitary matrix to give the mass eigenstates, denoted $(\tilde{f}_1, \tilde{f}_2)$. The resulting squark eigenstate masses can be proven to be [13, 114]:

$$m^2_{\tilde{f}_{1,2}} = m^2_f + \frac{1}{2}\left[m^2_{\tilde{f}_{\mathrm{L}}} + m^2_{\tilde{f}_{\mathrm{R}}} \mp \sqrt{(m^2_{\tilde{f}_{\mathrm{L}}} - m^2_{\tilde{f}_{\mathrm{R}}})^2 + 4m^2_f C^2}\right] , \tag{2.10}$$

with $m^2_{\tilde{f}_1} < m^2_{\tilde{f}_1}$, where $\tilde{f}_{\mathrm{L,R}}$ denotes the sfermion masses and m_f the masses of the partner fermions. The parameter C is a known value that can be obtained from the Yukawa and soft couplings and the ratio of the VEVs of H^0_u and H^0_d. Due to the large value of m_t, the mixing is particularly strong in the stop sector. This generates a large splitting between the masses of the two stop eigenstates, possibly leading to a lightest top squark much lighter than the other squarks.

2.4.4.5 Comment on quarks, leptons and bosons

The identification of quark, lepton and gauge boson eigenstates and the corresponding masses follows the usual Standard Model analysis. One constructs the quark mass matrix and extracts the CKM angles. A similar mixing is included in the neutrino sector (the MNS matrix) that expresses the charged lepton interaction eigenstates in terms of the mass eigenstates. The Z and γ are eigenstates of a 2×2 neutral gauge boson mass matrix. The Standard Model Higgs boson is replaced by the Higgs sector described above. This completes the enumeration of all the mass eigenstates of the MSSM. With the MSSM mass eigenstates in hand, and a complete list of supersymmetric interactions and the soft-supersymmetry-breaking terms, it is straightforward to compute all the Feynman rules of the MSSM. These can be found in [97].

2.4.5 Sparticles decays

This section introduces the decay patterns of sparticles in the MSSM, assuming that R-parity is conserved.

- **Decays of neutralinos and charginos**: each $\tilde{\chi}^0$ and $\tilde{\chi}^\pm$ contains at least a small admixture of the electroweak gauginos $(\tilde{B}, \tilde{W}_0, \tilde{W}^\pm)$, therefore $\tilde{\chi}^0$ and $\tilde{\chi}^\pm$ inherit couplings of weak interaction strength to (scalar, fermion) pairs. Thus, if sleptons or squarks are sufficiently light, $\tilde{\chi}^0$ and $\tilde{\chi}^\pm$ can decay to

slepton-lepton or squark-quark pairs. In addition, $\tilde{\chi}^0$ and $\tilde{\chi}^\pm$ can also decay into any lighter $\tilde{\chi}^0/\tilde{\chi}^\pm$ plus a higgs scalar or an electroweak gauge boson. The possible two-body decay modes for $\tilde{\chi}^0$ and $\tilde{\chi}^\pm$ in the MSSM are:

$$\tilde{\chi}_i^0 \to Z\tilde{\chi}_j^0,\ W^\pm\tilde{\chi}_j^\mp,\ h^0\tilde{\chi}_j^0,\ \ell\tilde{\ell},\ \nu\tilde{\nu},\ A^0\tilde{\chi}_j^0,\ H^0\tilde{\chi}_j^0, H^\pm\tilde{\chi}_j^\mp,\ q\tilde{q}\ . \tag{2.11}$$

$$\tilde{\chi}_i^\pm \to W^\pm\tilde{\chi}_j^0,\ Z\tilde{\chi}_1^\pm,\ h^0\tilde{\chi}_1^\pm,\ \ell\tilde{\nu},\ \nu\tilde{\ell},\ A^0\tilde{\chi}_1^\pm,\ H^0\tilde{\chi}_1^\pm,\ H^\pm\tilde{\chi}_j^0,\ q\tilde{q}'\ . \tag{2.12}$$

If two-body decays are kinematically forbidden for a given $\tilde{\chi}^0$ or $\tilde{\chi}^\pm$, three or more body decays take place through the same (but now off-shell) gauge bosons, Higgs scalars, sleptons, and squarks that appeared in Eqs. 2.11-2.12.

- **Slepton decays**: sleptons can have two-body decays into a lepton and a chargino or neutralino, because of their gaugino admixture, given by

$$\tilde{\ell} \to \ell\tilde{\chi}^0,\ \nu\tilde{\chi}^\pm \text{ and } \tilde{\nu} \to \nu\tilde{\chi}^0,\ \ell\tilde{\chi}^\pm\ . \tag{2.13}$$

  The right-handed sleptons do not have a coupling to the $SU(2)_L$ gaugino, so they typically prefer the direct decay to $\ell\tilde{\chi}_1^0$.

- **Gluino decays**: the decay of the gluino can only proceed through a squark, either on-shell or virtual. If two body decays are open, they will dominate because of the relevant gluino-quark-squark coupling with QCD strength. If instead, all of the squarks are heavier than the gluino, the gluino will decay only through off-shell squarks,

$$\tilde{g} \to q\tilde{q},\quad (\text{on}-\text{shell}) \tag{2.14}$$

$$\tilde{g} \to qq\tilde{\chi}^0 \text{ and } \tilde{g} \to qq'\tilde{\chi}^\pm\ \ (\text{off}-\text{shell squark})\ . \tag{2.15}$$

- **Squark decays**: squark can have two body decays into a (squark,gluino) if it is kinematically allowed, as it has QCD strength. Otherwise, the squarks can decay into a quark plus a neutralino/chargino,

$$\tilde{q} \to q\tilde{g},\ \text{and } \tilde{q} \to q\tilde{\chi}^0 \text{ or } \tilde{q} \to q'\tilde{\chi}^\pm\ . \tag{2.16}$$

  The gluino, chargino or neutralino resulting from the squark decay will in turn decay, and so on, until a final state containing $\tilde{\chi}_1^0$ is reached. This results in numerous and complicated decay chain possibilities called cascade decays.

2.4.6 Benchmark models and Phenomenological MSSM

During the last three decades, perhaps most of the theoretical work on supersymmetric theories was invested in understanding how SUSY is broken, what effects are responsable for spontaneous SUSY breaking and how SUSY breakdown

is communicated to the MSSM particles. It has been almost impossible to achieve the latter in a phenomenologically viable way working only with renormalizable interactions at tree-level. Thus, it is widely believed that the MSSM soft terms arise indirectly or radiatively rather than from tree-level renormalizable couplings to the supersymmetry-breaking order parameters. This breaking is assumed to be originated in a *hidden sector* of particles that have no direct couplings to the *visible sector* chiral supermultiplets of the MSSM. However, the two sectors do share some interactions that are responsable for transmitting the effects of supersymmetry breaking from the hidden sector to the visible sector, resulting in the MSSM soft terms. Then, at the electroweak scale, the values of the Lagrangian soft parameters can be used to extract the physical masses, cross-sections and decay widths of the particles. Since the MSSM is characterized by a large number of parameters, searches in a N-dimensional space (with $\mathcal{O}(N) \approx 100$) must be considered, which is practically impossible. Thus, in order to reduce the number of parameters and search for the most probable models, one could adopt specific assumptions for the SUSY breaking mechanism to reduce the parameters in the MSSM. There have been two main competing proposals for what the mediating interactions might be: gravity-mediated supersymmetry breaking (e.g., mSUGRA) [115] and gauge-mediated supersymmetry breaking (GMSB) models [117, 118]. Extra-dimensional and anomaly-mediated supersymmetry breaking scenarios have also become popular models and they have been intensively studied [119–121]. However, all these models still rely on various specific assumptions. An interesting approach, referred to as the phenomenological Minimal Supersymmetric Standard Model (pMSSM) [122, 123], attempts to relax some of the assumptions incorporated in the models mentioned above (see Section 2.4.3). The pMSSM assumes most general CP-conserving MSSM with R-parity and minimal flavour violation [124]. The lightest neutralino is the LSP, the first two sfermions generations are degenerate, the first two generations have negligible Yukawa couplings, and no assumptions about specifics of SUSY-breaking or GUT. Thus, the pMSSM gives 19 real TeV scale lagrangian parameters (10 sfermion masses, 3 gaugino masses, 3 couplings and 3 Higgs/higgsino parameters) to be scanned [122]. Finally, at this point, it is worth mentioning it would be a mistake to rely too heavily on specific scenarios for the MSSM mass and mixing spectrum, given the huge and vast available possibilities. In the last years, new model-independent approaches for characterizing new-physics processes have been explored, and may help reduce model dependence that often plagues top-down parameterizations of new physics. They are introduced in the next section.

2.5 Simplified Models

The Tevatron carried out a variety of searches in jets and missing energy and extended the bounds on specific SUSY parameters. Most searches, however, were optimized for mSUGRA-type benchmarked scenarios, that are affected by strong assumptions on the spectrum, mass splittings and branching ratios, and therefore underrepresent the kinematic possibilities and decay topologies. At the LHC, both on the theory and experiment sides, similar model-specific studies for new physics prospects have been carried out. Moreover, many analyses are often obscured by the presentation of the results in terms of high energy mSUGRA parameters, making it non-trivial to translate the bounds for alternative theories. Given the tremendous range of possibilities to search for evidence of new physics at the TeV scale, a coherent strategy for going from data to a still-unknown theory is necessary.

In the last years, a new specific approach to characterize the first robust evidence for new physics expected to be observed at the LHC has been developed, and referred to as "Simplified Models" [125–128]. These are effective field theories for collider physics aimed at developing searches and exploring common features of new physics and they are one of the most promising model-independent strategies for new physics searches. Simplified models are effective models built with the minimal particle content necessary to produce SUSY-like[5] final states contributing to the channels of interest and they are parametrized directly in terms of cross sections for production, branching ratios for decays, and masses of on-shell particles. The kinematics, masses and phase space, of production and decay vertices are treated exactly, whereas the highly model-dependent dynamics appearing in quantum amplitudes are approximated using effective parameterizations of $|\mathcal{M}|^2$.

For a general $2 \to 2$ process ($a+b \to c+d$), the kinematics of the particle production can be completely described in terms of the familiar Mandelstam variables [24] $\hat{s} = (p_a + p_b)^2$, $\hat{t} = (p_a - p_c)^2$ and $\hat{u} = (p_a - p_d)^2$, where p_i are the four-vectors for particles labeled as $i = a, b, c, d$. As an example, if the form of matrix elements is constrained using tree-level field theory, the gluino pair production through the gluon PDFs [129] has the matrix element [130]:

$$|\mathcal{M}(gg \to \tilde{g}\tilde{g})|^2 \propto \left(1 - \frac{\hat{t}_g \hat{u}_g}{\hat{s}^2}\right)\left[\frac{\hat{s}^2}{\hat{t}_g \hat{u}_g} - 2 + 4\frac{m_{\tilde{g}}^2 \hat{s}}{\hat{t}_g \hat{u}_g}\left(1 - \frac{m_{\tilde{g}}^2 \hat{s}}{\hat{t}_g \hat{u}_g}\right)\right], \tag{2.17}$$

with $\hat{t}_g = (p_{g,1} - p_{\tilde{g},1})^2 - m_{\tilde{g}}^2$, $\hat{u}_g = (p_{g,1} - p_{\tilde{g},2})^2 - m_{\tilde{g}}^2$. Within a given model, this expression involves a finite number of pieces, where further terms must be added appropriately to describe the different spin possibilities. Thus, the full quantum

[5] Operationally, "SUSY-like" includes theories with new particles that carry Standard Model quantum numbers (partner particles) and a parity (under which partner particles are odd) that makes the lightest such partner particle stable.

amplitudes for this process depends on many Lagrangian parameters of the SUSY theory. Interestingly, the kinematics of the gluino pair-production process of Eq. 2.17 have been found to be well reproduced by the truncated expression [125]

$$|\mathcal{M}|^2 = \text{constant} \ , \tag{2.18}$$

with a value for such constant chosen to reproduce the total hadronic production cross section[6]. The p_{T} and rapidity distributions for a gluino produced according to the full matrix element of Eq. 2.17 and the approximation of Eq. 2.18 are shown in Figure 2.2, where a remarkably agreement is observed. The success of such approximation relies on the fact that parton luminosities fall rapidly [80, 131, 132], whereas the matrix element $|\mathcal{M}|^2$ varies smoothly over energy, and thus the hadronic production is approximately insensitive to the details of $|\mathcal{M}|^2$ structure [125].

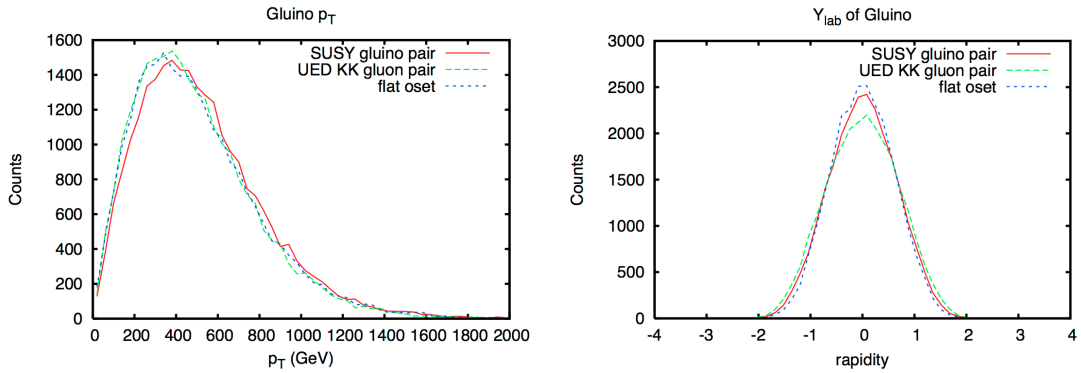

Figure 2.2 Distributions of inclusive transverse momentum and rapidity of the partonic gluino (left and right, respectively), for the SUSY $\tilde{g}\tilde{g}$ pair production process compared with a flat matrix element $|\mathcal{M}|^2 = \text{constant}$.

The approximation of Eq. 2.18 often fails when the threshold- or high-energy scaling of $|\mathcal{M}|^2$ is extreme. Thus, for parameterizing corrections to constant $|\mathcal{M}|^2$, a description of the form $|\mathcal{M}|^2 \propto (1-1/X)$ has been found to be extremely accurate, as it can be observed in Figure 2.3 [125]. Here, $X \equiv \frac{\hat{s}}{s_0}$ and $\xi \equiv \frac{\hat{t}-\hat{u}}{\hat{s}}$, where s_0 is the minimum possible value of $\hat{s}$ for production of species of masses m_c and m_d, i.e., $s_0 \equiv (m_c + m_d)^2$, and ξ is the z-component of momentum of the particles in the center-of-mass system scaled by half the center-of-mass energy, providing information about the relative velocity of the products, and the scattering angle in the center-of-mass frame.

On the other hand, correlations in the rest frame of a decaying particle have been found to be mostly washed out after boosting to the lab frame. Therefore, a $1 \to n$ decay is generally modeled at leading-order by $|\mathcal{M}_{\text{decay}}|^2 = \text{constant}$, with the decays weighted by phase space only [125].

[6] This constant $|\mathcal{M}|^2$ has no Lagrangian interpretation, but it serves as an effective leading order parameterization for various kinematic variables.

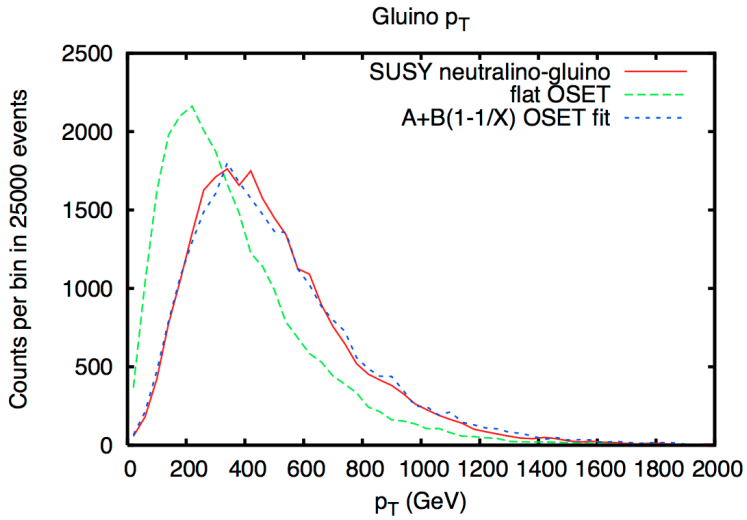

Figure 2.3 Distribution of inclusive transverse momentum for the partonic gluino for the SUSY $\tilde{\chi}_2^0\tilde{g}$ associated production process compared with a flat matrix element $|\mathcal{M}|^2 = \text{constant}$, and a threshold-corrected matrix element $|\mathcal{M}|^2 \propto 1 - 1/X$.

As consequence of the discussion above, within the description of Simplified Models, each vertex is represented by a gray *blob*, to identify the approximated matrix element $|\mathcal{M}|^2$ (see Figure 2.6 below). Thus, these models rely on the fact that only a few dynamical variables control the essential phenomenology of new physics at hadron colliders. The Simplified Models have been found to reproduce shapes and object multiplicity observables, invariant mass edges and endpoints, and locations and widths of peaks in kinematic distributions remarkably well in a wide variety of SUSY-like new physics models [125–128, 133, 134].

Simplified Models with a simple spectra compatible with SUSY-like structure are a natural starting point for building more accurate models, since deviations from the phenomenology of the Simplified Models can be taken as evidence for a larger set of particles playing a role in new physics. Recent efforts, including two joint experiment-theory workshops at CERN [135, 136] have focused on using pre-defined Simplified Models in the design of new-physics searches and characterization of their results. A catalog of Simplified Models, covering a wide variety of models and new-physics signatures is available online at [137]. The production and decay modes are generally linked together in all possible ways to generate a list of consistent *topologies*, allowing the results of the search be reported in terms of limits on cross-section times branching ratios as a function of new particle masses, separately for each event topology. Finally, it is worth mentioning these Simplified Models are not intended to displace signature-based analyses, or the interpretation of search results within other specific models but rather to complement them with a different emphasis. Therefore, the simplified model framework is used in this work as a complementary approach to the phenomenological Minimal Supersymmetric Standard Model.

2.6 Characterization of heavy flavour topologies

Third generation squarks (i.e., the stop and the sbottom) are expected to be lighter than the other squarks as discussed in Section 2.4.4, and therefore their production may be dominant at the LHC. In this chapter, the expected heavy flavour topologies considered in this work are described.

2.6.1 Production

The sparticles predicted by SUSY theories can be produced at hadron colliders in pairs from parton-parton collisions of electroweak and QCD strength. Given the fraction of momentum expected to be carried by gluons and quarks involved in the hard parton collisions needed to make sparticles of $\mathcal{O}(\sim 1$ TeV), the production of gluinos and squarks is dominated by gluon-gluon and gluon-quark fusion QCD processes at the LHC. The predicted NLO cross-sections for production of SUSY particles at the LHC running at $\sqrt{s} = 7$ TeV are shown in Figure. 2.4, as calculated using PROSPINO [12, 138].

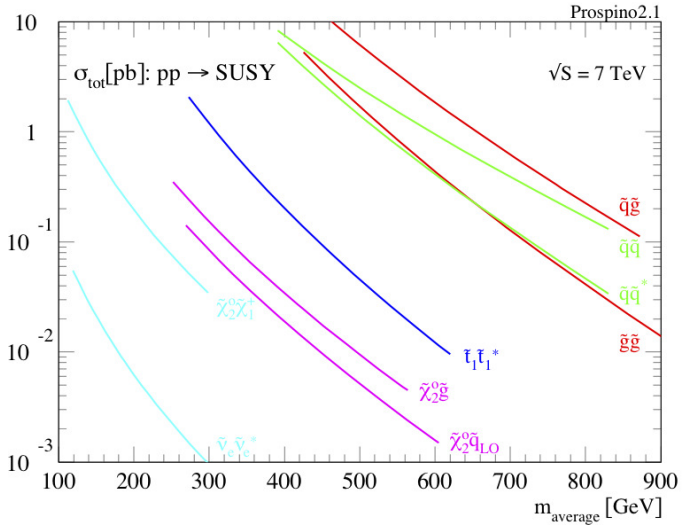

Figure 2.4 Cross-sections for SUSY sparticles production, as a function of their masses calculated to NLO using PROSPINO.

There are mainly two types of processes for the stop or the sbottom to be produced if they are relatively light (i.e. mass on the order of several hundreds GeV): via the decay from gluinos and via direct pair production. If the gluino is not much heavier than the stop (or sbottom), the gluino-mediated production of stop or sbottom dominates over direct stop (or sbottom) production as it can be observed in Figure. 2.4. On the other hand, if the stop (sbottom) was the only light colored

SUSY particle, and the other squarks and the gluinos are heavier than a few TeV, only direct stop (sbottom) pair production might be observed.

2.6.2 Stop and sbottom signatures

The decay modes of SUSY processes is of course highly dependent on the SUSY particle mass spectrum, with many possibilities as discussed in Section 2.4.5. The analysis presented in this thesis is focused on heavy-flavour topologies with multiple jets originated from b-quark hadronization (see Chapter 7), therefore only the lightest stop, sbottom, chargino and neutralino are considered as the active SUSY particles within the decay modes for simplicity. The other SUSY particles are assumed to be heavy enough (i.e., masses of the order above a few TeV) such that they can be considered as decoupled.

2.6.2.1 Stop and sbottom decay

If $m_{\tilde{g}} > m_{\tilde{t}_1}$ or $m_{\tilde{g}} > m_{\tilde{b}_1}$, the decay of these squarks to a quark plus a gluino ($\tilde{t}_1(\tilde{b}_1) \to \tilde{g} + t(b)$) is kinematically forbidden, and therefore the $\tilde{t}_1$ and $\tilde{b}_1$ will decay into a quark plus neutralino or chargino. Within this scenario, different decay modes may take place:

1. If $m_{\tilde{t}_1} > m_t + m_{\tilde{\chi}_1^0}$, the stop may decay via

$$\tilde{t}_1 \to t + \tilde{\chi}_1^0 \ . \tag{2.19}$$

   If the lightest neutralino is the LSP for a given SUSY model being considered, the $\tilde{\chi}_1^0$ is stable and it will not decay further. However, the top-quark will decay to $t \to bW$ mostly, with subsequent decays for the W boson. Thus, the final state consists of multi-jets including b-jets, leptons and $E_{\mathrm{T}}^{\mathrm{miss}}$.

2. If $m_{\tilde{t}_1} > m_b + m_{\tilde{\chi}_1^+}$, the stop may decay via

$$\tilde{t}_1 \to b + \tilde{\chi}_1^+ \ . \tag{2.20}$$

   The lightest chargino is considered heavier than the lighest neutralino in a wide-variety of SUSY models. As discussed in Section 2.4.5, the lightest chargino can decay further to $\tilde{\chi}_1^+ \to b + W^+ + \tilde{\chi}_1^0$ (Figure 2.5, left). Moreover, if one included an additional neutralino heavier than $\tilde{\chi}_1^0$, for instance the $\tilde{\chi}_2^0$, an extra-step in the decay chain may take place[7]. Thus, the final state consists of multi-jets including b-jets, leptons and $E_{\mathrm{T}}^{\mathrm{miss}}$.

[7]Further decays like $\tilde{\chi}^{\pm} \to f^{'}\tilde{f}$ are not taken into account since other fermions are considered as decoupled.

3. If $m_{\tilde{b}_1} > m_b + m_{\tilde{\chi}_1^0}$, the sbottom may decay via

$$\tilde{b}_1 \to b + \tilde{\chi}_1^0 \ . \tag{2.21}$$

As discussed for Eq. 2.19, if the lightest neutralino is the LSP, $\tilde{\chi}_1^0$ is stable. In this scenario, the final state therefore consists of multi-jets including b-jets and $E_{\mathrm{T}}^{\mathrm{miss}}$.

4. If $m_{\tilde{b}_1} > m_t + m_{\tilde{\chi}_1^-}$, the sbottom may decay via

$$\tilde{b}_1 \to t + \tilde{\chi}_1^- \ . \tag{2.22}$$

with the lightest chargino decaying further to $\tilde{\chi}_1^- \to W^- + \tilde{\chi}_1^0$. The final state consists of multi-jets including b-jets and $E_{\mathrm{T}}^{\mathrm{miss}}$ and possible leptons from the top and W decays.

5. If the previous decay modes are all suppressed, but $m_{\tilde{t}_1} > m_c + m_{\tilde{\chi}_1^0}$, the stop may decay via a one-loop process

$$\tilde{t}_1 \to c + \tilde{\chi}_1^0 \ . \tag{2.23}$$

Given the limited space parameter for this topology, it will not be considered in this thesis.

2.6.2.2 Gluino decay

The decay of the gluino can only proceed through a stop or sbottom, either on-shell or virtual, as other squarks have been decoupled.

1. If $m_{\tilde{g}} > m_{\tilde{t}_1} + m_t$ or $m_{\tilde{g}} > m_{\tilde{b}_1} + m_b$, the gluino can decay via

$$\tilde{g} \to \tilde{t}_1 + \bar{t} \ , \tag{2.24}$$

$$\tilde{g} \to \tilde{b}_1 + \bar{b} \ , \tag{2.25}$$

and the products $\tilde{t}_1$ and $\tilde{b}_1$ will experience the decay chains discussed in Section 2.6.2.1.

2. However, if the previous two-body decays are kinematically forbidden, the gluino will decay only through off-shell stop and sbottom (Figure 2.5, right), via

$$\tilde{g} \to \tilde{t}_1^* + \bar{t} \qquad \text{or} \qquad \tilde{g} \to \tilde{b}_1^* + \bar{b} \ , \tag{2.26}$$

where the $\tilde{t}_1^*$ and the $\tilde{b}_1^*$ will experience a decay chain as discussed above. The branching ratio of the gluino decaying to top or bottom quark pairs is

dominant for most SUSY scenarios, since the virtual squark has a propagator proportional to $m_{\tilde{q}*}^{-4}$, so even if there exists a small mass difference between the stop (or sbottom) and the other squarks, a decay through heavy-flavour squarks is enhanced by the fourth power [97].

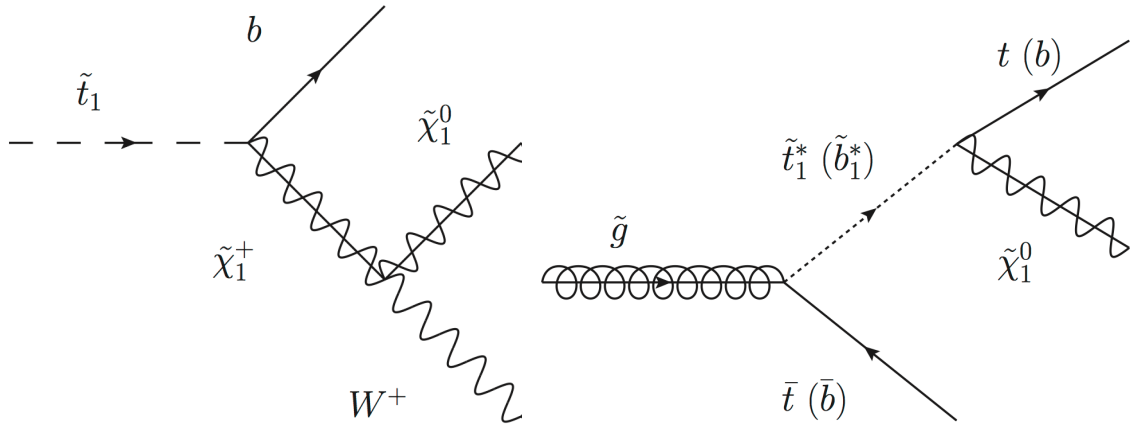

Figure 2.5 The tree-level Feynman diagrams for two cases of $\tilde{t}_1$ (left) and $\tilde{g}$ (right) three body decay, as discussed in 2.6.2.1 and 2.6.2.2, respectively.

2.7 Simplified Models for heavy-flavour jets and $E_{\mathrm{T}}^{\mathrm{miss}}$ topologies

The simplified model approach is generally driven by the final state signature (i.e., the objects in the final state). Even for an analysis restricted to final states with heavy flavour jets and $E_{\mathrm{T}}^{\mathrm{miss}}$, there is a multitude of possible configurations, both of multiplicities and kinematics. A small set of "topologies" that capture the main kinematic features of the possible final states are introduced in this section. Studying these topologies ensures a broad coverage for the range of kinematics of such a final state.

The key states in the set of simplified models considered in this work are $\tilde{g}$, $\tilde{t}$, $\tilde{b}$ and $\tilde{\chi}_1^0$. The heavy flavour topologies begin with $\tilde{g}$ and $\tilde{t}$ or $\tilde{b}$ being pair produced through its QCD interactions (Section 2.6.1). The most straight-forward addition of the simplified model is to consider intermediate particles in the decay chain which may significantly alter the decay kinematics. Commonly, two benchmark particle types are chosen: $\tilde{\chi}^{\pm}$ and $\tilde{\chi}_2^0$. The simplified model is described by a minimal set of parameters that often include the particle masses and the production cross sections. Each simplified model is usually considered with branching ratio set to 100%, as models with multiple decay modes can be studied by taking linear combinations of results for single decay modes [134]. The nomenclature of SUSY and sparticles is

used, but the results also apply to other models with particles of same quantum numbers as those presented here [125–128, 133, 134].

The topologies are built depending upon the pair-produced sparticles and decay paths. In this thesis, the search for top and bottom squarks from gluino pair production in final states with missing transverse energy and at least three b-jets is presented, therefore only gluino-mediated stop and sbottom production is considered hereafter[8]. Thus, the topology group consists of the production and decay of two gluinos ($\tilde{g} \to q\bar{q} + \tilde{\chi}^0$). This is divided into three specific topologies, depending on whether the gluino decays into (Figure 2.6):

1. only b-quarks: $\tilde{g} \to b\bar{b} + \tilde{\chi}^0$, denoted Gbb,
2. only t-quarks: $\tilde{g} \to t\bar{t} + \tilde{\chi}^0$, denoted Gtt,
3. b- and t- quarks: $\tilde{g} \to tb + \tilde{\chi}^0$, (via $\tilde{\chi}^\pm \to \tilde{\chi}^0 + W^\pm$) denoted Gtb.

Parameters of the simplified models for heavy flavour consists of production cross-section (σ), branching ratios (BR) and masses M of on-shell particles. For Gbb, Gtt and Gtb topologies, gluinos of mass $M_{\tilde{g}}$ are pair produced. They decay to the LSP in three modes, emitting each two bottom quarks, two top quarks or one bottom and one top quark, respectively. In order to study a wide range of final state kinematics, the mass of the gluino ($\tilde{g}$) and the LSP ($\tilde{\chi}^0$) are varied to create a grid of Monte Carlo samples with the pair produced particle masses covering a range of approximately 1 TeV, in slices of 50 GeV for each of these particles. The branching ratio of the decay is tuned to 100 % for Gbb and Gtt, by decoupling other particles as describe above. For Gtb topologies, the gluinos decay via virtual stops or sbottoms with a branching ratio tuned to 50 % for $\tilde{t} \to b + \tilde{\chi}_1^+$ and $\tilde{b} \to t + \tilde{\chi}_1^-$, respectively. In addition, the decay $\tilde{\chi}^\pm \to \tilde{\chi}^0 + W^\pm$ is assumed, where the W is off-shell when required by kinematics. If the chargino and neutralino are nearly degenerate, the decay products of $\tilde{\chi}^\pm$ are expected to be squeezed out. A small mass difference between charginos and neutralinos is assumed, $\Delta M(\tilde{\chi}^\pm, \tilde{\chi}_1^0) = 2$ GeV, such that charginos decay to neutralinos plus very soft quarks/leptons. Table 2.3 summarizes the set of topologies, the corresponding MSSM processes and the expected final states. All topologies can give rise to a *high multiplicity of b-tagged jets* and $E_{\mathrm{T}}^{\mathrm{miss}}$, with possible leptons in the final state from the subsequent top decays. The study and characterization of the kinematics of each decay topology within its parameterization in terms of the gluino and neutralino masses ($m_{\tilde{g}}, m_{\tilde{\chi}^0}$) is discussed in Chapter 7.

2.8 Previous experimental results

Final states with high transverse momentum $b-$jets, large $E_{\mathrm{T}}^{\mathrm{miss}}$ with or without leptons are sensitive to SUSY signal production involving third generation squarks.

[8] Direct stop and sbottom production processes result in final states with only two b-jets.

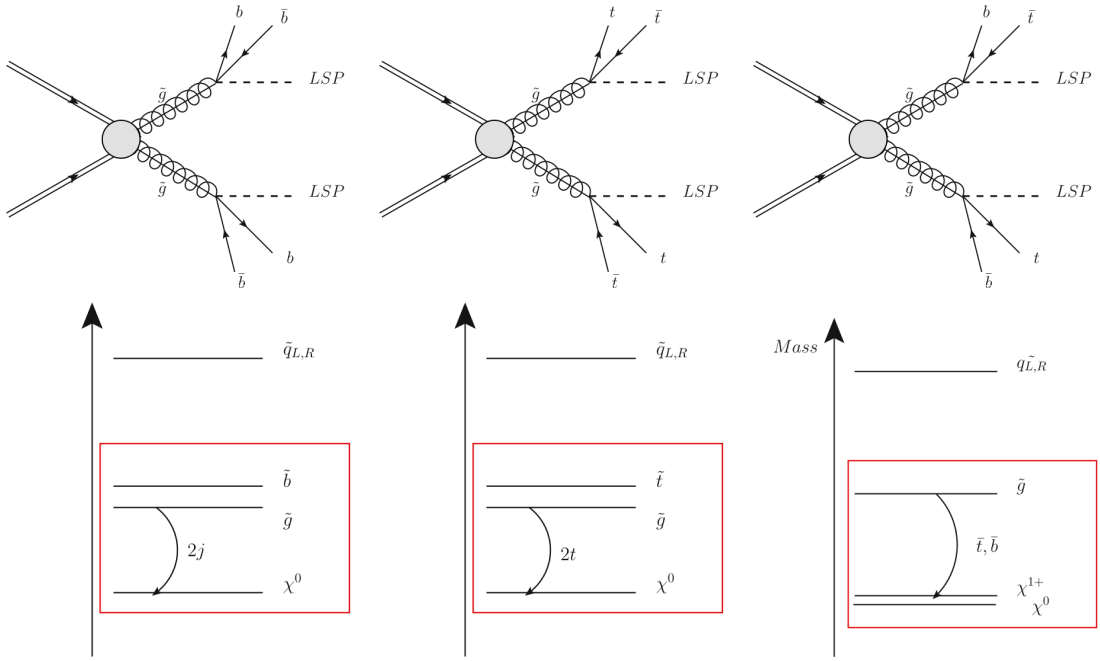

Figure 2.6 Diagrams of the production and schematics depicting the particle mass spectrum for Gbb, Gtt and Gtb topologies, with 4 b-jets and $E_{\mathrm{T}}^{\mathrm{miss}}$ expected in each of the final states.

Topology	Process	Final state
Gbb	$pp \to \tilde{g}\tilde{g}$, with $\tilde{g} \to b\bar{b} + \tilde{\chi}_1^0$	$b\bar{b}b\bar{b} + E_{\mathrm{T}}^{\mathrm{miss}}$
Gtb	$pp \to \tilde{g}\tilde{g}$, with $\tilde{g} \to \bar{t}b$ or $\bar{b}t + \tilde{\chi}_1^0$ (via $\tilde{\chi}_1^{\pm}$)	$t\bar{t}b\bar{b} + E_{\mathrm{T}}^{\mathrm{miss}}$
Gtt	$pp \to \tilde{g}\tilde{g}$, with $\tilde{g} \to t\bar{t} + \tilde{\chi}_1^0$	$t\bar{t}t\bar{t} + E_{\mathrm{T}}^{\mathrm{miss}}$

Table 2.3 Summary of the heavy flavor simplified models with the corresponding MSSM process. The expected final states are also presented.

Results of searches for SUSY have been reported in events with large missing transverse momentum plus 1 or 2 b-jets, using different amounts of integrated luminosity of pp collisions at $\sqrt{s} = 7$ TeV recorded with the ATLAS detector at the Large Hadron Collider during 2010 and part of 2011. Gluino pair production with $\tilde{g} \to \tilde{b}b(\tilde{t}t)$ was already the focus of a 2010 analysis done with 35 pb^{-1} of data [139], and of two analysis presented for EPS 2011 and Lepton-Photon 2011, with 0.83 fb^{-1} and 1.03 fb^{-1} of data collected during early 2011, respectively [140,141]. These have been updated using a data sample of 2 fb^{-1} [142]. Searches for scalar bottom quarks via $\tilde{g}\tilde{g}$ production have been also reported by the CMS Collaboration [143]. Searches sensitive to direct scalar bottom production irrespective of gluino mass have been

also published by the ATLAS collaboration [144]. Overall, no significant excess has been observed with respect to the prediction for Standard Model processes, with the results interpreted in a variety of model frameworks. Chapter 9 presents the results obtained in this thesis and compares them to these previous and other current searches performed within ATLAS and other experiments.

3

Statistical methods for exclusion limits and discovery

In this chapter the basic concepts needed for the understanding of the statistical treatment of the data is introduced. It is focused primarily on searching for new signals in high energy physics, aiming at stating the precise definition and notation of the key components for setting exclusion limits or claiming a discovery on new physics processes.

3.1 Hypothesis testing

An experimentalist often wants to decide, from a statistical point of view, whether some given physics model with pre-assigned or estimated values of the parameters is acceptable in light of the observations. This problem can be treated in terms of a test of a statistical hypothesis [145–147]. In this approach, a hypothesis (i.e., a physics model under testing) is chosen by the experimentalist to represent a certain data set, and referred to as the null hypotesis, H_0. In essence, the experiment will determine the probability to obtain the observed result assuming H_0 to be true.

On the basis of a given observation $\vec{x} \equiv (x_1 \dots x_n)$, of n events, a criteria to accept the null hypothesis and reject an alternative one (referred to as H_1) needs to be defined. The measure of compatibility (or incompatibility) between a certain experimental dataset and a hypothesis is generally quantified by a test statistic $q(\vec{x}) = q(x_1 \dots x_n)$, described by probability density functions (p.d.f) denoted by $f_0(q|H_0)$ and $f_1(q|H_1)$ for each hypothesis, respectively. Within the possible outcomes of $q(\vec{x})$ and assuming the null hypothesis H_0 to be true, a critical region (R) can be defined such that the probability that q belongs to R is less than or equal to any pre-assigned value. The implication is that if the observed value q_{obs} falls

in R, the null hypothesis H_0 is rejected, otherwise it is accepted. The pre-assigned probability α that the outcome of $q(\vec{x})$ belongs to the region R is called the *size* of the test:

$$P(q \in R) = \int_R f_0(q|H_0)dq \quad \equiv \alpha \ , \tag{3.1}$$

and it determines the significance level of the test at $100\alpha\%$. The mistake of rejecting H_0 when it is true is so-called a type-I error. Therefore, a low numerical value is usually taken for α. On the other hand, accepting H_0 when in fact it was false leads to the so-called type-II error, and the probability of its occurrence (denoted β), depends on the alternative hypothesis H_1. The *power* of a test is defined as the probability of rejecting a hypothesis when it is false:

$$\text{Power} \equiv 1 - \beta = \int_R f_1(q|H_1)dq \ . \tag{3.2}$$

The test statistic $q(\vec{x})$ compresses all H_0 versus H_1 discriminating information into one number. It can be proven through the Neyman-Pearson lemma that the ratio of likelihoods is the most powerful discriminator [145–147]. The likelihood ratio is defined as

$$q(\vec{x}) = -2 \ln \frac{\mathcal{L}(\vec{x}|H_0)}{\mathcal{L}(\vec{x}|H_1)} \ , \qquad -\infty < \mathrm{q} < \infty \ . \tag{3.3}$$

Thus, if $q(\vec{x})$ turns out to be smaller than zero, the null hypothesis H_0 is such that it has a large probability of being true. On the other hand, values of $q(\vec{x})$ higher than zero indicate that H_0 is unlikely.

3.2 Statistical significance

The level of agreement of the observed data with a given hypothesis H is quantified by computing the p-value, defined as the probability, under assumption of H, of finding data of equal or greater incompatibility with the predictions of H:

$$p - \text{value} = P(q > q^{obs}|H) \ , \tag{3.4}$$

where q_{obs} is the value of the test statistic obtained from comparing the observed data with a hypothesis H. The hypothesis is regarded as excluded if its p-value is observed below a specified threshold given by the size of the test α:

$$p - \text{value} \leq \alpha \ , \qquad \text{where } \alpha \in [0, 1]. \tag{3.5}$$

In addition, one can define the Z-value corresponding to a given p-value as the number of standard deviation Z at which a Gaussian random variable of zero mean

would give a one-sided tail area equal to the p-value. Thus, the significance Z is related to the p-value by

$$p - \text{value} = \int_Z^\infty \frac{1}{\sqrt{2\pi}} e^{-x^2/2} dx = 1 - \Phi(Z) \quad \longrightarrow \quad Z = \Phi^{-1}(1-p) \ , \tag{3.6}$$

where Φ^{-1} is the quantile (inverse of the cumulative distribution Φ) of the standard Gaussian. The particle physics community has tended to regard rejection of the background hypothesis with a significance of at least $Z = 5$ as an appropiate level to consitute a discovery. This corresponds to p-value $= 2.87 \times 10^{-7}$. For purposes of excluding a signal hypothesis, a threshold p-value of $\alpha = 0.05$, is often used, which corresponds to $Z = 1.64$.

3.3 Frequentist significance test

The first step in defining an analysis of search results is to state the relevant null and alternative hypotheses and identify the observables in the experiment which comprise the search results (e.g., number of candidates satisfying a certain set of criteria, reconstructed invariant mass, etc.). In a general procedure to search for a new phenomenon in the context of a frequentist statistical inference [145–147], the next step is to define a test-statistic (function of the observables and the model parameters, as production rate, particle mass, etc.) of the known background and hypothetical signal which ranks experiments from the least to most signal-like. To illustrate the use of the likelihood ratio (Eq. 3.3), one can consider an experiment where, for each selected event, one measures the values of certain kinematic variables and assumes a simple case for a single channel, with one signal and one background contribution and no systematics considered yet. For each event in the signal sample, one measures a given variable x and represents the resulting data by constructing a histogram denoted as $\vec{n} = (n_1 \dots n_n)$. The expectation value of signal and background events are denoted as S and B, respectively. The shapes $f_S(x)$ and $f_B(x)$ are the probabilitity density functions of the variable x for signal and background events. Given the full dataset $\vec{x} = (x_1 \dots x_n)$, one wanted to ask what the probablity is for obtaining n events in the data where the discriminating variable for the event e has a value x_e. First, one must include the Poisson probability of obtaining n events when a rate $\nu = \mu S + B$ is expected:

$$\text{Poisson}(n|\nu) = \frac{\nu^n e^{-\nu}}{n!} \ = \frac{(\mu S + B)^n \ e^{-(\mu S + B)}}{n!} \ , \tag{3.7}$$

where the parameter μ is referred to as the signal strength modifier. Thus, $\mu = 0$ and $\mu = 1$ correspond to the background-only hypotesis and the nominal signal + background hypothesis, respectively. The mean number of entries in the i-th bin

from signal (S_i) and background (B_i) are related to the shapes $f_S(x)$ and $f_B(x)$ by

$$S_i = S \int_{\text{bin i}} f_S(x_e) dx_{i_e} \ , \tag{3.8}$$

$$B_i = B \int_{\text{bin i}} f_B(x_e) dx_{i_e} \ , \tag{3.9}$$

where i_e is the index of the bin containing x_e. Secondly, one must take into account the probability density of obtaining x_e based on the relative mixture $f_S(x)$ and $f_B(x)$ for a given value of μ. Combining those two ingredients together one obtains the binned probability to observe n_i events in bins i:

$$\mathcal{L}(\{x_1 \dots x_n\}|\mu) = \prod_i \frac{(\mu S_i + B_i)^{n_i}}{n_i!} \ e^{-\mu S_i - B_i} \ . \tag{3.10}$$

Similarly, by replacing Eqs. 3.8-3.9 into Eq. 3.10, one gets the unbinned probability:

$$\mathcal{L}(\{x_1 \dots x_n\}|\mu) = \frac{1}{n} \prod_e \left[\mu S f_S(x_e) + B f_B(x_e)\right] \ e^{-(\mu S + B)} \ . \tag{3.11}$$

If one imagines the data as being fixed, then these equations depend on μ only, and they can be shortly denoted as $\mathcal{L}(\mu)$.

3.4 Profile likelihood-ratio

Different statistical approaches aiming to characterising a non-observation of a signal or establishing a significan excess of event have been implemented in previous colliders [148]. In addition to parameters of interest such as rate of the signal process (i.e., cross section), the predictions for both the signal and background yields, prior to the scrutiny of the observed data entering the statistical analysis, are subject to multiple uncertainties that are handled by introducing *nuisance* parameters, denoted by $\vec{\theta}$. Therefore, the signal and background expectation become functions of these parameters: $S = S(\vec{\theta})$ and $B = B(\vec{\theta})$. The systematic uncertainties on these rates are generally introduced via modifications to the test statistic and/or the way pseudo-data are generated using Monte Carlo experiments. In order to handle the nuissance parameters in the likelihoods for testing the compatibility of the data with the background-only and the signal+background hypotheses, the LHC has chosen the profile likelihood-ratio test statistic [149], defined as

$$\tilde{q}_\mu = -2 \ln \tilde{\lambda}(\mu) \equiv -2 \ln \frac{\mathcal{L}(\vec{x}|\mu, \hat{\theta}_\mu)}{\mathcal{L}(\vec{x}|\hat{\mu}, \hat{\theta})} \ , \qquad 0 \leq \hat{\mu} \leq \mu \ . \tag{3.12}$$

Here, $\hat{\theta}_\mu$ refers to the conditional maximum likelihood estimators of θ, given the signal strength parameter μ, and $\vec{x}$ may refer to the actual experimental observation or pseudo-data events. The pair of parameters $\hat{\mu}$ and $\hat{\theta}$ gives the global maximum of the likelihood. The lower constraint $0 \leq \hat{\mu}$ is imposed by physics, since signal rate is defined positive. On the other hand, the upper constraint $\hat{\mu} \leq \mu$ is added by hand in order to guarantee a one-sided confidence interval. Physics-wise, this means that upward fluctuations of the data such that $\hat{\mu} > \mu$ are not considered as evidence against the signal hypothesis, namely a signal with strength μ. The values of $\vec{\theta}$ are not taken as known a priori, but rather must be either assumed to some degree by a suitable model or fitted from the data. The presence of the nuisance parameters broadens the profile likelihood as a function of μ relative to what one would have if their values were fixed. This reflects the loss of information about μ due to the systematic uncertainties.

3.5 Profile likelihood asymptotic approximation

It frequently occurs that it is not possible to put the likelihood ratio in an unique and exact correspondence to a statistic whose distribution is known exactly. Fortunately, a satisfactory solution often exists when dealing with large samples. For purposes of setting limits, it is worth introducing a test statistic q_μ, based on the profile likelihood ratio $\tilde{q}_\mu$ but without the physical requirement $\hat{\mu} > 0$, defined as

$$q_\mu = -2 \ln \lambda(\mu) = -2 \ln \frac{\mathcal{L}(\vec{x}|\mu, \hat{\theta}_\mu)}{\mathcal{L}(\vec{x}|\hat{\mu}, \hat{\theta})} \ , \qquad \hat{\mu} \leq \mu \ . \tag{3.13}$$

On the other hand, for purposes of claiming a discovery, one can introduce the test statistic q_0 as

$$q_0 = -2 \ln \lambda(0) = -2 \ln \frac{\mathcal{L}(\vec{x}|0, \hat{\theta}_0)}{\mathcal{L}(\vec{x}|\hat{\mu}, \hat{\theta})} \ , \qquad \hat{\mu} \geq 0 \ , \tag{3.14}$$

where one should note that q_0 is not simply a special case of q_μ with $\mu = 0$, but rather has a different definition. The constraint $\hat{\mu} \geq 0$ is imposed since one is not interested in interpreting a deficit of events with respect to the expected background on an equal footing with an excess. Let consider the test q_μ, and suppose the data are distributed according to a strength parameter μ'. The desired distribution $f(q_\mu|\mu')$, where the subscript of q refers to the hypothesis being tested, and the second argument of f gives the value of μ assumed in the distribution of the data, can be found using results due to Wilks [150] and Wald [151]. For the case of a single parameter of interest (μ), they have shown that

$$-2 \ln \lambda(\mu) = \frac{(\mu - \hat{\mu})^2}{\sigma^2} + \mathcal{O}(1/\sqrt{N}) \ , \tag{3.15}$$

where $\hat{\mu}$ follows a Gaussian distribution with a mean μ' and standard deviation σ, and N represents the data sample size. If $\hat{\mu}$ is Gaussian distributed and one neglects the $\mathcal{O}(1\sqrt{N})$ term, then it can be shown that in the asymptotic regime, the statistic q_μ follows a non-central χ^2 distribution for one degree of freedom. This approximation is sufficiently accurate for total background events $B \gtrsim \mathcal{O}(10)$ [149]. Nevertheless, with the physical requirement $\hat{\mu} > 0$, the asymptotic behaviour of $f(\tilde{q}_\mu|\mu)$ does not follow a non-central χ^2 anymore, yet it follows a well defined formula:

$$f(\tilde{q}_\mu|\mu) = \frac{1}{2}\delta(\tilde{q}_\mu) + \begin{cases} \frac{1}{2}\frac{1}{\sqrt{2\pi}}\frac{1}{\sqrt{\tilde{q}_\mu}}\exp\left[-\tilde{q}_\mu/2\right] & 0 < \tilde{q}_\mu \leq \mu^2/\sigma^2 \ , \\ \frac{1}{\sqrt{2\pi}(2\mu/\sigma)}\exp\left[-\frac{1}{2}\frac{(\tilde{q}_\mu+\mu^2/\sigma^2)^2}{(2\mu/\sigma)^2}\right] & \tilde{q}_\mu > \mu^2/\sigma^2 \ , \end{cases} \tag{3.16}$$

with $\sigma^2 = \mu^2/q_{\mu,A}$, where $q_{\mu,A}$ is the test statistics evaluated with the expected background and the nominal nuisance parameters (setting all fluctuations to be zero), generally referred to as the Asimov data set. Similarly, an asymptotic formulae for $f(\tilde{q}_\mu|\mu = 0)$ can be obtained [149]. Interestingly, in the asymptotic limit, the two test statistics $\tilde{q}_\mu$ and q_μ are equivalent, leading to the same p-values. Thus, within this limit, it is more convenient to use the simpler asymptotic formulae for q_μ. Then, in the asymptotic regime, the test statistic q_μ can be approximated as

$$q_\mu = \begin{cases} \frac{(\mu-\hat{\mu})^2}{\sigma^2} & \hat{\mu} \leq \mu \\ 0 & \hat{\mu} > \mu \ . \end{cases} \tag{3.17}$$

The p-value of the hypothesized μ is given by

$$p_\mu = \int_{q_{\mu,\mathrm{obs}}}^{\infty} f(q_\mu|\mu)dq_\mu = 1 - \Phi(\sqrt{q_\mu}) \tag{3.18}$$

and its corresponding significance is therefore obtained from

$$Z_\mu = \Phi^{-1}(1 - p_\mu) = \sqrt{q_\mu} \ . \tag{3.19}$$

Following the same arguments, the test statistic q_0 can be approximated as

$$q_0 = \begin{cases} \hat{\mu}^2/\sigma^2 & \hat{\mu} \geq 0 \\ 0 & \hat{\mu} < 0 \ . \end{cases} \tag{3.20}$$

The p-value of the hypothesized $\mu = 0$ is given by

$$p_0 = \int_{q_{0,\mathrm{obs}}}^{\infty} f(q_0|0)dq_0 = 1 - \Phi(\sqrt{q_0}) \tag{3.21}$$

and its corresponding significance can be obtained from

$$Z_0 = \Phi^{-1}(1 - p_0) = \sqrt{q_0} \ . \tag{3.22}$$

3.6 CL_s method

The last step is to define rules for exclusion and discovery, i.e., specify ranges of values of the test statistic in which observations lead to one conclusion or the other. Having defined the test statistic, one constructs probability density functions of $\tilde{q}_\mu$ under the signal+background hypothesis (e.g., by means of tossing toy pseudo-observations or implementing the asymptotic formulae) assuming a signal with strength μ. The test-statistic $\tilde{q}_\mu$ can be constructed to decrease monotonically for decreasing signal-like experiments so that the confidence in the signal+background hypothesis is given by the probability that the test-statistic is bigger than or equal to the value observed in the experiment, $\tilde{q}_\mu^{obs}$, for a given signal strength modifier μ under test. This probability is referred to as CL_{s+b}:

$$p_\mu = P(\tilde{q}_\mu \geq \tilde{q}_\mu^{obs} | \mu S + B) = \int_{\tilde{q}_\mu^{obs}}^{\infty} f(\tilde{q}_\mu | \mu, \hat{\theta}_\mu^{obs}) d\tilde{q}_\mu \equiv CL_{s+b} \ , \tag{3.23}$$

where small values of CL_{s+b} indicate poor compatibility with the signal+background hypothesis. In the classical frequentist approach, one says that the signal is excluded at e.g., 95 % confidence level (CL), if $CL_{s+b} = 0.05$. However, such definition has a pitfall: by taking the signal strength equal to zero, one expects, by construction, that $CL_{s+b} \leq 0.05$ with a 5% chance. Thus, 5% of all searches will end up excluding a signal of zero strength. In this scenario, one must identify the actual statistical meaning of what has been observed in such cases; a downward fluctuation of the background. In order to prevent the inference of a signal from such downward fluctuations, a modified frequentist approach, referred to as the CL_s method, is introduced [28, 152, 153]. Following the discussion for 3.23, the confidence in the background hypothesis, denoted as CL_b, is defined as

$$1 - p_b = P(\tilde{q}_\mu \geq \tilde{q}_\mu^{obs} | B) = \int_{\tilde{q}_\mu^{obs}}^{\infty} f(\tilde{q}_\mu | 0, \hat{\theta}_0^{obs}) d\tilde{q}_\mu \equiv CL_b \ . \tag{3.24}$$

Here, one has defined $p_b = P(\tilde{q}_\mu < \tilde{q}_\mu^{obs} | B)$, excluding the point $\tilde{q}_\mu = \tilde{q}_\mu^{obs}$. Thus, values of CL_b very close to one indicate poor compatibility with the background hypothesis. Then, the CL_s method is defined as the following ratio:

$$CL_s(\mu) \equiv \frac{CL_{s+b}}{CL_b} = \frac{p_\mu}{1 - p_b} \ . \tag{3.25}$$

For an observation close to the top of the background-only expectation (i.e., $CL_b \approx 0.05$), the CL_s method gives a value about twice as large as the CL_{s+b}. Thus, this definition avoids not only the pitfall described above, but also the undesirable property in the classical approach of the CL_{s+b} method, that of two experiments with the same (small) expected signal rate but different backgrounds, the experiment with the larger background may have a better expected performance. For the CL_s method, the signal hypothesis is regarded to be excluded at the confidence level CL when

$$1 - CL_s \leq CL \ . \tag{3.26}$$

A value of 95 % CL is widely used in ATLAS to set an exclusion limit on signal models [154], following the agreed decision made by the particle physics community, as introduced in Section 3.2. This convention will be followed thoughtout this work, unless specified.

3.7 Quantifying an excess of events

In case of observing an excess of events, a characterisation begins by evaluating the p-value of the upward fluctuation of the background only hypothesis. From the profile likelihood test statistic q_0, its p-value is given by

$$p_0 = P(q_0 \geq q_0^{obs}) = \int_{q_0^{obs}}^{\infty} f(q_0|0, \hat{\theta}_0^{obs}) dq_0 \ . \tag{3.27}$$

By using Eq. 3.6, the p-value is converted into a significance Z. In the asymptotic regime, the profiled likelihood q_0 has the attractive property of being distributed as half χ^2 distribution for one degree of freedom, which allows one to appoximately estimate the significance through Eq. 3.22 as $Z = \sqrt{q_0^{obs}}$. Thus, the estimate can be obtained from the observed value q_0^{obs} itself, without having to generate pseudo-data. Finally, if one tests the background-only hypothesis many times while scanning a given parameter (e.g. a mass), a dilution effect associated with multiple testing should be taken into acount, known as trial factor or look-elsewhere effect [155].

4

The ATLAS experiment

4.1 The Large Hadron Collider

The Large Hadron Collider (LHC) [1] is the largest and highest-energy particle accelerator world-wide. The LHC and the experiments therein constitute the most complex scientific instruments ever built in human history, with enormous potential to shed light on fundamental physics, and it is expected to take scientists into the deepest understanding of Nature. After decades of preparation, the experiments at the LHC are taking the first steps toward resolving many long-standing puzzles about fundamental physics at the weak scale and their results are eagerly waited by the scientific community.

4.1.1 Machine design

The LHC is a proton-proton (pp) synchrotron built by the European Organization for Nuclear Research (CERN) and installed, from 1998 to 2008, in a tunnel of 26.7 kilometres in circumference at a depth ranging from 50 to 175 metres underground, beneath the Franco-Swiss border near Geneva, Switzerland. The LHC has been designed to produce head-on collisions between beams of protons at a center-of-mass energy, $\sqrt{s}$, of 14 TeV.[1]

Prior to being injected into the LHC, the protons undergo an acceleration chain through a series of smaller accelerators that successively increase their energy, and

[1] The LHC physics program is mainly based on proton–proton collisions. However, shorter running periods, typically one month per year, with heavy-ion collisions are included in the program, where lead ions beams collide at design energies of $\sqrt{s} = 1150$ TeV.

imprint on the resulting beam, structure and stability. The chain is shown in Figure 4.1 and the flow is as follows. Protons are initially separated from hydrogen atoms ionized in an electric field and sent throughout the first system, the linear particle accelerator Linac 2, where protons achieve an energy at extraction from the accelerating device of 50 MeV. These feed the Proton Synchrotron Booster (PSB), where protons are further accelerated to 1.4 GeV and injected then into the Proton Synchrotron (PS). Within this facility, the protons achieve 25 GeV. Finally, the Super Proton Synchrotron (SPS) takes place in the chain to further increase their energy up to 450 GeV, before protons are at last injected into the LHC.

The accelerating devices are radio-frequency electromagnetic resonator cavities that consists in essence of an oscillating electric field in the direction of the beam, with an oscilation frequency (f_{RF}) that is multiple of the revolution frequency of the accelerator (f_{rev}). These devices generate stable regions of the phase space in momentum and phase oscillation, dubbed *buckets*. When the beam is injected into an accelerating cavity, protons with the right energy and arriving at the cavity at the right time, receive the correct incremental change in kinetic energy. In addition, particles that arrived earlier or later receive less or more of an increase that those that are synched. Thus, the initially off-tuned particles are caught in energy-phase oscillations, and consequently, the beam is confined to well-defined buckets with particles in it, referred to as *bunches*. Generally, protons are not inmediately accelerated when entering an accelerating device, but rather they are first bunched within the stable regions of phase space, by adjusting the frequency so that no net acceleration on the synched protons takes place. After the beam has been actively captured with an imposed time structure, the beam is accelerated by slowly changing the RF cavity frequency. Consequently, the synched protons start feeling a net force, and the so-called synchrotron acceleration process begins. The LHC uses eight cavities per beam, grouped in two cryomodules, operating at 4.5 K, each delivering an accelerating field of 5 MV/m at $f_{\mathrm{RF}} = 400$ MHz. For the LHC, the number of buckets is given by $n_{\mathrm{reg}} = f_{\mathrm{RF}}/f_{\mathrm{rev}}$, with $f_{\mathrm{rev}} = 11223$. Nominally, every tenth of these buckets can contain a bunch. Thus, the LHC fills 2808 out of the 3564 available slots with protons at design specifications. Other gaps are left for beam injection and abort procedures. Bunches are further organized in bunch trains, i.e., groups of proton bunches with a fixed inter-bunch spacing (τ_{bunch}). The nominal spacing between the bunches within a train is 25 ns, while bunch trains are generally further appart.

The LHC contains two adjacent, parallel, high-vacuum beam pipes (10^{-13} atm), each containing a proton beam, which travel in opposite directions around the LHC ring. Particles circulating in beams are further manipulated using a large variety of magnets, where each type contributes to optimizing the trajectory of protons. At the LHC, there are 1232 superconductors dipole magnets, implemented to keep the protons in their nearly circular orbits. These operate at 1.9 K and 11.85 kA,

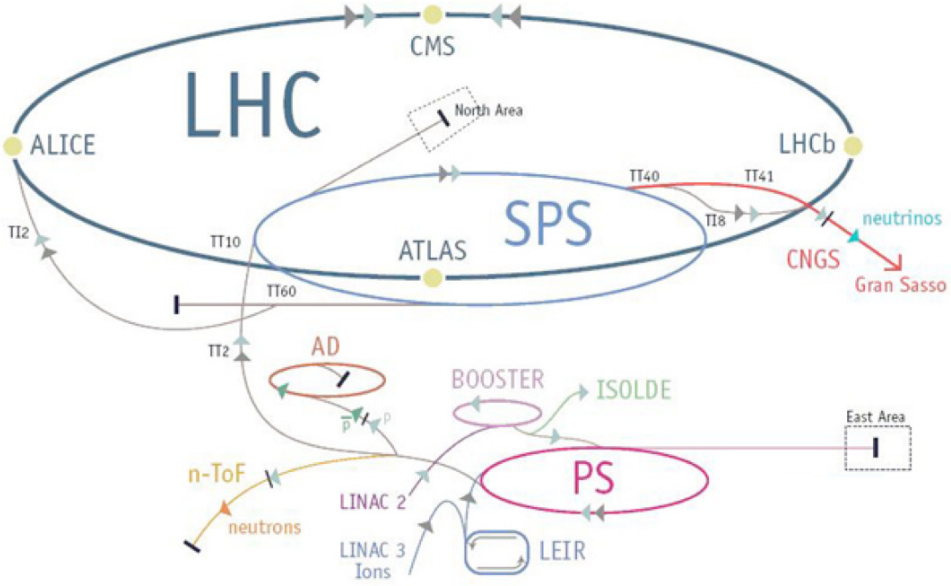

Figure 4.1 The CERN accelerator facility. First, a linear particle accelerator, so-called Linac 2, generates protons with an energy at extraction of 50 MeV. These feed the Proton Synchrotron Booster (PSB), where protons are further accelerated to 1.4 GeV and injected then into the Proton Synchrotron (PS). Within this facility, the protons achieve 25 GeV. Finally, the Super Proton Synchrotron (SPS) is implemented in the chain to further increase their energy to 450 GeV, before protons are at last injected into the LHC. Thus, the protons undergo an acceleration chain through a series of smaller accelerators that successively increase their energy, and imprint on the resulting beam, structure and stability.

generating a magnetic field of 8.4 T. The existing strong Coulomb forces within a bunched beam make protons tend to separate from each other. This effect is resisted by using 392 quadrupole magnets of 6.8 T, which take care of focusing the beam in its transverse plane.

The beam traveling through the Linac 2 is deflected and steered towards the Booster, allowing the beam intensity and emittance to be adjusted. Then, the bunch structure and placement into the LHC occur, via the PS and SPS, and the required bunch-filling scheme is thus fulfilled. Therefore, a coherent and optimized operation of each system is needed to provide a high-quality and stable final high-energy proton beam, necessary for physics studies in the detectors. The protons bunches are accumulated, accelerated and finally circulated in each of the two rings of the LHC, throughout its 26.7 km, at the design energy of 7 TeV each. Both beams travel in opposite directions and intersect at four points with high rates, where the detectors are placed: The multipurpose detectors of the ATLAS [2] and CMS [41] experiments, and the specialized detectors of the ALICE [156] and LHCb [157] experiments.

4.1.2 Luminosity and pile-up

The rate of collisions, denoted by $\mathcal{R}_i$, that yields to a certain process i can be expressed as

$$\mathcal{R}_i = \mathcal{L}\sigma_{pp\to i} \ , \tag{4.1}$$

where $\sigma_{pp\to i}$ corresponds to the cross-section of such process, and the instantaneous luminosity $\mathcal{L}$ accounts for all beam dependent parameters that impact the rate of collisions. The physics program at the LHC includes searches for physics processes with a small cross section (e.g., SUSY), thus it is crucial to maximise the delivered luminosity in order to be able to observe such events. Figure 4.2 presents the cross-sections for various processes as a function of the center-of-mass energy ($\sqrt{s}$). The instantaneous luminosity is

$$\mathcal{L} = \frac{f_{\text{rev}} n_b N_1 N_2}{A} \ , \tag{4.2}$$

where n_b is the number of colliding bunches and N_i is the number of protons per bunch in a given beam ($i = 1, 2$). The parameter A is the transverse cross section of the overlap between the beams, and it is defined as

$$A = \frac{4\pi\epsilon_n\beta^*}{\gamma F} \tag{4.3}$$

with ϵ_n the normalized transverse emittance, β^* is the beta-function at the interaction point (both beam quality concepts reflecting the process of bunch preparation), γ is the gamma Lorentz factor and F takes into account that beams do not completely intersect head-to-head but with a certain angle. The procedure to measure the luminosity in ATLAS is discussed in Section 4.2.9.

The LHC parameters are expected to evolve, aiming at increasing the delivered luminosity to fulfill the detectors requirements for physics analysis. In addition to enhancing the beam energy, several changes in the LHC parameters can take place to augment the luminosity, by means of squeezing the beams and reducing their transverse size, or increasing the number of colliding protons per bunch. Furthermore, the number and spacing of circulating bunches can be increased or shortened, respectively. Squeezing effects and an augmented number of colliding protons lead to a proportional increase of pp collisions within the same bunch crossing. The different LHC conditions may be described in terms of number of inelastic interactions per bunch crossing μ (with the expected average of the Poisson distribution that μ follows denoted by $\langle\mu\rangle$). Thus, Eq. 4.2 can be expressed as

$$\mathcal{L} = \frac{\mu f_{\text{rev}} n_b}{\sigma_{\text{inel}}} \ , \tag{4.4}$$

where σ_{inel} corresponds to the pp inelastic cross-section, of 71.5 mb [158]. For the LHC operating at design conditions, around 25 pp inelastic interactions per bunch

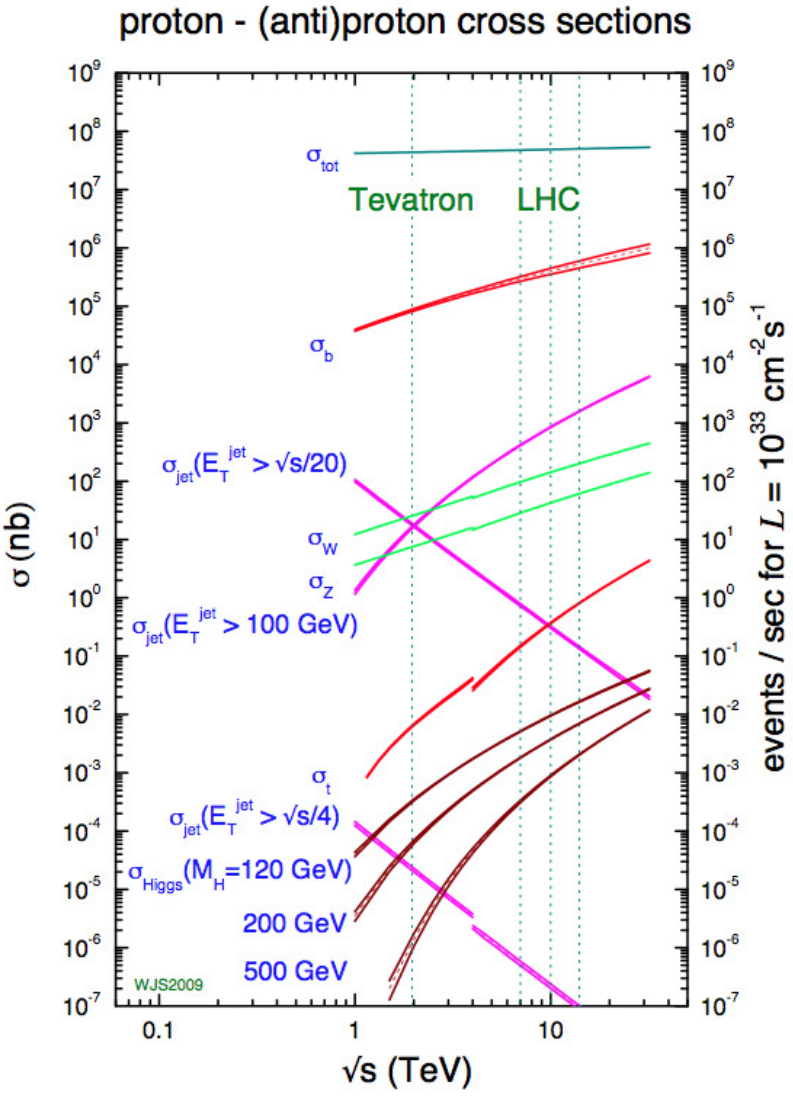

Figure 4.2 Cross-sections for various processes as a function of the center-of-mass energy ($\sqrt{s}$).

crossing are expected on average, with one of these corresponding to the hard scatter, as discussed in Section 1.4. The remaining pp interactions that go with the hard scatter when two bunches collide are referred to as in-time pile-up.

The bunch separation of the LHC has been shortened since data-taking started (see Table 4.1). For instance, during the 2011 data taking period, the LHC has run with the bunch trains configuration with $\tau_{\text{bunch}} = 50$ ns. Even if only one proton-proton interaction happened in a given bunch crossing, those that took place in a previous bunch crossing may also affect the signal response of a given ATLAS sub-detector. As consequence of longer electronic read-out windows at certain parts of the ATLAS detector (see Section 4.2) than τ_{bunch}, the response to energy deposition or charge collection is sensitive to short multiple bunch crossings spacing. This effect

yields the collision of interest that took place at a certain bunch, to be affected by residual multiple interactions, from different bunches, during the time required for the detector to process the pp interaction of interest. This phenomenon is known as out-of-time pile-up.

4.1.3 LHC operation during 2011

Since November 23^{rd} of 2009, when the LHC produced its first proton-proton collision at $\sqrt{s} = 450$ GeV (i.e., the injection energy), the accelerator has been running in different operating phases, each with specific parameters and center-of-mass energies. The performance of the LHC during 2011 was considered by everyone involved in the operations as outstanding. The LHC has run steadily, colliding protons at $\sqrt{s} = 7$ TeV (i.e., a beam energy of 3.5 TeV), with instantaneous luminosities reaching peak values above $3.5 \times 10^{33}\text{cm}^{-2}\text{s}^{-1}$ and 50 ns bunch spacing. Under such conditions, the average number of collisions per crossing is 12. Table 4.1 summarizes the range of typical parameters at the ATLAS interaction point during the different phases of the LHC operation, and design parameters at the nominal energy.

LHC Parameter	$\sqrt{s} = 0.9$ TeV (2009)	$\sqrt{s} = 7$ TeV (2010)	$\sqrt{s} = 7$ TeV (2011)	$\sqrt{s} = 14$ TeV (design)
n_b	1-9	1-368	1380	2808
N_i (10^{10} p/bunch)	1.5	1-11	15	11.5
τ_{bunch} [ns]	-	150	50	25
ϵ_n [μm-rad]	2-4	1.5-10	1.9-2.3	3.75
β^* [m]	11	11-2	1	0.55
$\mathcal{L}$ [$\text{cm}^{-2}\text{s}^{-1}$]	1-3 $\times$ 10^{26}	10^{27}-2 $\times$ 10^{32}	3.6 $\times$ 10^{33}	1.0 $\times$ 10^{34}
$\langle\mu\rangle$	$\ll 1$	1-5	12	25

Table 4.1 Values of LHC parameters at the ATLAS interaction point, for the 2009, 2010 and 2011 LHC operation, and the design parameters at the nominal energy. From top to bottom: n_b is the number of colliding bunch pairs, N_i (i = 1,2) is the number of protons per bunch in beam i, τ_{bunch} is the fixed inter-bunch spacing, ϵ_n is the normalized tranverse emittance, β^* is the β-function at the ATLAS IP, $\mathcal{L}$ is the instantaneous luminosity, and $\langle\mu\rangle$ is the expected average number of pp interactions per bunch crossing.

4.2 The ATLAS detector system

The LHC will extend the frontiers of particle physics with its unprecedented high energy and luminosity. Bunches of $\mathcal{O}(10^{11})$ protons are expected to collide 40

millions times per second to provide 14 TeV proton-proton collisions at a design luminosity of $10^{34}\text{cm}^{-2}\text{s}^{-1}$. ATLAS ("A Toroidal LHC ApparatuS") is a general-purpose detector built to cope with the enormous interaction rates and radiation doses at the LHC environment. Spanned over 44 m length and 25 m height, ATLAS represents the biggest multi-purpose particle detector ever built in all mankind history. The following sections presents an overview of the ATLAS detector used for the analysis presented in this thesis. It consists of several high-granularity and resistent sub-detectors designed to correctly identify particles and precisely determine their corresponding multiplicities, trajectories and energies. Requirements for the ATLAS detector system have been chosen to both fullfill precision measurements within the Standard Model and to characterize a wide set of processes covering much of the new phenomena it is hoped to observe at the TeV scale. The general performance goals for ATLAS are summarized in Table 4.2. The detector layout is forward-backward symmetric with respect to the interaction point, consisting of a series of ever-larger concentric cylinders and wheels detector devices around the interaction point where the LHC proton beams collide. It can be divided into four major parts: the Magnet System (Section 4.2.2), the Inner Detector (Section 4.2.3), the Calorimeter system (Section 4.2.4) and the Muon Spectrometer (Section 4.2.5), as shown in Figure 4.3. The technologies, arrangements and challenges for each of these sub-systems are introduced next.

Detector component	Resolution (design goal)	Precision	Trigger
Tracking	$\sigma_{p_\text{T}}/p_\text{T} = 0.05\% p_\text{T} \oplus 1\%$	$\lvert\eta\rvert < 2.5$	-
EM calorimetry	$\sigma_E/E = 10\%/\sqrt{E} \oplus 0.7\%$	$\lvert\eta\rvert < 3.2$	$\lvert\eta\rvert < 2.5$
Hadronic calorimetry	$\sigma_E/E = 50\%/\sqrt{E} \oplus 3\%$	$\lvert\eta\rvert < 3.2$	$\lvert\eta\rvert < 3.2$
Forward calorimeter	$\sigma_E/E = 100\%/\sqrt{E} \oplus 10\%$	$3.1 < \lvert\eta\rvert < 4.9$	$3.1 < \lvert\eta\rvert < 4.9$
Muon Spectrometer	$\sigma_{p_\text{T}}/p_\text{T} = 10\%$ at $p_\text{T} = 1$ TeV	$\lvert\eta\rvert < 2.7$	$\lvert\eta\rvert < 2.4$

Table 4.2 General performance goals of the ATLAS detector. The muon-spectrometer performance is independent of the inner-detector tracking system for high-p_T muons. Energy (E) and transverse momentum (p_T) are in [GeV]. The two rightmost columns summarize the η coverage of the detectors, each implementing different technologies for selecting events of interest (Trigger) and perform accurate measurements (Precision).

4.2.1 Coordinate system

The coordinate system and nomenclature used to describe the ATLAS detector and the particles emerging from the pp collisions are briefly introduced here. The nominal interaction point is defined as the origin of the coordinate system, while

the beam direction defines the z-axis and the x-y plane is transverse to the beam direction. The positive x-axis is defined as pointing from the interaction point to the centre of the LHC ring and the positive y-axis is defined as pointing upwards. The side-A of the detector is defined as that with positive z and side-C is that with negative z. The azimuthal angle ϕ is measured around the beam axis, and the polar angle θ is obtained from the beam axis. The rapidity y, in terms of energy (E) and momentum projection along the z-axis (p_z), is defined as $y = 1/2 \ln[(E + p_z)/(E - p_Z)]$ and the pseudorapidity is defined as $\eta = -\ln \tan(\theta/2)$[2]. The transverse momentum p_{T}, the transverse energy E_{T} and the missing transverse energy $E_{\mathrm{T}}^{\mathrm{miss}}$ are defined in the $x - y$ plane (unless stated otherwise). The distance ΔR in the pseudorapidity-azimuthal angle space is defined as $\Delta R = \sqrt{\Delta\eta^2 + \Delta\phi^2}$.

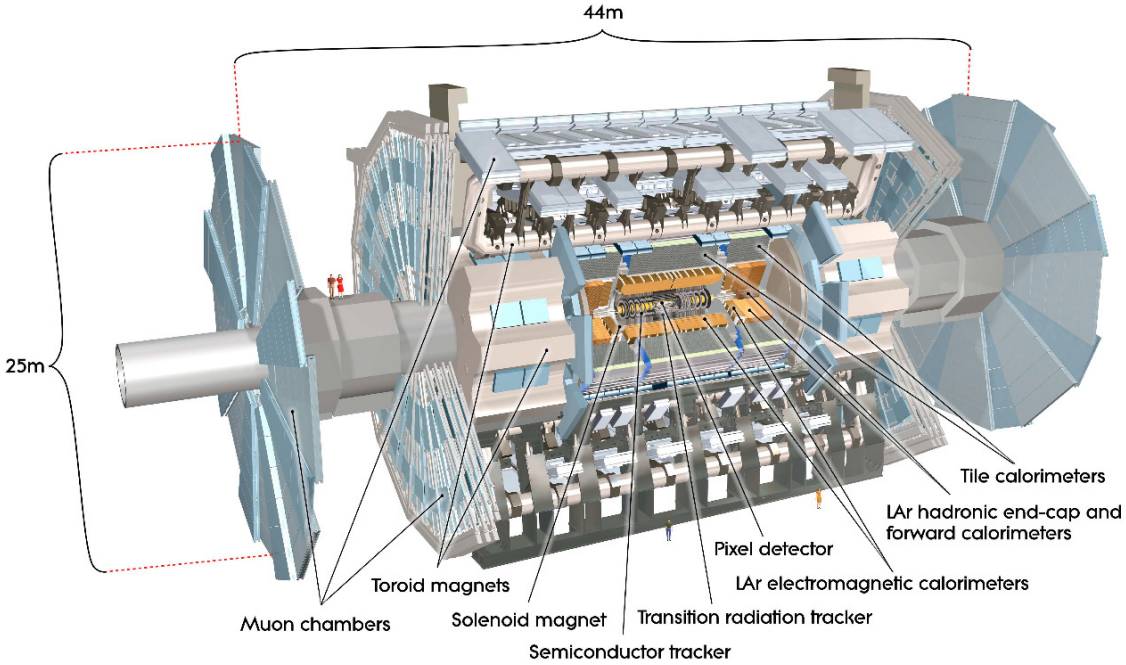

Figure 4.3 Cut-away view of the ATLAS detector. The sub-systems of the Inner Detector, the Calorimeter and the Muon Spectrometer are shown, along with the Magnet System. The dimensions of the detector are 25 m in height and 44 m in length. The overall weight of the detector is approximately 7000 tonnes.

4.2.2 The solenoidal and toroidal magnet systems

The magnetic field responsible for bending the trajectory of charged particles is provided by the ATLAS magnet system. Thus, the momentum of particles can be measured via the radius of curvature of the tracks left within the detector systems.

[2]In the limit of massless particles, $y = \eta$, both invariant under Lorentz boosts along the beam axis (z).

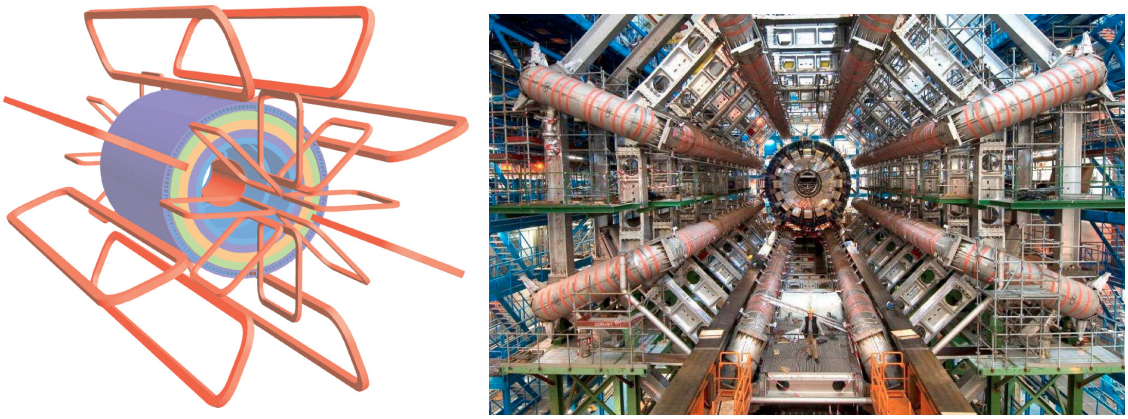

Figure 4.4 Magnet system arrangement of the ATLAS detector (left). The eight barrel toroid cells, with the end-cap coils interleaved are visible. The solenoid windings lie inside the calorimeter volume. The calorimeter is depicted as four layers with different magnetic properties, plus an outside return yoke. Barrel toroid as installed in the underground cavern where ATLAS lies (right).

The magnet configuration comprises a thin superconducting solenoid surrounding the Inner Detector cavity, and three large superconducting toroids (one barrel and two end-caps), arranged with an eight-fold azimuthal symmetry around the calorimeters, which provide bending power for the Muon Spectrometer. The solenoid, placed with its field axis matching the beam direction (z), is made of a single-layer aluminum coil wound by a NbTi conductor, optimizing thus its thickness in order to have a small impact on the energy measurement in the calorimeters. The solenoid has an inner radius of 1.23 m, a total length of 5.8 m, and provides a magnetic field of 2 T for the Inner Detector. The flux of the solenoid is returned by the steel of the ATLAS hadronic calorimeter, as shown in Figure 4.4. The toroidal magnet implements coils consisting of a conductor made of a mixture of aluminum, niobium, titanium and copper, and they extend the magnet system to a total of 26 m length and 20 m diameter. This configuration provides a magnetic field for the Muon Spectrometer of 0.5 T and 1 T in the barrel and end-caps, respectively. The magnet system operates with nominal currents of 8 kA for the solenoid, and of 25 kA for the toroids, respectively. This system is housed inside a cryogenic device that uses a mixture of nitrogen and liquid Helium, allowing the superconducting magnets to operate at required temperatures, of around 4 K.

4.2.3 Inner Detector

The Inner Detector (ID) is primary designed to provide pattern recognition, momentum and vertex measurements for charged tracks above $p_{\mathrm{T}} \approx 500$ MeV within the pseudorapidity range $|\eta| < 2.5$, and electron identification for energies 0.5 GeV - 150 GeV, over $|\eta| < 2.0$. Submerged in a solenoidal magnetic field of 2 T, the

ID spans a cylindrical envelope of ±3512 mm (1150 mm) length (radius), and its layout is introduced in Figure 4.5. The high position and momentum resolution required for the ATLAS physics program is achieved by implementing a combination of three independent but complementary subsystems: the Pixel detector (Pixel), the SemiConductor Tracker (SCT) and the Transition Radiation Tracker (TRT). The technologies and arrangement of these devices are introduced next.

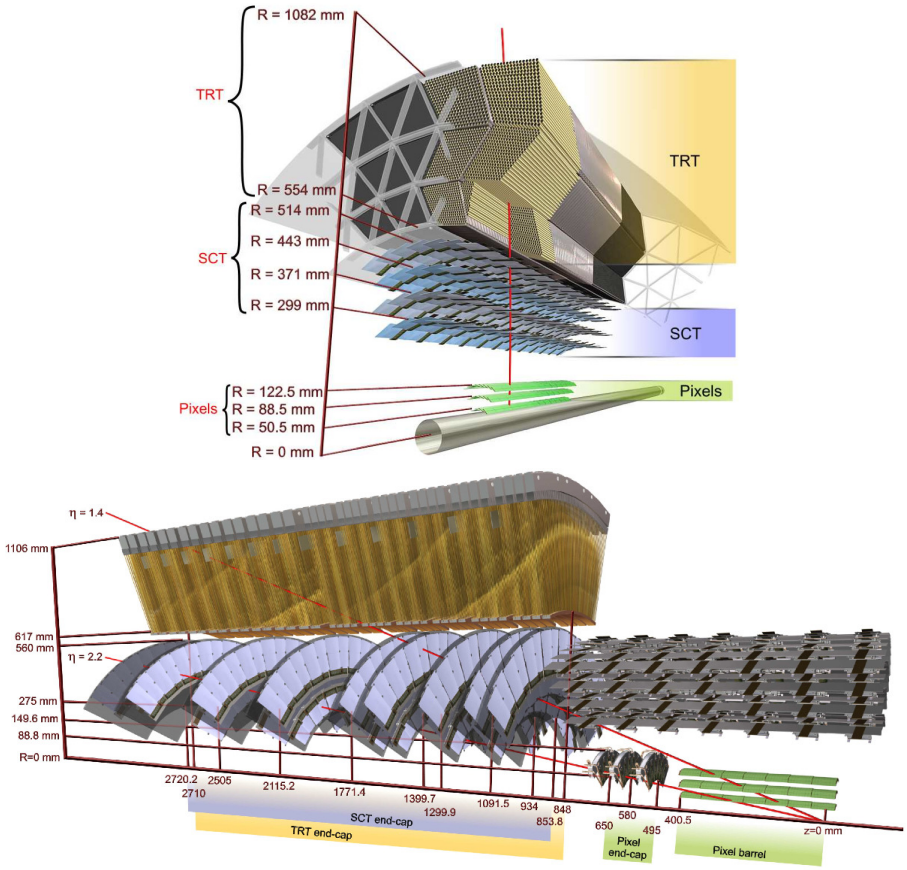

Figure 4.5 Scheme of the ATLAS Inner Detector layout.

4.2.3.1 The Silicon detectors

The two innermost detectors exploit the electronic properties of semiconductor materials. Ionizing particles that traverse a semiconductor create free electron-hole pairs, yielding to current conduction inside the material that can be controlled by an electric field. The collected current generates then a pulse signal, which is referred to as a "hit", if above a certain tunable threshold. Semiconductor conductivity can be easily manipulated using doping patterns to improve signal-to-background ratio. The ATLAS semiconductor detectors use junctions of one more (p-doped) and one less (n-doped) valence electron in the semiconducting materials.

Silicon pixel detectors (Pixel) with high-resolution pattern recognition capabilities are used for the innermost ATLAS sub-detector (hence its name), in order to withstand the high-density tracking scenario expected at the LHC. The pixel detector is designed with radiation-hard electronics for effective charge collection even after long exposure to the harsh LHC environment. All pixel sensors are identical and have a nominal size of 50×400 μm^2. The direction of the shorter pitch corresponds to the high precision position measurement in the $R - \phi$ plane. The pixel detector setup consists of 1744 modules, each with an area of 24.4 mm $\times$ 63.4 mm, assembled on 3 cylindrical layers in the barrel, and 3 disks on each end-cap. The three cylindrical layers are placed at 50.5, 88.5 and 122.5 mm from the interaction point in the radial direction, whereas the disks are settled at distances of 495, 580 and 650 mm from the IP, along the beam direction. The three pixel layers, are typically crossed by each track. The intrinsic resolution in the barrel (end-cap) is of 10 μm in $R - \phi$ and 115 μm in z (R). Full ϕ coverage is achieved using modules within cylindrical layers tilted 20° with respect to the tangent to the cylinder and partially overlap with the neighbour module. In the end-caps, disks modules are shifted 3.75° in ϕ. The Pixel is flushed with N_2 and operates at voltages ranging 150 V - 600 V at -10 °C temperature. The total extension of the Pixel is 1.3 m in z and 30 cm in diameter, and it contains approximately 80.4 million readout channels.

The SemiConductor Tracker (SCT) implements long, narrow silicon strips rather than small pixels devices, making the coverage of a larger area more economical and practical. The SCT detector consists of 2112 rectangular-shaped modules, assembled on 4 cylindrical layers in the barrel, and 1976 trapezoidal-shaped modules organized in 18 disks, 9 on each end-cap. The four cylindrical layers are placed at 299, 371, 443 and 514 mm from the interaction point, in the radial direction. The disks are placed at a distance ranging from 934 to 2720 mm from the interaction point along the beam direction. The SCT modules are made of two pairs of single-sided silicon micro-strip sensors. The two layers in each pair are placed one on top of each other, with one of them rotated a small angle (0.040 rad) with respect to the other, keeping one set of strips parallel to the beam direction (stereo-strip configuration). Each side of the module consists of two 6.4 cm daisy-chained sensors. The spacing of the strips is an approximately constant pitch of 80 μm, with 768 strips per sensor, resulting in a strip module of 12.8 cm in length and 6.4 cm wide in the barrel. In the end-cap region, the strip varies its size from 5.2 cm to 12.6 cm in length. The stereo-strip sensors on both sides of a given module are tilted by $\pm$0.020 radians with respect to the center of its corresponding module. This configuration provides three-dimensional hit information and determines the resolution in the z direction. The eight strip layers in the barrel (i.e., four space points) are typically crossed by each charged particle track. The intrinsic resolution per module in the barrel (disk) are 17 μm in $R - \phi$ and 580 μm in z (R). Full ϕ coverage in both the barrel and disk layers is achieved using a layout of tilted and overlapped modules. The SCT

operates in the same environmental conditions as the pixel detector, sharing the cooling system for the modules, with operating voltages ranging between 150 V - 450 V depending on the radiation damage. The total number of readout channels in the SCT is approximately 6.3 million.

The Pixel and the SCT detectors are the key ingredients for primary vertex identification and high-precision particle trajectory reconstruction, the main purposes of the ATLAS semiconductor sub-detectors. The semiconductor devices allow impact parameter measurements and vertexing for heavy-flavour and τ-lepton tagging. The secondary vertex measurement performance is enhanced by the innermost layer of pixels, at a radius of about 5 cm.

4.2.3.2 The Transition Radiation Tracker (TRT)

The Transition Radiation Tracker (TRT) is the outermost component of the ID. Small drift tubes (straws) are implemented for tracking purposes. Each straw is filled with gas that becomes ionized whenever a charged particle passes through it. Charged atoms and electrons are separated by an existing electric field between the tube walls and a thin anode wire placed through the center of the tube. This mechanism produces a current pulse in the wire, where negative charges are collected. The combination of many wires with signals creates a pattern of *straw hits* that allow the path of the particle to be determined (tracker). In addition to the tracking capabilities, the TRT allows to discriminate heavy charged particles from electrons by measuring the transition radiation (TR), which consists of X-rays emitted by charged particles when they pass through the frontier between two materials with different dielectric constants. The charged particles going through the material between the tubes are accompanied by the radiated photons, where the probability of emitting these photons depends essentially on the γ-Lorentz factor and the number of material transitions used within the detector device. As the photons also interact with the molecules in the gas, they release more negative charges, depending on the mass of the initiating particle. Particles of a given energy have a higher speed the lighter they are, and therefore the amount of transition radiation is expected to be the greatest for highly relativistic ones, resulting in specific signals for different mass particles of the same energy. Thus, materials with widely varying indices of refraction placed between the straw tubes will cause ultra-relativistic charged particles to produce much stronger signals.

The transition radiation tracker (TRT) comprises many layers of straw tube elements interleaved with transition radiation material (Figure 4.6). A large number of hits (typically 36 hits on average per track) provides continuous tracking to enhance the pattern recognition and improve the momentum resolution over $|\eta| < 2.0$. The detecting elements are Polyimide straws, each 4 millimetres in diameter and up to 144 centimetres long, filled with a Xenon-based gas mixture (70% X_e, 27% CO_2 and

3% O_2). The straw walls, acting as cathode, are held at about -1500 V, drifting the electrons towards a 31 μm diameter gold-coated tungsten wire going through their center that serves as an anode, with a maximum collection time of around 50 ns for drift electrons. The barrel module consists of 72 layers in total, of 144 cm long straws, parallel to the beam axis. Each of the two end-cap modules are made of 160 disk-shaped layers of 37 cm long straws, perpendicular to the beam direction, arranged radially in wheels. The TRT layout provides thus $R-\phi$ information only, for which it has an intrinsic accuracy of 130 μm per straw, not as precise as the Pixel and SCT, but necessary for reducing the cost of covering a large volume and having transition radiation detection capability. The ambiguities in the third coordinate are resolved using additional information from both the Pixel and the SCT detectors. The straws are organized in 96 modules (in the barrel) and 20 wheels (end-cap), that provide the support structure for the straws, containing 52544 straws in the barrel and 122880 straws per side in the end-cap, respectively. Each module is composed of a carbon-fiber shell and an array of straws embedded in a matrix of polypropylene fibers, that enable the transition radiation. The discrimination between electrons and pions is the main purpose of the transition radiation detector. Particle paths with many very strong signals can be identified as belonging to the lightest charged particles: the electrons. The Xenon-based gas mixtured is used to increase the number of straws with strong signal, further enhancing the discriminating capabilities between electrons and pions. The TRT is designed to operate at room temperature, with a total number of readout channels around 400.000. Overall, the combination of precision silicon trackers at small radii with the TRT at a larger radius gives very robust pattern recognition and high precision in both $R-\phi$ and z coordinates. The straw hits at the outer radius contribute significantly to the momentum measurement, since the lower precision per point compared to the silicon is compensated by the large number of measurements and longer measured track length. In addition, the TRT provides electron identification complementary to that of the calorimeter over a wide range of electron energies.

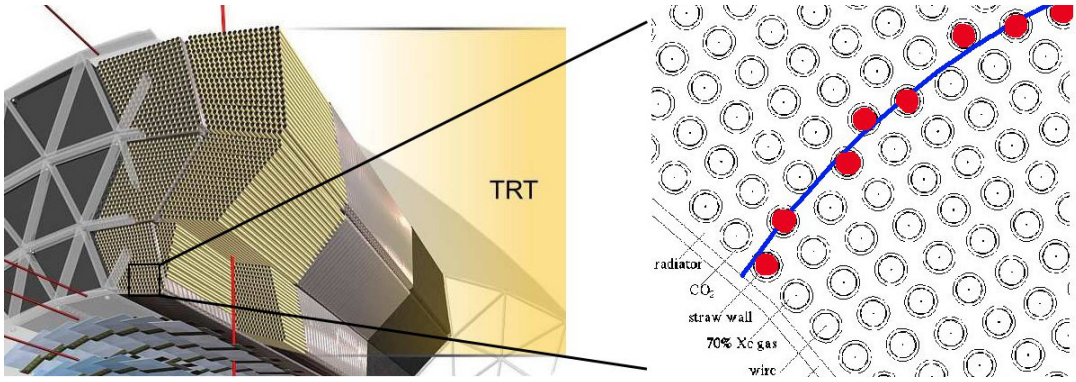

Figure 4.6 Diagram with an indication of a partially reconstructed track in the TRT detector.

4.2.4 Calorimeter

The contribution of the calorimeter information to the data analysis in ATLAS is of key importance, and ranges from event selection to identification and precision measurements of the four-vectors of individual particles and jets, and of the energy flow in the events (e.g., missing transverse energy) coming from the pp interaction. The calorimeters are prime devices to measure the energy of particles through total absorption. High-energy particles entering a given material originate a shower of decreasingly lower-energy ones as consequence of the interactions with the material. These can be periodically absorbed in a high-density material and sampled using generally ionization or scintillation light proportional to the number of particles in the active medium, thus inferring the energy of the original particles from this measurement. This arrangement is referred to as sampling calorimeters consisting of an *absorber/active* material.

Several processes may take place during the passage of particles through matter, such as bremsstrahlung, e^+e^- pair production, hadron-nucleon collisions, etc. The relevance of each process depends on the nature of the incident particle, its kinematics and the material chosen. High-energetic electrons, positrons and photons interacting with the calorimeter material yield to the so-called electromagnetic showers, an interplay between bremsstrahlung photons and the subsequent e^+e^- pair production, until the produced particles have low enough energy that Compton scattering and absorption through the photo-electric effect become important. The longitudinal development of the shower is described almost independently of the details of the absorber material in terms of the radiation length (X_0)[3]. Showers initiated by hadrons and mesons impose additional complications, due to the role played by the strong interaction. In hadronic showers, the vast majority of the secondary particles produced are pions and kaons. The neutral pions decay ($\pi^0 \to \gamma\gamma$) yields an electromagnetic shower as explained above. The behaviour of the remaining particles is dictated by the occurrence of nuclear reactions. The hadronic shower component is characterized by a nuclear interaction length (λ) of particles undergoing an inelastic nuclear interaction. The fraction of the shower energy needed to break the atomic nuclei is lost, and therefore it does not contribute to the calorimeter signals (invisible-energy phenomenon). These characteristics have important consequences for calorimetry:

- *non-compensation*: The calorimeter signals for hadrons are in general smaller than for electrons of the same energy ($e/h > 1$), as some fraction in the hadronic shower is lost to nuclear recoils and dissociation, thus not captured by the active calorimeter material.

[3] A radiation length (X_0) refers to as both (1); the mean distance over which a high-energy electron loses $1/e$ of its energy by bremsstrahlung and (2); 7/9 of the mean free path for pair production by a high-energy photon.

- *non-linearity*: The calorimeter is non-linear for hadron detection, as the electromagnetic energy fraction is energy dependent.

The ATLAS experiment has chosen a non-compensating sampling calorimeter system that consists of a number of sub-detectors with full ϕ-symmetry and coverage around the beam axis, over $|\eta| < 4.9$. The innermost calorimeters envelope the region closest to the beam-line, and use sampling technology with liquid argon (LAr) as the active detector medium. These are housed in three cryostats, one barrel and two end-caps. The barrel cryostat contains the lead/LAr electromagnetic barrel calorimeter (EMB), whereas the two end-cap cryostats each contain the lead/LAr electromagnetic end-cap calorimeter (EMEC), the copper/LAr hadronic end-cap calorimeter (HEC), and the copper-tungsten/LAr forward calorimeter (FCal). The outermost sampling detector is the steel/scintillator-tile hadronic calorimeter (HAD), divided in three parts: the central barrel (Tile) and the two extended barrels (Extended Tile). The overall ATLAS calorimeter system is depicted in Figure 4.7. The primary systems involved are described next.

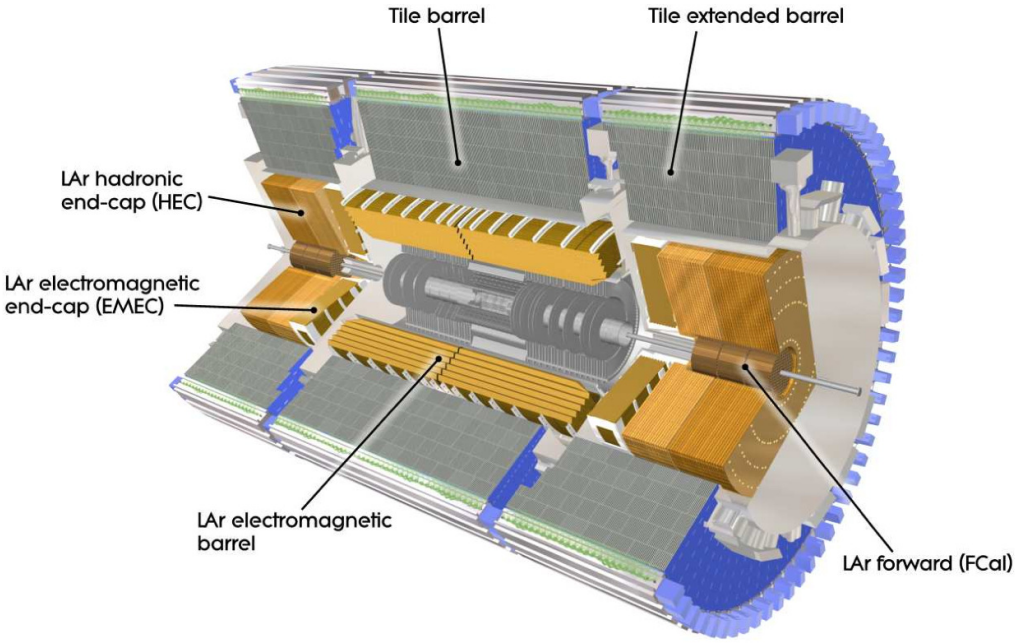

Figure 4.7 Cut-away view of the ATLAS calorimeter system. The primary systems involved are shown: the electromagnetic barrel (EMB) and end-cap calorimeters (EMEC), the hadronic barrel and extended barrel calorimeters (Tile), the hadronic end-cap calorimeter (HEC) and forward calorimeter (FCal).

4.2.4.1 Electromagnetic calorimeters

The lead/LAr electromagnetic calorimeter implements an accordion geometry that provides a complete ϕ symmetry without azimuthal cracks (non-instrumented regions). The EMB covers the region $|\eta| < 1.475$, and consists of two identical

half-barrels (separated by a 4 mm gap at $z = 0$), each of 3.2 m length and inner (outer) diameter of 2.8 m (4 m). A half-barrel is made of 1024 accordion-shaped absorbers, interleaved with readout electrodes. Each half-barrel has been divided into 16 modules, each covering a section of $\Delta\phi = 22.5°$. In this configuration, the accordion waves are axial and run in ϕ. The total thickness of a module is at least 22 radiation lengths (X_0), increasing to 30 X_0 and 33 X_0 for $|\eta| < 0.8$ and $0.8 < |\eta| < 1.3$, respectively. The two end-cap components cover the region $1.375 < |\eta| < 3.2$. Each of them is mechanically divided into two coaxial wheels: an outer wheel covering the region $1.375 < |\eta| < 2.5$, and an inner wheel covering the region $2.5 < |\eta| < 3.2$. In the end-caps, the accordion waves are parallel to the radial direction and run axially. The lead thickness in the absorber plates has been optimised as a function of η, driven by performance in energy resolution. Readout accordion-shaped kapton electrodes are positioned by honeycomb spacers in the middle of the gaps between the absorbers, and consist of three conductive copper layers separated by insulating polyimide sheets. The size of the drift gap on each side of the electrode is 2.1 mm, which corresponds to a total drift time of about 450 ns for an operating voltage of 2000 V. The arrangement is shown in Figure 4.8 (left).

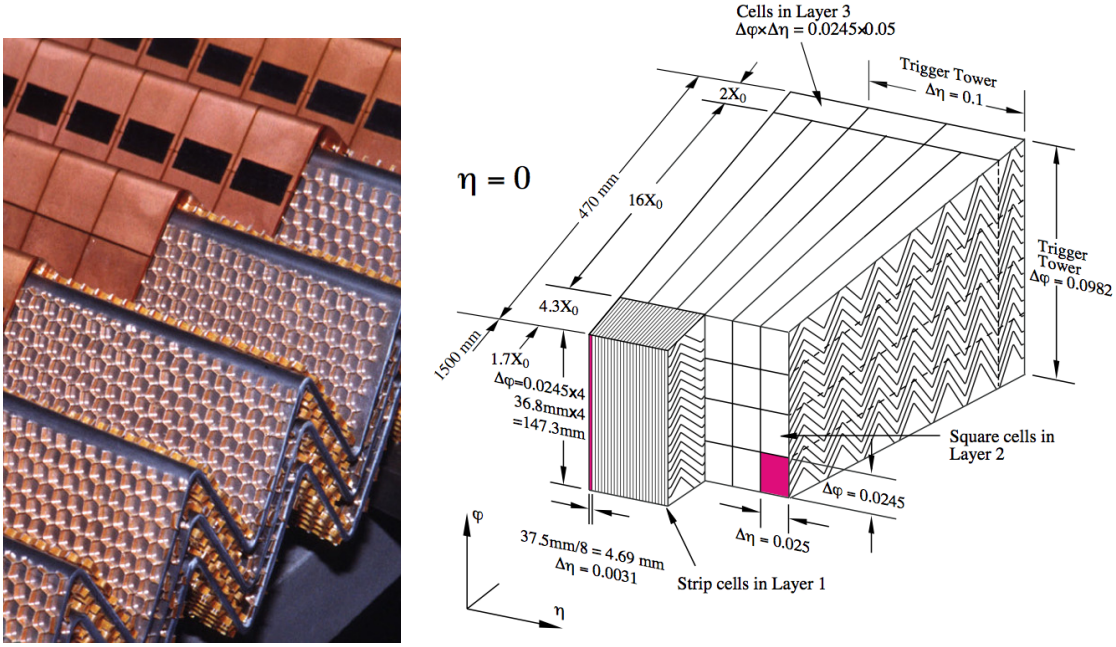

Figure 4.8 Left: Photograph showing a side view of a lead/LAr electromagnetic calorimeter module. The implementation of an accordion-shaped absorbers, interleaved with readout electrodes and honeycomb spacers in the middle of the gaps between the absorbers is visible. Right: Sketch of a barrel module where the different layers are clearly visible with the ganging of electrodes in ϕ. The granularity in η and ϕ of the cells of each of the three layers and of the trigger towers is also shown.

The segmentation of the calorimeter in η and in depth is obtained by etched patterns on the different layers, whereas the ϕ-segmentation is obtained by ganging together the appropriate number of electrodes. Over the region devoted to precision physics ($\eta < 2.5$), the EM calorimeter is segmented in three sections in depth, as can be seen in Figure 4.8 (right). The first layer is finely segmented along η. It provides not only a precise measurement of η-position, but also an efficient discrimination between photons and π^0s. The second layer collects the largest fraction of the energy of the electromagnetic shower, and it is segmented in square towers of $\Delta\phi \times \Delta\eta = 0.025 \times 0.025$ in the transverse plane (4×4 cm^2 in $\eta = 0$). The third layer collects only the tail of the electromagnetic shower and is therefore less segmented in η.

The calorimeter is provided with analogue sums of subsets of its different electronic channels, which forms the so-called *trigger towers*, of $\Delta\phi \times \Delta\eta = 0.1 \times 0.1$, implemented by the L1 trigger (see Section 4.2.7). The region $|\eta| < 1.8$ is complemented with a presampler device, used to correct for the energy lost in the cryostat material by electrons and photons upstream of the calorimeter. The presampler consists of an active LAr layer of thickness 1.1 cm (0.5 cm), placed in front of the inner surface of the barrel (end-cap) region. For the end-cap inner wheel, the calorimeter is segmented in two sections in depth and has a coarser lateral granularity than for the rest of the acceptance.

4.2.4.2 Hadronic calorimeters

The steel/scintillator-tile hadronic calorimeter spans over the region $|\eta| < 1.7$, and it is subdivided into a central barrel (5.8 m in length) and two extended barrels (2.6 m in length), each having an inner (outer) radius of 2.28 m (4.25 m). The HAD is segmented in 64 modules (each subtending 5.625° in ϕ) for its three sections, with a radial depth of approximately 7.4λ. These modules, dubbed wedges, are of size $\Delta\phi = 0.1$ and made of steel plates and scintillating tiles. The module forms an almost-periodic steel-scintillator structure, and its geometry is sketched in Figure 4.9. Eleven sizes of scintillating tiles, of 3 mm thickness and radial (azimuthal) length ranging from 97 (200) mm to 187 (400) mm, form the active medium of the tile calorimeter. The orientation of the scintillator tiles is radially and normal to the beam line. Ultraviolet scintillation light in the active material (polystyrene) is induced by ionising particles crossing the tiles, and then collected by two wavelength-shifting fibres (each 1 mm diameter) placed in contact with each of the tile edges. The fibres are grouped together and coupled to photomultiplier tubes housed at the outer edge of each module. The fibre grouping is used to define a three-dimensional cell structure in such a way as to form three radial sampling depths, approximately 1.5, 4.1 and 1.8 λ thick at $\eta = 0$. These cells have dimensions $\Delta\eta \times \Delta\phi = 0.1 \times 0.1$ (0.2×0.1) in the first two layers (last layer). The tile calorimeter is also provided with analogue sums of subsets of its different electronic channels, forming trigger

towers implemeted for the L1 trigger.

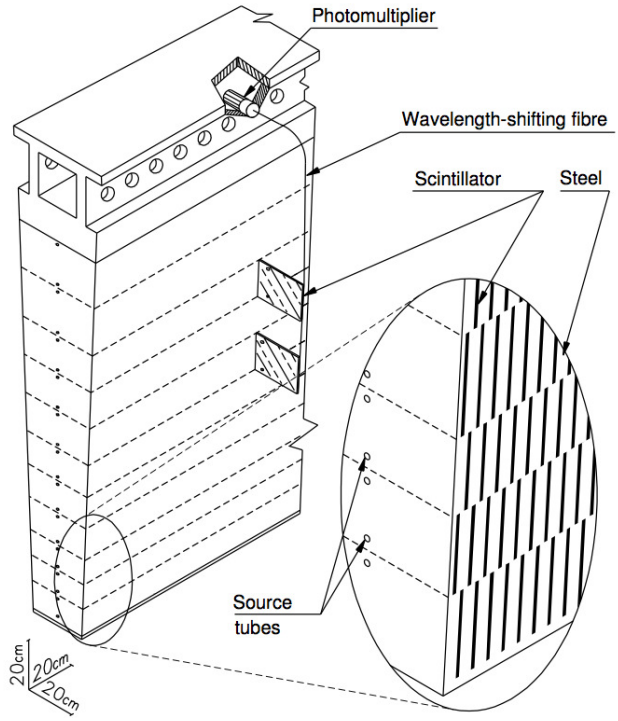

Figure 4.9 Mechanical assembly of the steel-scintillator structure and the optical readout of the tile calorimeter. The various components, namely the tiles, the fibres and the photomultipliers, are shown.

The gap regions between the barrel and the extended ones are additionally instrumented with special steel/scintillator modules, that implement the same sampling fraction as the rest of the tile calorimeter but thinner scintillator counters. The gap scintillators cover the region $1.0 < |\eta| < 1.2$ and provide signals which can be used to correct for energy losses in the inactive material in the gap. The cryostat scintillators cover the region $1.2 < |\eta| < 1.6$ and provide a signal which can be used to correct for energy losses in the outer wall of the barrel cryostat and in the inner-detector services.

The hadronic end-cap copper/liquid-argon sampling calorimeter (HEC) covers the range $1.5 < |\eta| < 3.2$, and consists of two wheels in each end-cap cryostat: a front wheel (HEC1) and a rear wheel (HEC2), each wheel containing two longitudinal sections. The wheels are cylindrical with an outer radius of 2030 mm. Each of the four HEC wheels is constructed of 32 identical wedge-shaped modules. The modules of the front (rear) wheels are made of 24 (16) copper plates, each 25 (50) mm thick, plus a 12.5 (25) mm thick front plate. Three electrodes divide the 8.5 mm gaps into four separate LAr drift zones of 1.8 mm width each. For the nominal high voltage of 1800 V, the typical drift time for electrons in the drift zone is 430 ns. The arrangement of the etched-pad readout provide a semi-pointing geometry in

$R - z$. The size of the readout cells is $\Delta\eta \times \Delta\phi = 0.1 \times 0.1$ (0.2×0.2) in the region $\eta < 2.5$ $(2.5 < |\eta| < 3.2)$.

4.2.4.3 Forward calorimeters

The design of the forward calorimeter is heavily driven by the radiation resistance required for detectors placed very close to the beam at the harsh LHC environment, and therefore is summarized separately. The forward calorimeters (FCal) are located at each end-cap cryostat at a distance of approximately 4.7 m in z, and they provide coverage over $3.1 < |\eta| < 4.9$. The FCal is the calorimeter device closest to the beam ($R = 70$ mm), and it is therefore exposed to high particle fluxes. This characteristic has resulted in a different design. The FCal implements very small liquid-argon gaps, which have been obtained by using an electrode structure of small-diameter rods, centred in tubes which are oriented parallel to the beam direction. The two forward calorimeters are split into three modules of 45 cm depth in z: an innermost copper/LAr module (FCal1), and two outermost cooper-tungsten/LAr modules (FCal2 and FCal3). The FCal1 layer is made of copper plates stacked one behind the other, to optimise the resolution and the heat removal. The plates have more than twelve thousand holes drilled in them through which the electrode structures are inserted. An electrode consists of a co-axial copper rod and copper tube separated by a precision, radiation-hard plastic fibre wound around the rod. The arrangement of the modules can be seen in Figure 4.10.

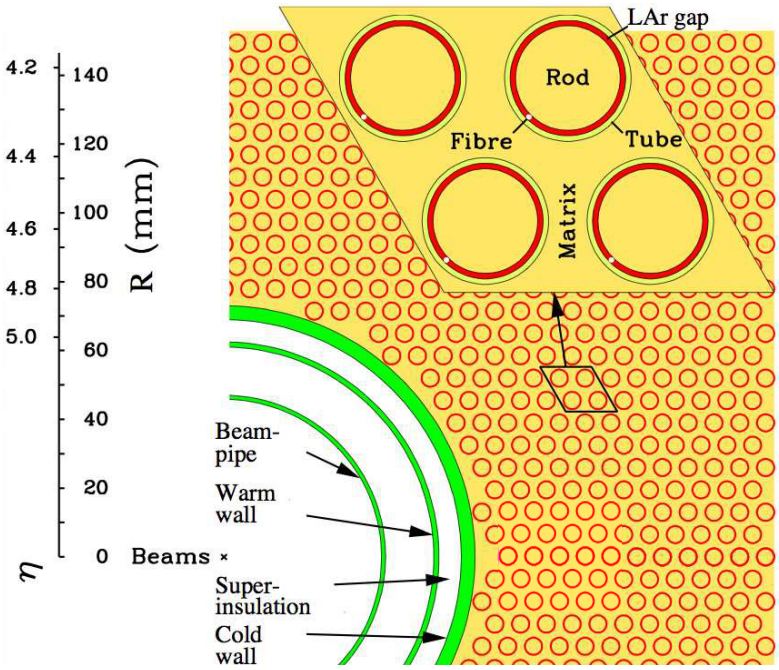

Figure 4.10 Electrode structure of one forward calorimeter (FCal1), showing the matrix of copper plates and tubes, and the rods with the LAr gap for the electrodes.

The FCal2 and FCal3 are optimised for a high absorption length, achieved by maximising the amount of tungsten in the modules. This provides containment and minimise the lateral spread of hadronic showers. These modules consist of two copper end-plates, each 2.35 cm thick, which are spanned by electrode structures, similar to the ones used in FCal1, except for the use of tungsten rods instead of copper rods. The current pulse at the electrode has a full drift time of 60 ns for the FCal1, whereas for FCal2 and FCal3, the drift time scales with the gap size, as the operating voltage is similar for all three modules.

4.2.5 The Muon Spectrometer

The Muon Spectrometer (MS) is the largest and outermost part of the ATLAS detector, and it has been designed to detect charged particles exiting the barrel and end-cap calorimeters and to measure their momentum in the pseudorapidity range $|\eta| < 2.7$. The driving performance goal is a stand-alone reconstruction of trajectories with a transverse momentum resolution of $\approx 10\%$ for 1 TeV tracks. The MS is located within the large air-core toroidal magnetic field and its instrumentation includes trigger chambers with excellent timing resolution (within 1.5 ns - 4.0 ns), design to select events of interest in the region $|\eta| < 2.4$. The overall layout of the Muon Spectrometer is shown in Figure 4.11, and it comprises four types of devices implementing different technologies for both triggering and precise momentum measurement purposes, introduced next.

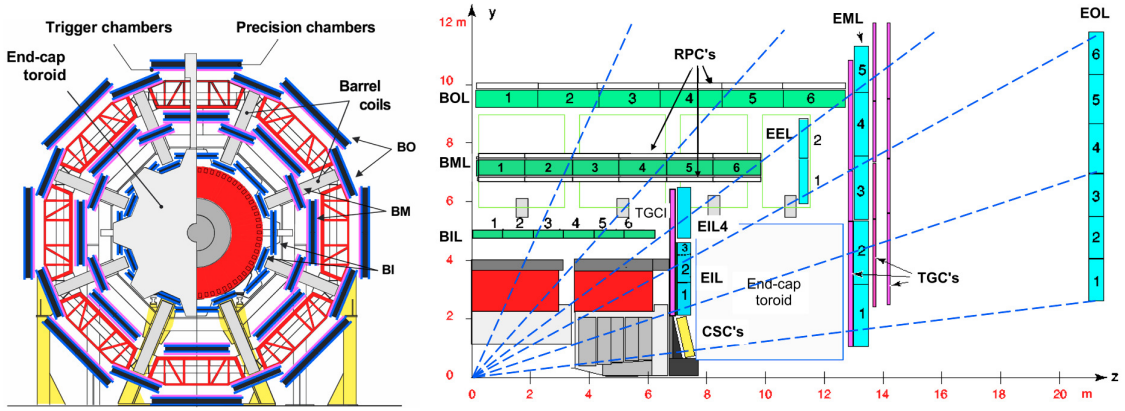

Figure 4.11 Left: Cross-section of the ATLAS Muon Spectrometer barrel (B), perpendicular to the beam axis (non-bending plane). Chambers are organised in projective towers, with three concentric cylindrical layers: inner (BI), middle (BM), and outer (BO), each of 8 large (L) and 8 small (S) chambers. Two trigger RPC chambers are mounted per BM MDT chamber, and one RPC chamber is mounted per BO MDT chamber. Right: Cross-section of the muon system in a plane containing the beam axis (bending plane). Precision (CSC) and trigger (TGC) chambers within the end-cap (E) region are depicted.

4.2.5.1 The precision tracking chambers

The precision momentum measurement is mostly performed by the Monitored Drift Tube chambers (MDT), spanned over the range $|\eta| < 2.7$, except in the innermost end-cap layer where their coverage is limited to $|\eta| < 2.0$. In the barrel region, the precision tracking chambers are located between the eight coils of the superconducting barrel toroid magnet, while the end-cap chambers are in front and behind the two end-cap toroid magnets. The ϕ symmetry of the toroids is reflected in the symmetric structure of the muon chamber system, consisting of eight octants. Each octant is subdivided in the azimuthal direction in two sectors with slightly different lateral extensions, a large and a small sector, leading to a region of overlap in ϕ. The chambers in the barrel are arranged in three concentric cylindrical shells around the beam axis at radii of approximately 5 m, 7.5 m, and 10 m. In the two end-cap regions, muon chambers form large wheels, perpendicular to the z-axis and located at $|z|$ distances of 7.4 m, 10.8 m, 14 m, and 21.5 m from the interaction point.

The basic element of the monitored drift tube chambers (MDT) is a pressurised drift tube. Whenever muons go through the tube, electrons resulting from ionisation are collected at a central anode, producing a signal pulse. A track passing close (far) to the wire generates a pulse of a small (large) duration, that is then converted into a drift radius (R_{min}), as shown in Figure 4.12. Thus, tracks can be reconstruced from adjusting the drift radius of the relevant tubes within a chamber. The MDT chambers are rectangular in the barrel and trapezoidal in the end-cap. Their shapes and dimensions were chosen to optimise solid angle coverage, while respecting the envelopes of the magnet coils, support structures and access ducts.

The MDT chambers consist of two groups of tube layers, called multi-layers, separated by a mechanical spacer. In the innermost layer of the muon detector, each multi-layer consists of four tube layers to enhance the pattern-recognition performance; in the middle and outer layer of the muon detector, each multi-layer consists of three tube layers only. Figure 4.12 shows the structure of a barrel chamber with 2×3 tube layers. The height of the spacer between the multi-layers depends on the chamber type, varying from 6.5 mm to 317 mm. The drift tubes have a diameter of 30 mm, and operate with a gas mixture of Ar/CO2 (93/7 %) at 3 bar pressure. The electrons resulting from ionisation are collected at the central tungsten-rhenium wire of 50 μm diameter, with a maximum drift time from the wall to the wire of about 700 ns, if operated at a nominal potential of 3080 V. The direction of the tubes in the barrel and end-caps is along ϕ, and the intrinsic average resolution per tube (chamber) is 80μm (35μm).

Cathode-Strip Chambers (CSC) are implemented for the pseudo-rapidity region $2.0 < |\eta| < 2.7$, due to their higher rate capability and time resolution. The CSC implements multi-wire proportional devices. These consist of one layer of anode

wires surrounded by two strip-segmented layers of cathodes, with one the strips perpendicular (parallel) to the wires providing the precision (transverse) coordinate. The layout is shown in Figure 4.13. The position of the track is obtained by interpolation between the charges induced on neighbouring cathode strips. The CSC chambers are located at a distance of about 7 m from the interaction point, and mounted on disks (wheels) occupying the radial space between 881 mm and 2081 mm, corresponding to the pseudorapidity range $2 < |\eta| < 2.7$. Two sizes of CSC chambers are arranged in two tilted disks of eight chambers each to provide full coverage in ϕ.

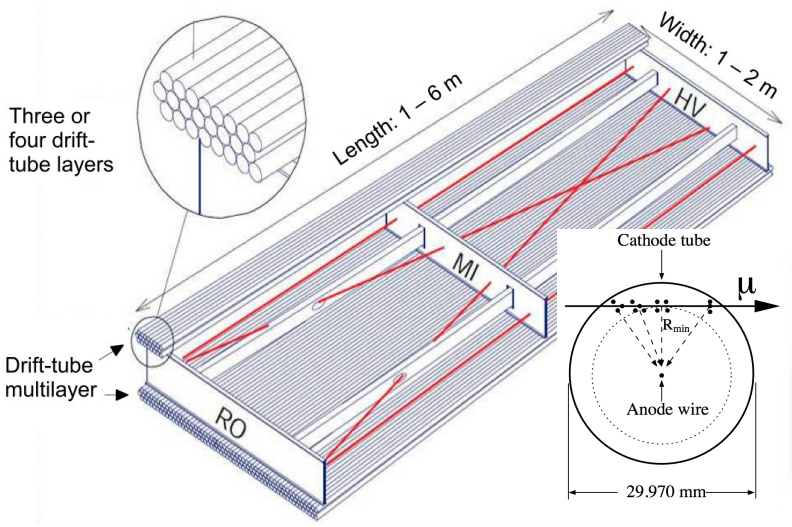

Figure 4.12 Mechanical structure of a MDT chamber. Three spacer bars connected by longitudinal beams form an aluminium space frame, carrying two multi-layers of three or four drift tube layers. The cross-section of a MDT tube along with the ionizing particles is shown. A track going through the tube generates a pulse of a certain duration that is converted into a drift radius (R_{min}).

A CSC chamber consists of four wire planes oriented in the radial direction. For large (small) CSC chambers, the cathode layer is segmented by individual strip of width 1.5 mm (1.6 mm) and an interstrip gap of 0.25 mm. The CSC design utilises low-mass materials to minimise multiple scattering and detector weight. The four layer chamber is formed by five flat rigid panels, each made of an 18.75 mm thick sheet of polyurethane foam and two 0.82 mm thick copper-clad laminates, where 17 μm thick copper cladding forms the cathodes. Precision strips glued on the panels provide the 2.5 mm step for the anode wire plane. The anode wires have a diameter of 30 μm and they are made of gold-plated tungsten/rhenium mixture (97/3 %), making a total of 250 (402) wires per chamber plane along the bending direction in the small (large) chambers. This configuration leads thus to a much finer granularity than for the MDT system, resulting in an intrinsic resolution of 40 μm (5 mm) per

CSC plane in the bending (transverse plane) direction.

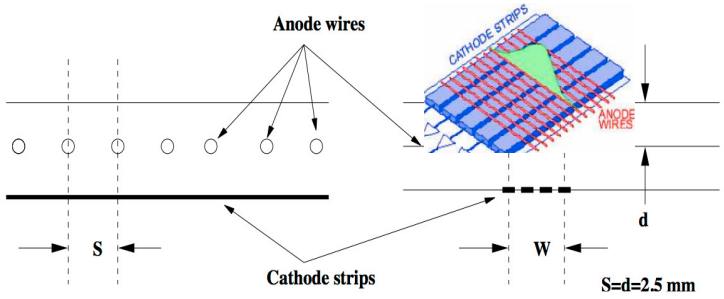

Figure 4.13 Structure of the CSC layout with the wire pitch equal to the anode-cathode spacing (d = 2.5 mm), and an inducted avalanche spread out over 3–5 readout strips.

4.2.5.2 The trigger tracking chambers

The precision-tracking chambers are complemented by a system of fast trigger chambers capable of delivering track information within a few nanoseconds after the passage of the particle. Resistive Plate Chambers (RPC) were selected for this purpose in the barrel region ($|\eta| < 1.05$), while Thin Gap Chambers (TGC) were chosen for the end-cap ($1.05 < |\eta| < 2.4$). Both chamber types deliver signals within 25 ns, thus providing the ability to tag the beam-crossing. The trigger chambers measure both coordinates of the track, one in the bending (η) plane and one in the non-bending (ϕ) plane.

The RPC implements gaseous parallel electrode-plate detector devices, consisting essencially of two parallel resistive plates surrounding a certain gas at a given potential. Whenever a charged particle passes through, the external electric field between the plates allows avalanches of negative charged particles to form along the ionising tracks towards the anode. As consequence, a pulse signal is produced thus providing a position measurement. The RPC trigger chamber is made of two rectangular detectors, contiguous to each other, called units. Each RPC unit consists of two independent detector layers (gas volumes) and four readout strip panels. The structure of a gas volume consists of two resistive plates (phenolic-melaminic plastic laminate) kept parallel to each other at a distance of 2 mm by insulating spacers, with a nominal electric field between the plates of about 4.9 kV/mm. The gap is filled with a mixture of $C_2H_2F_4$/Iso-C_4H_{10}/SF_6 (94.7/5/0.3 %). Each outer surface of the resistive plates has metallic strips electrodes attached that readout the signal induced on the strips by the drift motion of the avalanche electrons. The detector layers are interleaved with three support panels made of light-weight paper honeycomb held in position by a solid frame of aluminium profiles. The total thickness of a RPC unit with two gas volumes, support panels and aluminium covers ranges

from 96 mm to 122 mm. The two units forming a chamber have an overlap region of 65 mm to avoid dead areas for curved tracks.

TGC chambers provide two functions in the end-cap muon spectrometer: the muon trigger capability and the determination of the second, azimuthal coordinate to complement the measurement of the MDT's in the bending direction (i.e., radial). TGCs are multi-wire proportional chambers with the characteristic that the wire-to-cathode distance of 1.4mm is smaller than the wire-to-wire distance of 1.8 mm, filled with a gas mixture of CO_2 and n-C_5H_{12} (n-pentane). The size of the wire groups varies from 6 to 31 as a function of $|\eta|$, corresponding to a variation in width from 10.8 mm to 55.8 mm. A gas volume containing a wire plane and two cathodes is referred to as a TGC chamber, while the entirety of three (two) chambers in a triplet (doublet) arrangement is called a unit. In the outer ring four (five) chambers in triplet (doublets) respectively, are mounted in the way of a ladder forming modules. The triplet is design to cope with false coincidences from background hits, which are more likely in the end-cap region than in the barrel. TGCs are mounted in two concentric rings, an outer (end-cap) one covering the rapidity range $1.05 \leq |\eta| < 1.92$ and an inner (forward) one covering the rapidity range $1.92 < |\eta| \leq 2.4$.

In order to be used for the trigger, a signal from a RPC has to be compared with those in the two other RPC's along the path of the particle (i.e., in the same sector and tower), a task which is accomplished by a system of fast coincidence units close to the chambers. Thus, coincidences between strips in RPC1 (inner) and RPC2 (medium) are used to create the low-p_{T} muon trigger whereas a high-p_{T} muon trigger generally requires hits in all three trigger stations. A similar approach is implemented for the TGC for triggering purposes.

4.2.6 Luminosity detectors

The Luminosity Cherenkov Integrating Detectors (LUCID) and the Beam Condition Monitor (BCM) are two additional devices that play an important role in this thesis, complementing the information provided by the ATLAS ID detector to obtain the final luminosity estimate. LUCID detectors are placed surrounding the beampipe at a distance of 17 m on each side of the IP, and they cover the range $5.6 < |\eta| < 6.0$. These devices are made of 32 aluminum tubes filled with C_4F_{10} gas. The Cherenkov light created whenever particles go through them is reflected in the tube walls until it is finally collected by a photomultipliers, thus resulting in a hit. LUCID is primarily designed to measure the integrated luminosity and provide online monitoring of the beam conditions and instantaneous luminosity. The Beam Condition Monitor (BCM), placed at $|\eta| = 4.2$, consists of four small diamond sensors arranged around the beam-axis in a cross pattern. The BCM is located at $z = \pm 184$ cm at each side of the IP, and $R = 5.5$ cm in the transverse plane. The implementation of diamond provides both a resistant and fast device. The BCM is

designed mainly to monitor background levels and to request an aborting procedure, given the potential risk to ATLAS detectors in case of beam losses.

4.2.7 Trigger and data acquisition

The proton-proton interaction rate at the LHC design luminosity of 10^{34} cm^{-2}s^{-1} is approximately 1 GHz, whereas the event data recording, based on technology and resource limitations, is limited to $\mathcal{O}$ (200-400 Hz) for ATLAS. Therefore, a well-defined strategy for selecting events of interest is of key importance. The challenging task of rejecting $\mathcal{O}(5 \times 10^6)$ events while maintaining maximum efficiency for new physics candidates is performed by the Trigger and Data Acquisition (TDAQ) system. Essentially, the trigger system consists of three levels of increasingly refined and stepwise event selection: Level-1 (L1), Level-2 (L2), and Event Filter (EF). The last two form together the so-called High-Level Trigger (HLT). The L1 trigger is implemented using custom-made electronics, while the HLT is almost entirely based on commercially available computers and networking hardware.

The L1 trigger is primarily design to unambiguously identify the bunch-crossing of interest and perform the initial event selection based on reduced-granularity information from a subset of the detectors (calorimeter and muon spectrometer). The selection based on information from the calorimeter sub-system is driven by the L1 Calorimeter Trigger (L1Calo). It aims at identifying high-transverse energy (E_{T}) objects, such as electrons and photons, jets, and τ-leptons decaying into hadrons, as well as events with large missing and total transverse energy. The L1 muon trigger (L1Muon) is based on signals originated in the muon trigger chambers (RPCs in the barrel and TGCs in the end-caps). L1Muon searches for patterns of hits consistent with high-p_{T} muons originated from the interaction region. The overall decision of acceptance/rejection the event is made by the Central Trigger Processor (CTP), which combines the information for different object types and thresholds. A set of criteria, referred to as trigger menu, can be programmed with up to 256 distinct L1 items, each or these being a combination of requirements on the input data. The trigger decision (together with the 40.08 MHz clock and other signals) is distributed to the detector front-end and readout systems via the Timing, Trigger and Control (TTC) system, using an optical-broadcast network. While the trigger decision is being formed, the information for all detector channels has to be retained in pipeline memories. These memories are contained in custom electronics placed on (or near) the detector. The L1 latency, i.e., the time from the proton-proton collision until the L1 trigger decision, must therefore be kept as short as possible[4]. The design of

[4]There are many contributions to the latency. For a L1 trigger decision, these generally include the time of flight to the detector, the propagation of signals within the sensitive elements of the detector, the signal processing, cable runs within the detector hall and/or from the detector to processing farms, time to form regional trigger components and global decision trigger, and time to distribute the trigger accept signal back to the crates placed in the relevant subdetector devices.

the trigger and front-end systems (crates) requires the L1 latency to be less than 2.5 μs. Thus, the L1 decision must reach the front-end electronics within 2.5 μs after the bunch-crossing with which it is associated, otherwise the event is lost. The maximum L1 accepting rate which the detector readout systems can handle is $\mathcal{O}$(75 kHz).

Upon the event being accepted by the L1 trigger, the information about the geometric location of L1 trigger objects (retained in the muon and calorimeter trigger processors) is sent to the next level as Regions-of-Interest (RoI). These seed the L2 trigger, and they consist of regions of the detector where the L1 trigger has identified possible trigger objects within the event, and correspond to 1–2 % of the full data of an event. The L2 trigger uses RoI information on coordinates, energy, and type of signatures to limit the amount of data which must be transferred from the detector readout. The principal component of the L2 trigger is the L2 processing farm, where the event selection is executed. The system is designed to provide an event rejection factor of about 30, with an average throughput per farm node of about 200 Hz, using only the data located in the RoI's. The L2 trigger reduces the event rate to below $\mathcal{O}$(3.5 kHz), with an average event processing time per L2 processing unit below 40 ms. The L2 trigger decisions are applied in a series of steps, each refining existing information by acquiring additional data from different sub-detectors. A list of physics signatures (trigger chains), implementing event reconstruction (feature extraction) and selection algorithms are used to build signature and sequence tables for all HLT steps. Feature extraction algorithms typically request detector data within the RoI and attempt to identify features, e.g. a track or a calorimeter cluster. Subsequently, a hypothesis algorithm determines whether the identified feature meets the criteria (such as a shower shape, track-cluster match or E_{T} threshold) necessary for the event to be promoted to the next level.

The EF is the more refined and latest level. Unlike the L2 trigger, the EF uses the full granularity and precision of calorimeter and muon chamber data, as well as the information from the inner detector. These fully-built events are analysed through algorithms with a certain resemblance to those applied on standard ATLAS event reconstruction and analysis applications. The EF consists on processing farms where events are received, proccessed, and selected down to a rate which can be recorded for subsequent offline analysis. The event rate is approximately 200-400 Hz, with an average event processing time of around 4 s. The events selected are moved to permanent event storage. Finally, for those events passing the selection criteria, a subset of the data generated during the event analysis is appended to the event data structure (denoted ATLAS physics streams), enabling subsequent offline analysis to be seeded by the results from the EF.

An increase in the luminosity generally brings about an enhancement of the kinematics thresholds implemented within the trigger, in order to keep the event

rates within the allocated bandwidth of each level. However, events with high rates must also be collected for complementary trigger and performance studies, along with those required for the SM physics program. Given the limited trigger bandwidth for selecting these events, for each item/signature of the L1/L2/EF trigger, a scale factor dubbed *prescale* (PS) is assigned, that defines the frequency with which a given item/signature is accepted by the trigger (i.e., only one out-of the number assigned for PS). The trigger chain is said to be unprescaled if it is accepted on an event-by-event basis (PS = 1) for each trigger level. Moreover, the assignation of these factors can be dynamically modified on-line to keep the processing rate approximately constant given the decreasing instantaneous luminosity during data-taking.

The ATLAS data taking periods are grouped per different trigger menus based on the evolution of the peak luminosity. The convention adopted in the trigger menu has the general form `L_ipX_Y`, where `L` stands for the trigger level, `i` the multiplicity, `p` the particle or signature, `X` the minimum p_{T} required, and `Y` corresponds to information related to the identification of the object of interest. In case of combined signatures, the respective blocks `L_ipX_Y` are concatenated. The L1 item associated to the signatures of the HLT defines a trigger chain, each optimized for a given physics analysis. These chains are then grouped in the trigger menu which summarizes the strategy for collecting events of interest.

4.2.8 ATLAS operation during 2011

The ATLAS detector has recorded a total integrated luminosity of 5.25 fb^{-1} of proton-proton collisions at $\sqrt{s} = 7$ TeV during 2011, out of a total 5.61 fb^{-1} delivered by the LHC [159, 160]. This amount corresponds to 93 % of data-taking efficiency, and reflects the outstanding performance of the ATLAS detector with all its sub-detectors running in optimal conditions. The primary source of inefficiency is due to the required high-voltage ramping up for the Pixel and SCT detectors, which is typically turned off at the beginning of an LHC fill to prevent damage to the sensors in case of beam losses, more likely to occur before stable beams are declared.

The analysis presented in this thesis is based on the total sample of proton-proton collisions at $\sqrt{s} = 7$ TeV collected by the ATLAS experiment during 2011, from March 22$^{\mathrm{nd}}$ to October 31$^{\mathrm{st}}$. Only data collected during stable beam periods in which all sub-detectors were fully operational are used. Figure 4.14 (left) shows the cumulative luminosity versus day/month. The luminosity-weighted distribution of the mean number of interactions per crossing ($\langle\mu\rangle$) is shown in Figure 4.14 (right), for two different LHC β^* configurations during the 2011 operation. During 2011, the L1, L2 and EF output rates were kept below 60 kHz, 5 kHz and 400 Hz, respectively, averaged over the LHC fills [159]. The next section describes how the measurement

of the luminosity was performed.

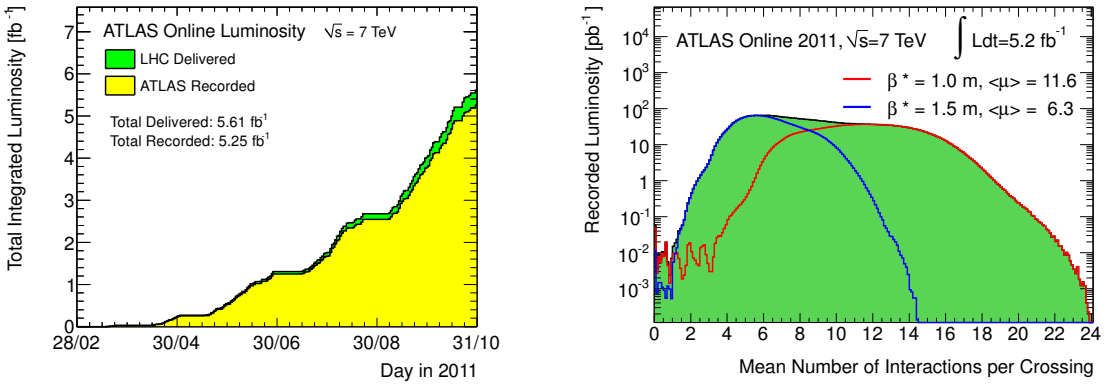

Figure 4.14 Left: Cumulative luminosity versus day delivered to (green), and recorded by ATLAS (yellow) during stable beams and for pp collisions at $\sqrt{s} = 7$ TeV in 2011. Right: luminosity-weighted distribution of the mean number of interactions per crossing ($\langle\mu\rangle$) for 2011. The plot is shown for data taken before and after the September Technical Stop where the β^* was reduced from 1.5m to 1.0m. The integrated luminosities and the mean μ values are given in the figure.

4.2.9 Luminosity measurement

The strategy to measure the luminosity [158] is common to all ATLAS analysis. It is essentially based on a method developed by Simon van der Meer (*vdM*) [161], in which the beams are moved and the relative rate of collisions is measured as a function of beam separation. Then, the absolute luminosity is calibrated by measuring simultaneously the collision rate and the fundamental accelerator parameters that determine the luminosity.

For the determination of the luminosity, ATLAS relies on event-counting methods. Within this approach, one determines the fraction of bunch crossings during which a specified detector registers an event satisfying a given selection requirement. For instance, a bunch crossing can be said to contain an event if at least one pp interaction in that crossing induces at least one observed hit in the detector being considered. However, the detectors used to measure the luminosity (see Section 4.2.6) are not fully efficient for determining whether an inelastic scattering took place. Therefore, is it useful to express Eq. 4.4 as

$$\mathcal{L} = \frac{\mu_{\text{vis}} f_{\text{rev}} n_b}{\sigma_{\text{vis}}} \,, \tag{4.5}$$

where $\mu_{\text{vis}} \equiv \epsilon\mu$ is the average number of visible inelastic interactions per bunch crossing (i.e. the mean number of pp collisions per bunch crossing that pass that event selection), and ϵ is the efficiency for one inelastic pp collision to satisfy the

event selection criteria for a particular detector implementing a certain algorithm. The visible inelastic cross-section $\sigma_{\text{vis}} \equiv \epsilon\sigma_{\text{inel}}$ is the calibration constant that relates the measurable quantity μ_{vis} to the luminosity $\mathcal{L}$.

ATLAS monitors the delivered luminosity by measuring μ_{vis} independently with a variety of detectors and using several different algorithms. In the limit $\mu_{\text{vis}} \ll 1$, the average number of visible inelastic interactions per bunch crossing can be obtained from the number of selected events divided by the total number of bunch crossings, during a given time interval. As the number of events per bunch crossing increases, proper consideration needs to be given to the Poisson statistics governing the event production. Two simple algorithms use LUCID and report whether one or both sides of the detector had at least one hit. A similar algorithm uses the BCM and reports whether at least one module had a hit. The measurement of σ_{vis} is done using dedicated runs where *vdM* scans are performed. The luminosity may be inferred from direct measurements of colliding-beam parameters (for beams that collide with zero crossing angle) as [158]

$$\mathcal{L} = \frac{f_{\text{rev}} n_b N_1 N_2}{2\pi \Sigma_x \Sigma_y} \ , \tag{4.6}$$

where Σ_x and Σ_y characterize the widths of the horizontal (x) and vertical (y) profiles of the colliding beams. In a *vdM* scan, the observed event rate is recorded while scanning the two beams across each other, first in the x direction and then in the y direction, by steps of a known distance. This measurement yields two bell-shaped curves with the maximum rate at zero separation, from which one extracts the values of Σ_x and Σ_y. During the *vdM* scan, the visible cross section for a given detector can be calculated as

$$\sigma_{\text{vis}} = \mu_{\text{vis}}^{\text{MAX}} \frac{2\pi \Sigma_x \Sigma_y}{N_1 N_2} \ , \tag{4.7}$$

where $\mu_{\text{vis}}^{\text{MAX}}$ is the maximum average number of collisions observed with a given detector and algorithm when the beams collide head on. The peak luminosity is compared to $\mu_{\text{vis}}^{\text{MAX}}$ during the *vdM* scan. These results are combined with an external measurement of the bunch charge product ($N_1 N_2$) by beam current transformers (installed around the beam at eight locations along the LHC ring) that measure the charge carried by each beam [162]. Then, the luminosity can be extracted from the measured quantities μ_{vis} and σ_{vis} using Eq. 4.4.

The main uncertainties in the luminosity measurements come from the determination of $N_1 N_2$ performed through the current transformers, and in the calibration performed during runs in which van der Meer scans happened. The latter includes the knowledge of the orientation of the beam ellipsoid, the knowledge of the exact position of the beams as the scan progresses, the stability of the beam size within a scan, and the accuracy of the fits to the collision rates as a function of beam separation. Overall, the luminosity measurement of ATLAS in the 2011 data sam-

ple has a total relative uncertainty of 3.7%, dominated by the uncertainty in the determination of the bunch charge product (3.1%) [163, 164].

4.3 Monte Carlo simulation

Detector simulation is performed with the ATLAS simulation framework [165] based on GEANT4 [166], which includes a detailed description of the geometry and the material of the detector. The set of processes that describe hadronic interactions in the GEANT4 detector simulation are outlined in [167, 168]. The energy deposited by particles in the active detector material is converted into detector signals to mimic the detector read-out. Finally, the Monte Carlo generated events are processed through the trigger simulation of the experiment and are reconstructed and analysed with the same software as that used for data. The MC samples are produced using parameters tuned as described in [85,86]. The collision events considered in this search contain on average 8 proton-proton interactions per bunch crossing (see Section 4.2.8). This effect is included in the simulation, and MC events are reweighted to reproduce the mean expected number of collisions per bunch crossing estimated for data. Contributions from out of time pile-up have been also taken into account. The different MC samples used to simulate the relevant processes for this work are introduced next.

4.3.1 Standard Model processes

The most important background processes for the analysis presented in this thesis are described below, and they are summarized in Table 4.3.

W/Z + jets production: Samples of W and Z events produced in association with light and heavy flavour jets are generated with ALPGEN [65], where $Z \to \ell^+\ell^-$ + jets ($\ell = e,\mu,\tau$) events are generated with up to 5 additional partons, and samples of $W \to l\nu$ + jets and $Z \to \bar{\nu}\nu$ + jets events are generated with up to 6 additional partons at the matrix element level. The PDF set CTEQ6L1 [78] is used in this case. The fragmentation and hadronisation for the ALPGEN samples are performed with HERWIG [69], using JIMMY [169] for the underlying event. The W and Z production processes are normalised to the next-to-next-to-leading order (NNLO) cross sections computed with FEWZ [170–172]. The ALPGEN generator does not match heavy flavour (b and c) quark jets explicitly for contributions from $W(\to l\nu) + b\bar{b}$, $W(\to l\nu) + c\bar{c}$, $W(\to l\nu) + c$ and $Z(\to \ell^+\ell^-) + b\bar{b}$. As a consequence, there are cases where the same heavy flavour final states arise when combining ALPGEN samples with different additional partons. Therefore, it is necessary to veto certain classes of events in each of the samples to avoid double-counting. This is achieved by implementing a tool developed by the top group [173], which essentially associates

Physics process	$\sigma\times$ BR [nb] (perturbative order)	Generator
$W \to \ell\nu$ (+jets)	31.4 (NNLO)	`Alpgen+Herwig`
$Z \to \nu\bar{\nu}$ (+jets)	5.82 (NNLO)	`Alpgen+Herwig`
$Z \to \ell^+\ell^-$ (+jets)	3.20 (NNLO)	`Alpgen+Herwig`
$t\bar{t}$	0.165 (NLO + NNLL)	`Alpgen+Herwig`
Single t	0.085 (NLO + NNLL)	`MC@NLO+Herwig`
WW, WZ, ZZ	0.071×10^{-2} (NLO)	`Alpgen+Herwig`
$t\bar{t}$+$b\bar{b}$	0.9×10^{-3} (LO)	`Alpgen+Herwig`
$t\bar{t}$+W/Z	0.4×10^{-3} (LO)	`Madgraph+Pythia`

Table 4.3 The most important SM background processes and their production cross sections, multiplied by the relevant branching ratios (BR). The l indicates all the three types of leptons (e,μ,τ) summed together. Contributions from higher order QCD corrections are included for $t\bar{t}$, W and Z boson, and di-boson production. The cross sections for $t\bar{t}$+$b\bar{b}$ and $t\bar{t}$+W/Z production are given at leading order.

each jet to a parton based on a ΔR matching between these objects to ensure no overlap between the Monte Carlo samples.

Top pair production: Samples of $t\bar{t}$ events produced in association with light and heavy flavour jets (mostly $t\bar{t}$ + $b\bar{b}$) are generated with `ALPGEN` [65], with up to 5 additional partons, and the PDF set `CTEQ6L1` [78]. The fragmentation and hadronisation for the `ALPGEN` samples are performed with `HERWIG` [69], using `JIMMY` [169] for the underlying event. The $t\bar{t}$ production in association with W/Z ($t\bar{t}$+Z and $t\bar{t}$+W) is generated with `MADGRAPH` [66] interfaced to `PYTHIA` [68]. A top mass of 172.5 GeV is assumed. The $t\bar{t}$ production in association with light jets is normalised to the NLO+NNLL (next-to-next-to-leading logarithms resummation corrections) cross sections [174–176], whereas the $t\bar{t}$ production in association with W/Z or $b\bar{b}$ is normalised to LO [65, 66].

The $t\bar{t}$ estimation is cross-checked using `MC@NLO` [67] samples which include full next-to-leading order corrections to the matrix element for the hard process. The fragmentation and hadronisation for the `MC@NLO` samples are performed with `HERWIG` [69], using `JIMMY` [169] for the underlying event.

Single top production: Single top quark production is simulated with `MC@NLO` [67], fixing the top quark mass at 172.5 GeV, and using the next-to-leading-order (NLO) parton density function (PDF) set `CTEQ6.6` [79]. For the `MC@NLO` samples, the final state parton showers and the underlying event are simulated via interfaces to

HERWIG [69] and JIMMY [169], respectively. The single top production is normalised to the NLO+NNLL (next-to-next-to-leading logarithms) cross sections [174–177].

Di-boson production: Events with WW, WZ, and ZZ production are simulated with ALPGEN [65] and the PDF set CTEQ6L1 [78]. The fragmentation and hadronisation for the ALPGEN samples are performed with HERWIG [69], using JIMMY [169] for the underlying event. The normalisation of the di-boson production is based on cross sections determined at NLO using MCFM [178, 179]

Multi-jet production: For background from jet production from parton scattering processes (multi-jet in the following), no reliable prediction can be obtained from the available leading-order Monte Carlo simulation (see Section 6.1) and data-driven methods are used to determine the residual contributions of this background to the selected event samples, as discussed in Section 8.1.

4.3.2 SUSY signals

The signal samples are generated using HERWIG++ [70, 71], according to the mass spectrum and branching ratios calculated using different tools. In describing the features needed to simulate Beyond the Standard Model (BSM) processes, HERWIG++ only concerns with the hard collisions, either producing known particles through modified couplings or the exchange of new particles, or producing new particles in the final state, and with decays of the new particles. All other steps of event generation are handled in the same way as for Standard Model processes (see Section 1.4). Both of these steps involve calculating an amplitude, which in turn relies on knowledge of the Feynman rules within the model being used.

For generating a SUSY model, HERWIG++ receives an input file based on the so-called SUSY Les Houches Accord (SLHA) [180, 181], which defines a unique set of conventions for supersymmetric extensions of the Standard Model in order to provide a universal interface between spectrum calculation programs, decay packages, and high energy physics event generators [182]. First, the supersymmetric model specifications and input parameters are chosen, together with a set of Standard Model parameters (to be used as low–scale boundary conditions for the spectrum calculation). From these inputs, a spectrum calculation program is run to obtain the SUSY mass and coupling spectrum at the electroweak (EW) scale. The resulting spectrum is stored, together with a copy of the model input parameters (so that subsequent calculations may be performed consistently). A decay package is run in order to generate a list of decay modes and widths for selected particles. A copy of the model input parameters as well as the complete spectrum information is included together with the decay information in this file. Lastly, HERWIG++ reads in all this information and start generating events.

The simplified models are calculated using MADGRAPH [66, 126], with all masses set to high values except those involved in the production and decay to effectively decouple the particle spectrum[5]. For phenomenological MSSM, SUSYHIT [183] is implemented. The MRST 2007 LO* parton densities set are used [81]. Samples are normalized to next-to-leading order (NLO) cross section predictions calculated using PROSPINO [12, 138].

[5]The simplified models are produced using the framework of MSSM, where the particles and mass spectrum are set by hand. Note that the exact framework used for the production of the simplified models is not important as the other unwanted particles or correlations are decoupled as far as is possible. For example, the pair production of a colored scalar particle decaying with 100 % branching ratio to a b-jet and the LSP is produced in MSSM by setting a low sbottom mass with all other squark masses and the gluino mass to high values. Other pure final state signatures are constructed following the same logic.

5

Event reconstruction

The experimental objects resulting from particles originated in the *pp* collision (i.e., *signatures*) are reconstructed from the enormous variety of signals that the detector systems of the ATLAS experiment provide. These signatures are used in the analysis in order to provide a complete characterization of the event through the kinematics and dynamics of the particles involved. This process is not performed in real time while the detector is collecting data (i.e., on-line), but implemented using the information recorded already by the experiment after the data-taking (i.e, off-line), and it is referred to as "offline event reconstruction". Given the complexity and variety of reconstruction algorithms, further information can be found elsewhere [184]. The experimental objects of importance for the analysis presented in this thesis are introduced next.

5.1 Track reconstruction

The primary ID pattern recognition implements an inside-out strategy for track finding as first stage, designed for the efficient reconstruction of primary[1] charged particles of transverse momentum $p_{\mathrm{T}} > 400$ MeV and $|\eta| < 2.5$ [185]. Initially, the high-granularity of the silicon detectors is used to find prompt tracks originating from the interaction region, through the creation of three-dimensional space-points from the measurements obtained by the Pixel and SCT modules and their corresponding location within the ID. Track seeds are formed from a combination of space-points in the three Pixel layers and the first SCT layer. These seeds are

[1] These are defined as particles with a mean lifetime greater than 3×10^{-11}s directly produced in a *pp* interaction or from the subsequent decays or interactions of particles with a lifetime shorter than 3×10^{-11}s.

then extended through the SCT to form track candidates, by adding hits moving away from the interaction point using a combinatorial Kalman filter. This approach updates progressively the track information and predicts precisely the track representation on the next measurement surface, leading to the most likely extension of the trajectory, while detecting the space-points with bad quality (i.e., outliers) via their large contribution to the χ^2 of the track fit. The resulting candidate tracks are then ranked using a scoring strategy which takes into account the quality parameters of the candidates. Those with the highest scores are bundled and promoted to silicon tracks, whereas the remaining ones are neglected for further processing. The extension from the silicon detector into the TRT consist of an extrapolation from the silicon tracks that incorporates the TRT hit coordinates and performs a line fit to estimate whether the hit is compatible with the pure silicon track or not. These extended tracks are refitted with the full information of all three detectors and their quality is compared to the silicon-only track candidates. If the silicon track score is higher than the extended version, it is promoted to an ID track and the TRT hits are put as outliers measurements onto it, otherwise the extended is kept as the ID track. In a second stage, the track search starts from segments reconstructed in the TRT and extends them inwards by adding silicon hits (back-tracking approach), in order to efficiently reconstruct tracks from secondary interactions. The tracks with a TRT segment but no extension into the silicon detectors are referred to as TRT-standalone tracks. The tracking has been studied in low- and high pile-up environments, with an excelent performance observed [186, 187].

5.2 Vertex reconstruction

The reconstruction of vertices is organized in two steps: a) the vertex finding algorithm, dedicated to associate reconstructed tracks to a particular vertex candidate, and b) the vertex fitting algorithm, dedicated to reconstruct the vertex position and its corresponding covariance matrix [188].

The tracks compatible with originating in the luminous region or beam-spot are used for finding the event primary vertex, i.e., the one associated with the hardest-scatter in the event. The beam-spot refers to the place where the beams can interact, and may differ from the nominal collision point, denoted as $(0, 0, 0)$ in the ATLAS coordinate system[2]. Reconstructed tracks of $p_T^{\text{track}} > 400$ MeV with at least 7 silicon

[2]The luminous region in ATLAS is determined during a physics run for every luminosity block (of about two minutes of data-taking), by applying an unbinned maximum likelihood fit to the distribution of primary vertices recorded in this period of time, where the primary vertex reconstruction algorithm used is the same as described in this section, but without applying the beam-spot constraint. A detailed description of how the beam-spot is determined and on the uncertainties connected with its determination can be found in [189].

hits and at most two holes in the Pixel detector[3] must fulfill $|d_0| < 4$ mm, $\sigma(d_0) < 5$ mm, and $\sigma(z_0) < 10$ mm. The transverse impact parameter d_0 is the distance of closest approach of the track to the centre of the luminous region in the $r - \phi$ projection. The longitudinal impact parameter is the z coordinate of the track at this point of closest approach: $|z_0| \sin\theta$, with θ the polar angle of the track. The corresponding uncertainties as estimated in the track fit are denoted as $\sigma(d_0)$ and $\sigma(z_0)$, respectively.

A vertex seed is initially built by looking at the maximum in the distribution of the number of tracks along the z-axis at the beam-line. An iterative χ^2 fit is made using the seed and nearby tracks. Each track carries a weight which is a measure of its compatibility with the fitted vertex depending on the χ^2 of the fit. Tracks displaced by more than 7σ from the vertex (being σ the uncertainty on the position estimated by the track reconstruction algorithm) are used to seed a new vertex and the procedure is repeated until no additional vertices can be found.

The primary vertex from a pile-up event may be mistakenly used as the event vertex, or a fake primary vertex built from tracks from two different pp interactions may be reconstructed. Among all the reconstructed primary vertices, the one with the highest $\sum[p_{\mathrm{T}}^{\mathrm{tracks}}]^2$ is chosen as the event vertex.

5.3 Electrons

The standard electron reconstruction and identification procedure, that combines signals from the silicon detectors, the transition radiation tracker and the longitudinally layered electromagnetic calorimeter system with fine lateral segmentation, has been developed for an optimal reconstruction of the four-momentum of electrons within a pseudo-rapidity range $|\eta| < 2.47$. The strategy implemented is based on clusters reconstructed in the electromagnetic calorimeter which are then associated to tracks of charged particles reconstructed in the Inner Detector [190], and it is discussed next.

5.3.1 Reconstruction

Electron reconstruction begins with the creation of a preliminary set of seed calorimeter clusters. Seed clusters with energies above 2.5 GeV are formed by a sliding window algorithm [191], where the seed clusters are 3×5 in $\eta \times \phi$ middle layer cell units (i.e., 0.025×0.025). Duplicated clusters are removed from nearby seed clusters using an energy comparison criterion. A track-to-cluster matching procedure forms the central part of the electron reconstruction in the region of the

[3] A hole is a non-existing but expected measurement point given a track trajectory. If a track passes through an inactive module, this is not counted as a hole, but instead added to the hits used to meet the hit requirement.

tracker detectors ($|\eta| < 2.5$). Reconstructed tracks are matched to seed clusters by extrapolating them from their last measurement point to the second layer of the calorimeter. The track impact point (η^t, ϕ^t) is then compared to the corresponding seed cluster (η^c, ϕ^c) in that layer. If their difference is below a certain distance threshold then the track is considered matched to the cluster. In the case of tracks that do not contain silicon hits, the matching is restricted to the ϕ coordinate, due to the fact that the accuracy on the η coordinate as measured by the TRT is limited. Among all the tracks that may match the same seed cluster, tracks with silicon hits have priority over those without them (and therefore more likely to belong to electrons originating from photon conversions). The track with the smallest $\Delta R(\text{track}, \text{cluster})$ difference is chosen. The information related to the track-to-cluster matching is retained for all the tracks assigned to the reconstructed electron object and is used during the particle identification.

Electromagnetic showers characterized by tracks matched to the seed cluster are considered as electron candidates to ensure high reconstruction efficiency (the ambiguities between prompt electron and converted photons are solved later by their corresponding particle identification criteria). The electromagnetic cluster is recomputed using a 3×7 (5×5) sliding window in $\eta \times \phi$ middle layer cell units in the barrel (end caps). The cluster energy is determined by summing four different contributions [2]: (1) the estimated energy deposit in the material in front of the EM calorimeter, (2) the measured energy deposit in the cluster, (3) the estimated external energy deposit outside the cluster (lateral leakage), and (4) the estimated energy deposit beyond the EM calorimeter (longitudinal leakage). The four-momentum of central electrons is computed using information from both the final cluster and the best track matched to the original seed cluster. The energy is computed as a weighted average between the cluster energy and the track momentum. The η and ϕ directions are taken from the corresponding track parameters at the vertex, unless the track contains no silicon hits, in which case η and ϕ are provided by the cluster.

5.3.2 Identification

The baseline electron identification within $|\eta| < 2.47$ relies on a cut-based selection using variables that provide good separation between signal electrons and those from photon conversions, Dalitz decays and jets faking them. These variables include calorimeter, tracker and combined calorimeter/tracker information, that can be applied independently. Three reference sets of cuts have been defined with increasing background rejection power while keeping high efficiency for signal electrons: *loose, medium* and *tight* [190]. Shower shape variables of the EM calorimeter middle layer and hadronic leakage variables are used in the loose selection. Variables from the EM calorimeter strip layer, track quality requirements and track-cluster matching are added to the medium selection. Finally, the tight selection incorporates cluster

energy over track momentum information (E/p), particle identification using the TRT, and discrimination against photon conversions via a b-layer hit requirement and information about reconstructed conversion vertices. The shower variables used in the loose and medium selection are given as an input to a multi-variate analysis program [192] in order to perform a cut optimisation in bins of cluster η (defined by calorimeter geometry, detector acceptances and regions of increasing material in the inner detector) and bins of cluster E_{T}, to assure the highest possible electron efficiency and rejection power and the proper treatment of correlations.

5.3.3 Isolation

An isolation criterion is defined to further discriminate electrons and background from jets. A calorimetric isolation discriminator is computed from the reconstructed energy in a cone of half opening angle $\Delta R_I = 0.4$ around the electron candidate direction, where the energy of the electron itself is excluded. The transverse energies of all EM and hadronic calorimeter cells are summed except for those which are in the 3×7 EM calorimeter cells in $\Delta\eta \times \Delta\phi$ space around the cluster barycentre. For isolated electrons, the $\Delta R_I = 0.4$ distribution is expected to peak at values close to zero, with a width determined by the combination of electronic noise, shower leakage, underlying event and pile-up contributions. For the background from jets, a much wider distribution is expected. Thus, the criterion is defined by requiring the calorimetric isolation discriminator to be below a certain threshold. Another similar available approach is based on a tracking discriminator, which implements the summed scalar p_{T} of tracks in a cone of $\Delta R_I = 0.4$ around the electron, instead.

5.3.4 Performance

The electron performance has been extensively studied by combining measurements of $Z \to e^+e^-$, $W \to e\nu_e$ and $J/\psi \to e^+e^-$ processes [193]. The well known masses of the Z, W and J/ψ particles can be used to improve considerably the knowledge of the electron energy scale and its uncertainty. These measurements allow to derive an energy-scale correction factor (α) as a function of the electron energy, in order to correct for discrepancies when comparing data and Monte Carlo simulation, in the barrel and end-cap regions. The energy-scale correction factor is defined as $\alpha \equiv (E_{meas} - E_{true})/E_{meas}$, where E_{meas} is the energy measured by the calorimeter after the MC-based energy-scale correction and E_{true} is the true electron energy as determined from MC. In addition, the energy resolution of electrons in MC samples is also additionally smeared to follow the data measurements. Figure 5.1 (left) shown the alpha energy-scale correction factor as a function of the electron energy for $|\eta| < 0.6$, as determined using $Z \to ee$ (circles), $J/\psi \to ee$ (square) and $W \to e\nu_e$ decays (triangles), where the band represents the systematic errors on

the electron energy scale. Finally, the electron selection efficiencies (i.e., trigger, reconstruction, identification, isolation, etc.) determined in MC are corrected to those measured in data, and delivered for physics analysis usage in terms of correction factors with their corresponding uncertainties. Figure 5.1 (right) presents the efficiencies measured from $Z \to ee$ events for medium identification criterion from both data and Monte Carlo simulation, as a function of η and integrated over a p_{T} range of 20 GeV - 50 GeV.

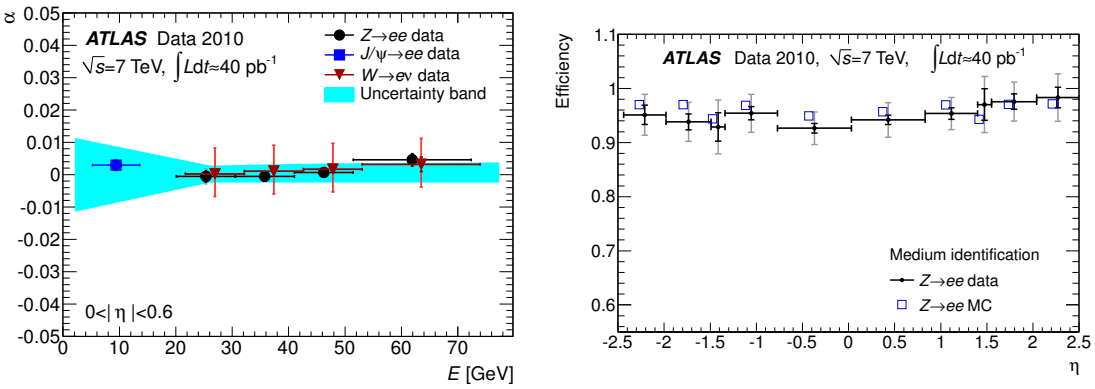

Figure 5.1 Left: The alpha energy-scale correction factor as a function of the electron energy for $|\eta| < 0.6$, as determined using $Z \to ee$ (circles), $J/\psi \to ee$ (squares) and $W \to e\nu_e$ decays (triangles). The band represents the systematic errors on the electron energy scale. Right: Efficiencies measured from $Z \to ee$ events for medium identification criterion from both data (dots) and Monte Carlo simulation (squares), as a function of η and integrated over a p_{T} range of 20 GeV - 50 GeV.

5.4 Muons

Muon identification and high momentum measurement accuracy is crucial to fully exploit the physics potential that will be accessible with the ATLAS experiment at the LHC. The muon reconstruction and identification strategies are introduced next.

5.4.1 Reconstruction

The relative muon momentum resolution $\sigma_{p_{\mathrm{T}}}/p_{\mathrm{T}} < 3.5\%$ ($< 10\%$) for $p_{\mathrm{T}} \approx 200$ GeV (1 TeV) is achieved by a combination of measurements from the inner detector (ID) and the muon spectrometer (MS) [2]. ATLAS has developed three strategies for reconstructing muons. These approaches are referred to as:

- Stand-alone (SA) muon: The muon trajectory is only reconstructed in the MS, by building track-segments in each of the three muon stations and then link

the segment to form tracks. The direction of flight and the impact parameter of the muon at the interaction point are determined by extrapolating the spectrometer track back to the beam line taking the energy loss of the muon in the calorimeters into account.

- Combined (CB) muon: Track reconstruction is performed independently in the ID and MS, and a track is formed from the successful combination of a MS track with an ID one. The primary track reconstruction algorithm for the ID has been introduced in Section 5.1. The muon combination algorithms pair MS tracks with ID ones to identify combined muons. A χ^2 matching procedure is implemented through the difference between the outer MS and inner ID track vector, of five parameters expressed at the point of closest approach to the beam-line, weighted by their covariance matrix. The measure of the quality of this match is used to decide which pairs are retained.

- Segment tagged (ST) muon: The algorithms propagate all ID tracks with sufficient momentum out to the first station of the MS and search for nearby segments. A track in the ID is identified as a muon if the track extrapolated to the MS is associated with straight track segments in the precision muon chambers.

For the analysis presented in this thesis, the STACO-family algorithm (default) has been used for reconstructing muons [194].

5.4.2 Identification

The muon identification implements three reference set of cuts tuned to efficiently suppress fake tracks and muons sometimes created from high hit multiplicities in the muon spectrometer in events where some particles from very energetic jets punch through the calorimeter into the muon system, and discriminate against background muons from leptonic decay of heavy-flavor hadrons. Following a similar approach to that of electrons, *loose, medium* and *tight* criteria are also defined for muons. Essentially, these refine the p_{T} thresholds, enhance the number of hits requirements and impose conditions on their layer location, tune the transverse and longitudinal impact parameter with respect to the primary vertex to reject possible overlapping cosmic rays, among others. A summary of the identification criteria can be found in [2].

5.4.3 Isolation

Two isolation criteria using track or calorimeter information are implemented, in order to further eliminate background muons from semi-leptonic decays of b quarks, mostly. These are:

- Track isolation: the total transverse momentum summed over all charged tracks within a cone of $\Delta R < 0.4$ around the muon (excluding itself) is less than $p_{\mathrm{T}}^{\mu} \times 0.2$.

- Calorimeter isolation: the transverse energy deposition in the calorimeter (E_{T}) in a cone of size $\Delta R < 0.4$ around the muon is less than $p_{\mathrm{T}}^{\mu} \times (0.1)$, where the calorimeter isolation energy is corrected for the muon energy loss.

5.4.4 Performance

The muon reconstruction and identification efficiencies have been measured from the experimental data using a tag-and-probe method with the di-muon decay of the Z boson ($Z \to \mu^+\mu^-$) [195]. These measurements allow to derive scale factor corrections as a function of the muon momentum and pseudorapidity, in order to correct for discrepancies when comparing data and Monte Carlo simulation. Figure 5.2 (left) shows the efficiencies for CB plus ST muons, obtained from data and Monte Carlo simulation as function of muon η and integrated over a p_{T} range of 20 GeV - 100 GeV, using STACO-family algorithms. The scale factor correction and its corresponding uncertainty are shown in the lower part of the figure. The muon momentum resolution is extracted from the width of the di-muon mass distribution in $Z \to \mu^+\mu^-$ decay and the comparison of the independent measurements of muons from $Z \to \mu^+\mu^-$ and $W \to \mu\nu_{\mu}$ decays provided by the ID and the MS [196]. Figure 5.2 (right) presents the muon momentum resolution curve for muons in collision data and simulation as a function of the muon p_{T}, for the pseudo-rapidity region $|\eta| < 1.05$. The solid blue line shows determinations based on data and is continued as dashed line for the extrapolation to p_{T} ranges not accessible due to statistics. The shaded band represents the sum in quadrature of the statistical and systematic uncertainties. Thus, the imperfect muon p_{T} resolution as predicted by the MC simulation is corrected with respect to the data.

5.5 Jets

The signature of the outgoing partons originated in the pp collision are jets of stable particles resulting from the showering and their subsequent decay. Given the complexity of these signatures, it is mandatory to define how this bundle of particles are uniquely associated into a jet in order to provide solid and common foundations for understanding its physics. A jet definition [197] includes an algorithm that states how to group the four-momenta inputs (partons, particles, calorimeter objects, etc.) into jets, the full specification of the jet algorithm parameters and the set of rules for obtaining the four-momentum of a jet from its constituents, i.e., a recombination scheme.

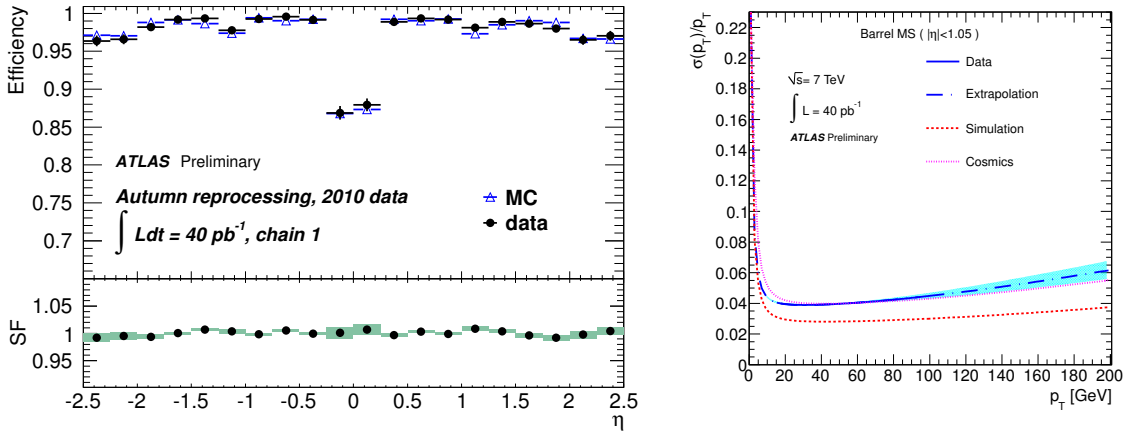

Figure 5.2 Left: Efficiencies for CB plus ST muons, obtained from data (dots) and Monte Carlo simulation (open triangles) as function of muon η and integrated over a p_{T} range of 20 GeV - 100 GeV, using STACO-family algorithms. The scale factor correction and its corresponding uncertainty are shown in the lower part of the figure. Right: Muon momentum resolution curve in collision data and simulation as a function of the muon p_{T}, for the pseudo-rapidity region $|\eta| < 1.05$. The solid blue line shows determinations based on data and is continued as dashed line for the extrapolation to p_{T} ranges not accessible due to statistics. The shaded band represents the sum in quadrature of the statistical and systematic uncertainties. The curve obtained from cosmic ray data is overlaid for comparison.

5.5.1 Inputs to jet reconstruction

The choice of *inputs* to jet reconstruction, prior to the implementation of a jet finding algorithm, dictates the type of signals that will be used to define the presence of jets. The granularity of the sub-detectors permits a variety of inputs [198]. For this thesis, three-dimensional calorimeter topological clusters [191] are considered, that have been designed to mimic the electromagnetic and hadronic shower deposits in the detector by exploiting the longitudinal and transverse calorimeter segmentation. Topological clusters are built starting from seeds, by using calorimeter cells with a signal at least four times higher than the root-mean-square (RMS) of the noise distribution. Cells neighbouring the seed which have a signal to RMS-noise ratio of two are then iteratively added. Finally, all nearest neighbour cells are added without any threshold to the cluster and negative energy clusters are rejected entirely from the jet reconstruction.

5.5.2 Jet algorithm

Among the set of jet algorithms currently available, ATLAS has adopted the anti-k_t algorithm as the default [199]. The choice is driven by multiple requirements ranging from those phenomenological to those intimately involved with the

computing, trigger, detector and pile-up conditions the experiment is expected to cope with [200]. The anti-k_t algorithm belongs to the *sequential recombination* class, where jets are built by combining the inputs to the jet reconstruction into larger objects according to a well defined condition, until it is no longer satisfied by any of the remaining inputs [201–203]. Sequential recombination algorithms start by assigning a distance to all input objects and all pairwise combinations of those objects. Distances between input entities i and j (d_{ij}) and between the entity i and the beam (d_{iB}) are defined as

$$d_{ij} = \min(p_{\mathrm{T},i}^{2p}, p_{\mathrm{T},j}^{2p}) \frac{\Delta_{ij}^2}{R^2} \ , \tag{5.1}$$

$$d_{iB} = p_{\mathrm{T},i}^{2p} \ , \tag{5.2}$$

where $\Delta_{ij}^2 = (y_i - y_j)^2 + (\phi_i - \phi_j)^2$, with $p_{\mathrm{T},i}, y_i$ and ϕ_i corresponding to the transverse momentum, rapidity and azimuthal angle of the entity i, respectively. The parameter p governs the relative power of the energy versus geometrical scales of Δ_{ij}^2. The clustering proceeds by identifying the smallest of the distances. If it happens to be d_{ij}, both entities i and j are recombined adding their two four-vectors into a new single entity [199]. On the other hand, if d_{iB} is found to be the smallest, the entity i is called a jet, and it is removed from the list of entities. The distances are recalculated in an iterative procedure until no entities are left. The anti-k_t algorithm, defined with $p \equiv -1$, not only features infrared and collinear safety (as other sequential recombination algorithms), but it also provides a boundary that is approximately circular in (η, ϕ), even under pile-up environments [204].

5.5.3 Jet energy calibration

The baseline calibration of the calorimeters correctly determines the energy deposited in the detector by electromagnetic showers only. This energy scale, referred to as EM-scale, is established using test-beam measurements for electrons in the barrel and end-cap calorimeters [205]. Initially, the calorimeter jets are reconstructed from calorimeter energy depositions measured at the EM scale. For hadronic showers, this leads to a jet energy measurement that is underestimated typically by 15–55 %, due to several detector effects, as partial measurement of the energy deposited by hadrons (non-compensation), energy losses in inactive regions of the detector (dead material), energy deposits from particles not contained in the calorimeter (leakage), energy deposits that are not included in the reconstructed jet (out-of-cone), and signal losses in calorimeter clustering and jet reconstruction. In order to compensate for the difference between the energy measurement of purely EM objects and the energy of a hadronic jet, an additional jet calibration must be applied to convert the EM scale of the ATLAS calorimeters to the hadronic scale. The procedure used

for the analysis presented in this thesis utilizes a simple energy and η-dependent calibration scheme to restore the hadronic energy scale on average, and it is referred to as the EM+JES calibration. This strategy is primarily based on Monte Carlo simulation plus additional direct in-situ measurements, and it is supported by in-situ tests of the resulting jet energy scale [206]. The EM+JES calibration scheme starts with jets built from EM clusters and initially corrects for the dependence of the reconstructed jet energy on pile-up. The average extra energy due to additional pp collisions is subtracted from the energy measured in the calorimeters using correction constants extracted from in-situ measurements [207]. Then a vertex correction is applied in which the direction of the jet is corrected such that the jet originates from the primary vertex of the interaction instead of the geometrical centre of the ATLAS detector. Finally, the jet energy and direction as reconstructed in the calorimeters are corrected using constants derived in Monte Carlo from the comparison of the kinematics of reconstructed jets and corresponding particle jets (also dubbed *truth jets*). These are defined as built from stable particles, i.e., with a lifetime of 10 picoseconds or more in the laboratory frame, produced by the fragmentation model (with the caveat that neutrinos and muons are generally excluded from the truth jet reconstruction). Thus, for jets reconstructed at some energy scale, the calorimeter response is defined as $\mathcal{R} = E_{\text{reco}}/E_{\text{truth}}$, with jets previously matched to isolated truth jets within $\Delta_{match} < 0.3$. The isolation requirement, applied in order to factorize the effects due to close-by jets from those due to purely detector related, requires that among all the jets (with a $p_{\text{T}} > 7$ GeV at the EM scale) the closest to the studied jet must satisfy $\Delta_{min} \equiv \sqrt{(\Delta y_{min})^2 + (\Delta\phi_{min})^2} > 2.5 \times R$. Figure 5.3 presents the average simulated jet energy response at the electromagnetic scale in bins of EM+JES calibrated jet energy and as a function of the detector pseudorapidity η^{det} (i.e., the pseudorapidity of the original reconstructed jet before the origin correction). Also shown are the η^{det}-intervals used to evaluate the JES uncertainty. The inverse of the response shown in each bin is equal to the average jet energy scale correction.

The precise determination of the jet energy scale (JES) and the jet energy resolution (JER) are the two major tasks of the ATLAS jet calibration program. Fluctuations of the hadronic shower due to the effects mentioned above lead to a degraded jet energy measurement and resolution compared to particles interacting only electromagnetically. The uncertainty on the JES and JER may constitute the dominant systematic uncertainties for many physics analyses, due to their tendency to migrate jets in and out of the analysis selections. The uncertainty on the EM+JES scale is determined by varying the physics models for hadronization and parameters of the Monte Carlo generators, evaluating the baseline calorimeter response to single particles, comparing multiple models for the detector simulation of hadronic showers, assessing the calibration scales as a function of pseudorapidity, and by adjusting the JES calibration method itself. Figure 5.4 (left) presents the fractional jet energy

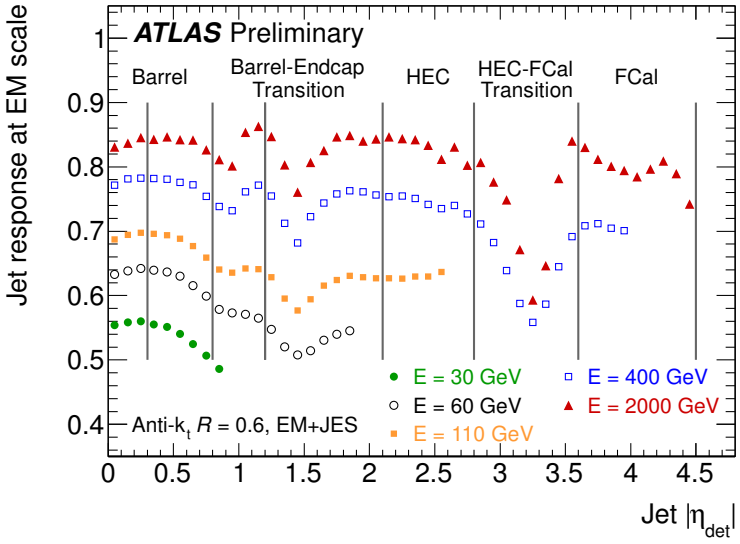

Figure 5.3 The average simulated jet energy response at the electromagnetic scale in bins of EM+JES calibrated jet energy and as a function of the detector pseudorapidity η^{det} (i.e., the pseudorapidity of the original reconstructed jet before the origin correction). Also shown are the η^{det}-intervals used to evaluate the JES uncertainty. The inverse of the response shown in each bin is equal to the average jet energy scale correction.

scale systematic uncertainty as a function of p_{T} for jets in the pseudorapidity region $0.3 < |\eta| < 0.8$ in the calorimeter barrel. The total uncertainty is shown as the solid area along with the individual sources. Furthermore, in-situ tests of the JES have been done, exploiting photon jet balance (direct balance or using the missing transverse momentum projection technique), the balance of a leading jet with a recoil system of two or more jets at lower transverse momentum (multi-jets) or using the momentum measurement of tracks in jets [206]. Figure 5.4 (right) shows the jet energy scale uncertainty as a function of p_{T} in $0.8 < |\eta| < 1.2$ along with the data to Monte Carlo simulation ratios for these in-situ techniques. It can be observed that the results obtained from the in-situ test indicate that the uncertainties presented in Figure 5.4 (left) accurately reflect the true uncertainties in the JES. The precise determination of the jet energy resolution and its uncertainty is explained in detail in Chapter 6.

5.5.3.1 Close-by jet effects

The impact on the non-isolated jet energy scale due to close-by jets is evaluated as a function of Δ_{min} using track-jets [208]. These are reconstructed with the same jet algorithm as calorimeter jets, but using reconstructed tracks as input [198], in order to expoit their better energy and angular resolution than calorimeter clusters. The jet energy scale uncertainty for non-isolated jets is evaluated through the ratio of

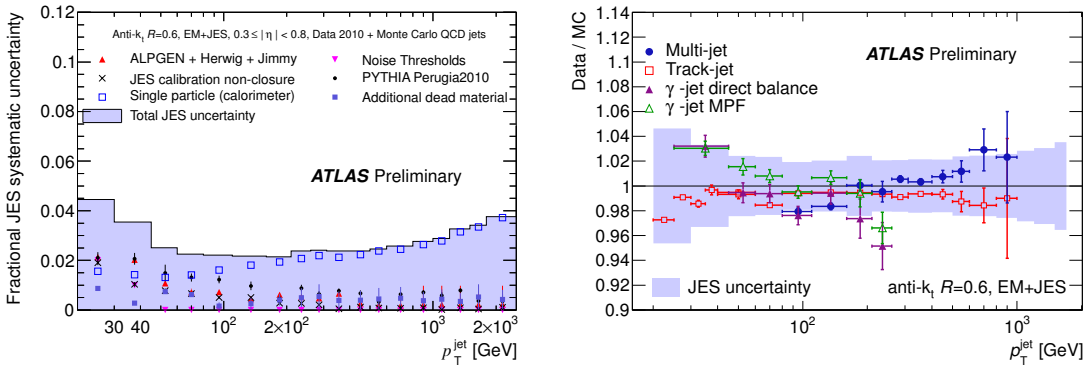

Figure 5.4 Left: fractional jet energy scale systematic uncertainty as a function of p_{T} for jets in the pseudorapidity region $0.3 < |\eta| < 0.8$ in the calorimeter barrel. The total uncertainty is shown as the solid area along with the individual sources. Right: the jet energy scale uncertainty as a function of p_{T} in $0.8 < |\eta| < 1.2$ along with the data to Monte Carlo simulation ratios for several in-situ techniques that test the jet energy scale exploiting photon jet balance (direct balance or using the missing transverse momentum projection technique), the balance of a leading jet with a recoil system of two or more jets at lower transverse momentum (multi-jets) or using the momentum measurement of tracks in jets.

the calorimeter jet response relative to its matched track-jet, denoted $r = p_{\mathrm{T}}^{cal}/p_{\mathrm{T}}^{track}$, and the relative difference of isolated with respect to non-isolated jets ($r_{non-iso}/r_{iso}$), after comparing data and Monte Carlo simulations. The jet energy scale systematic uncertainty assigned for non-isolated jets ranges from 2 % to 3 % if accompanied by a close-by jet within $1.0 < \Delta_{min} < 1.5$, for a jet $p_{\mathrm{T}} \approx 30$ GeV.

5.5.3.2 Flavour jet dependence

The jet energy scale determination is based on QCD di-jet samples that are expected to consist mostly of gluon-initiated jets at low p_{T} and central rapidity [206]. However, if quark-initiated jets may dominate for some physics analysis, the difference in the calorimeter response to gluon- and quark-jets must be treated as a systematic uncertainty to the jet energy scale. The jets are identified through the partons in the generator event record. The highest energy parton that points to the jet, within $\Delta R < 0.6$ (0.4) for jets with R = 0.6 (0.4), determines the flavor of the jet. Initially, gluon-initiated jets are separated from those originated from quarks. Furthermore, jets identified as originating from heavy c- and b-quarks (HQ) are considered separately from light quark-initiated jets (LQ). This separation is sufficient to study the dependence of the flavor-dependence of jet response [209]. Jet identified in the MC simulation as LQ-jets have significantly higher response from those identified as gluon-jets. This is in part a result of the differences in particle-level properties of the two types of jets. The jets identified as gluon-jets

tend to have more particles, and those particles tend to be softer than in the case of LQ-jets. Additionally, the gluon-jets tend to have lower energy density in the core of the jet before interacting with the detector. On the other hand, quark-jets tend to have harder particles and therefore they penetrate further into the calorimeter. These differences lead to an overestimate of the energy of LQ-jets comparing with the energy of gluon-jets. The difference is found to be at most 7% at $p_{\mathrm{T}} \approx 25$ GeV and decreasing for higher p_{T} values. Similarly, heavy-flavor jets tend to have smaller energy than gluon and LQ-jets, because of the loss of energy by the leptonic decay of heavy-flavor hadrons. Therefore, an additional systematic uncertainty of the JES from HQ-jets has to be assigned. For b-jets, the effect is found to be at most 2 % for all p_{T} ranges, therefore a 2.5 % added in quadrature to the JES uncertainty is considered, as a conservative estimate.

5.6 b-tagging

The ability to identify jets stemming from the hadronization of b-quarks (b-hadrons) through the so-called b-tagging algorithms play a crucial role for SUSY searches with heavy-flavour jets in ATLAS. While robust b-tagging algorithms have been swiftly commissioned and used in analyses during 2010 and early 2011 [210], high-performance b-tagging algorithms have been implemeted in physics analysis with the full 2011 data [211]. Those relevant for the work presented in this thesis are described in the next sections.

5.6.1 Track selection and properties

The reconstruction of the key objects for b-tagging purposes, namely the tracks, the primary vertex and the jets, have been previously described in Sections 5.1, 5.2 and 5.5, respectively. The primary vertex defines the reference point with respect to which impact parameters and displaced vertices from secondary (tertiary) $b(c)$-hadrons are measured. The track selection for b-tagging is designed to select high-quality tracks, while rejecting fakes and those from long-lived particles (K_s, Λ and other hyperon decays, generically referred to as V_0 decays in the following) and material interactions (photon conversions or hadronic interactions). The b-tagging quality selection requires at least seven precision silicon hits on the track, where at least two of them must be in the Pixel, with one out-of these two in its innermost layer. Only tracks with $p_{\mathrm{T}} > 1$ GeV are considered. The transverse and longitudinal impact parameters defined with respect to the primary vertex must fulfill $|d_0| < 1$ mm and $|z_0| \sin\theta < 1.5$ mm. This selection is used by all the tagging algorithms relying on the impact parameters of tracks. Tracks are associated to the jets with a spatial matching in ΔR(jet, track). This association cut is varied as a function of the jet p_{T} in order to have a smaller cone for high-p_{T} jets which are more collimated, with

$\Delta R < 0.45$ (0.25) for jet p_{T} around 20 GeV (150 GeV). On the basis that the decay point of the b-hadron must lie along its flight path, the impact parameter is signed to further discriminate the tracks from b-hadron decays from tracks originating from the primary vertex. The sign is positive if the track extrapolation crosses the jet direction in front of the primary vertex. Negative impact parameters arise from fluctuations. Therefore, tracks from b- and c-hadron decays tend to have a positive sign.

5.6.2 High-performance spatial b-tagging algorithms

The b-hadrons commonly retain about 70% of the original b-quark momentum, with masses $\gtrapprox 5$ GeV yielding decay products that may have a large transverse momentum with respect to the jet axis, and an opening angle large enough to distinguish them. The key feature is the relatively long lifetime of hadrons containing a b-quark, of around 1.5 ps (i.e., $c\tau \approx 450$ μm). This results in a b-hadron within a jet of $p_{\mathrm{T}} \approx 50$ GeV to have a flight path lenght, $\langle l \rangle = \gamma c\tau$, of about 3 mm on average in the transverse plane to the beam before decaying. The identification of b-jets profit from these specific properties to discriminate them from gluon- or light-quark initiated jets, and it is implemented through three spatial b-tagging algorithms: IP3D, SV1 and JetFitter [2, 212]

The IP3D is an impact parameter-based b-tagging algorithm that incorporates two- and one-dimensional information of the signed transverse impact parameter significance $d_0/\sigma(d_0)$ and of the longitudinal impact parameter significance $z_0/\sigma(z_0)$, respectively. In order to take advantage of the correlations between the two sets of variables, these distributions are combined using a likelihood ratio technique in which input variables are compared to pre-defined smoothed and normalized distributions for both the b- and light jet hypotheses.

The SV1 is a secondary vertex-based b-tagging algorithm that takes into account the inclusive vertex information formed by the decay products of the b-hadron, including the products of the eventual subsequent charm hadron decay to further increase the discrimination between b-jets and light jets. Tracks belonging to the jet and not associated to the primary vertex are combined in two-track pairs to form new vertices, where those compatible with a V_0 or material interaction are rejected[4]. All tracks from the remaining two-track vertices are combined into a single inclusive vertex, using an iterative procedure to remove the worst tracks until the χ^2 of the vertex fit satisfies a quality criteria. The discriminating variable between b-jets and light jets consists of the decay length significance $L_{3D}/\sigma_{L_{3D}}$ measured in 3D (i.e., $L_{3D} \equiv ||\vec{X}_{\mathrm{PV}} - \vec{X}_{\mathrm{track}}||$) and signed with respect to the jet direction. To increase

[4]The track quality selection is slightly loosened for the SV1 secondary vertex-based algorithm, primarily in order to maximize the efficiency to reconstruct V_0 decays and material interactions, whose corresponding tracks are subsequently removed for b-tagging purposes.

the discriminating power, additional variables are combined using a likelihood ratio technique. SV1 incorporates the distance between the jet axis and the line joining the primary vertex to the secondary one, and takes advantage of three of the vertex properties: the invariant mass of all tracks associated to the vertex, the ratio of the sum of the energies of the tracks in the vertex to the sum of the energies of all tracks in the jet, and the number of two-track vertices.

The likelihood-ratio, in which both IP3D and SV1 are based on, is implemented as follows. The measured value S_i of a discriminating variable is compared to predefined distributions for both the b- and light jets hypotheses $b(S_i)$ and $u(S_i)$, respectively. The ratio of these probabilities defines the track or vertex weight, which can be then combined into a jet weight w_{jet} as

$$w_{jet} = \sum_{i=1}^{\text{tracks/vertex}} \ln \frac{b(S_i)}{u(S_i)} \ , \tag{5.3}$$

therefore, a cut value on w_{jet} must be in principle chosen in order to select b-jets.

A different hypotesis is implemented in the JetFitter [212] algorithm, which exploits the topology of b- and subsequent c-hadron decays inside the jet. It assumes that the b- and c-hadron decay vertices lie on the same line defined through the b-hadron flight path. All charged particle tracks stemming from either the b- or c-hadron decay thus intersect this b-hadron flight axis. A Kalman filter is used to find a common line on which the primary vertex and the b- and c-vertices lie, as well as their position on this line, giving an approximated flight path for the b-hadron. With this approach, the b- and c-hadron vertices are not necessarily merged, even when only a single track is attached to each of them. The discrimination between b-, c- and light jets is done by means of a specific likelihood function [212], combining tracking information as number of vertices with at least two tracks, the total number of tracks at these vertices and number of additional single track vertices on the b-hadron flight axis, where the vertex information is condensed in three variables: the invariant mass of all charged particle tracks attached to the decay chain, the fraction of energy of these particles divided by the sum of the energies of all charged particles matched to the jet, and the weighted average position of the displaced vertices divided by their uncertainties.

5.6.3 Combination of algorithms

The likelihood ratio method used for IP3D and SV1 allows these algorithms to be easily combined: the weights of the individual tagging algorithms are simply summed up. Hence, the resulting b-tagging algorithm is dubbed IP3D+SV1. Recently, non-linear multivariate models have been studied in order to combine the output weights with those obtained from JetFitter. Two b-tagging algorithms based

on artificial neural networks techniques (NN) trained with Monte Carlo simulated samples have been implemented in the analysis of this thesis. The first is dubbed JetFitterCOMBNN b-tagging algorithm, and combines impact parameter information with the explicit determination of an inclusive secondary vertex and additional variables describing the topology of the decay chain. The second is referred to as the MV1 b-tagging algorithm, and combines the output weights of IP3D, SV1 and JetFitterCOMBNN as inputs. Being the combination of these three taggers, the MV1 b-tagging algorithm is expected to provide the best performance for b-jet identification.

5.6.4 Expected performance and operating points

In order for b-tagging to be used in physics analyses, the efficiency with which a jet originating from a b-quark is tagged by a b-tagging algorithm must be determined. In addition, it is necessary to evaluate the c-tag efficiency, which is the equivalent quantity for jets originating from c-quarks, and the mistag rate [210], which is the probability of mistakenly tagging a jet originating from a light-flavour parton (u-, d-, s-quark or gluon) as a b-jet. The jet flavour categorization is done based on Monte Carlo simulation, in order to distinguish between light-flavour, c-, b- and τ-initiated jets. The identification is as follow:

1. First, if a b-quark is found within $\Delta R < 0.3$ of the jet direction, the jet is labeled as a b-jet.

2. If not, but a c-quark is found within $\Delta R < 0.3$ of the jet direction, it is labeled as a c-jet.

3. If neither a b-quark nor c-quark are found, but a τ, the jet is labeled as τ-jet.

4. If none of the three previous criteria are satisfied, the jet is labeled as a light-flavor jet.

The tagging efficiency is defined as the fraction of jets labeled as b-jets that are properly tagged, while the rejection is the reciprocal of the fraction of jets that are labeled as light jets (left) and c-jets (right) that are mistakenly tagged as b-jets. For each b-tagging algorithm, a set of operating points (OP) corresponding to cut values applied to the b-tagging output discriminating variables are defined, based on the inclusive b-tag efficiency measured on simulated $t\bar{t}$, with the jet $p_{\mathrm{T}} > 15$ GeV and $|\eta| < 2.5$. The expected performance for the light-flavor jet rejection as a function of the b-jet tagging efficiency (ϵ_b) for the various ATLAS b-tagging algorithms[5] is shown in Figure 5.5. It is obtained by varying continuously the operating point of

[5]The JetFitterCombNNc algorithm is identical to JetFitterCombNN with the exception that the neural network is trained to reject c-jets rather than light-flavour jets.

each tagger. The best performance is obtained for MV1, and therefore it is used as default in the analysis presented in this thesis.

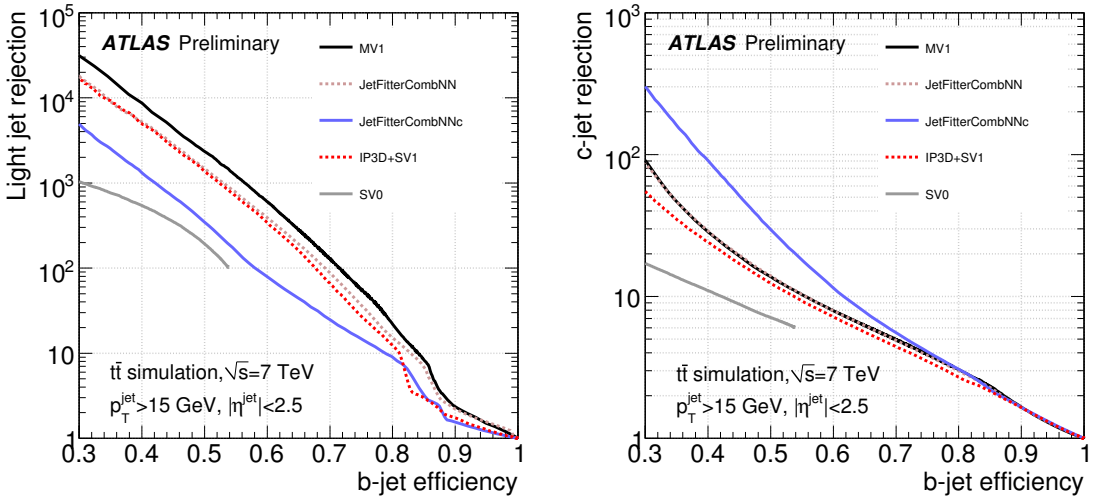

Figure 5.5 The expected performance of the light-jet (left) and c-jet (right) rejection as a function of the b-tag efficiency for different b-tagging algorithms, based on simulated $t\bar{t}$ events.

5.6.5 Calibration

The necessary ingredients for the calibration of flavour-tagging algorithms are jet samples characterized by a strong predominance of a single flavour, whose fractional abundance can be measured from data. The b-tagging efficiency has been measured in data through different methods [213,214], and the results are used to calibrate the b-tagging performance in simulation to that observed in data. The calibration results are presented as scale factors (SF) defined as the ratio of the b-tagging efficiency in data to that in simulation:

$$SF = \frac{\epsilon_b^{\text{data}}}{\epsilon_b^{\text{sim}}} \ , \tag{5.4}$$

where ϵ_b^{sim} (ϵ_b^{data}) is the fraction of b-jets which are tagged in simulated (data) events, with the jet flavour defined by matching to generator level partons. Similarly, efficiencies for c-quark initiated jets can be defined. In data, ϵ_b^{data} is measured using the $p_{\text{T}}^{\text{rel}}$ and $System8$ combination methods [213], which rely on measuring the b-tag efficiency in semileptonic b-jets, through direct ($b \to \mu + X$) and cascade ($b \to c/\bar{c} \to \mu + X$) decays. Thus, the number of b-jets before and after tagging can be obtained for a subset of all b-jets, namely those containing a reconstructed muon. To collect b-jet enriched samples, jets with a reconstructed soft muon ($p_{\text{T}} >$ 4 GeV) associated to it are selected, satisfying a spatial matching of $\Delta R(\mu, \text{jet}) <$

0.4. The variable $p_{\mathrm{T}}^{\mathrm{rel}}$ is defined as the momentum of the muon transverse to the combined muon plus jet axis (hence the name of the method). Muons originating from b-hadron decays have a harder $p_{\mathrm{T}}^{\mathrm{rel}}$ spectrum than muons in c- and light-flavour jets. Templates of $p_{\mathrm{T}}^{\mathrm{rel}}$ are constructed for b-, c- and light-flavour jets separately, and these are fit to the $p_{\mathrm{T}}^{\mathrm{rel}}$ spectrum of muons in jets in data to obtain the fraction of b-jets before and after requiring a b-tag.

The *System*8 method uses three uncorrelated selection criteria to construct a system of eight equations based on the number of events surviving any given subset of these criteria. The system, which is fully constrained, is used to solve for eight unknowns: the efficiencies for b and non-b jets to pass each of the three selection criteria, and the number of b and non-b jets originally present in the sample. As there are not sufficient degrees of freedom to make a complete separation into jet flavours, light-, c- and gluon- initiated jets are all combined into one category. The three selection criteria chosen are the lifetime tagging criterion under study, $p_{\mathrm{T}}^{\mathrm{rel}} >$ 700 MeV, and the requirement that the event contains an opposite-jet in ϕ, with $p_{\mathrm{T}} > 10$ GeV and $|\eta| < 2.5$, and required to be b-tagged by the presence of a reconstructed secondary vertex with $L/\sigma(L) > 1$.

The tagging efficiency for b-jets is evaluated by multiplying the value found in simulation by the scale factor measured with the $p_{\mathrm{T}}^{\mathrm{rel}}$ and *System*8 combination method. The variation of this scale factor within its error is propagated to the final results as a systematic uncertainty. As the b-tagging performance depends strongly on the jet momentum and rapidity, the scale factors and their uncertainties are determined and delivered for physics analysis in bins of jet p_{T} and $|\eta|$.

For the highest performance MV1 tagging algorithm operating at 70% b-tag efficiency as determined in a $t\bar{t}$ sample (Figure 5.5), the b-tag efficiencies in data and simulation for the $p_{\mathrm{T}}^{\mathrm{rel}}$ and *System*8 methods and the combined data-to-simulation scale factors are shown in Figure 5.6. As can be observed, the b-tagging efficiencies range from 50% at jet $p_{\mathrm{T}} = 20$ GeV to 80% for jet $p_{\mathrm{T}} \leq 150$ GeV for both methods, with the total uncertainty ranging from 5% up to 19% in the high p_{T} region.

The measurement of the c-tagging efficiency in data is done with enriched charm-jet samples obtained by reconstructing exclusive charm meson decays within a jet, such as $D^{*+} \to D^0(K^-\pi^+)\pi^+$[6]. In this case, the signal excess is predominantly due to charm meson decays, with some contamination from $b \to c$ decays. Thus, by requiring this decay to be reconstructed within a jet, a reasonably pure sample of charm jets is obtained, which can be used to cross-check different tagging algorithms and to measure their efficiency [214]. The measured c-tag efficiencies in data and simulation and the resulting scale factors for the highest-performance MV1 tagging algorithm operating at 70% efficiency as determined in $t\bar{t}$ events, are shown in Figure 5.7. The c-tag efficiency in data ranges from 20% at jet $p_{\mathrm{T}} = 20$ GeV to 50%

[6] Charge conjugate states are always included.

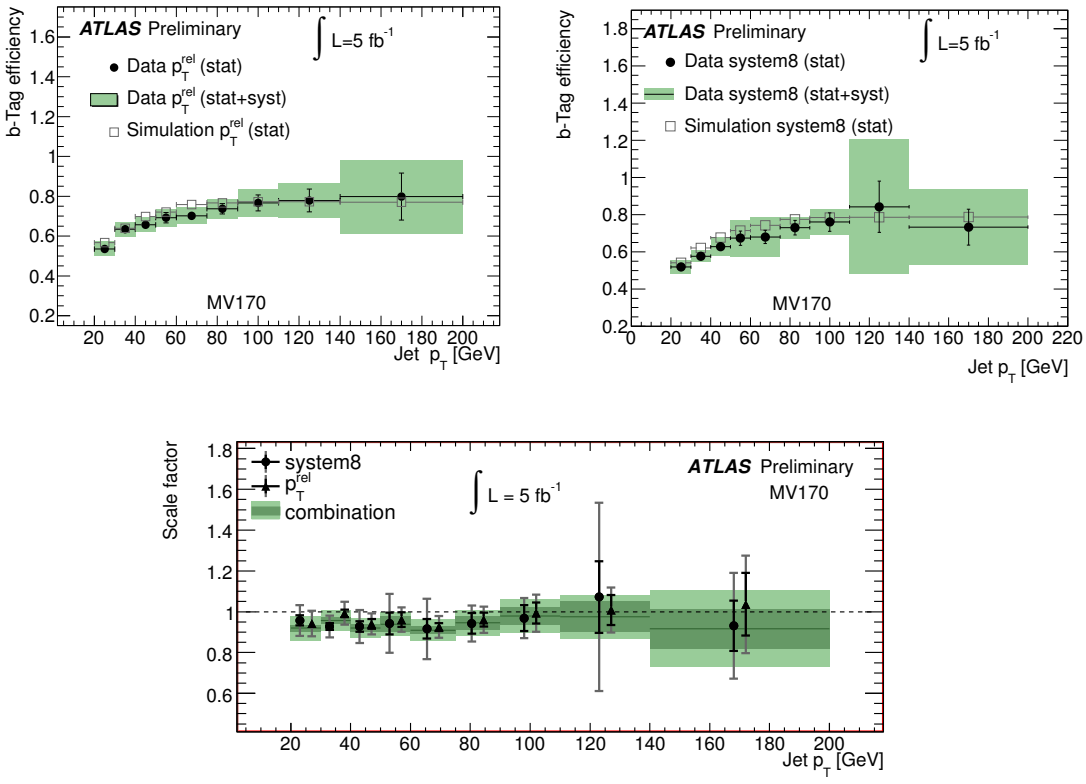

Figure 5.6 Top: The b-tag efficiency in data and simulation for the MV1 tagging algorithm at OP = 70% efficiency as a function of the jet p_{T}, obtained with the $p_{\mathrm{T}}^{\mathrm{rel}}$ (left) and the $System8$ (right) methods. Bottom: The data-to-simulation scale factor for the MV1 tagging algorithm at OP = 70% efficiency as a function of the jet p_{T}, obtained from the $p_{\mathrm{T}}^{\mathrm{rel}}$ and $System8$ results. The dark green band represents the statistical uncertainty of the combined scale factor while the light green band shows the total uncertainty. The data points showing the $p_{\mathrm{T}}^{\mathrm{rel}}$ and $System8$ measurements have been separated a little along the x-axis to make the plot more readable.

for jet $p_{\mathrm{T}} \leq 100$ GeV, with the total uncertainty ranging from 12% up to 25% in the high jet p_{T} region.

5.7 Missing transverse momentum

In a collider event the missing transverse momentum is defined as the momentum imbalance in the plane transverse to the beam axis, where momentum conservation is expected. Such an imbalance may signal the presence of unseen particles, such as neutrinos or stable, weakly-interacting supersymmetric particles. The vector momentum imbalance in the transverse plane is obtained from the negative vector sum of the momenta of all particles detected in a pp collison and is denoted as

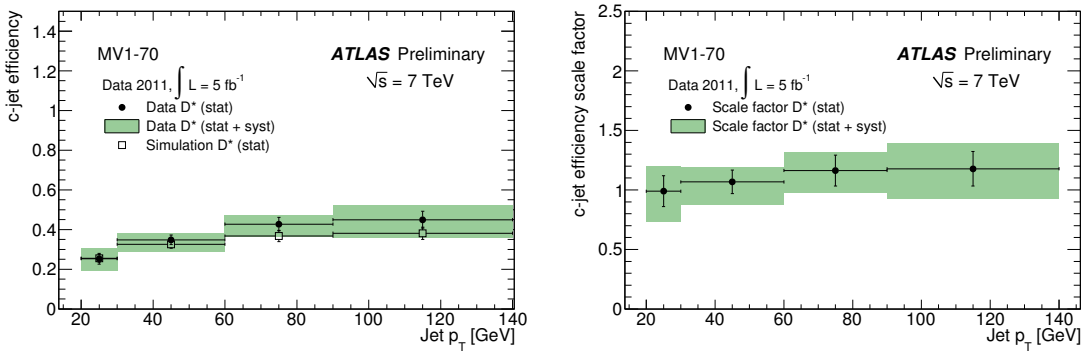

Figure 5.7 The c-tag efficiency in data and simulation (left) and the corresponding scale factors (right) as a function of the jet p_{T}, as measured for the MV1 b-tagging algorithm at OP = 70 % efficiency.

missing transverse momentum $E_{\mathrm{T}}^{\mathrm{miss}}$:

$$E_{\mathrm{T}}^{\mathrm{miss}} = |\sum \vec{p_{\mathrm{T}}}^{\,\mathrm{non-interacting}}| = |-\sum \vec{p_{\mathrm{T}}}^{\,\mathrm{interacting}}| \,, \tag{5.5}$$

where the values of the $E_{\mathrm{T}}^{\mathrm{miss}}$ and its azimuthal coordinate (ϕ^{miss}) are defined as:

$$E_{\mathrm{T}}^{\mathrm{miss}} = \sqrt{(E_{\mathrm{x}}^{\mathrm{miss}})^2 + (E_{\mathrm{y}}^{\mathrm{miss}})^2} \,, \quad \phi^{\mathrm{miss}} = \arctan(E_{\mathrm{y}}^{\mathrm{miss}}, E_{\mathrm{x}}^{\mathrm{miss}}) \,. \tag{5.6}$$

5.7.1 Reconstruction and calibration

The $E_{\mathrm{T}}^{\mathrm{miss}}$ reconstruction includes contributions from energy deposits in the calorimeters and muons reconstructed in the muon spectrometer. The two $E_{\mathrm{T}}^{\mathrm{miss}}$ components are calculated as:

$$E_{\mathrm{x(y)}}^{\mathrm{miss}} = E_{\mathrm{x(y)}}^{\mathrm{miss,calo}} + E_{\mathrm{x(y)}}^{\mathrm{miss},\mu} \,. \tag{5.7}$$

The $E_{\mathrm{T}}^{\mathrm{miss}}$ reconstruction uses calorimeter cells calibrated according to the reconstructed and identified high-p_{T} physics object to which they are associated. For the analysis presented in this thesis, the association is done in the following order: electrons, jets and muons. In addition, cells not associated with any such objects are also taken into account in the $E_{\mathrm{T}}^{\mathrm{miss}}$ calculation, and their contribution is dubbed $E_{\mathrm{T}}^{\mathrm{miss},\mathit{CellOut}}$.

Once the cells are associated with objects as described above, the $E_{\mathrm{T}}^{\mathrm{miss}}$ calorimeter term is calculated as follows:

$$E_{\mathrm{x(y)}}^{\mathrm{miss,calo}} = E_{\mathrm{x(y)}}^{\mathrm{miss},e} + E_{\mathrm{x(y)}}^{\mathrm{miss,jets}} + E_{\mathrm{x(y)}}^{\mathrm{miss,CellOut}} \,, \tag{5.8}$$

where each term is calculated from the negative sum of calibrated cell energies inside

the corresponding objects, as:

$$E_{\mathrm{x}}^{\mathrm{miss,term}} = -\sum_{i=1}^{N_{cell}^{term}} E_i \sin\theta_i \cos\phi_i \ , \tag{5.9}$$

$$E_{\mathrm{y}}^{\mathrm{miss,term}} = -\sum_{i=1}^{N_{cell}^{term}} E_i \sin\theta_i \sin\phi_i \ , \tag{5.10}$$

where E_i, θ_i and ϕ_i are the energy, the polar angle and the azimuthal angle, respectively, and the summations are over all cells associated with the selected objects.

The $E_{\mathrm{T}}^{\mathrm{miss}}$ muon term is calculated from the momenta of reconstructed muon tracks as

$$E_{\mathrm{x(y)}}^{\mathrm{miss},\mu} = -\sum_{\mathrm{muon}} p_{x(y)}^{\mathrm{muon}} \ , \tag{5.11}$$

where the summation is over selected muons. Then, the final $E_{\mathrm{T}}^{\mathrm{miss}}$ components are given by

$$E_{\mathrm{x(y)}}^{\mathrm{miss}} = -\sum_{\mathrm{electron}} p_{x(y)}^{\mathrm{electron}} - \sum_{\mathrm{jet}} p_{x(y)}^{\mathrm{jet}} - \sum_{\mathrm{muon}} p_{x(y)}^{\mathrm{muon}} - \sum_{\mathrm{CellOut}} p_{x(y)}^{\mathrm{CellOut}} \ . \tag{5.12}$$

5.7.2 Performance

The $E_{\mathrm{T}}^{\mathrm{miss}}$ performance has been studied in data using minimum bias, dijet, $Z \to l^+l^-$ and $W \to l\nu$ events, and compared with the expected distributions from the Monte Carlo samples, and good agreement has been found [215]. The systematic uncertainty on the $E_{\mathrm{T}}^{\mathrm{miss}}$ scale is evaluated using the uncertainty on each individual term given the knowledge of the reconstructed objects that are used to build it, which are then propagated and combined in order to determine the overall $E_{\mathrm{T}}^{\mathrm{miss}}$ scale uncertainty [215].

6

Jet energy resolution

Precise knowledge of the jet energy resolution is of key importance for the measurement of the cross-sections of inclusive jets, dijets, multijets or vector bosons accompanied by jets [216–219] and top-quark cross-sections and mass measurements [220]. The jet energy resolution has also a direct impact on the determination of the missing transverse energy, which plays an important role in many searches for new physics with jets in the final state [142, 144, 221–224].

This chapter presents the determination of the jet energy resolution with the ATLAS detector in pp collisions at a centre-of-mass energy of $\sqrt{s} = 7$ TeV [225]. The results are mostly obtained from a data sample that was collected during 2010 and corresponds to 35 pb^{-1} of integrated luminosity delivered by the LHC. The jet energy resolution is determined by exploiting the transverse momentum balance in events with jets at high transverse momenta (p_{T}). Sections 6.1, 6.2 and 6.3 introduce the Monte Carlo simulation, the event and jet selection criteria, and the jet calibration methods, respectively. The two techniques to estimate the jet energy resolution from calorimeter observables, the *dijet balance method* [226] and the *bisector method* [227], are discussed respectively in Sections 6.4.1 and 6.4.2. These methods involve distinct assumptions that can be validated in data and are sensitive to different sources of systematic uncertainty. As such, the use of two independent in situ measurements of the jet energy resolution is important to validate the Monte Carlo simulation. Section 6.5 presents the results obtained for data and simulation for the default jet energy calibration scheme implemented for ATLAS. Section 6.6 compares the Monte Carlo simulation in situ results against the resolutions determined by comparing the jet energy at calorimeter and particle level. This comparison will be referred to as a closure test. Sources of the systematic uncertainties in the jet energy resolution estimated using the available Monte Carlo simulations and collision data are discussed in Section 6.7. The results for other jet energy calibration

schemes are discussed in Section 6.8 and 6.9. The summary of the results obtained from the 2010 data sample can be found in Section 6.10. The rest of the chapter discusses the jet energy resolution performance with a data sample collected during 2011 that corresponds to 950 pb^{-1} of integrated luminosity. The same strategy based on the two in-situ methods described above has been used, and the results are summarized in Section 6.11. The final remarks and future prospects are discussed in Section 6.12.

6.1 QCD Monte Carlo samples

Data are compared to Monte Carlo (MC) simulations of jets at high transverse momentum produced via strong interactions described by Quantum Chromodynamics (QCD) in proton-proton collisions at a centre-of-mass of $\sqrt{s} = 7$ TeV. Furthermore, the jet energy resolution was derived from several simulations in order to study its dependence on the generator, parton showering method, hadronization model and tunes of other soft model parameters. The event generators used for the determination of the jet energy resolution are described below.

1. Pythia 6.4 MC10 tune: The event generator Pythia [68] simulates non-diffractive proton-proton collisions using a $2 \to 2$ matrix element at the leading order (LO) of the strong coupling to model the hard subprocess, and uses p_{T}-ordered parton showers to model additional radiation in the leading-logarithm approximation [228]. Multiple parton interactions [229], as well as fragmentation and hadronization based on the Lund string model [230] are also simulated. The parton distribution function (PDF) set used is the modified leading-order MRST LO* set [81]. The parameters used for tuning multiple parton interactions are denoted as the ATLAS MC10 tune [231]. This generator and tune are chosen as the baseline for the jet energy resolution studies.

2. The Pythia Perugia2010 tune is an independent tune of Pythia to hadron collider data with increased final-state radiation to better reproduce the jet and hadronic event shapes observed in LEP and Tevatron data [232]. Parameters sensitive to the production of particles with strangeness and related to jet fragmentation have also been adjusted. It is the tune favoured by ATLAS jet shape measurements [233].

3. The Pythia PARP90 modification is an independent systematic variation of Pythia. The variation has been carried out by changing the parameter that controls the energy dependence of the cut-off, deciding whether the events are generated with the matrix element and parton-shower approach, or the soft underlying event [234].

4. PYTHIA8 [235] is based on the event generator PYTHIA, but redesigned in the C++ programming language. It contains several modelling improvements, fully interleaved p_{T}-ordered evolution of multiparton interactions and initial- and final-state radiation, and a richer mix of underlying-event processes. Once fully tested and tuned, it is expected to offer a complete replacement for version 6.4.

5. The HERWIG++ generator [69, 236–238] uses a leading order $2 \to 2$ matrix element with angular-ordered parton showers in the leading-logarithm approximation. Hadronization is performed in the cluster model [239]. The underlying event and soft inclusive interactions use hard and soft multiple partonic interactions models [240]. The MRST LO* PDFs [81] are used.

6. ALPGEN is a tree level matrix element generator for hard multi-parton processes ($2 \to n$) in hadronic collisions [65]. It is interfaced to HERWIG to produce parton showers in leading-logarithm approximation, which are matched to the matrix element partons with the MLM matching scheme [241]. HERWIG is used for hadronization and JIMMY [169] is used to model soft multiple parton interactions. The LO CTEQ6L1 PDFs [242] are used.

The nominal MC simulation does not include additional proton-proton interactions (pile-up). In order to study its effect on the jet energy resolution, two additional MC samples have been used. The first one simulates additional proton-proton interactions in the same bunch crossing (in-time pile-up) while the second sample in addition simulates effects on calorimeter cell energies from close-by bunches (out-of-time pile-up). The average number of vertices per event is 1.7 (1.9) for the in-time (in-time plus out-of-time) pile-up samples, which is a good representation of the 2010 data.

6.2 Event and jet selection

The status of each sub-detector, trigger and reconstructed physics object in ATLAS is continuously assessed by inspection of a standard set of distributions, and data-quality flags are recorded in a conditions database in units of luminosity blocks (of about two minutes of data-taking). This analysis selects events satisfying data-quality criteria for the Inner Detector and the calorimeters, and for jet, missing transverse energy and tracking reconstruction [206].

For each event, the reconstructed primary vertex position is required to be consistent with the beamspot, both transversely and longitudinally, and to have at least five reconstructed tracks with transverse momenta $p_{\mathrm{T}}^{\mathrm{track}} > 150$ MeV associated with it. Events are selected by requiring a specific OR combination of inclusive single-jet and dijet calorimeter-based triggers [243, 244]. The combinations were chosen

such that the trigger efficiency, for a specific region of p_{T}, is greater than 99%. For the region 30–40 GeV, these requirements are relaxed, allowing the lowest-threshold calorimeter inclusive single-jet trigger to be used with an efficiency above 95%.

Jets are reconstructed with the anti-k_t jet algorithm using the FastJet software [245, 246] with distance parameters $R = 0.4$ or $R = 0.6$, a four-momentum recombination scheme, and three-dimensional calorimeter topological clusters as inputs (see Section 5.5.1). Jets from non-collision background (e.g. beam-gas events) and instrumental noise are removed using the selection criteria outlined in [206].

Jets are categorized according to their reconstructed rapidity in four different regions to account for differently instrumented parts of the calorimeter:

- Central region ($|y| < 0.8$).
- Extended Tile Barrel ($0.8 \leq |y| < 1.2$).
- Transition region ($1.2 \leq |y| < 2.1$).
- End-Cap region ($2.1 \leq |y| < 2.8$).

Events are selected only if the two leading jets are above the jet reconstruction threshold of 7 GeV at the electromagnetic scale[1] and within $|y| \leq 2.8$, at least one of them being in the central region. The analysis is restricted to $|y| \leq 2.8$ because of the limited number of jets at higher rapidities. Monte Carlo simulated "particle jets" are defined as those built using the same jet algorithm as described above, but using instead as inputs the stable particles from the event generator (with a lifetime longer than 10 ps) excluding muons and neutrinos.

6.3 Jet energy calibration

The analysis presented in this chapter aims to determine the jet energy resolution for jets reconstructed using various JES strategies. A simple calibration, referred to as the EM+JES calibration scheme has been chosen for the 2010 data. This calibration has been introduced in Section 5.5.3, and allows a direct evaluation of the systematic uncertainties from single hadron response measurements and is therefore suitable for first physics analyses [206]. More sophisticated calibration techniques to improve the jet resolution and reduce partonic flavour response differences have also been studied. They are the Local Cluster Weighting (LCW), the Global Cell Weighting (GCW) and the Global Sequential (GS) methods [206]. In addition to these calorimeter calibration schemes, a Track-Based Jet Correction (TBJC) [184, 247] has been derived to adjust the response and reduce fluctuations on a jet-by-jet

[1] The electromagnetic scale correctly reconstructs the energy deposited by electromagnetic showers in the calorimeter. No correction is applied for the lower calorimeter response to hadrons or for losses in the dead material (e.g. the cryostat and the solenoid).

basis without changing the average jet energy scale. These calibration techniques are briefly described below.

6.3.1 The Local Cluster Weighting (LCW) calibration

The LCW calibration scheme uses properties of clusters to calibrate them individually *prior* to jet finding and reconstruction. The calibration weights are determined from Monte Carlo simulations of charged and neutral pions according to the cluster topology measured in the calorimeter. The cluster properties used are the energy density in the cells forming them, the fraction of their energy deposited in the different calorimeter layers, the cluster isolation and its depth in the calorimeter. Corrections are applied to the cluster energy to account for the energy deposited in the calorimeter but outside of clusters and energy deposited in materials before and in between the calorimeters. Jets are formed from calibrated clusters, and a final correction is applied to the jet energy to account for jet-level effects. The resulting jet energy calibration is denoted as LCW+JES.

6.3.2 The Global Cell Weighting (GCW) calibration

The GCW calibration scheme attempts to compensate for the different calorimeter response to hadronic and electromagnetic energy depositions at cell level. The hadronic signal is characterized by low cell energy densities and, thus, a positive weight is applied. The weights, which depend on the cell energy density and the calorimeter layer only, are determined by minimizing the jet resolution evaluated by comparing reconstructed and particle jets in Monte Carlo simulation. They correct for several effects at once (calorimeter non-compensation, dead material, etc.). A jet-level correction is applied to jets reconstructed from weighted cells to account for global effects. The resulting jet energy calibration is denoted as GCW+JES.

6.3.3 The Global Sequential (GS) calibration

The GS calibration scheme uses the longitudinal and transverse structure of the jet calorimeter shower to reduce fluctuations in the jet energy measurement. In this scheme the jet energy response is first calibrated with the EM+JES calibration. Subsequently, the jet properties are used in order to exploit the topology of the energy deposits in the calorimeter to characterize fluctuations in the hadronic shower development. These corrections are applied such that the mean jet energy is left unchanged, and each correction is applied sequentially. This calibration is designed to improve the jet energy resolution without changing the average jet energy scale.

6.3.4 Track-based correction to the jet calibration

Regardless of the inputs, algorithms and calibration methods chosen for calorimeter jets, a deeper insight into the jet topology may be achieved by considering tracking information. Calibrated jets have an average energy response close to unity. However, the energy of an individual jet may have an over- or underestimated energy depending several factors, for example: the ratio of electromagnetic and the hadronic component of the jet; the fraction of energy lost in dead material, in either in the inner detector, the solenoid, the cryostat before the LAr, or in the cryostat between the LAr and the Tile (see Section 4.2.4). The reconstructed tracks associated to the jet are sensitive to these effects and therefore can be used to correct the calibration on a jet-by-jet basis.

In the method referred to as Track-Based Jet Correction (TBJC) [184, 247], the response is adjusted depending on the number of tracks associated to the jet. The jet energy response is observed to decrease with jet track mutiplicity mainly because the ratio of the electromagnetic to the hadronic component decreases on average with the number of tracks. In effect, a low charged-track multiplicity typically indicates a predominance of neutral hadrons, in particular π^0s which yield electromagnetic deposits in the calorimeter with $R \simeq 1$. A high number of charged particles, on the contrary, signals a more dominant hadronic component, with a lower response due to the non-compensating nature of the calorimeter ($h/e < 1$). The TBJC method is designed to be applied on an optional basis on top of any JES calibration scheme, since it does not change the overall response, to reduce the jet-to-jet energy fluctuations and improve the resolution.

6.4 In situ jet resolution measurement

Two methods are used in dijet events to measure in situ the fractional jet p_{T} resolution, $\sigma(p_{\mathrm{T}})/p_{\mathrm{T}}$, which at fixed rapidity is equivalent to the fractional jet energy resolution, $\sigma(E)/E$. These are the *dijet balance method* and the *bisector method*, and they are discussed in Sections 6.4.1 and 6.4.2, respectively.

6.4.1 The dijet balance method

The dijet balance method relies on the approximate scalar balance between the transverse momenta of the two leading jets and measures the sensitivity of this balance to the presence of extra jets directly from data. The main components and technicalities of this method are described in the following.

6.4.1.1 Measurement of resolution from asymmetry

The dijet balance method for the determination of the jet p_{T} resolution is based on momentum conservation in the transverse plane. The asymmetry between the transverse momenta of the two leading jets $A(p_{\mathrm{T},1}, p_{\mathrm{T},2})$ is defined as

$$A(p_{\mathrm{T},1}, p_{\mathrm{T},2}) \equiv \frac{p_{\mathrm{T},1} - p_{\mathrm{T},2}}{p_{\mathrm{T},1} + p_{\mathrm{T},2}}. \tag{6.1}$$

where $p_{\mathrm{T},1}$ and $p_{\mathrm{T},2}$ refer to the randomly ordered transverse momenta of the two leading jets. The width $\sigma(A)$ of a Gaussian fit to $A(p_{\mathrm{T},1}, p_{\mathrm{T},2})$ is used to characterize the asymmetry distribution and determine the jet p_{T} resolutions. Assuming transverse momentum balance and requiring the jets to be in the same rapidity region, the relation between $\sigma(A)$ and the relative jet resolution is given by

$$\sigma(A) = \frac{\sqrt{\sigma^2(p_{\mathrm{T},1}) + \sigma^2(p_{\mathrm{T},2})}}{\langle p_{\mathrm{T},1} + p_{\mathrm{T},2} \rangle} \simeq \frac{1}{\sqrt{2}} \frac{\sigma(p_{\mathrm{T}})}{p_{\mathrm{T}}}, \tag{6.2}$$

where transverse momentum balance implies the following: $\langle p_{\mathrm{T},1} \rangle = \langle p_{\mathrm{T},2} \rangle \equiv p_{\mathrm{T}}$ and $\sigma(p_{\mathrm{T},1}) = \sigma(p_{\mathrm{T},2}) = \sigma(p_{\mathrm{T}})$, since both jets are required to be in the same y region.

If only one jet is in the rapidity bin being probed (j) and the other one is in the central reference region (i), it can be shown that the fractional jet p_{T} resolution is given by

$$\left.\frac{\sigma(p_{\mathrm{T}})}{p_{\mathrm{T}}}\right|_{(j)} = \sqrt{4\,\sigma^2(A_{(i,j)}) - 2\,\sigma^2(A_{(i)})}\ , \tag{6.3}$$

where $A_{(i,j)}$ is measured in a topology with the two jets in different y regions and where $(i) \equiv (i,i)$ denotes both jets in the same y region.

The distribution of A for a $\bar{p}_{\mathrm{T}} \equiv (p_{\mathrm{T},1} + p_{\mathrm{T},2})/2$ bin of $60\,\mathrm{GeV} \leq \bar{p}_{\mathrm{T}} < 80\,\mathrm{GeV}$, in the central region ($|y| < 0.8$), is shown in Figure 6.1. This is for events with two back-to-back leading jets with azimuthal angle between them $\Delta\phi(j_1, j_2) \geq 2.8$ and a third jet with $p_{\mathrm{T},3}^{\mathrm{EM-scale}} < 10\,\mathrm{GeV}$ and no rapidity restriction. Reasonable agreement in the bulk is observed between data and Monte Carlo simulation.

6.4.1.2 Soft radiation correction

Although requirements on the azimuthal angle between the leading jets and on the third jet transverse momentum ($\Delta\phi(j_1, j_2)$ and $p_{\mathrm{T},3}^{\mathrm{EM-scale}}$, respectively) are designed to enrich the purity of the back-to-back jet sample, it is important to account for the presence of additional soft particle jets not detected in the calorimeter.

In order to estimate the value of the asymmetry for a pure particle dijet event, $\sigma(p_{\mathrm{T}})/p_{\mathrm{T}} \equiv \sqrt{2}\,\sigma(A)$ is recomputed allowing for the presence of an additional third jet in the sample for a series of $p_{\mathrm{T},3}^{\mathrm{EM-scale}}$ cut-off threshold values up to 20 GeV. The

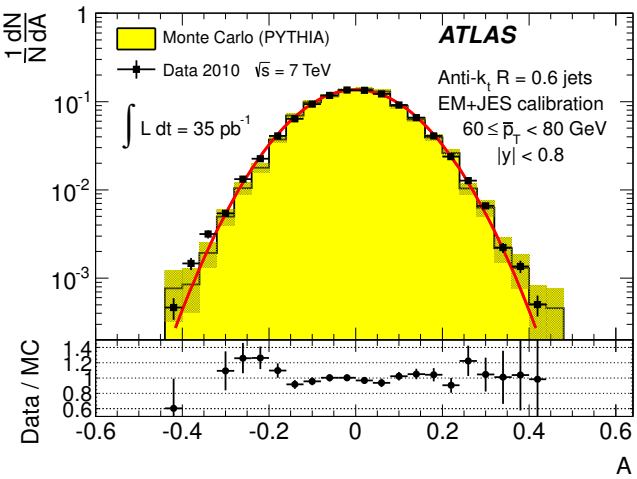

Figure 6.1 Asymmetry distribution as defined in Eq. (6.1) for $\bar{p}_{\mathrm{T}} = 60 - 80$ GeV and $|y| < 0.8$. Data (points with error bars) and Monte Carlo simulation (histogram with shaded bands) are overlaid, together with a Gaussian fit to the data. The lower panel shows the ratio between data and MC simulation.

cut on the third jet is placed at the EM-scale to be independent of calibration effects and to have a stable reference for all calibration schemes. For each p_{T} bin, the jet energy resolutions obtained with the different $p_{\mathrm{T},3}^{\mathrm{EM-scale}}$ cuts are fit with a straight line and extrapolated to $p_{\mathrm{T},3}^{\mathrm{EM-scale}} \to 0$, in order to estimate the expected resolution for an ideal dijet topology

$$\left.\frac{\sigma(p_{\mathrm{T}})}{p_{\mathrm{T}}}\right|_{p_{\mathrm{T},3}^{\mathrm{EM-scale}} \to 0}.$$

The dependence of the determined jet p_{T} resolution on the presence of a third jet is illustrated in Figure 6.2. The linear fits and their extrapolations for a $\bar{p}_{\mathrm{T}}$ bin of $60 \leq \bar{p}_{\mathrm{T}} < 80$ GeV are shown. Note that the resolutions become systematically broader, up to 25%, as the $p_{\mathrm{T},3}^{\mathrm{EM-scale}}$ cut increases. This is a clear indication that the jet resolution determined from two-jet topologies depends on the presence of additional radiation and on the underlying event. The linear fit that minimizes χ^2/dof among the set of points measured is considered the best.

A soft radiation (SR) correction factor, $K_{\mathrm{soft}}(\bar{p}_{\mathrm{T}})$, is obtained from the ratio of the value of the linear fit at 0 GeV over the value at 10 GeV:

$$K_{\mathrm{soft}}(\bar{p}_{\mathrm{T}}) = \frac{\left.\frac{\sigma(p_{\mathrm{T}})}{p_{\mathrm{T}}}\right|_{p_{\mathrm{T},3}^{\mathrm{EM-scale}} \longrightarrow 0 \text{ GeV}}}{\left.\frac{\sigma(p_{\mathrm{T}})}{p_{\mathrm{T}}}\right|_{p_{\mathrm{T},3}^{\mathrm{EM-scale}} = 10 \text{ GeV}}}. \tag{6.4}$$

This multiplicative correction is applied to the resolutions extracted from the dijet asymmetry for $p_{\mathrm{T},3}^{\mathrm{EM-scale}} < 10$ GeV events. The correction varies from 25% for events with $\bar{p}_{\mathrm{T}}$ of 50 GeV down to 5% for $\bar{p}_{\mathrm{T}}$ of 400 GeV. In order to limit the

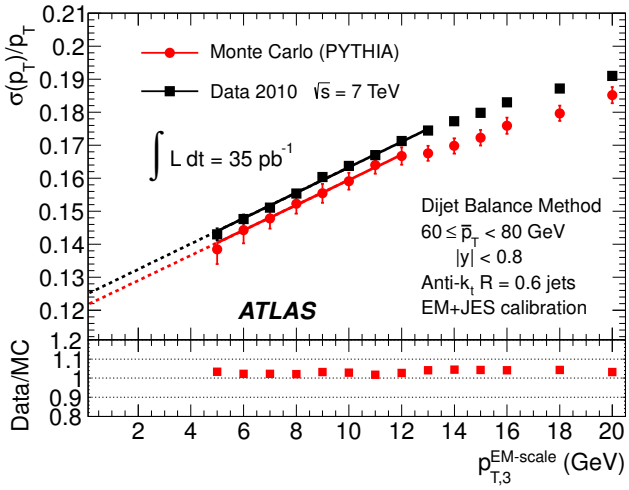

Figure 6.2 Relative jet p_{T} resolutions, from Equation 6.2, measured in events with $60 \leq \bar{p}_{\mathrm{T}} < 80$ GeV and with third jet with p_{T} less than $p_{\mathrm{T,3}}^{\mathrm{EM-scale}}$, as a function of $p_{\mathrm{T,3}}^{\mathrm{EM-scale}}$, for data (squares) and Monte Carlo simulation (circles). The solid lines correspond to linear fits while the dashed lines show the extrapolations to $p_{\mathrm{T,3}}^{\mathrm{EM-scale}} = 0$.

statistical fluctuations, $K_{\mathrm{soft}}(\bar{p}_{\mathrm{T}})$ is fit with a parameterization of the following form: $K(\bar{p}_{\mathrm{T}}) = a + b/\left(\log \bar{p}_{\mathrm{T}}\right)^2$, which was found to describe the distribution well, within uncertainties. The differences in the resolution due to other parameterizations were studied and treated as a systematic uncertainty, resulting in a relative uncertainty of about 6% (see Section 6.7).

6.4.1.3 Particle imbalance correction

The p_{T} difference between the two calorimeter jets is not solely due to resolution effects, but also to the imbalance between the respective particle jets,

$$p_{\mathrm{T,2}}^{\mathrm{calo}} - p_{\mathrm{T,1}}^{\mathrm{calo}} = (p_{\mathrm{T,2}}^{\mathrm{calo}} - p_{\mathrm{T,2}}^{\mathrm{part}}) - (p_{\mathrm{T,1}}^{\mathrm{calo}} - p_{\mathrm{T,1}}^{\mathrm{part}}) + (p_{\mathrm{T,2}}^{\mathrm{part}} - p_{\mathrm{T,1}}^{\mathrm{part}}).$$

The measured difference (left side) is decomposed in resolution fluctations (the first two terms on the right side) plus a particle-level imbalance (PI) term that originates from out-of-jet showering in the particle jet and from soft QCD effects. In order to correct for this contribution, the particle-level imbalance is estimated using the same method (asymmetry plus soft radiation correction) as for calorimeter jets. A fit of the relative standard deviation of the imbalance (using the functional form in Equation 6.8, see Section 6.5) is then subtracted in quadrature from the in situ resolutions (on both data and Monte Carlo simulation) after the SR correction, as shown in Figure 6.3. The size of the particle-level imbalance correction to the measured resolutions varies between 2% and 10% (relative).

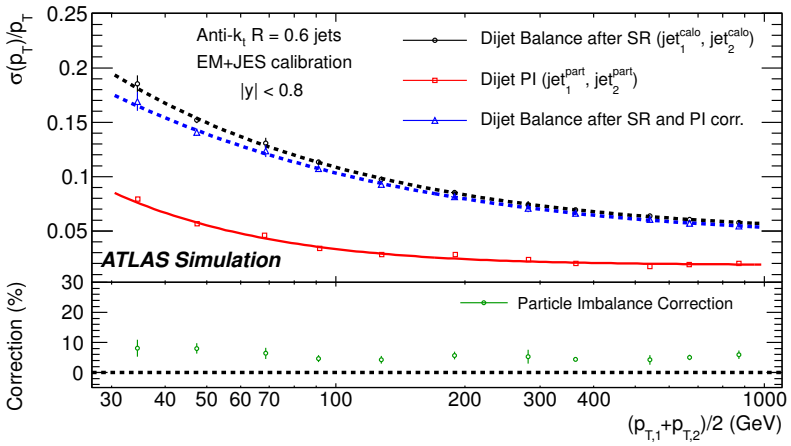

Figure 6.3 Particle-level imbalance (PI) between the two-leading particle jets (squares). The fractional jet resolution measured from the dijet balance method is shown both before (circles) and after the PI correction (triangles). The lower panel shows the relative size of the particle level imbalance correction to the measured resolutions.

6.4.2 The bisector technique

The bisector technique uses the projection of the vector sum of the leading jets' transverse momenta on the coordinate system bisector of the azimuthal angle between the transverse momentum vectors of the two jets. It takes advantage of the very different sensitivities of each of these projections to the underlying physics of the dijet system and to the jet energy resolution. The main components and technicalities of this method are described in the following.

6.4.2.1 Bisector rationale

The bisector method is based on a transverse imbalance vector, $\vec{P}_{\mathrm{T}}$, defined as the vector sum of the two leading jets in dijet events. This vector is projected along an orthogonal coordinate system in the transverse plane, (ψ, η), where η is chosen in the direction that bisects the angle formed by $\vec{p}_{\mathrm{T},1}$ and $\vec{p}_{\mathrm{T},2}$, $\Delta\phi_{12} = \phi_1 - \phi_2$. This is illustrated in Figure 6.4.

For a perfectly balanced dijet event, $\vec{P}_{\mathrm{T}} = 0$. There are a number of sources that give rise to fluctuations and thus to a non-zero variance of its ψ and η components, denoted $\sigma^2_\psi \equiv \mathrm{Var}(P_{\mathrm{T},\psi})$ and $\sigma^2_\eta \equiv \mathrm{Var}(P_{\mathrm{T},\eta})$, respectively. At particle level, $\vec{P}_{\mathrm{T}}^{\mathrm{part}}$ receives contributions mostly from initial-state radiation. This effect is expected to be isotropic in the (ψ, η) plane, leading to similar fluctuations in both components

$$\sigma_\psi^{2\ \mathrm{part}} = \sigma_\eta^{2\ \mathrm{part}} \ . \tag{6.5}$$

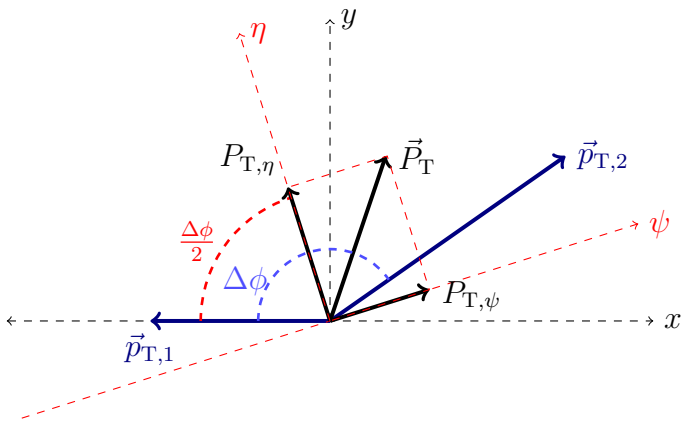

Figure 6.4 Variables used in the bisector technique. The η-axis corresponds to the azimuthal angular bisector of the dijet system while the ψ-axis is defined as the one orthogonal to the η-axis; all in the plane transverse to the beam axis.

The validity of this assumption, which is at the root of the bisector method, can be checked with Monte Carlo simulations and with data. The precision with which it can be assessed is considered as a systematic uncertainty (see Section 6.4.2.2). The ψ component has greater sensitivity to the energy resolution because $P_{\mathrm{T},\psi}$ is the difference between two large transverse momenta while $P_{\mathrm{T},\eta}$ is the sum of two small components. Effects such as contamination from 3-jet events or final-state radiation not absorbed in the leading jets by the clustering algorithm could give rise to a $\sigma_{\psi}^{2\ \mathrm{part}}$ larger than $\sigma_{\eta}^{2\ \mathrm{part}}$. At calorimeter level, $\sigma_{\psi}^{2\ \mathrm{calo}}$ is expected to be significantly larger than $\sigma_{\eta}^{2\ \mathrm{calo}}$, mostly because of the jet energy resolution.

If both jets belong to the same y region, such that they have the same average jet energy resolution, it can be shown that

$$\frac{\sigma(p_{\mathrm{T}})}{p_{\mathrm{T}}} = \frac{\sqrt{\sigma_{\psi}^{2\ \mathrm{calo}} - \sigma_{\eta}^{2\ \mathrm{calo}}}}{\sqrt{2}\, p_{\mathrm{T}} \sqrt{\langle |\cos \Delta\phi_{12}| \rangle}}. \tag{6.6}$$

The resolution is thus expressed in terms of calorimeter observables only. Soft radiation effects are removed by subtracting in quadrature σ_{η} from σ_{ψ} at calorimeter level.

If one jet belongs to the rapidity region being probed (j) and the other one (i) to a previously measured reference y region, then

$$\frac{\sigma(p_{\mathrm{T}})}{p_{\mathrm{T}}}\Big|_{(j)} = \sqrt{\frac{\sigma_{\psi}^{2\ \mathrm{calo}} - \sigma_{\eta}^{2\ \mathrm{calo}}}{p_{\mathrm{T}}^2 \langle |\cos \Delta\phi_{12}| \rangle}\Big|_{(i,j)} - \frac{\sigma^2(p_{\mathrm{T}})}{p_{\mathrm{T}}^2}\Big|_{(i)}}. \tag{6.7}$$

The dispersions σ_{ψ} and σ_{η} are extracted from Gaussian fits to the $P_{\mathrm{T},\psi}$ and $P_{\mathrm{T},\eta}$ distributions in bins of $\bar{p}_{\mathrm{T}}$. There is no $\Delta\phi$ cut imposed between the leading jets, but it is implicitly limited by a $p_{\mathrm{T},3}^{\mathrm{EM-scale}} < 10$ GeV requirement on the third

jet, as discussed in the next section. Figure 6.5 compares the distributions of $P_{\mathrm{T},\psi}$ and $P_{\mathrm{T},\eta}$ between data and Monte Carlo simulation. The distributions agree within statistical fluctuations. The resolutions obtained from the $P_{\mathrm{T},\psi}$ and $P_{\mathrm{T},\eta}$ components of the imbalance vector are summarized in the central region as a function of $\bar{p}_{\mathrm{T}}$ in Figure 6.6. As expected, the resolution on the η component does not vary with the jet p_{T}, while the resolution on the ψ component degrades as the jet p_{T} increases.

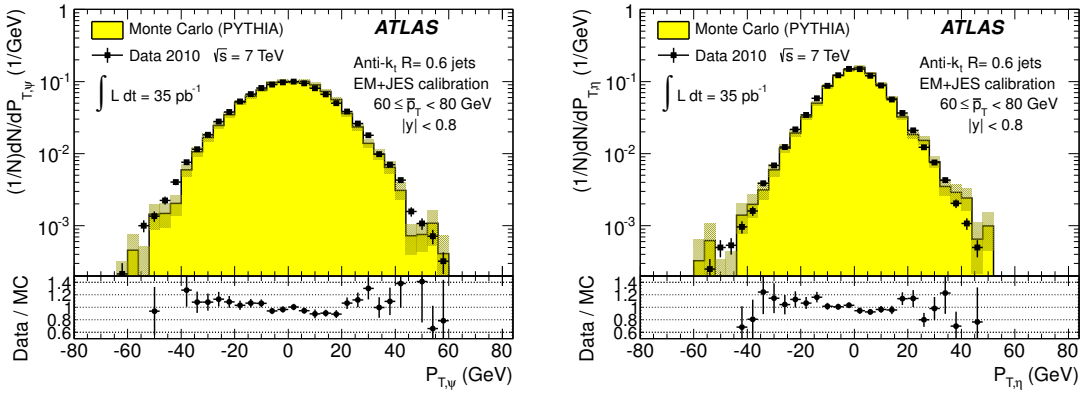

Figure 6.5 Distributions of the $P_{\mathrm{T},\psi}$ (left) and $P_{\mathrm{T},\eta}$ (right) components of the imbalance vector $\vec{P}_{\mathrm{T}}$, for $\bar{p}_{\mathrm{T}} = 60 - 80$ GeV. Data (points with error bars) and Monte Carlo simulation (histogram with shaded bands) are overlaid.

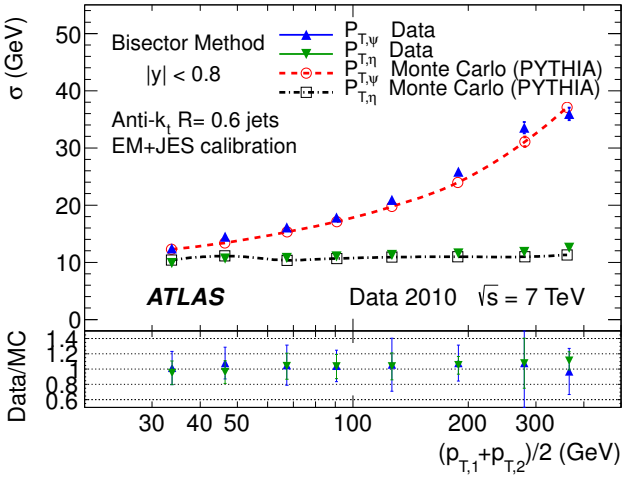

Figure 6.6 Standard deviations of $P_{\mathrm{T},\psi}$ and $P_{\mathrm{T},\eta}$, the components of the imbalance vector, as a function of $\bar{p}_{\mathrm{T}}$. The lower panel shows the ratio between data and MC simulation.

6.4.2.2 Validation of the soft radiation isotropy with data

The bisector hypothesis of soft radiation isotropy can be validated with data. Figure 6.7 shows the width of the ψ and η components of $\vec{P}_{\mathrm{T}}$ as a function of the

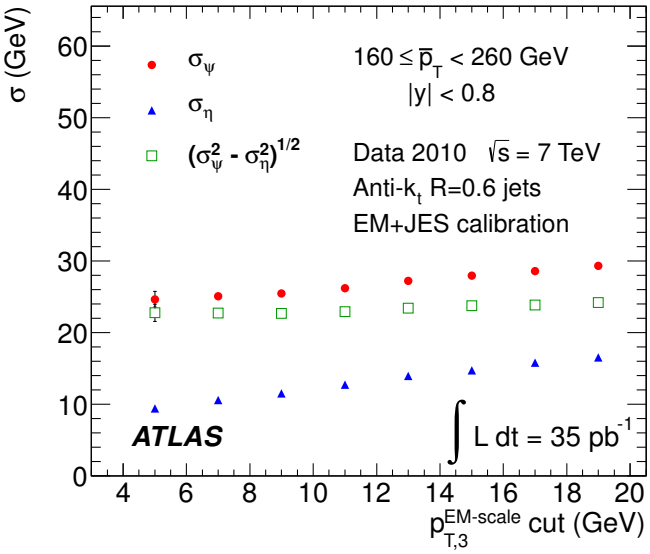

Figure 6.7 Standard deviations $\sigma_\psi^{\text{calo}}$, $\sigma_\eta^{\text{calo}}$ and $[(\sigma_\psi^2 - \sigma_\eta^2)^{\text{calo}}]^{1/2}$ as a function of the upper $p_{\text{T},3}^{\text{EM-scale}}$ cut, for $R = 0.6$ anti-k_t jets with $\bar{p}_{\text{T}} = 160 - 260$ GeV. The increase of the soft radiation contribution to $\sigma_\psi^{\text{calo}}$ and $\sigma_\eta^{\text{calo}}$ cancels in the squared difference, and within statistical uncertainties it remains constant up to $p_{\text{T},3}^{\text{EM-scale}} \simeq 20$ GeV.

$p_{\text{T},3}^{\text{EM-scale}}$ cut, for anti-k_t jets with $R = 0.6$. The two leading jets are required to be in the same rapidity region, $|y| < 0.8$, while there is no rapidity restriction for the third jet. As expected, it can be observed that both components increase due to the contribution from soft radiation as the $p_{\text{T},3}^{\text{EM-scale}}$ cut increases. Also shown as a function of the $p_{\text{T},3}^{\text{EM-scale}}$ cut is the square-root of the difference between their variances, which yields the fractional momentum resolution when divided by $2\langle p_{\text{T}}^2\rangle\langle\cos\Delta\phi\rangle$. It is observed that the increase of the soft radiation contribution to $\sigma_\psi^{\text{calo}}$ and $\sigma_\eta^{\text{calo}}$ cancels in the squared difference and that it remains almost constant, within statistical uncertainties, up to $p_{\text{T},3}^{\text{EM-scale}} \simeq 20$ GeV for $\bar{p}_{\text{T}}$ between 160-260 GeV. The same behavior is observed for other $\bar{p}_{\text{T}}$ ranges. This cancellation demostrates that the isotropy assumption used for the bisector method is valid over a wide range of choices of $p_{\text{T},3}^{\text{EM-scale}}$ without the need for requiring an explicit $\Delta\phi$ cut between the leading jets. The precision with which it can be ascertained in situ that $\sigma_\psi^{\text{part}} = \sigma_\eta^{\text{part}}$ is taken conservatively as a systematic uncertainty on the result, of about $4 - 5\%$ at 50 GeV (see Section 6.7).

6.5 Performance for the EM+JES calibration

The performances of the dijet balance and the bisector methods are compared for both data and Monte Carlo simulation as a function of p_{T}, for jets reconstructed in the central region with the anti-k_t algorithm with $R = 0.6$ and using the EM+JES

calibration scheme. The results are shown in Figure 6.8. The resolutions obtained from the two independent in situ methods are in good agreement with each other within the statistical uncertainties. The agreement between data and Monte Carlo simulation is also good with some deviations observed at low p_{T}.

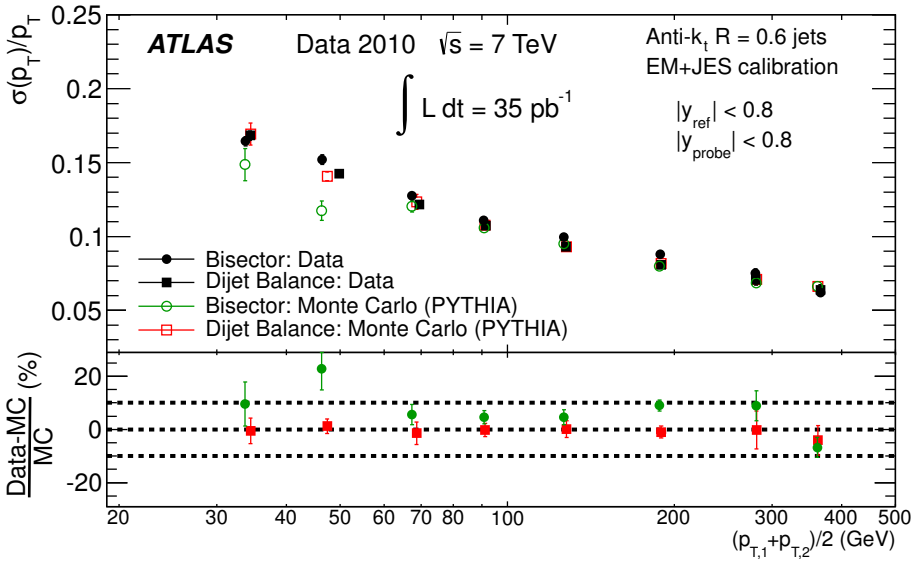

Figure 6.8 Fractional jet p_{T} resolution for the dijet balance and bisector techniques as a function of $\bar{p}_{\mathrm{T}}$. The lower panel shows the relative difference between data and Monte Carlo results. The dotted lines indicate a relative difference of $\pm 10\%$. Within the statistical precision of the results, both methods are found to be within 10% in agreement for Monte Carlo simulation and data.

The resolutions for the three jet rapidity bins with $|y| > 0.8$, the Extended Tile Barrel, the Transition and the End-Cap regions, are measured using Eqs. 6.3 and 6.7, taking the central region as reference. The results for the bisector method are shown in Fig. 6.9. The resolutions obtained for data and Monte Carlo simulation are in good agreement with each other within the statistical uncertainties.

Figure 6.9 shows that the p_{T} dependence is well described by a fit with the standard functional form expected for calorimeter-based resolutions, with three terms contributing independently,

$$\frac{\sigma(p_{\mathrm{T}})}{p_{\mathrm{T}}} = \frac{N}{p_{\mathrm{T}}} \oplus \frac{S}{\sqrt{p_{\mathrm{T}}}} \oplus C\,. \tag{6.8}$$

The noise term (N) is due to external noise contributions that are not (or only weakly) dependent on the jet p_{T}, and include the electronics and detector noise, and contributions from pile-up. It is expected to be significant in the low p_{T} region, below ~30 GeV. The constant term (C) encompasses the fluctuations that are a constant fraction of the jet p_{T}, due mainly to a fraction of the integrated signal

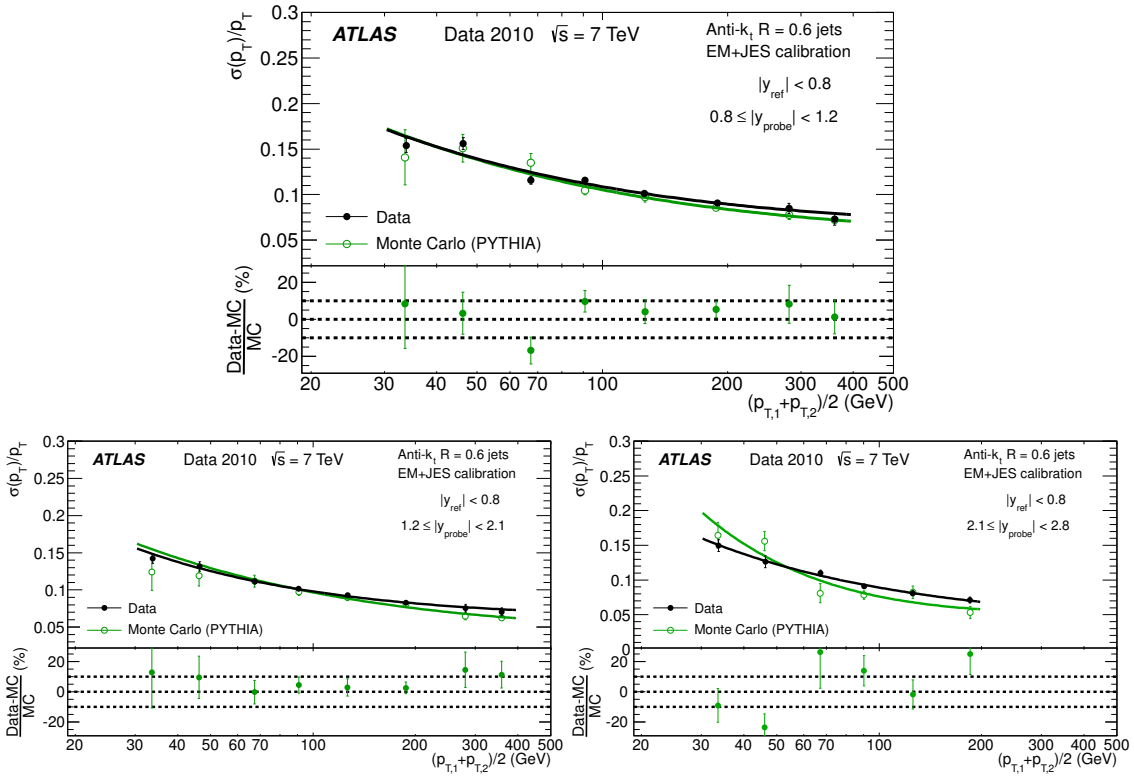

Figure 6.9 Fractional jet p_{T} resolution as a function of $\bar{p}_{\mathrm{T}}$ for anti-k_t with $R = 0.6$ jets in the Extended Tile Barrel (top), Transition (bottom left) and End-Cap (bottom right) regions using the bisector method. In the lower panel of each figure, the relative difference between the data and the MC simulation results is shown. The dotted lines indicate a relative discrepancy of $\pm 10\%$.

being lost in uninstrumented regions. It is expected to dominate the high p_{T} region, above 400 GeV. In the intermediate region the Poissonian fluctuations, represented by the stochastic term (S), become the limiting factor in the resolution. With the present data sample that covers a restricted p_{T} range, 30 GeV $\leq p_{\mathrm{T}} <$ 500 GeV, there is a high degree of correlation in the fitted parameters and it is not possible to unequivocally disentangle their contributions.

6.6 Closure test

The Monte Carlo simulation truth resolution is defined considering matched particle and calorimeter jets in the event, with no back-to-back geometry requirements. Matching is done in $\eta - \phi$ space, and jets are associated if the condition $\Delta R = \sqrt{(\Delta\eta)^2 + (\Delta\phi)^2} < 0.3$ is satisfied. The jet response is defined as $p_{\mathrm{T}}^{\mathrm{calo}}/p_{\mathrm{T}}^{\mathrm{part}}$, in bins of $p_{\mathrm{T}}^{\mathrm{part}}$, where $p_{\mathrm{T}}^{\mathrm{calo}}$ and $p_{\mathrm{T}}^{\mathrm{part}}$ correspond to the transverse momenta of the reconstructed jet and its matched particle jet, respectively. The jet response distribution is modelled with a Gaussian fit, and its standard deviation is defined as the

truth jet p_{T} resolution.

The Monte Carlo simulation truth jet p_{T} resolution is compared to the final results obtained from the dijet balance and the bisector in situ techniques in Figure 6.10. The agreement between the three sets of points is within 10%. This result confirms the validity of the physical assumptions discussed in Sections 6.4.1 and 6.4.2 and the inference that the observables derived for the in situ MC dijet balance and bisector methods correspond to the truth MC jet energy resolution. It can be therefore concluded that the same observables in data correspond to the actual jet energy resolution, with a systematic uncertainty of the order of 10% (15%) for jets with $R = 0.6$ ($R = 0.4$), as discussed in the following section.

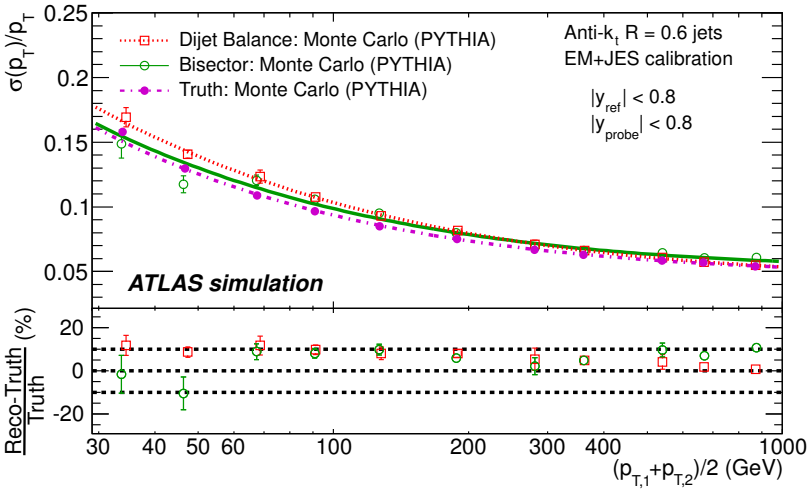

Figure 6.10 Comparison between the Monte Carlo simulation truth jet p_{T} resolution and the final results obtained from the bisector and dijet balance in situ techniques (applied to Monte Carlo simulation) for the EM+JES calibration, as a function of $\bar{p}_{\mathrm{T}}$. The lower panel of the figure shows the relative difference, obtained from the fits, between the in situ methods and Monte Carlo truth results. The black dotted lines indicate a relative discrepancy of $\pm 10\%$.

6.7 Jet energy resolution uncertainties

This section presents the sources of the systematic uncertainties in the jet energy resolution, as estimated using the available Monte Carlo simulations and collision data. The different sources are discussed next.

6.7.1 Experimental uncertainties

The squares (circles) in Figure 6.11 show the experimental relative systematic uncertainty in the dijet balance (bisector) method as a function of $\bar{p}_{\mathrm{T}}$. The different

contributions are discussed below. The shaded area corresponds to the larger of the two systematic uncertainties for each $\bar{p}_{\mathrm{T}}$ bin. For the dijet balance method, systematic uncertainties take into account the variation in resolution when applying different $\Delta\phi$ cuts (varied from 2.6 to 3.0), resulting in a 2–3% uncertainty for $p_{\mathrm{T}} =$ 30–60 GeV, and from different soft radiation correction modelling, which contributes up to 6% at $p_{\mathrm{T}} \approx 30$ GeV. For the bisector method, the systematic uncertainty is about 4–5% deriving from the precision with which the assumption that $\sigma_{\psi}^{\mathrm{part}} = \sigma_{\eta}^{\mathrm{part}}$ when varying the $p_{\mathrm{T},3}^{\mathrm{EM-scale}}$ cut can be verified.

The contribution from the JES uncertainties [206] is 1–2%, determined by re-calculating the jet resolutions after varying the JES within its uncertainty in a fully correlated way. The resolutions have also been studied in simulated events with added pile-up events (i.e., additional interactions as explained in Section 6.1) and compared to those determined in events with one hard interaction only. The sensitivity of the resolution to pile-up is found to be within 1% for an average number of vertices per event of 1.9.

In summary, the overall uncertainty from the in situ techniques varies from about 7% at $p_{\mathrm{T}} =$30 GeV down to 4% at $p_{\mathrm{T}} = 500$ GeV. Figure 6.11 also shows in dashed lines the absolute value of the relative difference between the two in situ methods, for both data and Monte Carlo simulation. They are found to be in agreement within 4% up to 500 GeV, and consistent with these systematic uncertainties.

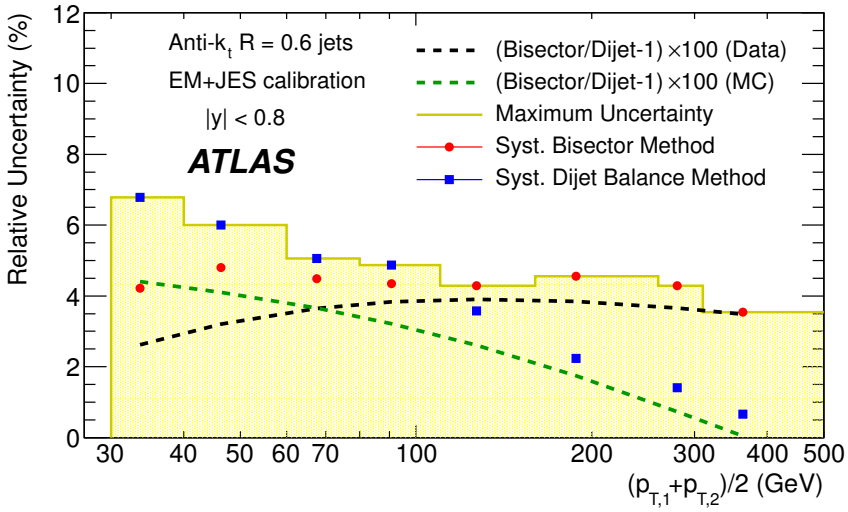

Figure 6.11 The experimental systematic uncertainty in the dijet balance (squares) and bisector (circles) methods as a function of $\bar{p}_{\mathrm{T}}$. The absolute value of the relative difference between the two methods is also shown for data and for Monte Carlo simulation (dashed lines). They are found to be in agreement within 4%, consistent with the larger of the systematic uncertainties for the two in situ methods at each $\bar{p}_{\mathrm{T}}$ bin (shaded area).

6.7.2 Uncertainties due to the event modelling in the Monte Carlo generators

The jet p_{T} resolution is calculated for other Monte Carlo simulations in order to assess the dependence of the truth resolution on different generator models (ALPGEN and HERWIG++), PYTHIA tunes (PERUGIA2010), and other systematic variations (PARP90, see Section 6.1). Differences between the nominal Monte Carlo simulation and PYTHIA8 [235] have also been considered. The effects, displayed in Figure 6.12, never exceed 4%. Although not relevant for in situ measurements of the resolution, physics analyses using the truth resolution as their baseline can apply a systematic uncertainty from event modelling estimated from the sum in quadrature of the different cases considered. This is shown by the shaded area in Figure 6.12 and found to be at most 5%, without any specific trend.

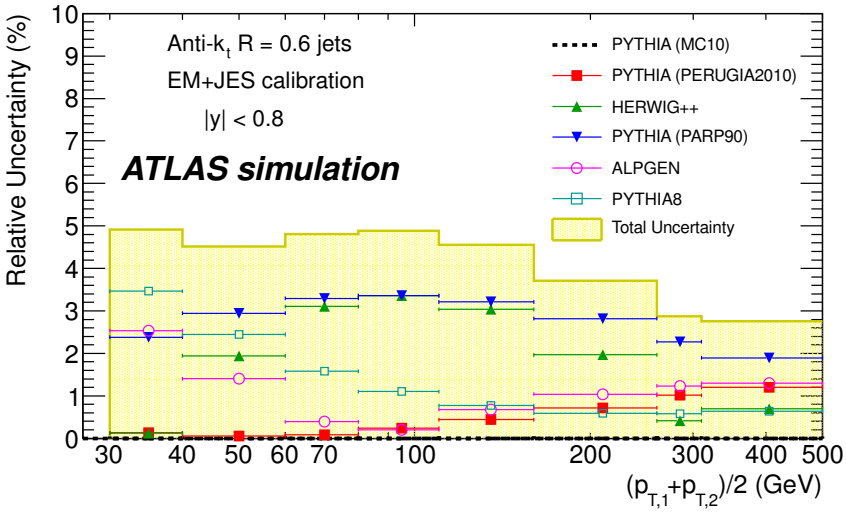

Figure 6.12 Dependence of the resolution on the event modelling in the Monte Carlo generators, taking PYTHIA MC10 as reference. Solid triangles and open circles show the systematic uncertainty from HERWIG++ and ALPGEN, respectively. Solid squares (PYTHIA PERUGIA2010) and inverted triangles (PYTHIA PARP90) summarize differences coming from different tunes and cut-off parameters, respectively. Open squares compare the nominal simulation with PYTHIA8. The effects were found to be about $4-5\%$ and without any specific trend.

6.7.3 Uncertainties of the measured resolutions

The uncertainties in the measured resolutions are dominated by the systematic uncertainties, which are shown in Table 6.1 as a percentage of the resolution for the four rapidity regions and the two jet sizes considered, and for three characteristic

ranges, low (~ 50 GeV), medium (~ 150 GeV) and high (~ 400 GeV) p_{T}. The results are similar for the four calibration schemes. The dominant sources of systematic uncertainty are the closure and the data/MC agreement.

The closure uncertainty, defined as the precision with which it is verified that the resolution determined in situ corresponds to the truth jet resolution, is larger for $R = 0.4$ than for $R = 0.6$, decreases with p_{T}, and is basically independent of the rapidity. The data/MC agreement uncertainty is observed to be independent of R, larger at low and high p_{T} than at medium p_{T}, and growing with rapidity because of the increasingly limited statistical accuracy with which checks can be performed to assess it. Other systematic uncertainties are significantly smaller. They include the validity of the soft radiation hypothesis, the jet energy scale precision and the dependence on the number of pile-up interactions. The uncertainty due to event modelling is not included, as it does not contribute to an in situ measurement. Also not included is the cross-check between the two in situ methods[2].

Jet radius	Rapidity range	Total Systematic Uncertainty		
		low p_{T}	med p_{T}	high p_{T}
$R = 0.6$	$0 \le \lvert y \rvert < 0.8$	12%	10%	11%
	$0.8 \le \lvert y \rvert < 1.2$	12%	10%	13%
	$1.2 \le \lvert y \rvert < 2.1$	14%	12%	14%
	$2.1 \le \lvert y \rvert < 2.8$	15%	13%	18%
$R = 0.4$	$0 \le \lvert y \rvert < 0.8$	17%	15%	11%
	$0.8 \le \lvert y \rvert < 1.2$	20%	18%	14%
	$1.2 \le \lvert y \rvert < 2.1$	20%	18%	14%
	$2.1 \le \lvert y \rvert < 2.8$	20%	18%	18%

Table 6.1 Total systematic uncertainties at low (~ 50 GeV), medium (~ 150 GeV) and high (~ 400 GeV) p_{T}, for the four rapidity regions and the two jet radii studied. The uncertainties are similar for the four calibration schemes.

The systematic uncertainties in Table 6.1 for jets with $R = 0.4$ are dominated by the contribution from the closure test. They decrease with p_{T} and are constant for the highest three rapidity bins. They are also consistently larger than for the $R = 0.6$ case. The systematic uncertainties for jets with $R = 0.6$ receive comparable contributions from closure and data/MC agreement. They tend to increase with rapidity and are slightly lower in the medium p_{T} range. The uncertainty increases at high p_{T} for the end-cap, $2.1 \le \lvert y \rvert < 2.8$, because of the limited number of events in this region.

[2]If the two in situ methods did not agree within errors one should find the source of the discrepancy rather than assigning a systematic error to account for it.

6.8 Results for other calibration schemes

The resolution performance for anti-k_t jets with $R = 0.6$ reconstructed from calorimeter topological clusters for the Local Cluster Weighting (LCW+JES), the Global Cell Weighting (GCW+JES) and the Global Sequential (GS) calibration strategies (using the bisector technique) is presented in Figure 6.13 for the Central, Extended Tile Barrel, Transition and End-Cap regions. The top part shows the resolutions determined from data, whereas the bottom part compares data and Monte Carlo simulation results. The relative improvement in resolution with respect to the EM+JES calibrated jets is comparable for the three more sophisticated calibration techniques. It ranges from 10% at low p_{T} up to 40% at high p_{T} for all four rapidity regions.

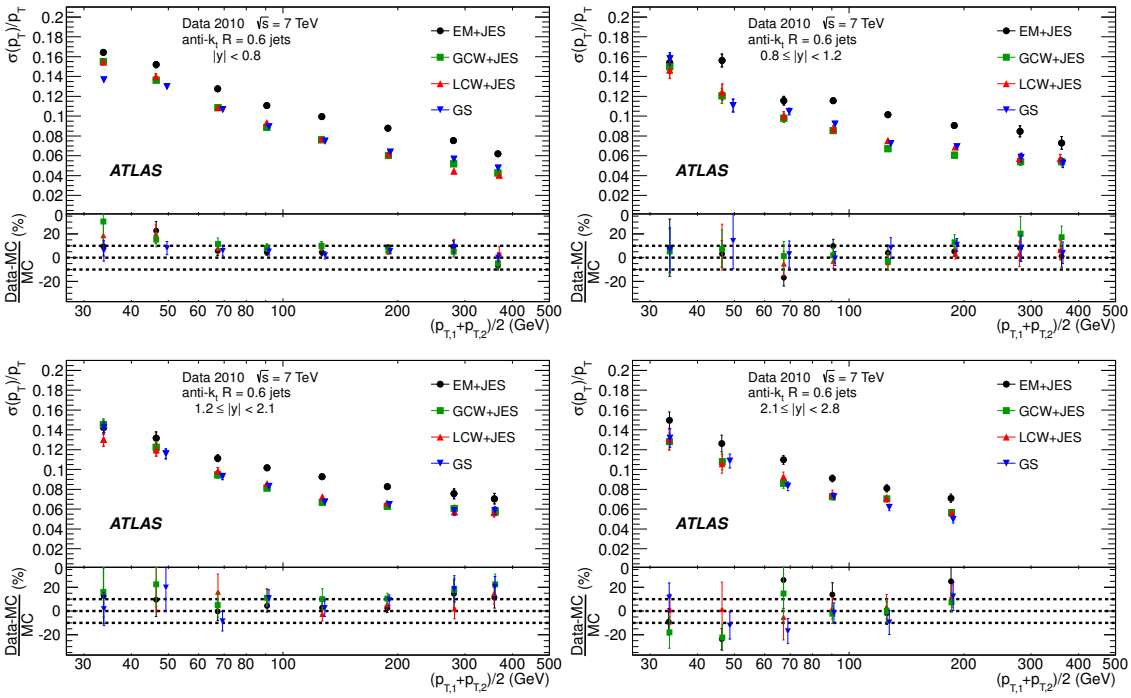

Figure 6.13 Fractional jet p_{T} resolution as a function of $\bar{p}_{\mathrm{T}}$ for anti-k_t jets with $R = 0.6$ with $|y| < 0.8$ (top left), $0.8 \leq |y| < 1.2$ (top right), $1.2 \leq |y| < 2.1$ (bottom left) and $2.1 \leq |y| < 2.8$ (bottom right), using the bisector in situ technique, for four jet calibration schemes: EM+JES, Local Cluster Weighting (LCW+JES), Global Cell Weighting (GCW+JES) and Global Sequential (GS). The lower panels show the relative difference between data and Monte Carlo simulation results. The dotted lines indicate a relative difference of ±10%.

Figure 6.14 displays the resolutions for the two in situ methods applied to data and Monte Carlo simulation for $|y| < 0.8$ (left plots). It can be observed that the results from the two methods agree, within uncertainties. The Monte Carlo simulation reproduces the data within 10%, with a largest statistical difference of

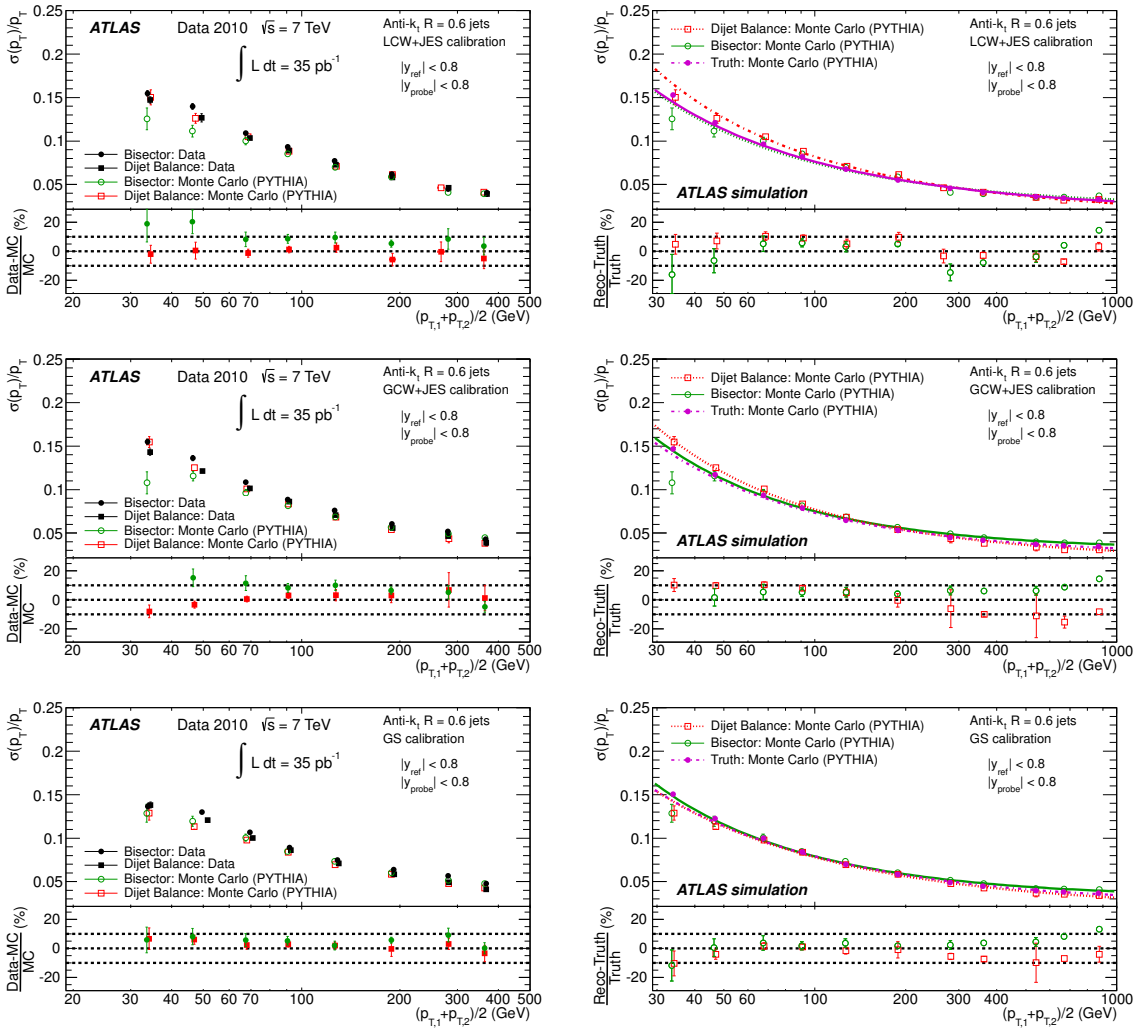

Figure 6.14 Fractional jet p_{T} resolutions as a function of $\bar{p}_{\mathrm{T}}$ for anti-k_t jets with $R = 0.6$ for the Local Cluster Weighting (LCW+JES), Global Cell Weighting (GCW+JES) and Global Sequential (GS) calibrations. Left: Comparison of both in situ methods on data and MC simulation for $|y| < 0.8$. The lower panels show the relative difference. Right: Comparison between the Monte Carlo simulation truth jet p_{T} resolution and the final results obtained from the bisector and dijet balance in situ techniques (applied to Monte Carlo simulation). The lower panels show the relative differences, obtained from the fits, between the in situ methods and MC truth results. The black dotted lines in the lower panels indicate a ±10% band.

2.5σ. The figures on the right show the results of a study of the closure for each case, where the truth resolution is compared to that obtained from the in situ methods applied on Monte Carlo simulation data. The agreement is within 10%. Overall, comparable agreement in resolution is observed in data and Monte Carlo simulation for the EM+JES, LCW+ JES, GCW+JES and GS calibration schemes, with similar systematic uncertainties in the resolutions determined using in situ methods.

6.9 Improvement in jet energy resolution using tracks

The addition of tracking information to the calorimeter-based energy measurement is expected to compensate for the jet-by-jet fluctuations and improve the jet energy resolution (see Section 6.3.4). The performance of the Track-Based Jet Correction method (TBJC) is studied by applying it to both the EM+JES and LCW+JES calibration schemes, in the central region. The measured resolution for anti-k_t jets with $R = 0.6$ and $R = 0.4$ are presented as a function of the average jet transverse momentum in Figure 6.15. The relative improvement in resolution due to the addition of tracking information is larger at low p_{T} and more important for the EM+JES calibration scheme. It ranges from 22% (10%) at low p_{T} to 15% (5%) at high p_{T} for the EM+JES (LCW+JES) calibration. For $p_{\mathrm{T}} < 70$ GeV, jets calibrated with the EM+JES+TBJC scheme show a similar performance to those calibrated with the LCW+JES+TBJC scheme. Overall, anti-k_t jets with $R = 0.6$ and $R = 0.4$ with LCW+JES+TBJC show the best fractional energy resolution over the full p_{T} range, and their performance is presented in Figure 6.16 along with that determined by the CMS experiment, as outlined in [248].

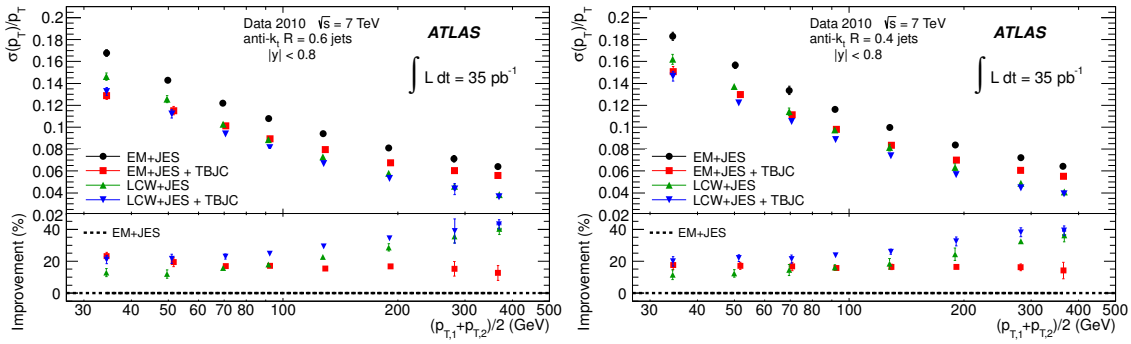

Figure 6.15 Fractional jet p_{T} resolution as a function $\bar{p}_{\mathrm{T}}$, measured in data for anti-k_t jets with $R = 0.6$ (left) and $R = 0.4$ (right), for four jet calibration schemes: EM+JES, EM+JES+TBJC, LCW+JES and LCW+JES+TBJC. The lower panel of the figure shows the relative improvement for the EM+JES+TBJC, LCW+JES and LCW+JES+TBJC calibrations with respect to the EM+JES jet calibration scheme as baseline (dotted line).

6.10 Summary of results with 2010 data

The jet energy resolution for various JES calibration schemes has been estimated using two in situ methods with a data sample corresponding to an integrated luminosity of 35 pb^{-1} collected by the ATLAS experiment at $\sqrt{s} = 7$ TeV. The Monte

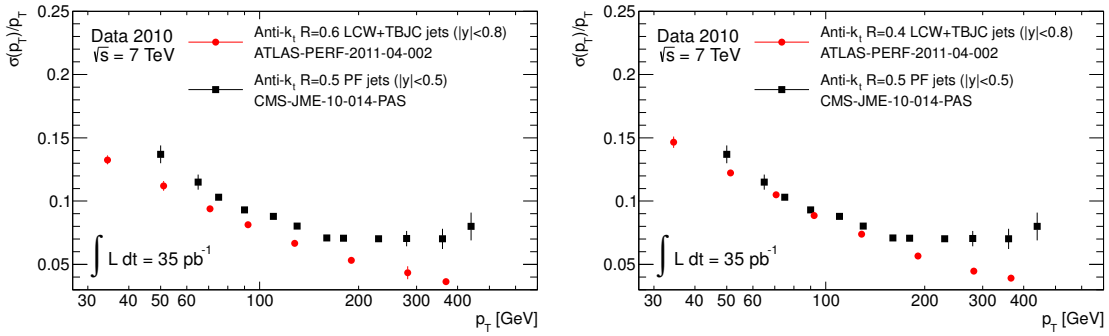

Figure 6.16 Fractional jet momentum resolution as a function of the average jet transverse momenta for two-jet events, using Track-based jet corrections (TBJC) applied on top of Local Cluster Weighting (LCW) anti-k_t jets with $R = 0.6$ and $R = 0.4$ in ATLAS (red circles) and Particle flow anti-k_t 0.5 jets in CMS (black squares). Points show the in situ resolution, as measured using the Bisector technique for ATLAS [225] and the di-jet balance method for CMS [248], with 2010 data.

Carlo simulation describes the jet energy resolution measured in data within 10% for jets with p_{T} values between 30 GeV and 500 GeV in the rapidity range $|y| < 2.8$. The resolutions obtained applying the in situ techniques to Monte Carlo simulation are in agreement within 10% with the resolutions determined by comparing jets at calorimeter and particle level. The total uncertainties on these measurements range from 20% to 10% for jets within $|y| < 2.8$ and with transverse momenta increasing from 30 GeV to 500 GeV. Overall, the results measured with the two in situ methods have been found to be consistent within the determined systematic uncertainties. Figure 6.17 presents the comparison of the fractional jet momentum resolution as a function of the average jet transverse momenta with GCW calibrated jets as determined using 2010 data, with respect to the truth resolution expected from Monte Carlo simulation before data-taking begins [2]. As it can be observed, the resolution measured from 2010 data is found to be competitive with the expected JER throughout the entire p_{T} range, and reflects thus the outstanding performance of the ATLAS detector.

6.11 JER performance with 2011 data

The jet energy resolution has been determined with 2011 data, using the same strategy based on the two in-situ methods described above. Figure 6.18 presents a comparison of the fractional jet energy resolution as a function of the average jet transverse momenta, measured with the bisector in-situ technique, for the EM+JES and LCW calibrations, with a data sample corresponding to an integrated luminosity of 950 pb^{-1} collected by the ATLAS experiment at $\sqrt{s} = 7$ TeV during 2011. By taking the EM+JES jet calibration scheme as baseline (black dotted line), the

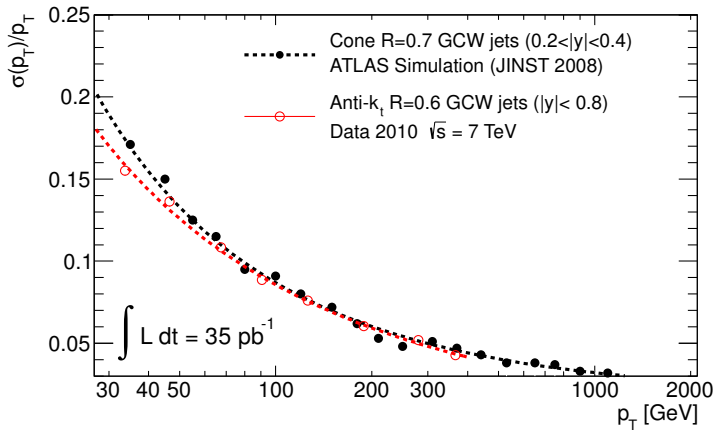

Figure 6.17 Fractional jet momentum resolution as a function of the average jet transverse momenta for two-jet events with Global Cell Weighting (GCW) calibrated jets in ATLAS. Black circles show the truth resolution expected from Monte Carlo simulation before data-taking begins [2], whereas the red squares is the in situ resolution measured using the Bisector technique on 2010 data [225]. The lines correspond to the fit on both data (red) and Monte Carlo simulation (black).

improvement in jet resolution is found to be up to 40 % at 1000 GeV for LCW. Figure 6.19 presents a comparison of the fractional jet energy resolution as a function of the average jet transverse momenta measured with the bisector in-situ technique from 2011 and 2010 data samples, for the EM+JES calibration (no pile-up corrections applied). As can be observed, for jet with $p_{\mathrm{T}} > 60$ GeV the resolution measured for 2011 (red) data is found to be in agreement within 5 %, with respect to the determined with 2010 data (black), up to 400 GeV, the limit of course imposed by the data collected during 2010. On the other hand, in the region $p_{\mathrm{T}} \leq 60$ GeV, the resolution measured for 2011 data is found to be up to $10 - 15$ % worse than the determined with 2010 data. This degradation in resolution is mainly due to the increasing amount of pile-up during 2011, and it is further discussed in the next section.

6.11.1 Impact of pile-up on jet energy resolution

The topo-clustering is seeded by cells with large signal over noise, as discussed in Section 5.5. The cell noise is computed as the sum in quadrature of electronic noise and pile-up [2]. The latter contribution is expected to dominate at high luminosity environments, with contributions up to 10 GeV beyond $|\eta| > 4.0$ at the design luminosity for the LHC [191]. The noise term (N) in Eq. 6.8 represents noise contributions that are not (or only weakly) dependent on jet energy. Thus, if one includes the electronics and detector noise ($N^{elect,det}$) and contributions from pile-up ($N^{pile-up}$), the expected noise may be expressed as $N^{expected} = (N^{pile-up} \oplus N^{elect,det})$.

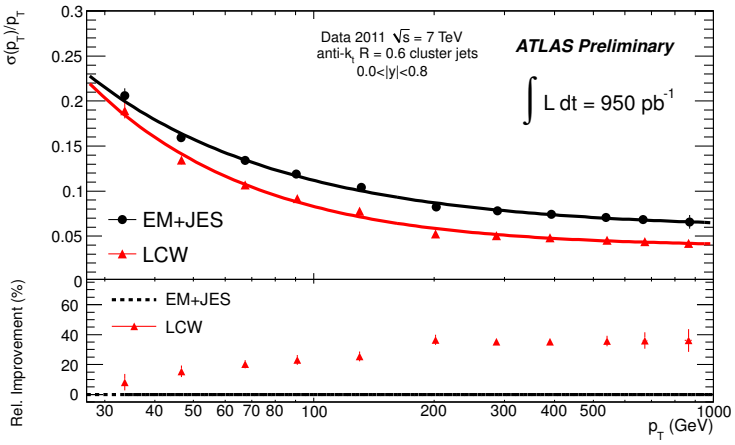

Figure 6.18 Fractional jet energy resolution as a function of the average jet transverse momenta measured with the bisector in-situ technique for events with two jet in the same rapidity bin for EM+JES and Local Cluster Weighting (LCW) calibrations with 2011 data. The lines correspond to the fits on data for each JES scheme respectively. The lower plot shows the relative improvement as a function of the average jet transverse momenta. The EM+JES jet calibration scheme is taken as baseline (black dotted line). The improvement is found to be up to 40 % at 1000 GeV for LCW. No pile-up corrections have been applied.

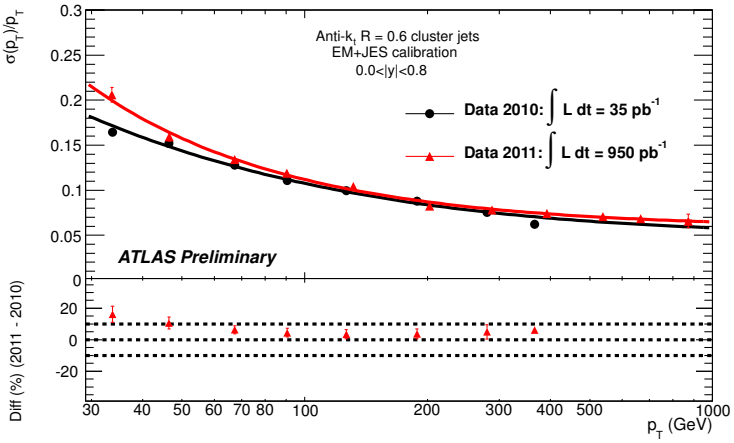

Figure 6.19 Fractional jet energy resolution as a function of the average jet transverse momenta measured with the bisector in-situ technique for events with two jet in the same rapidity bin for EM+JES calibration with 2011 (red) and 2010 (black) data. The lines correspond to the fits on data. The lower part shown the relative difference between 2011 and 2010 data results. The dotted lines indicate a relative difference of ± 10 %. No pile-up corrections have been applied.

As discussed in Section 6.7, the impact of pile-up on resolution was found to be negligible in 2010 data (< 1%). Therefore, if one denotes the contribution of pile-up to the resolution measured with 2010 and 2011 data samples as $\sigma_{\text{pu}}^{2010}$ and $\sigma_{\text{pu}}^{2011}$,

respectively, the latter is expected to be the most significant difference at low p_{T} between the resolutions determined with the two datasets. Thus, $\sigma_{\mathrm{pu}}^{2011}$ is estimated from the quadratic difference between the resolutions obtained from 2010 and 2011 data. For jets in the central region and calibrated at the EM+JES, the impact of pile-up is found to be approximately 10 % at $p_{\mathrm{T}} \sim 35$ GeV using the resolutions determined with the dijet balance and the bisector in-situ techniques from 2010 and 2011 data. For jets with $R = 0.4$, the effect is found to be up to 8% at low p_T, due to the small jet size. Similar performance for LCW calibrated jets is observed for both values of R.

6.11.2 Forward regions

The low statistics collected in several p_{T} bins for jets within the forward region ($|y| > 2.8$) dramatically reduce the possibility of using Eq. 6.8 to describe the jet energy resolution. However, the ratios of the asymmetry values as a function of the third jet p_{T} discussed in Section 6.4.1.2 provides a good estimate of the level of the agreement between data and Monte Carlo simulation. For instance, for jets in the central region with p_{T} ranging from 60 GeV to 80 GeV (Figure 6.2), the difference obtained between data and MC is found to be $\approx 1.5\%$, in agreement with the final results shown in Figure 6.8. Therefore, this approach is used to estimate the level of agreement between data and Monte Carlo simulation in the forward region. The region beyond $|y| > 2.8$ is split in two, in order to distinguish different instrumented parts of the ATLAS detector:

- HEC-FCal transition region: $2.8 \leq |y| < 3.6$.
- FCal region: $3.6 \leq |y| < 4.4$.

Figure 6.20 shows the dependence of the determined jet p_{T} resolution on the presence of a third jet for a $\bar{p}_{\mathrm{T}}$ bin of $60 \leq \bar{p}_{\mathrm{T}} < 80$ GeV, for $2.8 \leq |y| < 3.6$ (left) and $3.6 \leq |y| < 4.4$ (right), using anti-k_t 0.4 jets calibrated at the EM+JES. The level of agreement between data and Monte Carlo is found to be 15% and 60% for $2.8 < |\eta| < 3.6$ and $3.6 < |\eta| < 4.4$, respectively. For each of these rapidity regions, the results obtained for the two contiguous p_{T} bins present a level of agreement within 10 % with respect to those shown in Figure 6.20. A similar performance is observed for jets calibrated using LCW.

6.12 Final remarks and future prospects

The final results are placed into an official common tool to be used by the physics analysis within the ATLAS collaboration, dubbed `JetEnergyResolutionProvider`. It provides the estimate of the jet energy resolution and its uncertainty for anti-k_t

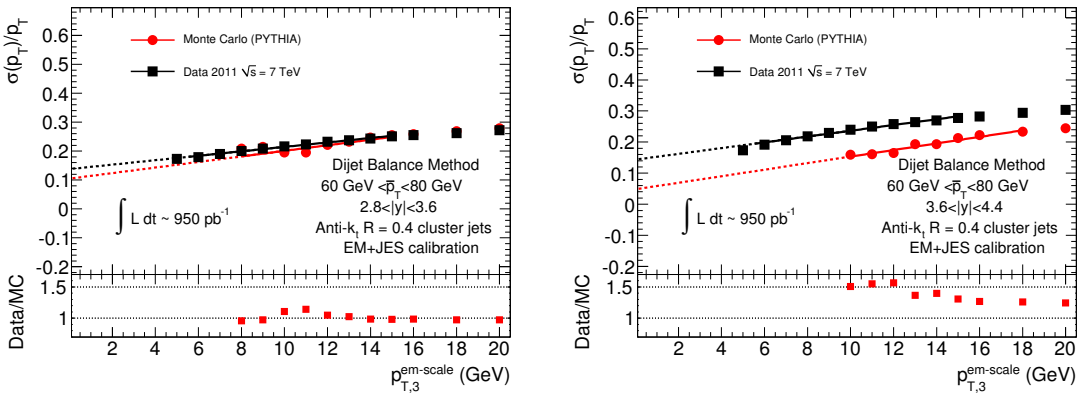

Figure 6.20 The determined jet p_{T} resolution on the presence of a third jet, using anti-k_t 0.4 jets calibrated at the EM+JES, for a $\bar{p}_{\mathrm{T}}$ bin of $60 \leq \bar{p}_{\mathrm{T}} < 80$ GeV, for $2.8 \leq |y| < 3.6$ (left) and $3.6 \leq |y| < 4.4$ (right). The level of agreement between data and Monte Carlo is found to be 15% and 60%, respectively.

with R= 0.4 and R= 0.6 jets calibrated with both EM+JES and LC calibration schemes, the two JES schemes pursued for 2011 data in ATLAS. The JER uncertainty is estimated from data and Monte-Carlo studies, as described in Section 6.7, and it is 100 % correlated point by point. The fractional jet transverse momentum resolution is parameterized as described by Eq 6.8. The coverage in rapidity has been separated into the six regions introduced in this Chapter, to distinguish among different instrumented parts of the ATLAS detector. Figure 6.21 shows the jet energy resolution and its uncertainty for anti-k_t with R= 0.6 jets calibrated with the EM+JES (left) and LCW (right) calibration schemes, for the central region.

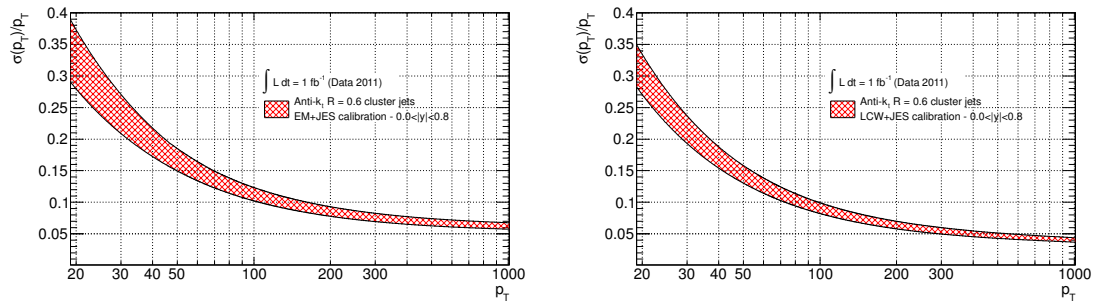

Figure 6.21 The jet energy resolution and its uncertainty for anti-k_t with R= 0.6 jets calibrated with the EM+JES (left) and LCW (right) calibration schemes, for the central region. The shaded band shows the total uncertainty, as estimated from data and Monte Carlo studies, as described in Section 6.7.

The proper adjustment of noise thresholds may control the creation of pile-up noise clusters [191]. Preliminary estimates from dedicated Monte Carlo samples with different noise thresholds conditions and pile-up scenarios have been obtained [249].

They have shown a dependence of the jet resolution with noise thresholds (for a fixed value of $\langle\mu\rangle$) to be at most 10% (7%) for anti-k_t jets with R = 0.6 (0.4), for both the EM+JES and LCW calibrations, within the entire p_{T} range. On the other hand, the dependence of the jet resolution with $\langle\mu\rangle = 40$ has been found to be up to 50% at 50 GeV in the central region (100% at 50 GeV for the HEC-FCal transition region) for anti-k_t jets with R = 0.6, where even harsh noise thresholds do not help reduce the high luminosity effect. These results are pessimistic in the sense that they are likely to be an over-estimation, since none of the various JES corrections to mitigate pile-up effects have been applied [250]. Thus, the understanding of jet resolution in very high pile-up environments is one of the main challenges for 2012 data. It is of key importance to establish the impact of higher pile-up conditions and harsh noise thresholds on jet resolution in order to help provide the best performance for topo-clustering and LCW calibration for future physics analyses.

7

Analysis strategy

This Chapter presents the analysis strategy to search for top and bottom squarks from gluino pair production in final states with missing transverse energy and b-jets. The analysis presented in this thesis uses data collected during 2011 corresponding to a total integrated luminosity of 4.7 ± 0.2 fb^{-1}. Data collected in 2010 are not used for this analysis as they were collected using a different trigger configuration and would enlarge the dataset by only 35 pb^{-1}. An overview of the selection strategy and its key components to identify SUSY candidate events is introduced in Section 7.1. The set of requirements that are applied to define the final state objects are described in Section 7.2. The common preselection to decide whether the event and the objects therein are suitable for further analysis is presented in Section 7.3. The description of the procedures to evaluate the systematic uncertainties for both the SM background and SUSY signal processes is presented in Section 7.4 and Section 7.5, respectively. These include the systematic uncertainties depending on the luminosity and pile-up running conditions, detector effects, objects reconstruction and identification, among others (*experimental uncertainties*), and the uncertainties in the generation model (*theoretical uncertainties*). A complete description of the optimization procedure implemented to determine the best set of enriched signal regions (SR) is presented in Section 7.6. These SR allow to identify possible SUSY-like event candidates with b-jets and missing transverse energy. For this purpose, Monte Carlo simulated event samples are used in order to aid in the description of the Standard Model background processes and to model the SUSY signals. Simplified model grids have been used in the optimization of the analysis targeting different topologies, in order to obtain a general strategy without relying on benchmark models. The final event selection is summarized in Section 7.7.

7.1 Event Selection

The decays of the produced sparticles result in final states with two neutralino LSPs, which escape the ATLAS detector, and result in transverse momentum imbalance which is measured as $E_{\mathrm{T}}^{\mathrm{miss}}$ (see Section 5.7). Therefore, the observable signals for SUSY generally involve $E_{\mathrm{T}}^{\mathrm{miss}}$ accompanied with jets and leptons, where the number of these two objects depends on the specific search.

The expected SUSY-like signatures are of the form n jets + m leptons + $E_{\mathrm{T}}^{\mathrm{miss}}$, where n and m stands for the number of jets and leptons in the final state, respectively. In order to identify candidate events, a selection strategy is defined, that consists of three main steps:

- Final state object definition: reconstructed electrons, muons, jets, b-jets, and $E_{\mathrm{T}}^{\mathrm{miss}}$ fulfilling baseline quality requirements are initially identified, and hence referred to as *baseline* objects. In principle, these can fall in more than one category, being therefore effectively double-counted. For example, one isolated electron is typically reconstructed as both as an electron and as a jet. In order to avoid that an object might be identified twice, a procedure to remove overlaps between final state objects is put in place, and applied on these baseline objects, and finally those satisfying the tightest quality requirements are promoted to *signal* objects to be used in the final stage of the analysis.

- Event preselection: although several final states are targeted in the following sections of this analysis, there are common general cuts which apply to all selections. Thus, once identified the baseline objects described above, a so-called event preselection is put in place, generally driven by the trigger requirements and additional quality criteria, in order to decide whether the event and the objects therein are suitable for further analysis.

- Final event selection: in addition to the preselection criteria, a number of selection cuts are further applied to significantly reduce the different SM backgrounds. The signal objects are used to determine whether candidate events satisfy the requirements defined by so-called signal-enriched regions (SR). These have been determined by using a rigorous optimization to fully exploit the possibilities of this search given the integrated luminosity recorded by ATLAS. The optimization procedure is explained in Section 7.6, where a set of SRs with best sensitivity for new physics scenarios involving gluino pair production with subsequent decays to final states with heavy flavour jets and $E_{\mathrm{T}}^{\mathrm{miss}}$ are defined.

7.2 Final state object definition

The set of requirements that are applied for the definition of baseline and signal final state objects is presented in this section.

Electron definition: Electrons are reconstructed by the cluster-based algorithm and pre-selected using the Medium++ definition[1] with $E_{\mathrm{T}} = E^{\mathrm{clust}}/\cosh\eta > 20$ GeV. Within this definition, η corresponds to η^{track} if the track contains at least 4 silicon hits, and η^{clust} otherwise. Furthermore, only electrons with $|\eta^{\mathrm{clust}}|$ <2.47 are kept. In addition, signal electrons are required to be flagged as Tight++, to have $E_{\mathrm{T}} = E^{\mathrm{clust}}/\cosh\eta > 25$ GeV, in order to meet the plateau of the single electron trigger, and to have an isolation requirement: the total transverse momentum of tracks in a cone of $\Delta R = 0.2$ around the candidate electron divided by the electron transverse momentum has to be smaller than 0.1.

Electrons reconstructed in any of the problematic calorimeter regions are rejected both in data and MC. Baseline electrons are used to perform the overlap removal between jets and leptons and to veto events with leptons in the 0-lepton selection. Additional smearing factors are applied to reconstructed electrons in the MC such as to reproduce the electron scale resolution measured in data. Scale factors have also been applied to MC events in order to take into account discrepancies between data and MC in the electron reconstruction and identification efficiencies.

Muon definition: Muons are reconstructed combining the inner detector and the muon spectrometer information using the `STACO` algorithm. To recover efficiency in the regions $|\eta| \approx 0$ and $|\eta| \approx 1.2$ segment-tagged muons are also used. Muons satisfying the loose criteria and required to have $p_{\mathrm{T}} > 10$ GeV and $|\eta| < 2.4$ are pre-selected for the analysis. In addition, the following quality cuts on the tracks are applied:

- At least one hit in the *b*-layer (if expected);
- At least one hit in any pixel layer;
- At least 6 SCT hits;
- The sum of the holes[2] in the pixel and the SCT should be less than 3;
- A successful TRT-Extension where expected (i.e. within the acceptance of the TRT). An unsuccessful extension corresponds to either no TRT hit associated,

[1] Re-optimised selection criteria provide three additional operating points (loose++, medium++, tight++) with improved performance over the standard criteria for a higher pile-up environment.

[2] A hole is an expected measurement given the track trajectory that has not been assigned to the track.

or a set of TRT hits associated as outliers (see Section 4.2.3). For $|\eta| < 1.9$ muons are required to have $N_{trt} = N_{trt}^{hits} + N_{trt}^{outliers} > 5$. For $|\eta| \geqslant 1.9$, tracks with $N_{trt} > 5$ should satisfy $N_{trt}^{outliers} < 0.9 * N_{trt}$ (N_{trt}^{hits} is the number of hits in the TRT associated to the track and $N_{trt}^{outliers}$ is the number of TRT outliers on the muon track);

Events containing any baseline muon are rejected in the 0-lepton channel selection. In addition to the preselection cuts, signal muons are selected in the 1 lepton channel if they have a $p_{\mathrm{T}} > 20$ GeV and if the total transverse momentum of tracks reconstructed in a cone of size $\Delta R = 0.2$ around the muon does not exceed 1.8 GeV (excluding the muon itself). To take into account the imperfect muon p_{T} resolution predicted by the MC with respect to that measured in data (Figure 5.2), an additional smearing of the muon p_{T} is applied. Scale factors have been applied to MC events in order to take into account discrepancies between data and MC in the muon reconstruction and identification efficiencies.

Jet definition: Jets are defined as those reconstructed by the anti-k_t algorithm with distance parameter R = 0.4 using topological clusters as inputs (`AntiKt4Topo`), and they are calibrated using the EMJES scheme. Jets are kept only if they have p_{T} >20 GeV and $|\eta| < 2.8$.

***b*-tagging definition:** The tagging of b-quark initiated jets is done using the `MV1` algorithm. Three different operating points are used in this analysis: those corresponding to 60%, 70% and 75% efficiency. Table 7.1 summarises the nominal b-tagging efficiency (computed on $t\bar{t}$ MC events) for jets with $p_T > 15$ GeV and $|\eta| < 2.5$ as well as the light quarks, c-quarks and τ leptons rejection factors for each opertaing point. The b-tagging efficiencies and their uncertainties have been determined as introduced in Section 5.6. A scale factor ($SF_{Flavour}$) is then defined as the ratio between the efficiency in data and in simulation, for b-jets, light jets and c-jets. The calculated scale factors are used to determine a weight value to apply to each jet in an event with $p_{\mathrm{T}} > 20$ GeV and $|\eta|$ <2.5 and subsequently a weight for the event as a whole. These weights correct the tagging rate in MC to that in data. They are obtained for the individual jets in two distinct ways. Firstly if the jet is tagged, the weight is given by:

$$w_{jet} = SF_{Flavour}(p_{\mathrm{T}})$$

whereas if the jet is not tagged, the weight is given by:

$$w_{jet} = \frac{1 - \epsilon^{data}_{Flavour}(p_{\mathrm{T}})}{1 - \epsilon^{MC}_{Flavour}(p_{\mathrm{T}})} = \frac{1 - SF_{Flavour}(p_{\mathrm{T}})\epsilon^{MC}_{Flavour}}{1 - \epsilon^{MC}_{Flavour}(p_{\mathrm{T}})}$$

The weight applied to the whole event is obtained by the product of all the weights of the individual jets in that event.

$$w_{event} = \prod_{jet} w_{jet}$$

The event weight w_{event} is included in all the MC estimations of event yields in the rest of the analysis. The scale factors are determined independently for b-jets, c-jets and light jets and their uncertainties are uncorrelated. Therefore the b-tagging uncertainty is calculated separately for each kind of jet and the final systematic uncertainty due to the b-tagging is obtained by summing these 3 uncertainties in quadrature. The τ jets are only partially supported and the uncertainty on their scale factors are treated as fully correlated with c-jets scale factors. In the following, only b-tagged jets with $p_{\mathrm{T}} > 30$ GeV will be identified as b-jets.

Operating point	b-jet efficiency	light RF	c RF	τ RF
60%	0.596	635	8	27
70%	0.696	134	5	13
75%	0.746	58	4	9

Table 7.1 Nominal b-tagging efficiency for jets with $p_T > 15$ GeV and $|\eta| < 2.5$ as well as the light quarks, c-quarks and τ leptons rejection factor (RF) for different opertaing points.

Overlap removal procedure: According to the above definitions, one single final state object can fall in more than one category, being therefore effectively double-counted. For example, one isolated electron is typically reconstructed both as an electron and as a jet. Therefore, a procedure to remove overlaps between final state objects is implemented, and applied on baseline objects for both 0 and 1 lepton selections. A spatial isolation $\Delta R = \sqrt{(\Delta\phi)^2 + (\Delta\eta)^2}$ is measured between baseline objects. The overlap removal criteria is defined as follows:

1. First, jets that are angularly close to a baseline electron, within $\Delta R(j, e) < 0.2$, are removed from the jet list in the event, and the object is regarded as an electron.

2. Then, baseline electrons within ($\Delta R < 0.4$) to the closest jet are removed from the electron list. Since jets are reconstructed with the distance parameter of R = 0.4, that electron is accounted in the original jet.

3. Similarly, baseline muons are rejected if their distance to the closest jet is $\Delta R < 0.4$. Even if a muon is close to a jet, the muon deposits only a small

amount of energy in the calorimeter. The removed muon is not counted as an isolated muon candidate but its momentum is included in the $E_{\mathrm{T}}^{\mathrm{miss}}$ calculation, as introduced next.

$E_{\mathrm{T}}^{\mathrm{miss}}$ definition: The $E_{\mathrm{T}}^{\mathrm{miss}}$ is calculated with an algorithm based on the vectorial sum of the transverse momenta of jets, muons, electrons and topological clusters not assigned to any reconstructed objects, dubbed `SimplifiedRefFinal`. The $E_{\mathrm{T}}^{\mathrm{miss}}$ is calculated as introduced in Section 5.7. Jets with $p_T > 20$ GeV at the jet energy scale and covering the whole η range are included. The muons term includes all baseline muons before the overlap removal. Contribution from electrons includes those passing the medium criteria, with $p_T > 20$ GeV and before the overlap removal. The cell-out term is calculated from topological clusters at the electromagnetic scale which are not included in any reconstructed objetct.

7.3 Event preselection

The common preselection to decide whether the event and the objects therein are suitable for further analysis is presented in this section.

7.3.1 Data quality

Each data taking period in ATLAS is commonly dubbed a run, which is subdivided into luminosity blocks (LB) of about two minutes worth of data-taking, where the instantaneous luminosity is approximately constant. The status of each sub-detector, trigger and reconstructed physics object in ATLAS is continuously assessed by inspection of a standard set of distributions, and data-quality flags (DQ) are recorded in a conditions database in units of these LBs. The DQ are used to build the so-called Good Run Lists (GLRs) to identify the LB suitable for each physics analysis within a run. The analysis presented in this thesis only considers events satisfying the GRL defined by the SUSY Working Group, that takes into account data-quality criteria for the Inner Detector, Calorimeter and Muon Spectrometer, as well as the reconstructed objects mentioned in Chapter 5.

7.3.2 Trigger selection and efficiency

Data events are initially taken from the so-called `JetTauEtMiss`, `Egamma` and `Muons` streams, i.e, those containing signatures of jets, $E_{\mathrm{T}}^{\mathrm{miss}}$, electrons and muons, respectively, and required to satisfy the SUSY GRLs. The events are then selected using a set of trigger items based on the decision made by the EF (Section 4.2.7). The unprescaled trigger items used for each data period are summarized in Table 7.2. Further information can be found at [251].

A selection with no lepton in the final state relies on a trigger based on jets and $E_{\mathrm{T}}^{\mathrm{miss}}$. Due to the large QCD cross section, the jet trigger threshold for unprescaled triggers was continuously enhanced with increasing instantaneous luminosity during the 2011 data taking. The trigger item chosen for a zero lepton analysis is dubbed `EF_j75_a4_EFFS_xe45_loose_noMu`. Here, the nomenclature stands for a trigger that performs a full scan of the event at the EF stage (`EFFS`), for all jets reconstructed from topological clusters in the calorimeter using an anti-k_t algorithm with a distance parameter R = 0.4 (`a4`). It requires at least one of these jets with a $p_{\mathrm{T}} > 75$ GeV and $E_{\mathrm{T}}^{\mathrm{miss}} > 45$ GeV at the electromagnetic scale, where the objects required for the $E_{\mathrm{T}}^{\mathrm{miss}}$ calculation are identified through the loose criteria without including the contribution of muons at this stage (`loose_noMu`). Offline cuts on jet transverse momenta are applied to ensure that the jet trigger efficiency is in the plateau, to avoid a systematic uncertainty connected with the trigger turn-on curve possibly being not well reproduced by the Monte Carlo simulation. For `EF_j75_a4_EFFS_xe45_loose_noMu`, the minimum offline cuts required on the $E_{\mathrm{T}}^{\mathrm{miss}}$ and the leading jet p_{T} to operate above 99 % efficiency are 130 GeV for both. Muons from QCD multi-jet process are removed due to overlap with jets and not considered in the offline $E_{\mathrm{T}}^{\mathrm{miss}}$ calculation. On the other hand, isolated muons coming from the W boson decay are considered in the offline $E_{\mathrm{T}}^{\mathrm{miss}}$ calculation. Figure 7.1 shows the turn-on curve for the 0-lepton trigger `EF_j75_a4tc_EFFS_xe45_loose_noMu` with respect to a reference trigger dubbed `EF_j75_a4tc_EFFS` after requiring at least one leading jet with transverse momentum greater than 130 GeV in order to be in the plateau of such reference trigger [251]. Good agreement is shown between data and $t\bar{t}$ Monte Carlo simulation. The trigger `EF_j75_a4tc_EFFS_xe45_loose_noMu` was prescaled for Period L onwards, and therefore a new unprescaled item with a higher threshold for $E_{\mathrm{T}}^{\mathrm{miss}}$ was implemented: `EF_j75_a4_EFFS_xe55_loose_noMu`, where the minimum offline cuts required on the $E_{\mathrm{T}}^{\mathrm{miss}}$ and the leading jet p_{T} to operate above 99 % efficiency are 160 GeV and 130 GeV, respectively. No trigger requirement was used for Monte Carlo simulations in the zero-lepton selection.

Events containing one lepton (electron or muon) in the final state are triggered using also the decision made by the EF. The single electron trigger `EF_e20_medium` has been used at the beginning of 2011. The item requires an electron satisfying the medium criteria and a transverse momentum threshold of $p_{\mathrm{T}}^{\mathrm{EF}}$ >20 GeV. Due to the increasing instantaneous luminosity, a migration to a new unprescaled item took place from period D to J: `EF_e22_medium`, requiring $p_{\mathrm{T}}^{\mathrm{EF}} > 22$ GeV. A tighter selection was applied for Period K onwards. This approach implemented a cut on the hadronic core isolation of ≤ 1 GeV at L1, and the trigger item is dubbed `EF_e22vh_medium1`. Due to the implementation of a fixed energy cut, some inefficiencies for $p_{\mathrm{T}} > 300$ GeV are originated. In order to recover the losses at such high p_{T}, the previous item is complemented with an extra item so-called `EF_e45_medium`, with a higher electron $p_{\mathrm{T}}^{\mathrm{EF}}$ threshold (45 GeV), for Period K onwards.

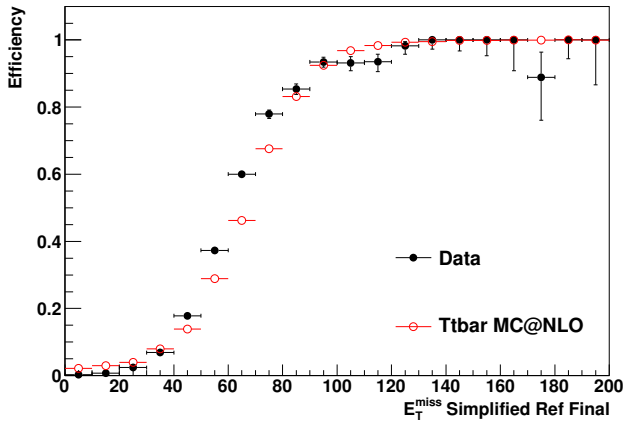

Figure 7.1 The 0-lepton trigger `EF_j75_a4tc_EFFS_xe45_loose_noMu` turn-on curve shown for data and $t\bar{t}$ Monte Carlo simulation, as measured with respect to `EF_j75_a4tc_EFFS` after requiring at least one leading jet with transverse momentum greater than 130 GeV in order to be in the plateau of the `EF_j75_a4tc_EFFS` reference trigger. Good agreement is shown between data and $t\bar{t}$ Monte Carlo simulation. The minimum offline cuts required on the $E_{\mathrm{T}}^{\mathrm{miss}}$ and the leading jet p_{T} to operate above 99 % efficiency are 130 GeV for both.

In order to trigger on events containing a muon, the item chosen from Period B to I requires a muon $p_{\mathrm{T}}^{\mathrm{L1}}$ and $p_{\mathrm{T}}^{\mathrm{EF}}$ above 10 GeV and 18 GeV, respectively. This item is referred to as `EF_mu18`. Due to the increase of the luminosity, this trigger is prescaled from period J onwards. Therefore, for these periods the `EF_mu18_L1J10` item is used instead. This trigger requires one additional jet with $p_{\mathrm{T}}^{\mathrm{L1}} > 10$ GeV to be present in the event, whereas the muon transverse momentum threshold is the same as for `EF_mu18`. The item is fully efficient for events with muon $p_{\mathrm{T}} > 20$ GeV and jet $p_{\mathrm{T}} > 60$ GeV, as calculated offline.

Period	JetEtMiss	Egamma	Muons
B	`EF_j75_a4_EFFS_xe45_loose_noMu`	`EF_e20_medium`	`EF_mu18`
D - I	`EF_j75_a4tc_EFFS_xe45_loose_noMu`	`EF_e22_medium`	`EF_mu18`
J	`EF_j75_a4tc_EFFS_xe45_loose_noMu`	`EF_e22_medium`	`EF_mu18_L1J10`
K	`EF_j75_a4tc_EFFS_xe45_loose_noMu`	`EF_e22vh_medium1`	`EF_mu18_L1J10`
L - M	`EF_j75_a4tc_EFFS_xe55_noMu`	`EF_e22vh_medium1`	`EF_mu18_L1J10`

Table 7.2 Trigger chains used for each data period.

7.3.3 Vertex selection

The primary vertex is required to be consistent with the beamspot envelope and to have at least five tracks with certain quality cuts (as discussed in Section 5.2), otherwise the event is rejected. When more than one such vertex is found, the vertex with the largest summed $|p_{\mathrm{T}}|^2$ of the associated tracks is chosen.

7.3.4 LAr hole veto

A problem in the LAr EM calorimeter took place on 30$^{\mathrm{th}}$ April, 2011, when the readout failed on six front-end boards located in the second and the third layers of the calorimeter. Thus, a rectangular region in $\eta - \phi$, of $0.0 < |\eta| < 1.45$ and $-0.788 < \phi - 0.592$, was not functional anymore. Although during the technical stop in summer of 2011, the problematic boards were replaced and the calorimeter performance was almost recovered, an integrated luminosity of 877 pb^{-1} was affected by this failure.

The electron reconstruction efficiency is impacted most by this problem. The MC does not take into account this "dead" calorimeter region. In order to treat both data and MC samples consistently, if an electron falls in this detector region, the electron is removed from the analysis in all data and MC samples.

The effect on the jet reconstruction is smaller than on electrons due to their larger area, but still there exists possible mis-measurement of the jet energy, which may cause fake missing energy. Therefore, the so-called "smart" LAr Hole veto has been used to mitigate any effect that can affect the data/MC comparison. The principle is to veto events containing a jet with p_T greater than 20 GeV pointing to the LAr Hole region (defined as $-0.1 < \eta < 1.5$, $-0.9 < \phi < -0.5$), and contributing significantly to the $E_{\mathrm{T}}^{\mathrm{miss}}$. The energy contribution of a jet to the $E_{\mathrm{T}}^{\mathrm{miss}}$ is estimated as follows:

$$E_{\mathrm{T}}^{\mathrm{miss}}(\mathrm{jet}) = p_{\mathrm{T}}^{\mathrm{jet}} \frac{1 - C_{cell}}{1 - C_{jet}} - p_{\mathrm{T}}^{\mathrm{jet}} \ , \tag{7.1}$$

where C_{cell} and C_{jets} are the correction factors that estimate the jet energy which is not measured in dead cells of the calorimeter. C_{cell} implements two-dimensional information of neighboring cells, from which the average energy density is calculated. Thus, the missing energy in the bad cell is estimated by extrapolating the energy density. C_{jets} assumes a jet profile, which gives the energy deposit distribution around the center of the jet. The profile is obtained from the MC simulation and parametrized as a function of jet p_{T}, jet η, calorimeter types and layers. Thus, the energy expected to be in the dead calorimeter region is calculated.

The $E_{\mathrm{T}}^{\mathrm{miss}}(\mathrm{jet})$ contribution is then projected on the direction of the whole $E_{\mathrm{T}}^{\mathrm{miss}}$ to quantify its impact:

$$\Delta E_T^{miss}(\mathrm{jet}) = E_{\mathrm{T}}^{\mathrm{miss}} \cos \Delta\phi(\mathrm{jet}, E_{\mathrm{T}}^{\mathrm{miss}}) \ . \tag{7.2}$$

Then, the event is vetoed if $\Delta E_{\mathrm{T}}^{\mathrm{miss}}$(jet) is greater than 10% of the whole $E_{\mathrm{T}}^{\mathrm{miss}}$.

7.3.5 Jet cleaning

Fake jets can arise from non-collision background or cosmic events with a catastrophic muon energy loss in the calorimeters or from fake signals in the calorimeter, arising either from noise bursts or the presence of coherent noise. A set of cuts having a high rejection against fake jets while preserving an efficiency close to 100% for signal jets has been designed. The selection criteria are based on the timing of the calorimeter signal with respect to that of the bunch crossing, on the quality of the fit on the calorimeter pulse shape, on the fraction of jet energy belonging to specific calorimeter samples and on the amount of jet charged energy fraction (as measured in the ID). The selections are summarised at [252]. Events are rejected if any of the jets with $p_{\mathrm{T}} > 20$ GeV (after removing overlapping objects as described in Section 7.2) satisfies the `VeryLooseBad` jet definition.

A further selection is applied on the signal jets for the 0-lepton channels to further reject spurious jet signals. If any of the selected n signal jets is central ($|\eta| < 2$) and its charged p_{T} fraction (denoted *chf*, and defined as the ratio between the sum of the p_{T} of all tracks associated to the jet and the jet p_{T}) is smaller than 2%, the event is rejected.

7.3.6 Cosmic cleaning

Events containing cosmic muons are rejected by requiring that any muon after the overlap removal has a transverse (longitudinal) impact parameter with respect to the primary vertex lower than 0.2 (1) mm. Events containing muons which do not satisfy this criteria are vetoed.

7.3.7 Bad muons cleaning

Fake muons, which can be reconstructed from high hit multiplicities in the muon spectrometer due to very energetic punch through jets, are a potential source of fake $E_{\mathrm{T}}^{\mathrm{miss}}$. Events containing such bad muons are rejected by vetoing any events where a baseline muon, before overlap removal, satisfies $\sigma(\frac{1}{p})/|\frac{1}{p}| > 0.2$, with p the momentum of the muon.

7.3.8 Lepton selection

Events with no leptons (electron or muon) reconstructed according to the preselection criteria mentioned in Section 7.2 are used for 0-lepton selection. The 1-lepton selection makes use of the additional tight lepton selection criteria. Only events with

exactly one selected electron (or muon) are used. Events with more than one lepton are not included in the analysis presented in this thesis.

7.4 Systematic uncertainties on the background

The description of the procedures to evaluate the systematic uncertainties common to all processes is discussed next. The systematic uncertainties depending on the luminosity and pile-up running conditions, detector effects, objects reconstruction and identification, among others, are labelled as *experimental uncertainties*, whereas the uncertainties in the generation model are labelled as *theoretical uncertainties*.

7.4.1 Experimental uncertainties

The dominant detector-related systematic effects are due to the jet energy scale (JES) and resolution (JER) uncertainties, and the uncertainty on the b-tagging efficiency and mistag rates. The JES uncertainty is derived from a combination of simulations, test beam data and in-situ measurements (see Section 5.5.3), and includes additional uncertainties due to the jet flavour and nearby jets. Uncertainties on the JER are obtained with an in-situ measurement, as discussed in Chapter 6. These uncertainties on jets are propagated to the $E_{\mathrm{T}}^{\mathrm{miss}}$ measurement, and additional uncertainties on $E_{\mathrm{T}}^{\mathrm{miss}}$ arising from energy deposits not associated with any reconstructed objects are also included. The b-tagging uncertainty is evaluated by varying the η-, p_{T}- and flavour-dependent scale factors applied to each jet in the simulation within a range that reflects the systematic uncertainty on the measured tagging efficiency and mistag rates. The different sources of experimental uncertainties considered in this analysis are presented next.

Luminosity: an uncertainty of 3.7% on the integrated luminosity is assumed, as discussed in Section 4.2.9. Further information can be found in Ref. [160, 163].

Pile-up: the MC events considered have been simulated with variable in-time pile-up rate configurations to match as closely as possible the different running conditions at the LHC during 2011. In addition, out-of-time pile-up corresponding to a bunch spacing of 50 ns is also taken into account. The MC simulated events have been reweighted on an event-by-event basis using a pile-up reweighting procedure to match the measured mean number of interaction per bunch crossing, $\langle\mu\rangle$, in data.

Jet Energy Scale: the jet energy is varied up and down (in a fully correlated way) by an amount corresponding to a $\pm 1\sigma$ uncertainty on the JES, using a tool

provided by the Jet/EtMiss Working Group [206, 253]. This tool returns a relative uncertainty on the jet energy scale, which is the sum in quadrature of three components dependent on:

1. the p_{T} and η of the jet,

2. the ΔR of the closest jet,

3. the average quark-gluon composition of the sample.

Additional pile-up related uncertainties have been added to the jet energy scale uncertainty to take into account the fact that the simulation of the calorimeter energy deposit associated to minimum bias event is not perfectly reproduced by the MC [206]. Thus, an additional pile-up related uncertainty on the jet energy scale has been added in quadrature to that provided by the three items above, as recommended by the Jet/EtMiss WG. Finally, an uncertainty of 2.5% was added to jets that are b-tagged to account for differences in energy scale between light and heavy flavour jets.

Jet Energy Resolution: in order to account for a possible underestimate of the jet energy resolution in the MC simulation, an over p_{T} smearing is added to the jets based on their p_{T} and η. Each jet is smeared according to a Gaussian distribution, with unit mean, and a width given by a p_{T} and η dependent resolution function. When evaluating the impact of the jet energy resolution systematic, the event yields obtained using the nominal jets are compared with the results obtained using jets whose p_{T} has been smeared by the Gaussian function described. The jet energy resolution is discussed in detail in Chapter 6.

Missing transverse momentum: the jet four-vectors are scaled according to the uncertainty and the $E_{\mathrm{T}}^{\mathrm{miss}}$ is recomputed taking into account the new jet energy scale:

$$\vec{\mathbf{E}}_{\mathrm{T}}^{\mathrm{miss,(up,down)}} = \vec{\mathbf{E}}_{\mathrm{T}}^{\mathrm{miss}} + \sum_{j} \vec{\mathbf{p}}_{\mathrm{T}j} - \sum_{j} \vec{\mathbf{p}}_{\mathrm{T}j}^{\mathrm{(up,down)}}$$

where $\vec{\mathbf{p}}_{\mathrm{T}j}$ is the vectorial transverse momentum of the jet j and $\sum_j \vec{\mathbf{p}}_{\mathrm{T}j}^{\mathrm{(up,down)}}$ is the rescaled one. The uncertainty related to the $E_{\mathrm{T}}^{\mathrm{miss}}$ term that adds the transverse energy of the clusters that are not part of a jet (referred to as CellOut in the following) was evaluated by varying the EM-scale energy of those clusters by a p_{T}- and η-dependent correction of order 5-10% [254]. The uncertainty was evaluated to be $< 2\%$. The impact of the cluster energy uncertainties on the reconstructed $E_{\mathrm{T}}^{\mathrm{miss}}$ due to pile-up is estimated using a tool provided by the Jet/EtMiss WG and found to be negligible.

b-tagging efficiency: the systematic uncertainties on the efficiencies (and hence the scale factors described in Section 7.2), are taken into account in the analysis. The uncertainty on the jet weight and event weight is calculated propagating the estimated uncertainties on the scale factors. The estimation of the b-tagging impact on the final uncertainty on the event yield is obtained rerunning the analysis on MC events and assuming a $\pm\sigma$ variation of the event weight. The uncertainty on the c-jets scale factors is doubled with respect to that on the b-jets, as recommended by the Flavour Tagging WG.

Lepton identification and energy scale: the uncertainties on leptons identification efficiency, energy scale and energy resolution are also taken into account. Scale factors that correct the lepton identification efficiency in MC to that measured in $Z \to \ell\ell$ events are provided by the eGamma and Muon WG. None of the scale factors differs from 1 by more than 3%. The lepton energy scale and resolution are also known with an uncertainty within the same order of magnitude. For a 0-lepton selection, these uncertainties must be taken into account because of the lepton veto applied. No scale factor is used for such selection, but a conservative 3% systematic uncertainty is assumed. The impact on the final event yield is evaluated by shifting all leptons up and down in momentum by 3% before the lepton veto. The effect is found to be smaller than 1% and therefore neglected.

QCD multijet uncertainties: the estimate of the QCD multi-jet background exploits a data driven technique discussed in Section 8.1, with its respective uncertainties.

7.4.2 Theoretical uncertainties

The theoretical uncertainties on the Monte Carlo used for each of the backgrounds are listed in this Section. Given the high-multiplicity of b-jets required in the final states, the top pair production is expected to be the dominant background. Thus, in most cases, the uncertainties used are essentially those recommended by the Top WG, and they are summarized next.

Top pair production uncertainties:

- Cross section: the theoretical cross section of $\sigma_{t\bar{t}} = 166.8^{+16.5}_{-17.8}$ is used for the top pair production, and its uncertainty is accounted as an additional systematic.
- Finite number of generated ME partons: the $t\bar{t} + n$ jets `ALPGEN` MC samples have been generated with 2 configurations:
  - First configuration: up to 3 extra partons from the ME,

– Second configuration: up to 5 extra partons from the ME,

where the highest jet multiplicity Monte Carlo sample is inclusive in both configurations. The uncertainty due to the finite number of additional partons at the matrix-element level is assessed by comparing the event yields obtained separately for each configuration.

- Theoretical scales: the uncertainty due to the factorisation and matching scale chosen in `ALPGEN` (denoted "ktfac" and "qfac", respectively) are estimated by independently varying their nominal settings up and down by factors of one half and two, separately.

- Monte Carlo generator: this uncertainty is estimated by comparing the leading-order `ALPGEN` generator to the next-to-leading-order `MC@NLO` generator, and the uncertainty is assessed by comparing the event yields obtained separately for each of them.

- PDF: the uncertainties on the PDFs are estimated from the MSTW2008NNLO sets [80,131], which provide five different values of α_s, by varying the standard value α_s^0 in MSTW ($\alpha_s(M_Z) = 0.12018$) in terms of $\pm 0.5\sigma$ and $\pm\sigma$, where σ is the 68% confidence level uncertainty on α_s^0.

For $t\bar{t} + b\bar{b}$ samples, a conservative uncertainty of 100% has been assigned to the cross-section, whereas for $t\bar{t} + W/Z$ events, an uncertainty of 55% on the cross-section is imposed, with an additional uncertainty of 50% on the scaling factors for each process.

Single top production uncertainties:

- Cross section: the theoretical cross section for the different single top production channels are $\sigma^{t-chan} = 64.57^{+3.32}_{-2.32}$ pb, $\sigma^{s-chan} = 4.63^{+0.29}_{-0.27}$ pb and $\sigma^{Wt} = 15.34^{+1.34}_{-1.36}$ pb. Since the Wt production channel is found to be dominant in the signal regions, a total systematic uncertainty of 8% is assigned to the single top production cross section.

- Monte Carlo generator: the default `MC@NLO` is compared to `AcerMC` [255].

- Parton shower: `AcerMC` samples with different PS content are used. The uncertainty is taken from the maximum difference between the estimate yields obtained with these enriched/depleted PS `AcerMC` samples, and the nominal `MC@NLO` Monte Carlo.

W+jets production uncertainties:

- W+jets normalization: for $W+N$ parton production processes, an uncertainty of $\sqrt{N} \times 0.24$ per additional parton is added in quadrature, and uncertainties for different values of partons are treated as uncorrelated.
- W+jets shape: the uncertainty connected with the change of `ALPGEN` parameters that can affect the shape of the distributions has been studied by varying the factorisation and renormalisation scales, both up and down (separately). Parton level samples generated with different `ALPGEN` settings are also available and have been used to cross check the results.
- W+heavy-flavour jets uncertainty: scaling factors of 1.63 ± 0.76 and 1.11 ± 0.35 are added to the Wbb/Wcc and Wc respectively to account for the measured cross section of b-jets in W events [256].

Z+jets production uncertainties:

- Z+jets normalization: the same recipe as for W+jets normalization is used.
- Z+heavy-flavour jets uncertainty: the production cross section of b-jets in Z events is in agreement with the theoretical prediction [257], so no rescaling factor is applied. An uncertainty of 100% is assumed.

7.5 Systematic uncertainties on the signal

Different sources of systematic uncertainty are considered on the SUSY signal efficiencies and yields, where large variations are expected depending on the SUSY scenario and selections. For each of the signal samples, the impact of the uncertainties is estimated after the signal region cuts (as defined in Section 7.7). The experimental uncertainties are estimated using the same tools employed for the SM background estimation reported in Section 7.4, whereas the theoretical uncertainties specific for the SUSY signals are calculated using a common procedure stated by the SUSY WG, which follows closely the PDF4LHC recommendations [258]. Starting from the default values, denoted as CTEQ^0 and MSTW^0, the procedure consists in:

- Vary CTEQ PDFs
- Vary MSTW PDFs
- Vary renormalization/factorization scale with CTEQ central value PDF
- Vary renormalization/factorization scale with MSTW central value PDF
- Vary strong coupling using CTEQ PDFs.

Thus, one obtains asymmetric PDF uncertainties for CTEQ and MSTW, asymmetric scale uncertainties for both CTEQ and MSTW central value PDF, and an asymmetric strong coupling uncertainty. From these variations, four values are computed:

$$\Delta^{\mathrm{UP}}_{\mathrm{CTEQ}} = \sqrt{[\Delta^{\mathrm{UP}}_{\mathrm{CTEQ}}(\mathrm{PDF})]^2 + [\Delta^{\mathrm{UP}}_{\mathrm{CTEQ}}(\mathrm{SCALE})]^2 + [\Delta^{\mathrm{UP}}_{\mathrm{CTEQ}}(\alpha_s)]^2} \tag{7.3}$$

$$\Delta^{\mathrm{DOWN}}_{\mathrm{CTEQ}} = \sqrt{[\Delta^{\mathrm{DOWN}}_{\mathrm{CTEQ}}(\mathrm{PDF})]^2 + [\Delta^{\mathrm{DOWN}}_{\mathrm{CTEQ}}(\mathrm{SCALE})]^2 + [\Delta^{\mathrm{DOWN}}_{\mathrm{CTEQ}}(\alpha_s)]^2} \tag{7.4}$$

$$\Delta^{\mathrm{UP}}_{\mathrm{MSTW}} = \sqrt{[\Delta^{\mathrm{UP}}_{\mathrm{MSTW}}(\mathrm{PDF})]^2 + [\Delta^{\mathrm{UP}}_{\mathrm{MSTW}}(\mathrm{SCALE})]^2} \tag{7.5}$$

$$\Delta^{\mathrm{DOWN}}_{\mathrm{MSTW}} = \sqrt{[\Delta^{\mathrm{DOWN}}_{\mathrm{MSTW}}(\mathrm{PDF})]^2 + [\Delta^{\mathrm{DOWN}}_{\mathrm{MSTW}}(\mathrm{SCALE})]^2} \tag{7.6}$$

which are used to calculate two quantities, denoted A and B, as:

$$A = \max(\mathrm{CTEQ}^0 + \Delta^{\mathrm{UP}}_{\mathrm{CTEQ}}, \mathrm{MSTW}^0 + \Delta^{\mathrm{UP}}_{\mathrm{MSTW}}) \ , \tag{7.7}$$

$$B = \min(\mathrm{CTEQ}^0 - \Delta^{\mathrm{DOWN}}_{\mathrm{CTEQ}}, \mathrm{MSTW}^0 - \Delta^{\mathrm{DOWN}}_{\mathrm{MSTW}}) \ . \tag{7.8}$$

Then, the best value for the cross-section is calculated as

$$\sigma^{\mathrm{best}} = 0.5 \times (A + B) \ , \tag{7.9}$$

and the symmetric uncertainty on this cross-section is obtained as

$$\frac{\Delta\sigma^{\mathrm{best}}}{\sigma^{\mathrm{best}}} = \frac{A - B}{A + B} \ . \tag{7.10}$$

7.6 Optimization of event selection

Heavy flavor final states are suggested as one of the most favored scenarios for physics beyond the Standard Model at the LHC given the limits imposed to BSM searches during the 2011 Summer conferences [15]. While searches with 1 and 2 b-tagged jets were done in the past [142, 144], a 3 b-tagged jets analysis is expected to be very promising for these final states given the amount of recorded data by the ATLAS experiment during 2011.

For each mass point in each heavy flavour topology (Section 2.7), there are one or more sets of cuts on kinematic quantities which result in the optimum balance between signal acceptance and background rejection, typically quantified by the significance $\mathcal{S}$ [149], defined as

$$\mathcal{S} = \frac{\mathrm{Signal}}{\sqrt{(\sqrt{B})^2 + (\Delta B)^2_{\mathrm{syst(exp)}} + (\Delta B)^2_{\mathrm{syst(theo)}}}} \ . \tag{7.11}$$

For maximum sensitivity, one would ideally run infinitely many analyses, each tuned to a specific mass point. Practically, this is impossible, and thus the goal becomes to find a few sets of selection which, while not strictly optimum, are close enough to optimum for a large enough region of mass points to provide sufficient sensitivity. These signal-enriched regions within the phase-space of parameters are simply referred to as signal regions in the following.

The signal regions are primarily targeted at new physics scenarios involving gluino pair production with subsequent decays to final states with heavy flavour jets and $E_{\mathrm{T}}^{\mathrm{miss}}$. In order to obtain a general strategy, simplified model grids have been used in the optimization of the analysis, and divided in three different topologies as introduced in Section 2.7:

- Gbb ($\tilde{g} \to b\bar{b} + \tilde{\chi}^0$)
- Gtb ($\tilde{g} \to t\bar{b} + \tilde{\chi}^0$ via chargino)
- Gtt ($\tilde{g} \to t\bar{t} + \tilde{\chi}^0$) .

These models assume a very heavy squark mass spectrum and thus describe only a single production process and final state. In addition, the 3rd-generation squarks are assumed to be significantly lighter than the 1st and 2nd-generation squarks. The main kinematic features of these topologies are discussed next.

7.6.1 Kinematic studies with heavy flavor Simplified Models

One of the main characteristics of the simplified models is the small number of parameters that determine the main kinematic features. In the models considered in this work, the difference between the mass of the pair produced particle and the LSP (the "mass-splitting") largely determines the kinematic properties of the decay, while the mass of the pair produced particle alone determines the production cross-section. These features were studied for various kinematic variables, such as p_{T}, $E_{\mathrm{T}}^{\mathrm{miss}}$ and overall energy sum in the event $\mathrm{m_{eff}}$, among others. In this work, $\mathrm{m_{eff}}$ is defined as the scalar sum of the p_{T} of the n jets selected in the analysis, the $E_{\mathrm{T}}^{\mathrm{miss}}$ and, if any, the isolated leptons:

$$\mathrm{m_{eff}} = \sum_{i \leq n} (p_{\mathrm{T}}{}^{\mathrm{jet}})_i + E_{\mathrm{T}}^{\mathrm{miss}} + \sum_{j \leq m} (p_{\mathrm{T}}{}^{\mathrm{lep}})_j \ . \tag{7.12}$$

Within each topology, the distributions for samples with constant mass-splitting and constant gluino mass were compared. Figure 7.2 presents the distributions of the first- and second-leading jet p_{T} (top and bottom, respectively) for events with the Gbb topology, where it can be clearly observed the effect of constant (left) and varying mass-splitting (right) between the pair produced gluino and the LSP. The same behaviour is observed for $E_{\mathrm{T}}^{\mathrm{miss}}$ and $\mathrm{m_{eff}}$, as shown in Figure 7.3. Overall,

for each kinematic variable studied, it was observed that samples with the same mass-splitting have very similar kinematic distributions. However, the distributions differ significantly for samples within a specific topology with the same gluino mass but different mass-splitting. Similar results have been also found when inspecting the Gtb and Gtt topologies. The features observed in Figures 7.2 and 7.3 result in an analysis efficiency within each topology that is mostly a function of the mass splitting. Furthermore, there is a residual dependence on the mass of the gluino arising from the mass dependent QCD radiation of a massive particle. These facts allow to frame the analysis in terms of the mass splitting. The final state from a single sample is thus representative of a large number of possible physical processes.

7.6.2 Optimization procedure

The signal regions are determined using an optimization procedure based on the kinematic quantities that have been found to be the most powerful in discriminating between signal and background. The optimization is a semi-automated process in which an N-dimensional cut matrix is constructed, with each point representing a set of cuts, one for each of the N dimensions (m_{eff}, $E_{\text{T}}^{\text{miss}}$, p_{T} thresholds, light- and heavy-flavour jet multiplicity, b-tagging operating point, etc.). The signal statistical significance (Eq. 7.11) is then computed for each signal Monte Carlo mass point at each point in the matrix. The significances take into account the systematic uncertainties derived from the jet energy scale and b-tagging efficiency, which are found to be the main sources for searches with heavy flavour jets and $E_{\text{T}}^{\text{miss}}$. In addition, the theoretical uncertainties (as known at the time of these studies) for the backgrounds were also incorporated. The optimization has been performed for an integrated luminosity of 5 fb^{-1}, as expected to be collected during 2011, and its systematic uncertainty ($\approx 4\%$) has also been taken into account. The optimal set of kinematic cuts for a given mass point is the one which maximizes the significance.

Experimentally there are several constraints imposed on the optimization. Typically a set of selection cuts (denoted as preselection for this analysis) are applied to the data in order to reduce the main backgrounds to a level that can be handled in detail, usually dominated by the trigger requirements imposed to avoid the complicated so-called trigger turn-on regions. Furthermore, any optimization also has to look carefully at how backgrounds are estimated as this may require a certain room in phase-space to define the so-called control regions (CR) where background contributions are measured. Thus, in this optimization study a preselection is defined as a baseline that satisfies the trigger requirement and also leaves room for selecting control regions, as discussed in detail on Chapter 8.

In order to find the set of optimal analyses that cover the final states represented by the three topologies with various mass splittings, $\mathcal{O}(10^3)$ test analyses were cre-

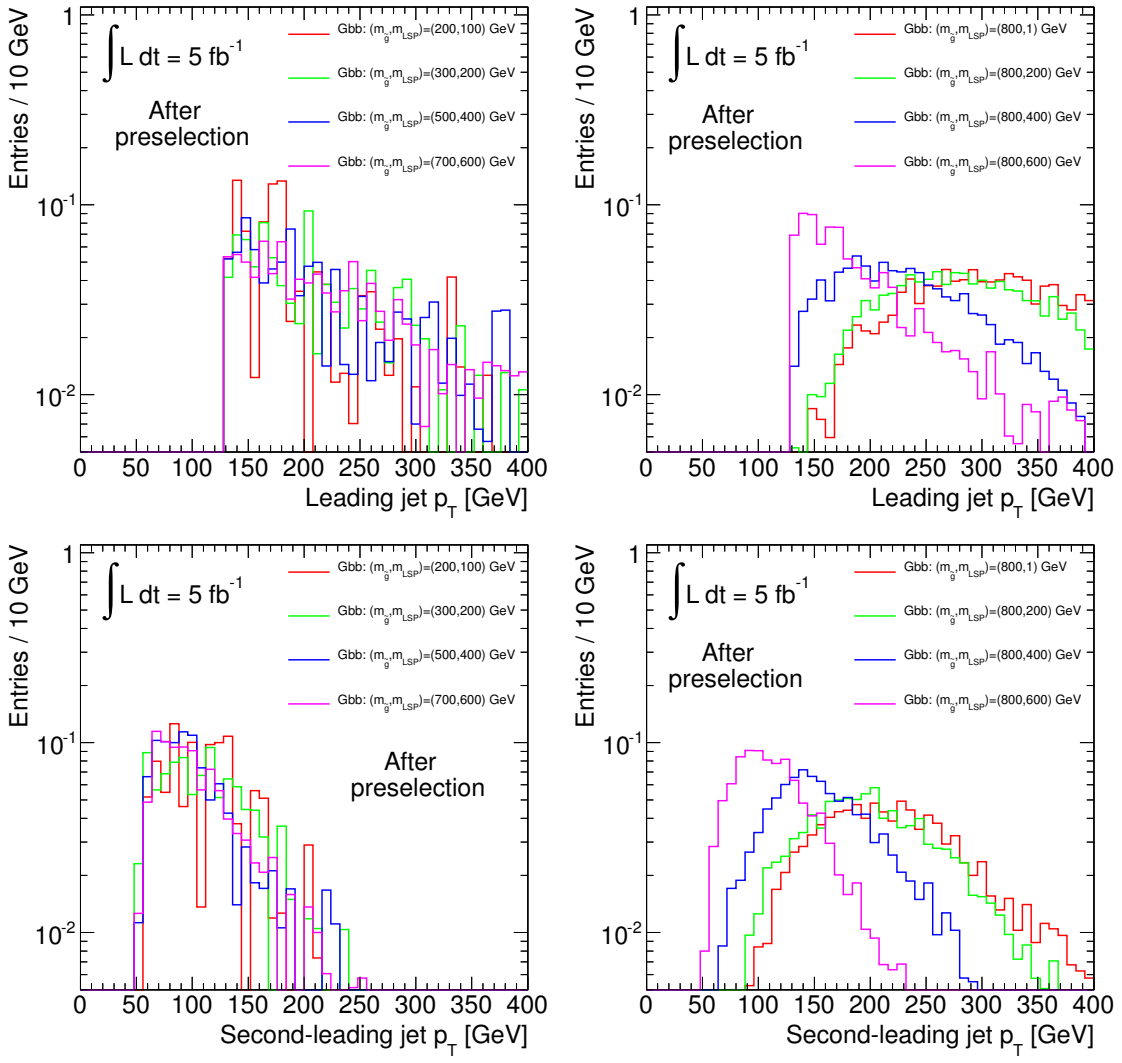

Figure 7.2 Distributions of first- and second-leading jet p_{T} (top and bottom, respectively) for the Gbb topology showing the effect of constant (left) and varying mass-splitting (right) of the pair produced gluino and the LSP.

ated. These analyses were built by requiring the preselection, as previously defined, as well as: jet and b-jet multiplicity and p_{T} threshold cuts, b-tag operating points and taggers, cuts on $E_{\mathrm{T}}^{\mathrm{miss}}$ and overall energy sum within the event, among others. From this set of optimal cuts (defining a set of signal regions larger than is realistic for analysis) the number of selections were reduced methodically with the intent to retain maximal sensitivity over all signal MC mass points while taking into account practical concerns, such as: the existence of data-driven background estimation methods, a Standard Model background prediction of $\mathcal{O}(10)$ events, a practical number of signal regions, among others.

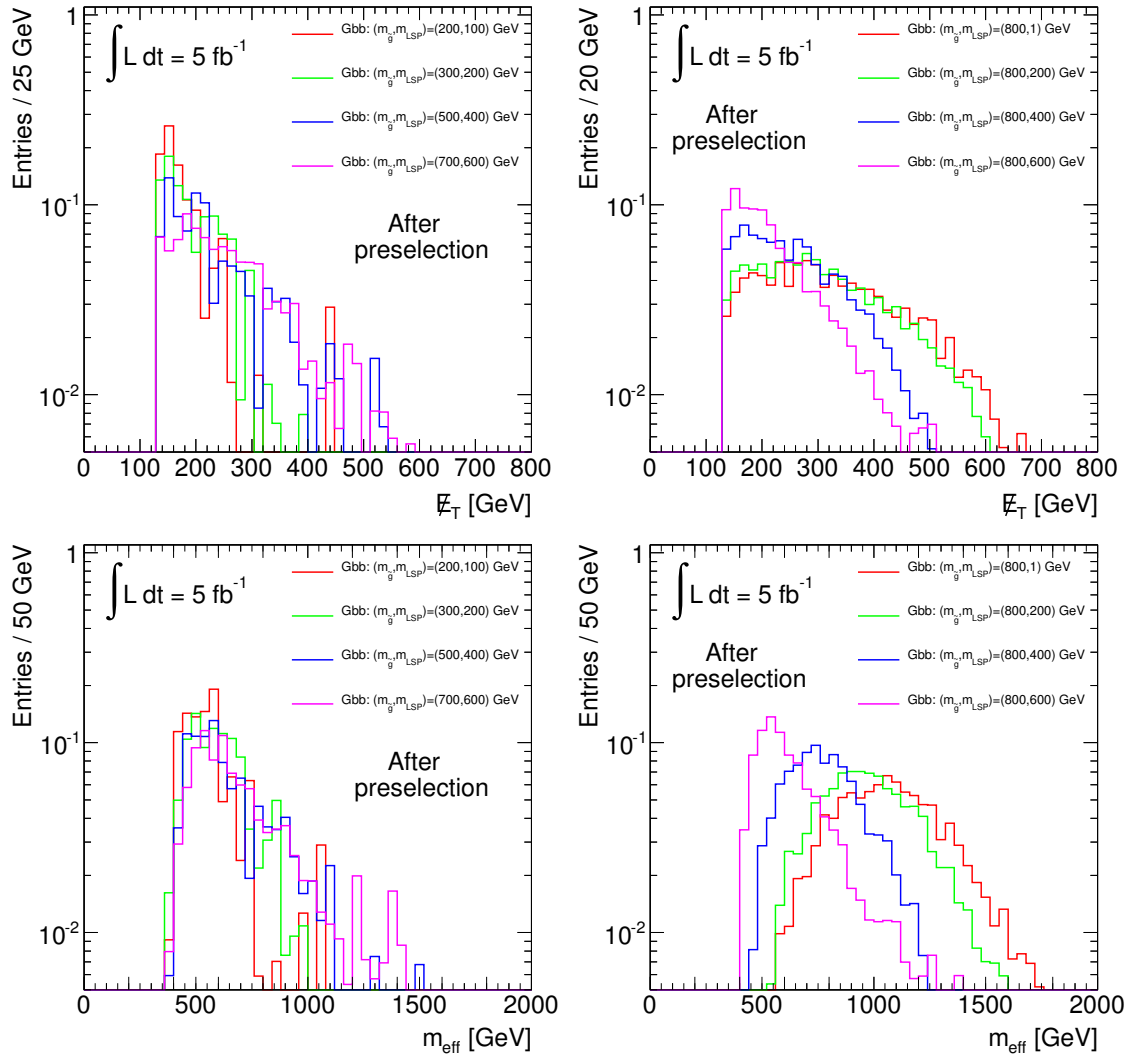

Figure 7.3 Distributions of $E_{\mathrm{T}}^{\mathrm{miss}}$ and overall energy sum in the event m_{eff} (top and bottom, respectively) for the Gbb topology showing the effect of constant (left) and varying mass-splitting (right) of the pair produced gluino and the LSP.

7.6.3 Optimization for Gbb topologies

The jet+$E_{\mathrm{T}}^{\mathrm{miss}}$ trigger chosen for the 0-lepton selection as benchmark for optimization purposes is `EF_j75_a4tc_EFFS_xe45_loose_noMu`, and the offline cuts required to reach the trigger plateau are a leading jet with $p_{\mathrm{T}}>$ 130 GeV, and $E_{\mathrm{T}}^{\mathrm{miss}}$ $>$ 130 GeV, as discussed in Section 7.3.2. Given the possible hard multi-jet final states expected in these topologies, the event is also required to have at least three jets with the third jet $p_{\mathrm{T}}>$ 30 GeV (see Section 2.7).

Several variables have proven to be useful to reject the SM background effectively, while keeping high efficiency in the expected signals. In most of the cases the exact

definition of these variable depends of the exact number of jets (n) required. The different possibilities examined for the optimization study of zero-lepton selection candidates are summarized in Table 7.3. Since leptons are not required in this

Variable	Values (or ranges)
Trigger	EF_j75_a4tc_EFFS_xe45_loose_noMu
Leading jet p_{T}	$\geq$ 130 GeV
$E_{\mathrm{T}}^{\mathrm{miss}}$	$\geq$ (130-200) GeV
Total jet multiplicity	$\geq$ (3,6)
Sub-leading jet p_{T} threshold	$\geq$ (30-60) GeV
$E_{\mathrm{T}}^{\mathrm{miss}}$/ $\mathrm{m_{eff}}$	$\geq$ (0-0.25)
$\Delta\phi_{min}$	$\geq$ (0-0.4)
Total b-tagged jet multiplicity	$\geq 1, \geq 2, \geq 3$
b-tagging algorithm	SV0, JetFitterCOMBNN
b-tagging operating point	(60-80) % efficient
b-jet p_{T} threshold	$\geq$ (30-60) GeV
$\mathrm{m_{eff}}$	$\geq$ (500-1500) GeV

Table 7.3 The set of cuts that have been examined for the optimization study for zero-lepton selection candidates.

selection, the QCD multi-jet is initially the dominant background process. In a given event, $\Delta\phi_{min}$ is defined as the minimum $\Delta\phi$ between any of the n jets and the $E_{\mathrm{T}}^{\mathrm{miss}}$:

$$\Delta\phi_{min} = \min(|\phi_1 - \phi_{E_{\mathrm{T}}^{\mathrm{miss}}}|, ..., |\phi_n - \phi_{E_{\mathrm{T}}^{\mathrm{miss}}}|) \tag{7.13}$$

where the index refers to the p_{T} ordered list of jets. In QCD events, the $E_{\mathrm{T}}^{\mathrm{miss}}$ derives from mismeasurement of the jet energy or from the semi-leptonic decay of a heavy flavour quark in a jet, therefore $\Delta\phi_{min}$ tends to be small, i.e. with $E_{\mathrm{T}}^{\mathrm{miss}}$ almost pointing in the same direction as one of the hard jets. On the other hand, events with SUSY-like signals and those where vector boson and top production take place (e.g., $W \to l\nu$), the source of $E_{\mathrm{T}}^{\mathrm{miss}}$ is true, and $\Delta\phi_{min}$ tends to be distributed uniformly, as can be observed in Figure 7.4. The QCD rejection is effected via a $\Delta\phi_{min} > 0.4$ rad cut between the three leading jets and the $E_{\mathrm{T}}^{\mathrm{miss}}$.

Moreover, the ratio of the missing transverse energy to the overall energy sum within the event, denoted $E_{\mathrm{T}}^{\mathrm{miss}}/\mathrm{m_{eff}}$, is expected to be smaller for QCD events than for other SM backgrounds, as shown in Figure 7.4 (right). Thus, the QCD background is further suppressed by implementing a $E_{\mathrm{T}}^{\mathrm{miss}}/\mathrm{m_{eff}} > 0.25$ cut.

The $E_{\mathrm{T}}^{\mathrm{miss}}$ in the signal topologies arises from the undetected LSPs in R-conserving SUSY models. Moderate cuts on $E_{\mathrm{T}}^{\mathrm{miss}}$ (or $\mathrm{m_{eff}}$) are found to largely suppress the QCD background, which has no true $E_{\mathrm{T}}^{\mathrm{miss}}$, and hard cuts on both variables can help separate high-$E_{\mathrm{T}}^{\mathrm{miss}}$ SUSY-like signals from semi-leptonic $t\bar{t}$ and W+jets back-

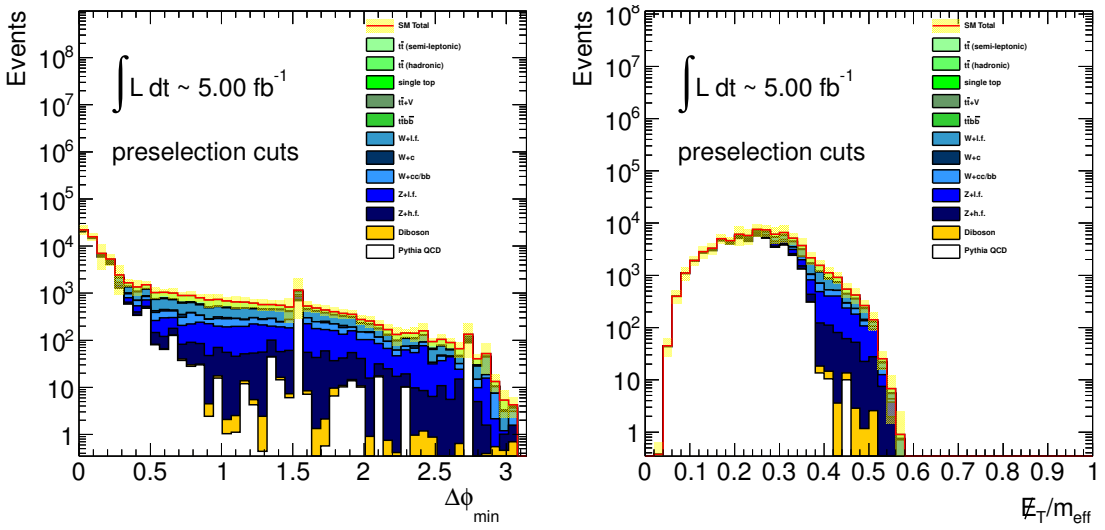

Figure 7.4 Distribution of $\Delta\phi_{min}$ (left) and $E_{\mathrm{T}}^{\mathrm{miss}}/\mathrm{m_{eff}}$(right), after requiring the event to have the leading jet with $p_{\mathrm{T}}>$ 130 GeV, $E_{\mathrm{T}}^{\mathrm{miss}} >$ 130 GeV and at least three jets with $p_{\mathrm{T}}>$ 30 GeV, in the zero-lepton selection.

grounds, which have true $E_{\mathrm{T}}^{\mathrm{miss}}$ but whose spectra tend to be softer. The distributions of $E_{\mathrm{T}}^{\mathrm{miss}}$ (left) and $\mathrm{m_{eff}}$ (right) for the SM backgrounds are shown in Figure 7.5.

The b-tag requirement is used to suppress processes with less heavy flavour jets than the signal topologies. A 1 b-tag requirement suppresses QCD and W+jets relative to the signal, and a 2 b-tag requirement even more so. Although the latter does not remove the $t\bar{t}$ production background, it helps reduce it further relative to gluino production signals due to the more favourable combinatorics in models with at least four heavy flavour jets. The 3 b-tag analysis suppresses the top background the most, provided the 3rd-leading b-jet p_{T} signal spectrum is not too soft. The points which usually favor the 1 and 2 b-tag analyses are Gbb and Gtb points which lie near the so-called forbidden line ($m_{\tilde{g}} - m_{\tilde{\chi}^0} \approx 0$), as the b-jets (in the Gtb case, the 3rd and 4th b-jets) have very little phase space available to them and thus are soft.

Furthermore, different b-jet p_{T} thresholds have been studied, between 30-60 GeV, in order to maximize the significance for this analysis, specially in the Gbb topologies. By setting b-jet $p_{\mathrm{T}} >$ 30 GeV, the sensitivity is found to increase by 40-80%, 80-160% and 30-60% for low, medium and high mass splitting values respectively, when compared to a b-jet p_{T} threshold of 50 GeV as implemented in previous searches with 1 and 2 b-tagged jets. The best performance is obtained in the middle region, as the phase space available to b-jets is larger than near the forbidden line, where b-jets are soft. For high mass splitting values the improvement is smaller, since there is a relatively large b-jet phase space available, and therefore the b-jets are mostly hard.

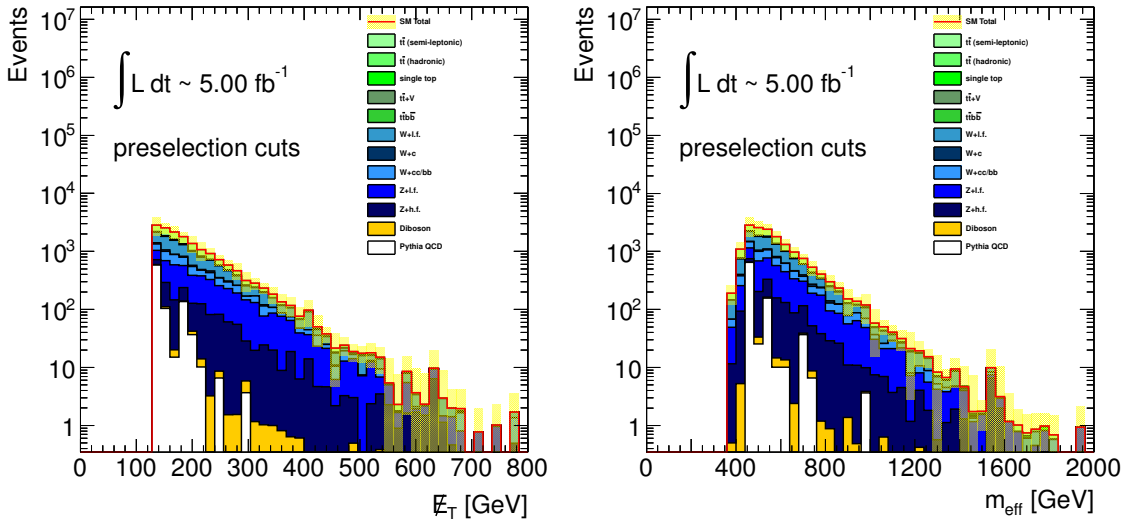

Figure 7.5 Distribution of $E_{\mathrm{T}}^{\mathrm{miss}}$ (left) and $\mathrm{m_{eff}}$ (right) after requiring the event to have the leading jet with $p_{\mathrm{T}}>$ 130 GeV, $E_{\mathrm{T}}^{\mathrm{miss}} >$ 130 GeV and at least three jets with $p_{\mathrm{T}}>$ 30 GeV, in the zero-lepton selection. The QCD rejection has been done by applying both a $\Delta\phi_{min} > 0.4$ cut and a $E_{\mathrm{T}}^{\mathrm{miss}}/\mathrm{m_{eff}} > 0.25$ cut.

The high-performance b-tagging algorithm `JetFitterCOMBNN` is used as the baseline b-tagger for the optimization, and it has been compared to lower-performance ones used in earlier analysis [140–142]. For the same rejection at a given operating point, the high-performance algorithm is found to be 5 times more efficient for those regions where kinematics are $t\bar{t}$-like. The `JetFitterCOMBNN` algorithm has been found to give the best significance throughout the entire mass plane. Furthermore, several operating points have been studied. The use of the loosest available operating point (80%) is very promising for high mass-splitting signal samples, as it increases the signal efficiency whereas the $t\bar{t}$ background is effectively suppressed by the corresponding high $\mathrm{m_{eff}}$ cut (up to 900 GeV). Higher cuts on $\mathrm{m_{eff}}$, within the range 900-1500 GeV, have also been studied. However, they are found not to improve the significance (even using the loosest operating points available) mainly due to statistics, since the SM event yields are required to be at least $\mathcal{O}$ (10). Therefore, these high $\mathrm{m_{eff}}$ combinations are expected to be extremely useful for future searches with larger statistics. For lower mass-splitting signals, high $\mathrm{m_{eff}}$ cuts are not feasible and tight b-tagging operating points are preferred as the effective way to suppress the $t\bar{t}$ background.

The most promising reduced set of signal regions for the Gbb topologies using the 0-lepton channel are labelled 0L_`nbi`, where 0L and `n` denote the number of leptons and b-tagged jets, respectively, and `i` specifies whether loose (l), medium (m) or tight (t) cuts are implemented. They are summarized in Table 7.4[3]. After

[3]The optimization has been performed with `MC@NLO` $t\bar{t}$ MC samples.

the optimization, the relative improvement in significance with respect to previous analyses [140–142] is found to be between 200% and 500% for Gbb topologies as shown on Figure 7.6. The best set of cuts as well as the corresponding significance for a given point in the gluino/LSP mass plane are also shown. The 3 b-tag analysis provides in general the highest sensitivity and it covers about 95% of the total mass plane. A 1(2) b-tagged analysis may remain the best strategy for points near the diagonal (i.e. $\Delta M(m_{\tilde{g}}, m_{LSP}) < 50$ GeV) for the Gbb topology.

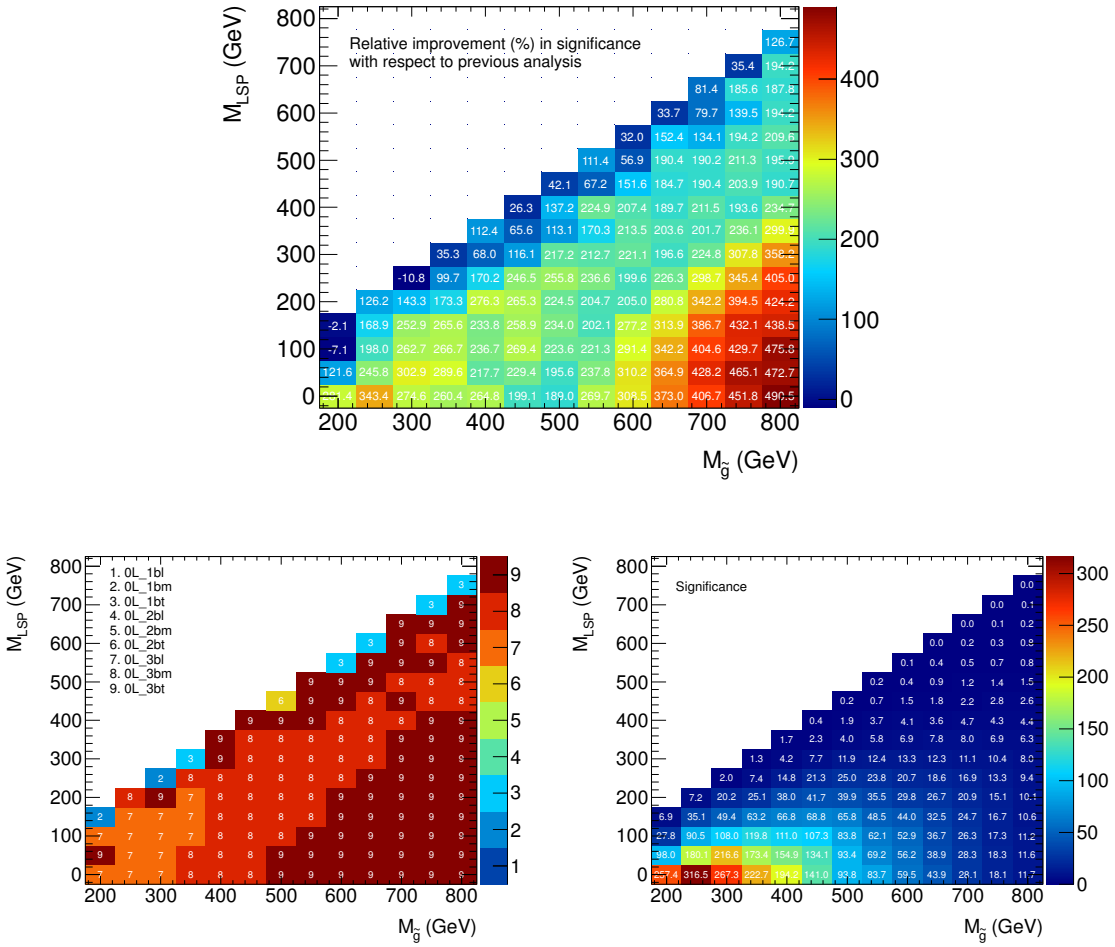

Figure 7.6 Top: Relative improvement in significance with respect to previous analyses after selecting a reduced set of 9 promising signal regions incorporating a 3rd b-tagged jet, for the Gbb topology. It has been observed that 3-tag signal regions in general provide the highest sensitivity. The improvement in significance is found to be between 200 % and 500 % for points not near the diagonal for Gbb. Bottom left: Best set of cuts for a given point in the gluino/LSP mass plane. The 3 b-tag analysis covers about 95 % of the total mass plane. Bottom right: The best set of cuts significances for each point.

0-lepton channel signal regions	SM (5 fb^{-1})
0L_1bl: $\geq$ 4j50, $\geq$ 1 b-tag (p_{T}> 30 GeV, OP = 2.00 (60%)), m_{eff} > 500 GeV	1583.5
0L_1bm: $\geq$ 4j50, $\geq$ 1 b-tag (p_{T}> 30 GeV, OP = 2.00 (60%)), m_{eff} > 700 GeV	516.81
0L_1bt: $\geq$ 4j50, $\geq$ 1 b-tag (p_{T}> 30 GeV, OP = 2.00 (60%)), m_{eff} > 900 GeV	112.69
0L_2bl: $\geq$ 4j50, $\geq$ 2 b-tag (p_{T}> 30 GeV, OP = 2.00 (60%)), m_{eff} > 500 GeV	556.79
0L_2bm: $\geq$ 4j50, $\geq$ 2 b-tag (p_{T}> 30 GeV, OP = 2.00 (60%)), m_{eff} > 700 GeV	170.62
0L_2bt: $\geq$ 4j50, $\geq$ 2 b-tag (p_{T}> 30 GeV, OP = 2.00 (60%)), m_{eff} > 900 GeV	35.6
0L_3bl: $\geq$ 4j50, $\geq$ 3 b-tag (p_{T}> 30 GeV, OP = 2.00 (60%)), m_{eff} > 500 GeV	42.9
0L_3bm: $\geq$ 4j50, $\geq$ 3 b-tag (p_{T}> 30 GeV, OP = 2.00 (60%)), m_{eff} > 700 GeV	13.9
0L_3bt: $\geq$ 4j50, $\geq$ 3 b-tag (p_{T}> 30 GeV, OP = 0.35 (70%)), m_{eff} > 900 GeV	8.4

Table 7.4 Reduced set of nine selection cuts aimed at Gbb topologies. The Standard Model background yield prediction for each region is also shown (the $t\bar{t}$ background is estimated with MC@NLO).

As adding a third b-tagged jet reduces the QCD background dramatically, the sensitivity of the 3 b-tag analysis to $\Delta\phi$ and $E_{\mathrm{T}}^{\mathrm{miss}}/m_{\mathrm{eff}}$ cuts was also studied for the three topologies, with the thought that relaxing one or both of these cuts could increase the statistics without compromising the sensitivity. The results for Gbb are presented in Figure 7.7. The impact on the 3 b-tag analysis after removing the $E_{\mathrm{T}}^{\mathrm{miss}}/m_{\mathrm{eff}}$ is found to be very small ($< 5\%$) in the region with large $\Delta M(\tilde{g}, LSP)$. For medium mass splitting, the significance gets deteriorated by 20% approximately. On the other hand, by removing the $\Delta\phi$ cut, the impact on the sensitivity is found to be -20% in the region with large $\Delta M(\tilde{g}, LSP)$. For medium mass splitting, the significance gets deteriorated down to 50%, whereas for low gluino masses, the impact is slightly higher, of 70% approximately. Overall, for the regions where the 3 b-jet analysis is the best (95% of the mass plane), the degradation in sensitivity is found to range from 10 % to 50 % depending on the mass-splitting and topology, therefore both cuts have been kept in the preselection.

Finally, the certainty of an evolving trigger menu for higher luminosities has motivated the study of the effect of higher kinematic thresholds (in particular higher leading jet p_{T} and $E_{\mathrm{T}}^{\mathrm{miss}}$ cuts) on the analysis sensitivity. For small mass-splittings, a degradation of 20% in the significance is observed after enhancing the $E_{\mathrm{T}}^{\mathrm{miss}}$ cut by 30 GeV. For medium mass-splittings, a 10% improvement is observed due to additional background reduction. No significant changes in significance are observed for high mass-splitting points.

7.6.4 Optimization for Gtt topologies

Earlier analyses with 1 and 2 b-tagged jets in the final state have shown that the 0-lepton channel usually performed worse than the 1-lepton channel when targeting

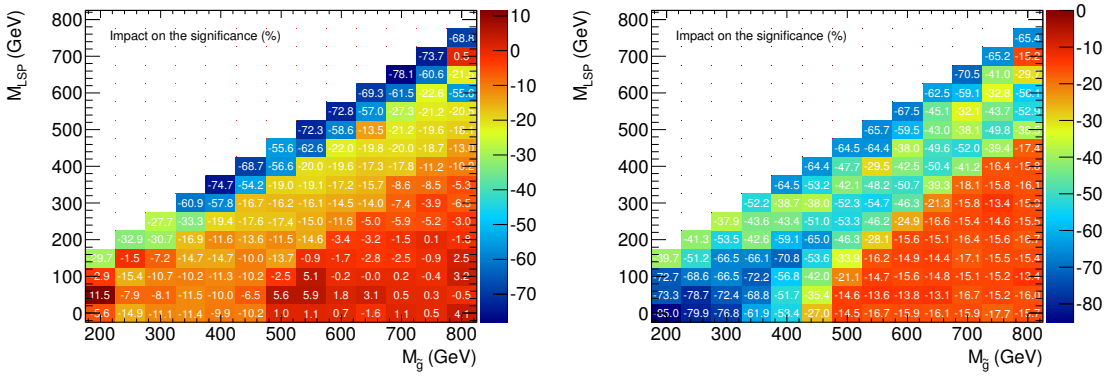

Figure 7.7 Impact on the significance after removing the $E_{\mathrm{T}}^{\mathrm{miss}}/\mathrm{m_{eff}}$ cut (left) and the $\Delta\phi_{min} > 0.4$ cut (right) for Gbb topologies. For the regions where the 3 b-jet analysis performs the best (95% of the mass plane, see Figure 7.6), the degradation in sensitivity is found to be from 10 % to 50 % depending on the mass-splitting and topology. Similar performance has been observed for Gtb and Gtt topologies.

at gluino pair production with subsequent decays to a stop (and its SM partner) plus $E_{\mathrm{T}}^{\mathrm{miss}}$[4]. The expected final states for the Gtt topologies consist of $t\bar{t}t\bar{t} + E_{\mathrm{T}}^{\mathrm{miss}}$. The top-quarks decay mostly to $t \to bW$, with subsequent decays for the W boson. Within a scenario of four tops, the all hadronic channel (i.e., 0-lepton selection) is not statistically favoured, as the probability of having the four W bosons decaying hadronically accounts for only 36% of the cases. Thus, the one-lepton channel is statistically favoured. In addition, the lepton triggers allow to operate with low p_{T} thresholds, which further increases the statistics. Moreover, the requirement of having either an electron or a muon effectively suppresses the QCD background. On the other hand, the $t\bar{t}$ contribution to the analyses with 1 and 2 b-tagged jets for the 0-lepton channel is larger than for the 1-lepton channel, as the probability of having a fully hadronic $t\bar{t}$ decay accounts for 60%, approximately. Clearly, none of these reasons favours the 0-lepton selection and therefore it is expected the 1-lepton channel to perform the best. However, the choice of which strategy one should follow for a 3 b-jets selection is not evident, as the requirement of having at least 3 b-tagged jets not only largely reduces the QCD background, but it also effectively suppresses the $t\bar{t}$ background (which has two real b-jets). Therefore, special care in the optimization was taken in order to fully maximize the significance for both the 0-lepton and 1-lepton channel for this particular topology, and the results are presented next.

Events containing leptons are selected by single electron and muon triggers, with

[4]The mSUGRA model with $\tan\beta = 40$, $A_0 = -500$ GeV and $\mu > 0$ model was used as a benchmark SUSY signal.

exactly one lepton (i.e., electron or muon) satisfying the tight criteria, as described in Section 7.1. In order to avoid the trigger turn-on regions, the electron and the muon are selected if they have $p_{\mathrm{T}} > 25$ GeV and $p_{\mathrm{T}} > 20$ GeV, respectively. The single-muon trigger implemented from Period J requires one jet with $p_{\mathrm{T}}^{\mathrm{L1}} > 10$ GeV in addition to the muon, therefore a leading offline jet with $p_{\mathrm{T}} > 60$ GeV is required throughout all data periods for consistency in both electron and muon channels. If there are other leptons in the event satisfying loose criteria, the event is rejected. Given the possible hard multi-jet final states expected in these topologies the event is also required to have at least four jets with the fourth jet $p_{\mathrm{T}} > 30$ GeV.

The QCD background is efficiently rejected by the lepton requirement and therefore neither a cut on $\Delta\phi_{min}$ nor on $E_{\mathrm{T}}^{\mathrm{miss}}/\mathrm{m_{eff}}$ is imposed. To eliminate SM events where the only source of $E_{\mathrm{T}}^{\mathrm{miss}}$ is a neutrino from the decay $W \to l\nu$, a cut is placed on the transverse mass, $\mathrm{m_T}$, defined in terms of the transverse momentum of the lepton in the event (${p_{\mathrm{T}}}^{lep}$) and the $E_{\mathrm{T}}^{\mathrm{miss}}$ as follows:

$$\mathrm{m_T} = \sqrt{2(p_{\mathrm{T}}^{lep} E_{\mathrm{T}}^{\mathrm{miss}} - \vec{\mathbf{p}}_{\mathrm{T}} \cdot \vec{\mathbf{E}}_{\mathrm{T}}^{\mathrm{miss}})} \,. \tag{7.14}$$

Thus, if the only source of missing energy is one neutrino originated from the decay $W \to l\nu$, the $\mathrm{m_T}$ corresponds to the transverse mass of the W. On the other hand, if there are other sources of missing energy, the $\mathrm{m_T}$ distribution is expected to be distorted. Figure 7.8 shows the distribution of $\mathrm{m_T}$ (left) and $E_{\mathrm{T}}^{\mathrm{miss}}$ (right), after requiring the event to have either an electron or a muon with $p_{\mathrm{T}} > 25$ GeV and $p_{\mathrm{T}} > 20$ GeV, respectively. In addition, the event must have at least four jets with $p_{\mathrm{T}} > 30$ GeV and the leading jet with $p_{\mathrm{T}} > 60$ GeV. A cut on $\mathrm{m_T} > 100$ GeV is set to reject the SM backgrounds mentioned above, with such value initially chosen in order to leave room for a control region.

In order to find the optimum set of cuts for the 1-lepton channel, different subleading p_{T} cuts, jet multiplicity, b-tagging operating points, $\mathrm{m_T}$ and $\mathrm{m_{eff}}$ cuts among others observables were studied. The variations examined for the optimization study of 1-lepton selection candidates are summarized in Table 7.5.

After the optimization, three and four promising signal regions are determined for the 0- and 1-lepton selection, respectively. These are labelled `mL_nbi`, where `m` and `n` denote the number of leptons and b-tagged jets, respectively, and `i` specifies whether loose (l) or tight (t) cuts were implemented. They are summarized in Table 7.6 and Table 7.7. The Standard Model background yield prediction for each region is also shown.

For the Gtt topology, even on the forbidden line the 3rd-leading b-jet is reasonably energetic since there is a relatively large b-jet phase space minimum imposed by the top mass. Thus the 3 b-tag analyses are found to be invariably the best choice for Gtt in both the 0- and 1-lepton selections.

The total jet multiplicity (light + heavy flavor) has been found to be another

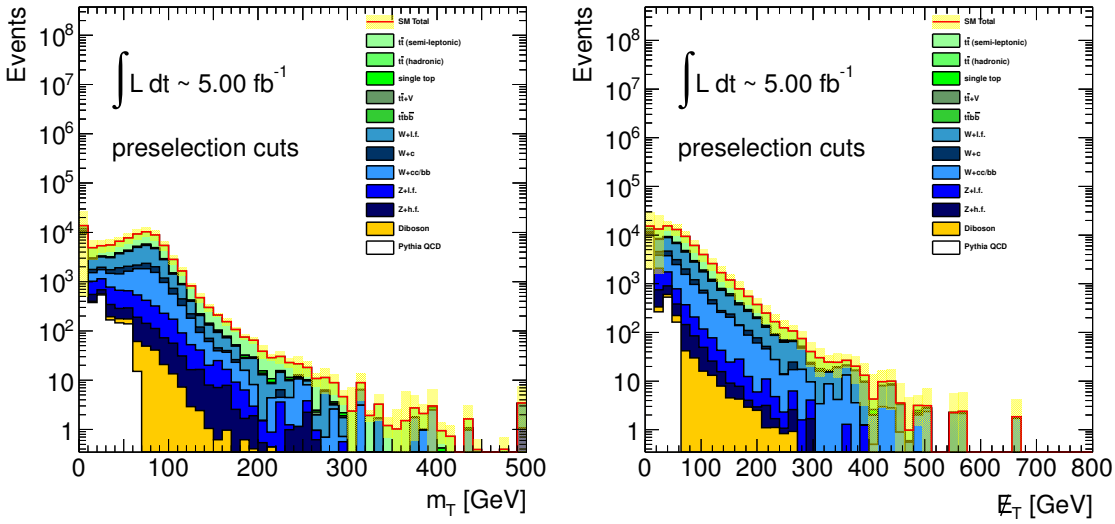

Figure 7.8 Distribution of m_T (left) and E_T^{miss}(right), after requiring the event to have either an electron or a muon with $p_T > 25$ GeV and $p_T > 20$ GeV, respectively. In addition, the event must have at least four jets with $p_T > 30$ GeV and the leading jet with $p_T > 60$ GeV.

Variable	Values (or ranges)
Trigger	EF_e22_medium or EF_mu18_L1J10
Leading electron (muon) p_T	$\geq$ 25 (20) GeV
E_T^{miss}	$\geq$ (80-200) GeV
Total jet multiplicity	(4,6)
Leading jet p_T	$\geq$ 60 GeV
Sub-leading jet $p_T$threshold	$\geq$ (30-60) GeV
m_T	$\geq$ 100 GeV
Total b-tagged jet multiplicity	$\geq 1, \geq 2, \geq 3$
b-tagging algorithm	SV0, JetFitterCOMBNN
b-tagging operating point	(60-80) % efficient
b-jet $p_T$threshold	$\geq$ (30-60) GeV
m_{eff}	(500-1500) GeV

Table 7.5 The set of cuts that has been examined for the optimization study of 1-lepton selection candidates.

important tool to preferentially reject background, as the Gtt topology may result in a final state with 12 partons at tree-level (i.e., a larger multiplicity than that of the Gbb topology, with 4 partons expected). During the optimization of the 0-lepton channel for Gtt topologies, the 6-jet inclusive channel, with the sixth jet p_T required to be above 50 GeV provides the 3 b-tag selections that generally perform the best

0-lepton channel signal regions	SM (5 fb^{-1})
0L_3bll: $\geq$ 6 jets ($p_{\mathrm{T}} > 50$ GeV), $\geq$ 3 b-jets ($p_{\mathrm{T}} > 30$ GeV, OP = 0.35 (70%)), $m_{\mathrm{eff}} > 500$ GeV, $E_{\mathrm{T}}^{\mathrm{miss}} > 150$ GeV,	12.9
0L_3bmm: $\geq$ 6 jets ($p_{\mathrm{T}} > 50$ GeV), $\geq$ 3 b-jets ($p_{\mathrm{T}} > 30$ GeV, OP = 0.35 (70%)), $m_{\mathrm{eff}} > 700$ GeV, $E_{\mathrm{T}}^{\mathrm{miss}} > 150$ GeV,	11.1
0L_3btt: $\geq$ 6 jets ($p_{\mathrm{T}} > 50$ GeV), $\geq$ 3 b-jets ($p_{\mathrm{T}} > 30$ GeV, OP = -1.25 (80%)), $m_{\mathrm{eff}} > 900$ GeV, $E_{\mathrm{T}}^{\mathrm{miss}} > 200$ GeV,	10.7

Table 7.6 Most promising reduced set of signal regions for the 0-lepton channel targeting Gtt topologies. The Standard Model event yield predictions for each particular region are also shown (the $t\bar{t}$ background is estimated with MC@NLO).

1-lepton channel signal regions	SM (5 fb^{-1})
1L_2bl: $\geq$ 6 jets, $\geq$ 2 b-jets ($p_{\mathrm{T}} > 30$ GeV, OP = -1.25 (80%)), $m_{\mathrm{T}} > 100$ GeV, $m_{\mathrm{eff}} > 500$ GeV, $E_{\mathrm{T}}^{\mathrm{miss}} > 140$ GeV	34.9
1L_2bt: $\geq$ 6 jets, $\geq$ 2 b-jets ($p_{\mathrm{T}} > 30$ GeV, OP = -1.25 (80%)), $m_{\mathrm{T}} > 100$ GeV, $m_{\mathrm{eff}} > 800$ GeV, $E_{\mathrm{T}}^{\mathrm{miss}} > 200$ GeV	8.9
1L_3bl: $\geq$ 4 jets, $\geq$ 3 b-jets ($p_{\mathrm{T}} > 30$ GeV, OP = -1.25 (80%)), $m_{\mathrm{T}} > 100$ GeV, $m_{\mathrm{eff}} > 500$ GeV, $E_{\mathrm{T}}^{\mathrm{miss}} > 140$ GeV	49.9
1L_3bt: $\geq$ 4 jets, $\geq$ 3 b-jets ($p_{\mathrm{T}} > 30$ GeV, OP = -1.25 (80%)), $m_{\mathrm{T}} > 100$ GeV, $m_{\mathrm{eff}} > 800$ GeV, $E_{\mathrm{T}}^{\mathrm{miss}} > 200$ GeV	9.9

Table 7.7 Most promising reduced set of signal regions for the 1-lepton channel targeting Gtt topologies. The Standard Model event yield predictions for each particular region are also shown (the $t\bar{t}$ background is estimated with MC@NLO).

(with similar results obtained for Gtb topologies). The same feature is observed when optimizing the 1-lepton channel, with the caveat that the 1-lepton 3 b-tag selection requires 4 jets only, due to the lack of statistics (see Table 7.7).

When optimizing the signal regions for the Gbb topologies, the use of loose operating points had been found very promising for high mass-splitting signal samples (see Table 7.4, 0L_3bt selection), where the $t\bar{t}$ background is effectively suppressed by the corresponding high m_{eff} cut. For the Gtt topologies, several operating points have also been studied. The two loosest operating points (70% and 80%) and a low p_{T} requirement for the b-jets have been found to perform the best in both the 0- and 1-lepton selections, as they allow enhancing both the signal and the background efficiency for 3 b-tags, with the background suppressed by tightening the m_{eff} and the $E_{\mathrm{T}}^{\mathrm{miss}}$ cuts.

Overall, after the optimization for Gtt topologies the relative improvement in significance with respect to a 0-lepton selection with 1 and 2 b-tagged jets is found to range between 300-650% depending on the mass-splitting values. Such perfor-

mance is obtained after requiring a higher total jet multiplicity in combination with looser b-tagging operating points, and enhanced m_{eff} and E_T^{miss} cuts. Interestingly, these signal regions candidates are found to be competitive with the 1-lepton selection sensitivity, as it can be observed in the Figure 7.9. Although the 0- and 1-lepton selections might have been combined to increase the coverage of the search, it is worth mentioning that preliminary studies found that the lack of statistics for building reliable CRs for the 1-lepton and 3 b-jets selection (plus the hypothetically large signal contaminations in those CRs when interpreting the results in the context of the gluino-mediated stop pair production, see Section 9.2) prevented the 1-lepton channel to be used at this stage of the data-taking. Therefore, only 0-lepton signal regions are considered for this analysis.

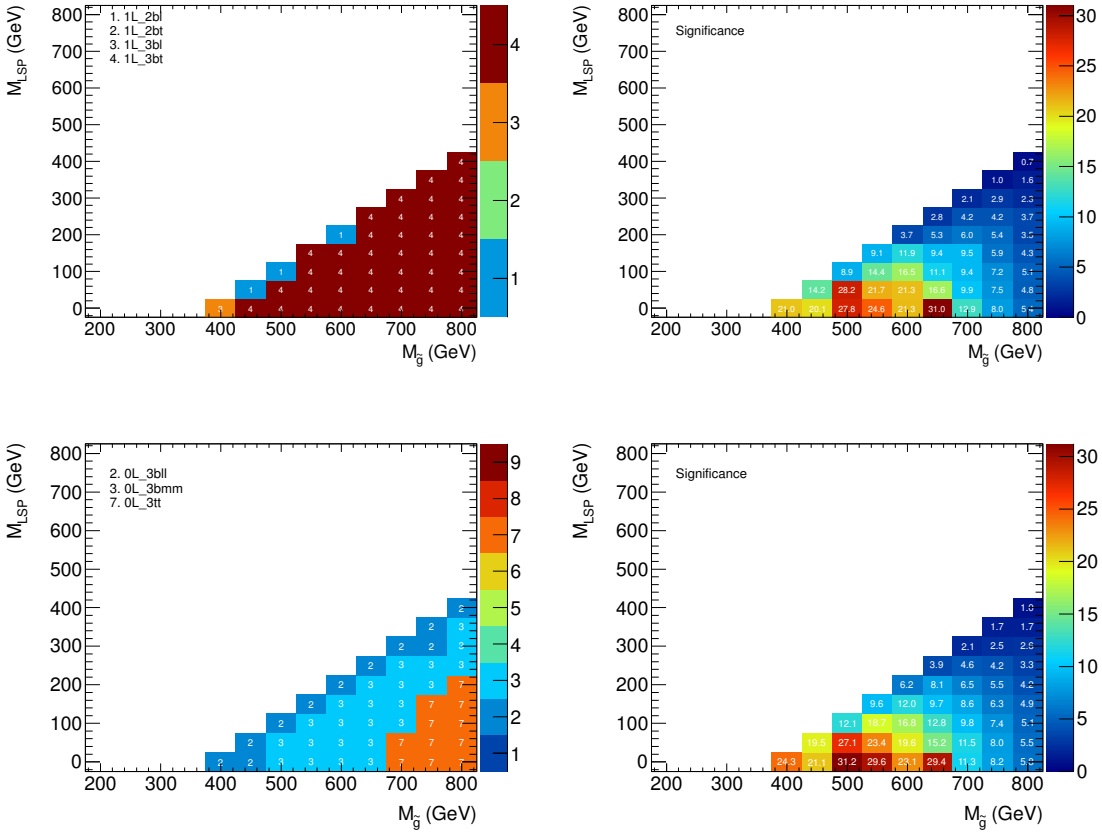

Figure 7.9 Top left: best selection cuts using the 1-lepton selection. The 3 b-tag analysis is found to be the best strategy for more than 95% of the mass plane for the Gtt topology. Top right: the significance for the best set of cuts at a given point for the 1-lepton. Bottom left: best selection cuts using the 0-lepton selection. Bottom right: 0-lepton significance after requiring a higher total jet multiplicity in combination with looser b-tagging operating points, and enhanced m_{eff} and E_T^{miss} cuts, while keeping the SM prediction yield around $\mathcal{O}(10)$ events. The resulting 0-lepton selections are found to be competitive with the 1-lepton selection sensitivity.

7.6.5 Other trigger strategies

Given the enormous collision rate at the LHC, the possibility of either to identify events with multiple jets or to distinguish between heavy flavour and light jets already at trigger level may offer significant improvements for physics analyses. During 2011, the ATLAS trigger menu has included multi-jet and b-jet triggers. These may avoid cutting harshly on offline $E_{\mathrm{T}}^{\mathrm{miss}}$ and p_{T} in the 0-lepton selection while effectively rejecting the QCD background by requiring several light and heavy flavour jets. Therefore, these trigger strategies are also worth exploring for the SUSY signals this analysis targets.

Dedicated studies have been done relying on multi-jet and b-jet triggers during the optimization, in order to understand whether the analysis may benefit from using them by comparing their performance in sensitivity with respect to the jet+$E_{\mathrm{T}}^{\mathrm{miss}}$ trigger. The multi-jet trigger chosen is referred to as `EF_5j30_a4tc_EFFS`, and it requires five jets with $p_{\mathrm{T}} > 30$ GeV at the EF. The offline requirements to avoid the turn-on region for such trigger are a fifth jet with $p_{\mathrm{T}} > 60$ GeV and a spatial isolation of $\Delta R(\mathrm{jet}_i, \mathrm{jet}_j) > 0.7$, for $i, j : 1 \ldots 5$, with $i \neq j$ [244, 259]. The technique adopted in 2011 by ATLAS for the online selection of events containing b-jets is referred to as the jet probability method (`JetProb`) [260–262], which essentially computes the probability for a jet to originate from the primary vertex based on the transverse impact parameter significance of tracks near the jet. The b-jet trigger chosen is denoted `EF_2b10_medium_j75_j30_a4tc_EFFS`, and it requires two b-jets seeded by a L1 jet trigger satisfying $p_{\mathrm{T}}^{L1} > 10$ GeV (`2b10`), the online b-tagger operating at 70% b-jet efficiency (`medium`) as measured on a simulated $t\bar{t}$ sample, and the first- and second- leading jets with $p_{\mathrm{T}}^{EF} > 75$ GeV and $p_{\mathrm{T}}^{EF} > 30$ GeV, respectively. Analyses using the b-jet trigger require that the jets tagged online are verified using the offline b-tagging algorithm (`IP3D+SV1`). This requirement is referred to as "fat-tag", and it corresponds to an offline-matched-to-online jet, using a geometrical requirement of $\Delta R(\mathrm{ROI}, \mathrm{jet}) < 0.2$, tagged by both online and offline b-tagging algorithms. The event weighting procedure follows closely the pure offline case described in Section 5.6. The online b-tagging algorithm relies on track reconstruction at the trigger level, which is "seeded" from a L1 jet that pass certain tunable energy thresholds. Thus, in order to avoid the turn-on region the same offline jet p_{T} requirement to all online b-tagging candidates are applied. Since the b-jet triggers are seeded by the single jet trigger `L1_J10`, a jet is considered as a candidate for a fat-tag only if $p_{\mathrm{T}} > 60$ GeV.

Several variations have been examined for the optimization study of zero-lepton selection candidates using these two trigger strategies, following the same approach as described in Sections 7.6.3 and 7.6.4. The reduced set of cuts using a multi-jet and the b-jet trigger strategies are summarized in Table 7.8 and Table 7.9, respectively.

The most promising set of cuts and their corresponding significances for Gbb and

Multi-jet trigger strategy: 0-lepton channel signal regions common cuts: $\geq$ 5 jets ($p_{\mathrm{T}} > 60$ GeV), $E_{\mathrm{T}}^{\mathrm{miss}} > 130$ GeV, $\Delta\phi_{min} > 0.4$.	SM (5 fb^{-1})
0L_mjt_1bl: $\geq$ 1 b-tag (p_{T}> 60 GeV, OP = 2.00 (60%)), $\mathrm{m_{eff}} > 500$ GeV	161
0L_mjt_1bm: $\geq$ 1 b-tag (p_{T}> 60 GeV, OP = 2.00 (60%)), $\mathrm{m_{eff}} > 700$ GeV	96
0L_mjt_1bt: $\geq$ 1 b-tag (p_{T}> 60 GeV, OP = 2.00 (60%)), $\mathrm{m_{eff}} > 900$ GeV	35
0L_mjt_2bl: $\geq$ 2 b-tag (p_{T}> 60 GeV, OP = 2.00 (60%)), $\mathrm{m_{eff}} > 500$ GeV	59
0L_mjt_2bm: $\geq$ 2 b-tag (p_{T}> 60 GeV, OP = 2.00 (60%)), $\mathrm{m_{eff}} > 700$ GeV	34
0L_mjt_3bl: $\geq$ 3 b-tag (p_{T}> 60 GeV, OP = 0.35 (70%)), $\mathrm{m_{eff}} > 500$ GeV	12.8
0L_mjt_3bm: $\geq$ 3 b-tag (p_{T}> 60 GeV, OP = 0.35 (70%)), $\mathrm{m_{eff}} > 700$ GeV	7.6
0L_mjt_3bt: $\geq$ 3 b-tag (p_{T}> 60 GeV, OP = -1.25 (80%)), $\mathrm{m_{eff}} > 900$ GeV	7.9

Table 7.8 Reduced set of eight selection cuts using a multi-jet trigger strategy. The Standard Model background yield prediction for each region is also shown (the $t\bar{t}$ background is estimated with MC@NLO).

b-jet trigger strategy: 0-lepton channel signal regions common cuts: $\geq$ 4 jets ($p_{\mathrm{T}} > 50$ GeV), $p_{\mathrm{T}}^{1} > 130$ GeV, $p_{\mathrm{T}}^{2} > 60$ GeV, $E_{\mathrm{T}}^{\mathrm{miss}} > 130$ GeV, $\Delta\phi_{min} > 0.4$.	SM (5 fb^{-1})
0L_bjt_3bml: $\geq$ 3 b-tag (p_{T}> 60 GeV, OP = 1.55 (70%)), $\mathrm{m_{eff}} > 500$ GeV	55
0L_bjt_2bll: $\geq$ 2 b-tag (p_{T}> 60 GeV, OP = -0.85 (80%)), $\mathrm{m_{eff}} > 500$ GeV	374
0L_bjt_3bll: $\geq$ 3 b-tag (p_{T}> 60 GeV, OP = -0.85 (80%)), $\mathrm{m_{eff}} > 500$ GeV	126
0L_bjt_2bmm: $\geq$ 3 b-tag (p_{T}> 60 GeV, OP = 1.55 (70%)), $\mathrm{m_{eff}} > 700$ GeV	132
0L_bjt_3bmm: $\geq$ 3 b-tag (p_{T}> 60 GeV, OP = 1.55 (70%)), $\mathrm{m_{eff}} > 700$ GeV	27.3
0L_bjt_3blm: $\geq$ 2 b-tag (p_{T}> 60 GeV, OP = -0.85 (80%)), $\mathrm{m_{eff}} > 700$ GeV	158
0L_bjt_2bmt: $\geq$ 2 b-tag (p_{T}> 60 GeV, OP = 1.55 (70%)), $\mathrm{m_{eff}} > 900$ GeV	35.1
0L_bjt_3blt: $\geq$ 3 b-tag (p_{T}> 60 GeV, OP = -0.85 (80%)), $\mathrm{m_{eff}} > 900$ GeV	7.1

Table 7.9 Reduced set of eight selection cuts using a b-jet trigger strategy. The Standard Model background yield prediction for each region is also shown (the $t\bar{t}$ background is estimated with MC@NLO).

Gtt topologies are presented in Figure 7.10 and Figure 7.11 using the multi-jet and the b-jet trigger strategies, respectively. As it can be observed, the 3 b-tag analysis is found to cover more than 95 % of the total mass plane in each case. In addition, the implementation of tight $\mathrm{m_{eff}}$ cuts combined with loose b-tagger operating points have been found to increase the sensitivity by 30-70% and 60-90% in the medium and high mass splitting region, respectively, when compared to selections with 3 b-tagged jets (OP = 60%) and $\mathrm{m_{eff}} > 500$ GeV. The possibility of reducing the $E_{\mathrm{T}}^{\mathrm{miss}}$ cut has also been studied in order to extend the boundaries of this search, specially in the region close to the diagonal. For $E_{\mathrm{T}}^{\mathrm{miss}} > 100$ GeV, a degradation in sensitivity of around 80%, 30-50% and 20% has been observed for the low, medium and high

mass splitting regions, respectively, for both trigger strategies, when compared to the results obtained in the 3 b-tag set of selections with $E_{\mathrm{T}}^{\mathrm{miss}} > 130$ GeV (Table 7.8 and Table 7.9). Scenarios with $E_{\mathrm{T}}^{\mathrm{miss}} < 100$ GeV are not discussed in this thesis. Finally, the impossibility of loosening the p_{T} thresholds on light and heavy flavour jets has been found to be the key limiting factor to increase the sensitivity of the search for these two strategies. The b-jet and multi-jet triggers are seeded by the L1 jet trigger `L1_J10`, therefore the offline selection must require the jets to have $p_{\mathrm{T}} > 60$ GeV, with the total jet multiplicity depending on the strategy pursued. Overall, none of the selections relying on these two trigger are found to perform better than the jet+$E_{\mathrm{T}}^{\mathrm{miss}}$ trigger strategy for the three topologies studied.

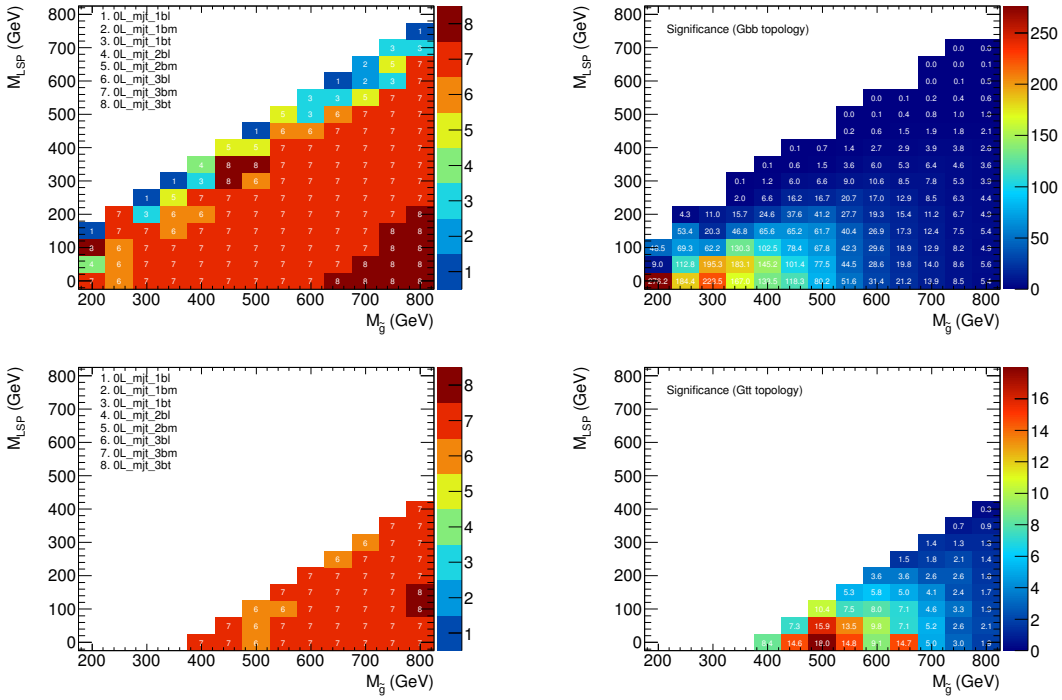

Figure 7.10 Best set of cuts (left) and the corresponding significances (right) using a multi-jet trigger strategy for a given point in the gluino/LSP mass plane, for the Gbb (top) and Gtt (bottom) topologies. The 3 b-tag analysis covers more than 95% of the total mass plane in each case.

7.6.6 Summary of most promising 0-lepton signal regions

The final selection is composed of five signal regions, each sensitive to a different region in the gluino/LSP mass plane, targeting the Gbb and the Gtt topology, mostly. These SRs are denoted Gbb-loose, Gbb-medium, Gbb-tight, Gtt-loose and Gtt-tight (with obvious notation), and they are summarized in Table 7.10. The set of five selections, despite being primarily targeted at the Gbb and Gtt topologies, is

found to be sufficient to maintain close to within 30-50% of optimal sensitivity for the Gtb topologies as well.

Overall, a 3 b-tag analysis is found to be the best scenario for more than 95% of the mass plane in the 3 different topologies studied. For Gbb, a 3 b-tag search can improve the significance with respect to previous analyses relying on 1 and 2 b-tag selections [140–142] from 200% to 500% depending on the LSP and gluino masses. Furthermore, for Gtt the gain observed with respect to the analyses mentioned above has been found to range 300-650%. This performance is obtained by requiring a higher total jet multiplicity in combination with looser b-tagging operating points, and enhanced m_{eff} and E_T^{miss} cuts. These final selections allow the 0-lepton channel to be competitive with the 1-lepton channel in the Gtt topology. Specific searches using 1 and 2 b-tagged jets may remain the best strategy for the region closest to the diagonal.

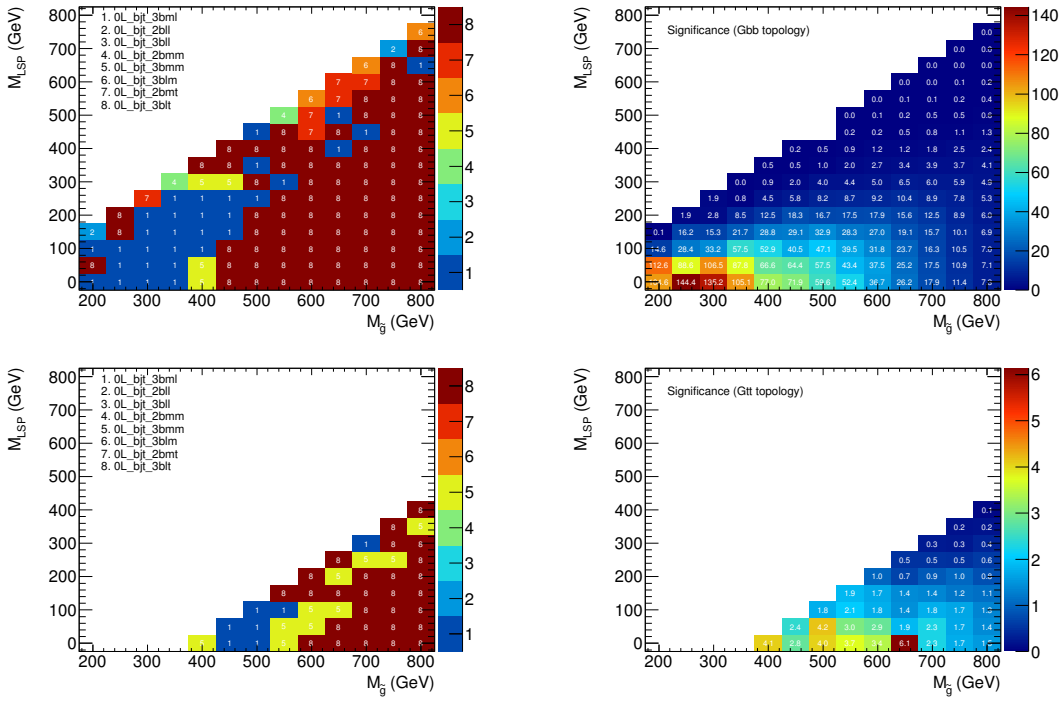

Figure 7.11 Best set of cuts (left) and the corresponding significances (right) using a b-jet trigger strategy for a given point in the gluino/LSP mass plane, for the Gbb (top) and Gtt (bottom) topologies. The 3 b-tag analysis covers more than 95% of the total mass plane in each case.

0-lepton channel signal regions	SM (5 fb^{-1})
Gbb-loose: $\geq$ 4 jets ($p_{\mathrm{T}} > 50$ GeV), $\geq$ 3 b-jets ($p_{\mathrm{T}} > 30$ GeV, OP = 2.00 (60%)), $m_{\mathrm{eff}} > 500$ GeV, $E_{\mathrm{T}}^{\mathrm{miss}} > 130$ GeV	42.9
Gbb-medium: $\geq$ 4 jets ($p_{\mathrm{T}} > 50$ GeV), $\geq$ 3 b-jets ($p_{\mathrm{T}} > 30$ GeV, OP = 2.00 (60%)), $m_{\mathrm{eff}} > 700$ GeV, $E_{\mathrm{T}}^{\mathrm{miss}} > 130$ GeV	13.9
Gbb-tight: $\geq$ 4 jets ($p_{\mathrm{T}} > 50$ GeV), $\geq$ 3 b-jets ($p_{\mathrm{T}} > 30$ GeV, OP = 0.35 (70%)), $m_{\mathrm{eff}} > 900$ GeV, $E_{\mathrm{T}}^{\mathrm{miss}} > 130$ GeV	8.4
Gtt-loose: $\geq$ 6 jets ($p_{\mathrm{T}} > 50$ GeV), $\geq$ 3 b-jets ($p_{\mathrm{T}} > 30$ GeV, OP = 0.35 (70%)), $m_{\mathrm{eff}} > 700$ GeV, $E_{\mathrm{T}}^{\mathrm{miss}} > 150$ GeV,	11.1
Gtt-tight: $\geq$ 6 jets ($p_{\mathrm{T}} > 50$ GeV), $\geq$ 3 b-jets ($p_{\mathrm{T}} > 30$ GeV, OP = -1.25 (80%)), $m_{\mathrm{eff}} > 900$ GeV, $E_{\mathrm{T}}^{\mathrm{miss}} > 200$ GeV,	10.7

Table 7.10 Summary of the most promising b-jets + $E_{\mathrm{T}}^{\mathrm{miss}}$ signal regions (three (two) targeting Gbb (Gtt) topologies) after the optimization procedure. The Standard Model background yield prediction for each particular region is also shown.

7.7 Final event selection

The optimization analysis presented in the sections above was performed before the end of the 2011 data-taking campaing. Two major changes took place during the second half of 2011 that forces us to reassess the optimization:

1. the trigger menu used for the data periods L and M reaches the plateau for an offline $E_{\mathrm{T}}^{\mathrm{miss}}$ cut of 160 GeV,

2. the brand-new `MV1` b-tagging algorithm is currently recommended by the ATLAS Flavour Tagging WG since it has a lower mistag rate efficiency than `JetFitterCOMBNN`.

The signal regions Gbb-loose, Gbb-medium, Gbb-tight, Gtt-loose and Gtt-tight have been slightly changed after the re-optimization, and from now on they are denoted as SR4-L, SR4-M, SR4-T, SR6-L, and SR6-T, respectively. The final event selection is summarized for each signal region in Table 7.11.

Cut	Description	Signal region				
		SR4-L	SR4-M	SR4-T	SR6-L	SR6-T
1	Data quality	Run / lumi block appears in SUSY GRL				
2	Trigger	Period B : EF_j75_a4_EFFS_xe45_loose_noMu Periods D-K : EF_j75_a4tc_EFFS_xe45_loose_noMu Periods L-M : EF_j75_a4tc_EFFS_xe55_noMu MC : None				
3a	Jet cleaning	No VeryLooseBad bad jets with $p_T > 20$ GeV after jet-electron overlap removal				
3b	Jet cleaning	No jet with chf < 0.02 and $\|\eta\| < 2.0$ after jet-electron overlap removal amongst the				
		4 leading jets			6 leading jets	
4	LAr hole treatment	Apply the "Smart" LAr hole veto				
5	Cosmic cleaning	No muon after overlap removal with $\|z_\mu - z_{PV}\| > 1$ mm, $d_0 > 0.2$ mm				
6	Bad muons cleaning	No pre-selected muons before overlap removal with $\sigma(1/p)/\|1/p\| > 0.2$				
7	Event cleaning	Leading primary vertex with > 4 tracks				
8	Lepton veto	No pre-selected e/μ after overlap removal with $p_{\mathrm{T}} > 20/10$ GeV				
9	$E_{\mathrm{T}}^{\mathrm{miss}}$	> 160 GeV				> 200 GeV
10	Leading jet	$p_{\mathrm{T}}(j_1) > 130$ GeV, $\|\eta\| < 2.8$				
11	jet multiplicity	$\geqslant 4$ jets with $p_T > 50$ GeV, $\|\eta\| < 2.8$			$\geqslant 6$ jets with $p_T > 50$ GeV, $\|\eta\| < 2.8$	
12	$\Delta\phi_{min}(E_{\mathrm{T}}^{\mathrm{miss}}, \mathrm{j}_i)$	> 0.4 ($i = \{1, 2, 3\}$)				
13	$E_{\mathrm{T}}^{\mathrm{miss}}/\mathrm{m}_{\mathrm{eff}}(\mathrm{Nj})$	> 0.2 (4j)			> 0.2 (6j)	
14	# b-jets	$\geqslant 3$ b-jets with $p_T > 30$ GeV, $\|\eta\| < 2.5$ (MV1-tagger)				
	OP	60%		70%		75%
15	$\mathrm{m}_{\mathrm{eff}}$ (Nj)	> 500 GeV $> (4j)$	> 700 GeV (4j)	> 900 GeV (4j)	> 700 GeV (6j)	> 900 GeV (6j)

Table 7.11 Summary of the event selection in each signal region.

8

Background estimation

This chapter presents the strategies implemented to estimate the SM background yields in all signal regions. The SM processes with exactly the same final state as those expected from the SUSY signals are referred to as irreducible background, whereas those processes that pass the SR cuts because at least one of the final objects in the event is incorrectly identificated (i.e., it derives from a different physics object) are referred to as reducible background.

Section 8.1 describes a data-driven method, based on the jet response smearing technique, implemented to estimate the reducible background contribution from multi-jet events. Section 8.2 presents the different techniques used to estimate the non-multi-jet SM backgrounds. The production of $t\bar{t}$ in association with additional jets, followed by the leptonic decay of one W boson, where the lepton is not reconstructed or misidentified as a jet (mainly through the hadronic decays of a τ lepton) is expected to be the main source of reducible background. This contribution is estimated using a semi data-driven method that essentially relies on control regions enriched in $t\bar{t}$ events, and chosen to be kinematically similar to the signal regions. The number of $t\bar{t}$ events in each signal region is then estimated by multiplying the event yield observed in data in the corresponding control region by a transfer factor, extracted from MC simulations. The reducible background from single top, $t\bar{t}$+W/Z and W/Z+heavy-flavour jets, and the irreducible $t\bar{t}$+$b\bar{b}$ background are all estimated from MC simulation. Finally, Section 8.3 presents the $t\bar{t}$ background transfer factors validation using the 1-lepton channel, in order to study the reliability of the MC extrapolation for different b-jet multiplicities.

8.1 Multi-jet background estimation

The multi-jet background arises from events where the energy of one or possibly many jets fluctuate to give rise to $E_{\mathrm{T}}^{\mathrm{miss}}$. The very small probability for a multi-jet event to pass the signal region selection cuts (which include a hard $E_{\mathrm{T}}^{\mathrm{miss}}$ cut) combined with the large multi-jet cross section, makes this background very difficult to estimate. In particular, to obtain statistically meaningful results using a Monte Carlo technique, the simulation of a prohibitively large sample would be required. Therefore, this background needs to be estimated in a data-driven way. The procedure used in this work is referred to as the jet smearing method [263]. Essentially, it consists in repeatedly smearing the momentum of jets in clean multi-jet data events with little $E_{\mathrm{T}}^{\mathrm{miss}}$ to generate pseudoevents with possibly large $E_{\mathrm{T}}^{\mathrm{miss}}$ values. The jet smearing method proceeds in four steps:

1. Selection of low $E_{\mathrm{T}}^{\mathrm{miss}}$ significance seed events with at least the same number of jets as in the analysis. These events are dominated by QCD multi-jet process, as shown in Section 7.6.3.

2. Construction of the full smearing function using a sample of simulated dijet events. The differences between data and MC are corrected by in-situ measurements.

3. Smearing of the momentum of jets in the seed events selected in (1) using the smearing function defined in (2). This operation is repeated N_{smear}=10000 times per seed event to randomly generate configurations where the $E_{\mathrm{T}}^{\mathrm{miss}}$ comes from multiple fluctuating jets.

4. Once a large sample of pseudo-events is generated, these are passed through the same analysis cuts as the data and the non-multi-jet MC to give the multi-jet distribution of any variable of interest. The resulting distributions are then normalized to a multi-jet enriched control region which is constructed by reverting the $\Delta\phi_{min}$ cut and substracting the non-multi-jet component based on MC expectations.

8.1.1 Seed selection

The seed events must mirror the analysis selection as much as possible but it must also ensure that the jets in the events are well-measured, with little or no jet energy fluctuations. The seed selection cannot use events from the signal trigger as this includes a hard $E_{\mathrm{T}}^{\mathrm{miss}}$ cut (Section 7.3.2). Hence a set of prescaled single-jet triggers with different p_{T} thresholds are used instead, as listed in Table 8.1.

The events passing a given trigger are retained only if they have a jet within the plateau of the turn on curve of such trigger, to avoid biasing the event distributions

towards high p_{T} jet fluctuations. In addition, the events are weighted by the average prescale within their corresponding period (Table 8.1). Since events with a high p_T jet also pass the single-jet triggers with low p_T thresholds, the prescale chosen is that of the hardest trigger for which the jet in the event is on the plateau. Thus, e.g., if `EF_j180_a4tc_EFFS` is fired and the leading jet has 300 GeV $\leq p_{\mathrm{T}}^{1} <$ 400 GeV, then the prescale for this item is used. Soft jet triggers are essential as they allow for the selection of events with softer jets than those in the default analysis. These events might be promoted into the signal region by jet energy mismeasurement and hence must be included in the seed sample.

In order to select events with small jet energy fluctuations, a cut on the $E_{\mathrm{T}}^{\mathrm{miss}}$ significance

$$S = \frac{E_{\mathrm{T}}^{\mathrm{miss}}}{\sqrt{\sum E_{\mathrm{T}}}} \tag{8.1}$$

is applied. $\sum E_T$ is the event scalar sum, where the sum runs over all reconstructed objects and also the clusters not belonging to any selected objects, as discussed in Section 5.7. Only the events satisfying $S < 0.6$ GeV$^{1/2}$ are kept. The set of cuts used to select seed events is the following:

- Trigger requirement dependent on the leading jet p_{T} (Table 8.1).
- At least three jets with $p_T > 30$ GeV.
- $S < 0.6$ GeV$^{1/2}$.

Trigger Name	leading jet p_{T} range	Average Prescale	
		Period B	Period H
`EF_j55_a4tc_EFFS`	$110 \leq p_{\mathrm{T}}^{1} < 140$	592	6445
`EF_j75_a4tc_EFFS`	$140 \leq p_{\mathrm{T}}^{1} < 180$	159	1730
`EF_j100_a4tc_EFFS`	$180 \leq p_{\mathrm{T}}^{1} < 230$	46.9	475
`EF_j135_a4tc_EFFS`	$230 \leq p_{\mathrm{T}}^{1} < 300$	1.94	122
`EF_j180_a4tc_EFFS`	$300 \leq p_{\mathrm{T}}^{1} < 400$	1.00	28.5
`EF_j240_a4tc_EFFS`	$400 \leq p_{\mathrm{T}}^{1}$	1.00	1.00

Table 8.1 The 2011 single-jet trigger chains used to select seed events in the Jet Smearing method.

8.1.2 The smearing function

The jet smearing function is derived using the PYTHIA QCD samples (Section 6.1), and obtained from the ratio of the reconstructed jet p_{T} to the truth jet p_{T}:

$$R = \frac{p_{\mathrm{T}}^{\mathrm{reco-jet}}}{p_{\mathrm{T}}^{\mathrm{true-jet}}} \ , \tag{8.2}$$

where its shape is built by calculating R for each reconstructed jet in bins of $p_{\mathrm{T}}^{\mathrm{true-jet}}$, of 20 GeV each. The p_{T} of any neutrinos within $\Delta R(\mathrm{jet}, \nu) < 0.4$ of the jet are added back to the $p_{\mathrm{T}}^{\mathrm{true-jet}}$, to ensure that the full true jet momentum is taken into account. The resulting two-dimensional response is shown in Figure 8.1.

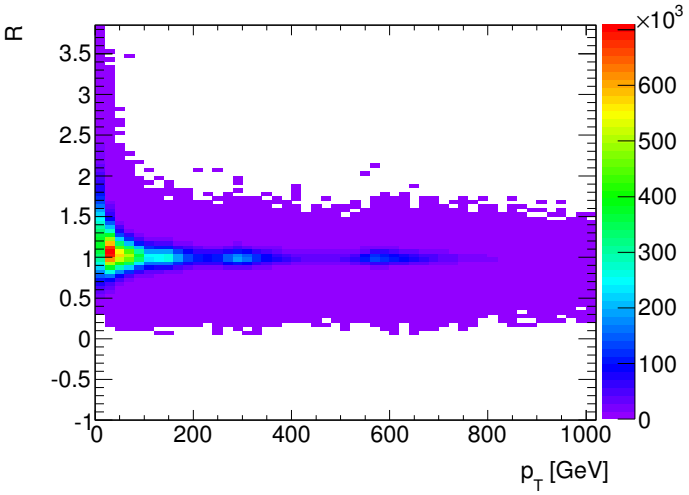

Figure 8.1 The respose function binned in true p_{T} as calculated using PYTHIA QCD samples.

Since heavy flavour jets have in general a different response function than light jets, the response for b-tagged jets is stored separately and jets are smeared using the appropriate function depending on their JetFitterCOMBNN weight. An OP corresponding to 60% efficiency as determined in $t\bar{t}$ events is used to define a b-jet, both in the construction of the response and to decide which function is to be used to smear a jet. The larger number of neutrinos present in heavy flavour jets results in a broader low side tail response as it can be seen in Figure 8.2 which compares the response functions in different true p_{T} ranges for true b-jets, b-tagged jets and un-tagged jets.

The MC modelling of the Gaussian component of the response, σ_R, is investigated using the dijet balance asymmetry (see Section 6.4.1), as defined in Eq. 6.1, where its width, denoted by σ_A, is related to σ_R by means of Eq. 6.2. The jet p_{T} resolutions in MC are narrower than in the data, therefore the Gaussian component obtained

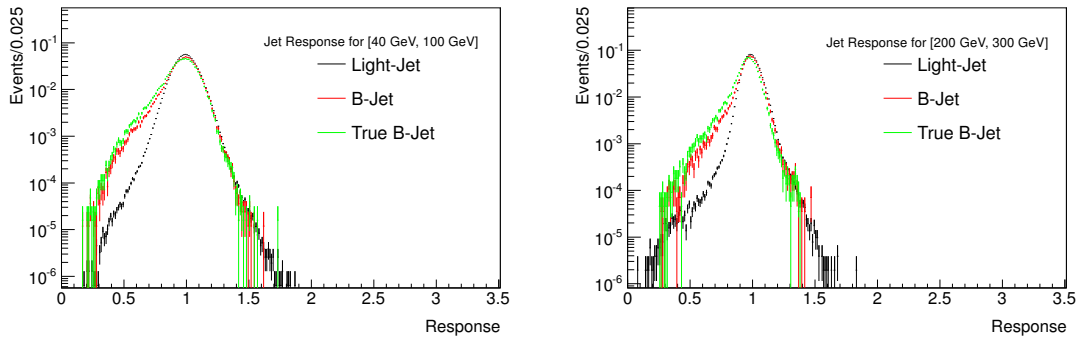

Figure 8.2 The response function for b-tagged jets (red), true b-jets (green) and untagged jets (black), as calculated using MC samples in the truth p_{T} ranges $[40, 100]$ GeV (left) and $[200, 300]$ GeV (right).

from MC is oversmeared to reduce the difference between the data and the smeared samples. The values of the correction run between 2% for jets with $p_T > 500$ GeV to 4% for jets with $p_T < 130$ GeV, in agreement with the results presented in Chapter 6.

In the case of the di-jet asymmetry, upper and lower fluctuations of jet p_{T} cannot be distinguished. The analysis of the so-called 3-jet "Mercedes" events[1] allows for an examination of both the up-side and low-side response tails of jets. Thus, the tails of the smearing function are validated on data using a sample of three-jet events where the $E_{\mathrm{T}}^{\mathrm{miss}}$ is unambiguously aligned with one of the jets, and hence can be attributed to the fluctuation of that jet. In these cases one can estimate the true transverse momentum vector of the jet by adding back an $\vec{E}_{\mathrm{T}}^{\mathrm{miss}}$ vector whose components are $E_{\mathrm{x(y)}}^{\mathrm{miss}}$. The response of this jet, denoted by R_2, is defined as (in analogy with Eq. 8.2)

$$R_2 \simeq \frac{\vec{p}_{\mathrm{T}}^{J} \cdot (\vec{p}_{\mathrm{T}}^{J} + \vec{E}_{\mathrm{T}}^{\mathrm{miss}})}{|\vec{p}_{\mathrm{T}}^{J} + \vec{E}_{\mathrm{T}}^{\mathrm{miss}}|^2}, \tag{8.3}$$

where $\vec{p}_{\mathrm{T}}^{J}$ is understood to be the reconstructed p_{T} of the jet associated with the $E_{\mathrm{T}}^{\mathrm{miss}}$. The Mercedes analysis is done with events satisfying the following selection:

- At least three jets with $p_T > 130, 40, 40$ GeV.
- $E_{\mathrm{T}}^{\mathrm{miss}} \geq 30$ GeV parallel or anti-parallel to one of the jets. To ensure this condition, the jets are ordered in increase azimuthal distance from $E_{\mathrm{T}}^{\mathrm{miss}}$ as: $\phi_i = \Delta\Phi(J_i, E_{\mathrm{T}}^{\mathrm{miss}})$, with $i = 1 \ldots n$. Two configurations are considered:
  - Parallel: In this case the $E_{\mathrm{T}}^{\mathrm{miss}}$ is a product of an underfluctuation and one requires that $|\phi_1| < 0.1$. To rule out the cases where the source of the

[1] Such events are known as Mercedes events because of their resemblence to the three-pronged Mercedes logo.

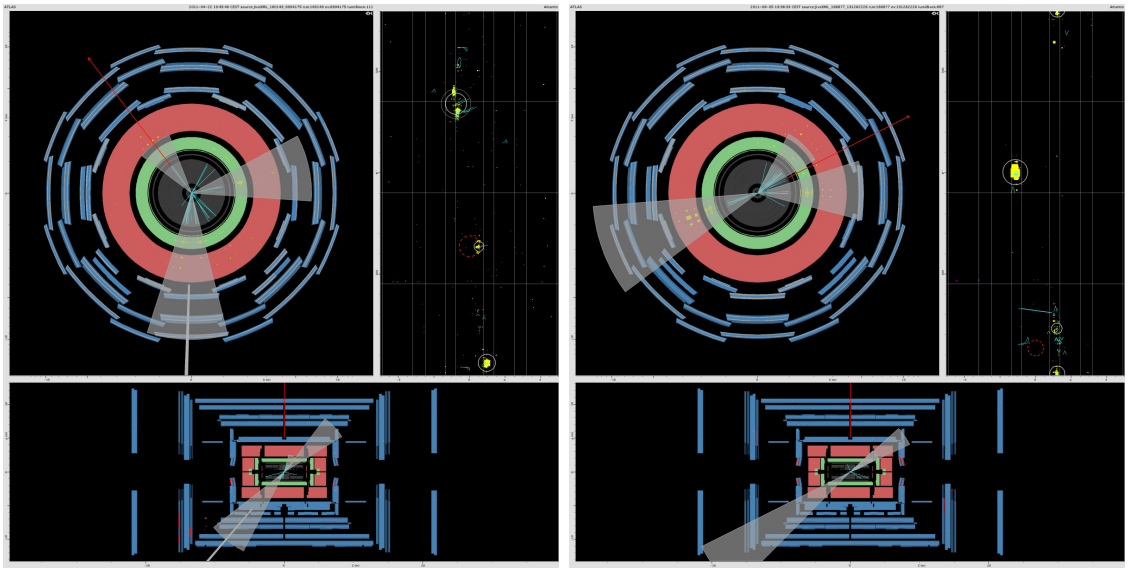

Figure 8.3 Event display of a Mercedes event in the parallel configuration (left) taken from Run 184169 (Event 89595740) and one in the anti-parallel configuration taken from Run 180481 (Event 28450185).

$E_{\mathrm{T}}^{\mathrm{miss}}$ is ambiguous, the $E_{\mathrm{T}}^{\mathrm{miss}}$ is also required to be well separated from the jets in ϕ by requiring $|\phi_1| < \pi - |\phi_n|$, and $|\phi_{(n-1)}| > 0.5$.

– Anti-Parallel: in this scenario, the $E_{\mathrm{T}}^{\mathrm{miss}}$ is the product of a jet energy over-estimate and so it is required to be on the opposite side of the event from one of the jets. This topology is enforced by requiring $\pi - |\phi_n| < |\phi_1|$, $\pi - |\phi_1| < 0.1$ and $\pi - |\phi_{(n-1)}| > 0.5$.

Figure 8.3 shows two examples of the parallel and antiparallel selection in the data. The results obtained from the jet smearing method (coupled with the dijet balance corrections) are found to be a reasonable estimate of the response tails of jets in data. The comparison between the Jet Smearing method and data estimates, within multi-jet enriched control regions, is discussed next.

8.1.3 Normalization and validation

The final numbers pertaining to the normalization of the smeared events can be calculated within a multi-jet-enriched control region, constructed in essence by reversing the $\Delta\phi_{min}$ cut. The labeling of the QCD CRs and their corresponding SRs is as follows:

- Gbb-CR (with OP = 60% and OP = 70%): for SR4-L/SR4-M and SR4-T, respectively.
- Gtt-CR (with OP = 60% and OP = 70%): for SR6-L and SR6-T, respectively.

The selection cuts for the QCD CRs are summarized below:

- Preselection cuts.
- Lepton (e,μ) veto.
- Leading jet with $p_T > 130$ GeV and $|\eta| < 2.8$.
- $N_j \geqslant 4$ and 6, with jet $p_T > 50$ GeV and $|\eta| < 2.8$, for the control regions labelled Gbb-CR and Gtt-CR, respectively.
- $E_{\mathrm{T}}^{\mathrm{miss}} > 160$ GeV.
- $\Delta\phi_{min} < 0.4$ (reversed cut).
- At least 3 b-jets with $p_T > 30$ GeV and $|\eta| < 2.5$, using different operating points for Gbb-CR and Gtt-CR according to their corresponding signal regions.
- $\mathrm{m_{eff}}(N_j) > 500$ GeV, with $N_j = 4$ and 6, for the control regions labelled Gbb-CR and Gtt-CR, respectively.

These QCD CRs are used to validate the smearing method and to determine the expected contribution of multi-jet events for each of the signal regions, denoted $N_{\mathrm{QCD}}^{\mathrm{SR}}$, by normalizing the smeared samples to data as follows:

$$N_{\mathrm{QCD}}^{\mathrm{SR}} = \frac{\left[N_{\mathrm{data}}^{\mathrm{QCDCR}} - N_{\mathrm{non-QCD,MC}}^{\mathrm{QCDCR}}\right]}{N_{\mathrm{QCD,smeared}}^{\mathrm{QCDCR}}} N_{\mathrm{QCD,smeared}}^{\mathrm{SR}} \,. \tag{8.4}$$

Figure 8.4 shows the distributions of the first- and second-leading jet p_{T}, $E_{\mathrm{T}}^{\mathrm{miss}}$, and $\mathrm{m_{eff}}$, for Gbb-CR (with OP = 60 %), after normalizing the smeared samples to data. The error bars show the statistical uncertainty and the shaded band the systematics. Good agreement with respect to data is observed within the uncertainties. A similar performance has been obtained for the other multi-jet enriched control regions.

8.1.4 Systematic uncertainties in the multi-jet background

Several sources of systematic uncertainties on the jet smearing function have been investigated. They are described in this section. After modifying the smearing function by each of these sources, the resulting difference in the yields is used as a systematic uncertainty on the number of expected multi-jet events in each of the signal regions.

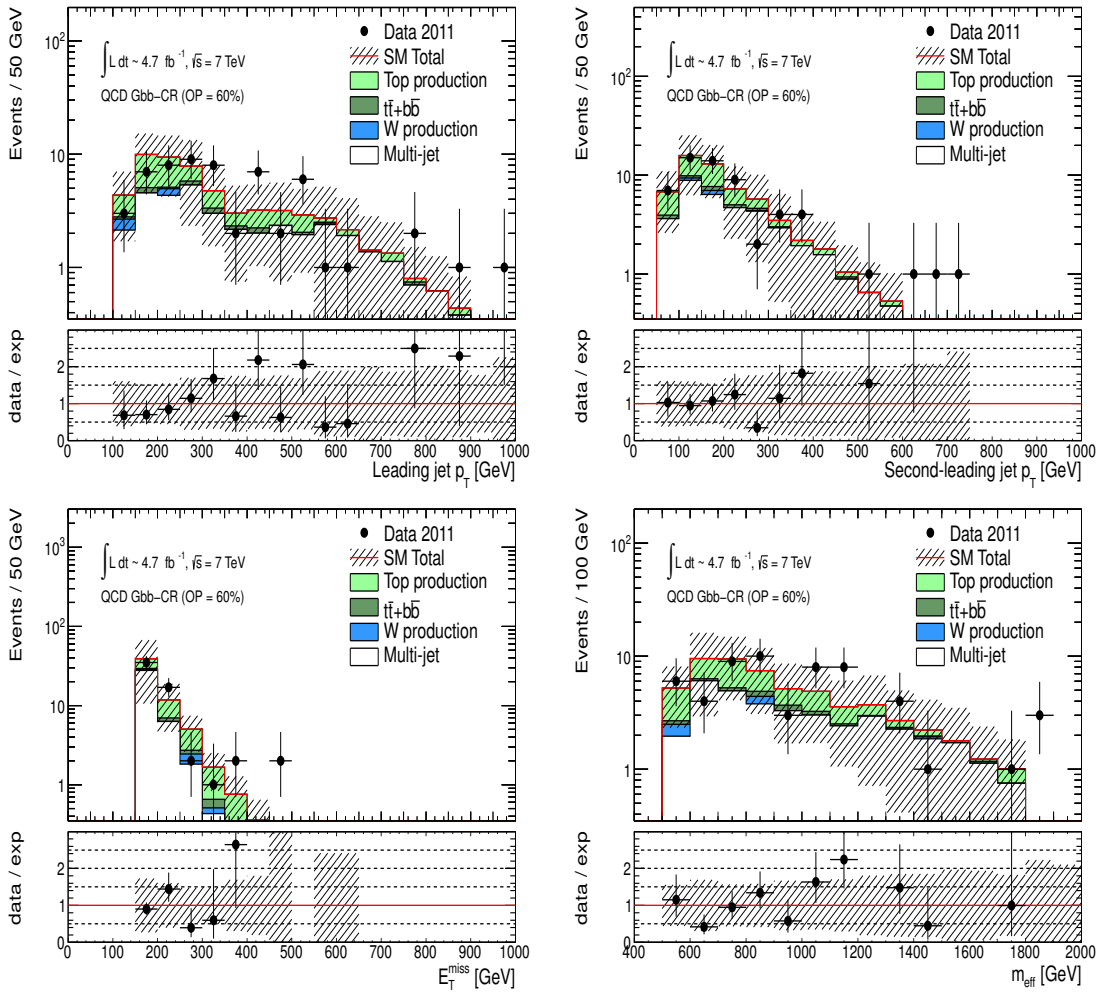

Figure 8.4 Distributions of the first- and second-leading jet p_{T}, $E_{\mathrm{T}}^{\mathrm{miss}}$, and $\mathrm{m_{eff}}$ for a multi-jet enriched control region, after requiring $\Delta\phi_{min} < 0.4$, at least 4-jets above 50 GeV, 3 b-tagged selection (with OP = 60 %), and $\mathrm{m_{eff}} > 500$ GeV (Gbb-CR). The error bars show the statistical uncertainty and the shaded band the systematics. Good agreement with respect to data is observed within the uncertainties.

Jet Energy Scale uncertainty: to evaluate the JES uncertainty in the response functions the smearing analysis is repeated with response functions having increased and descreased JES, as allowed by the data, using the JES uncertainty tool. The impact of the JES uncertainty on the multi-jet event yield in each of the SRs is summarized in Table 8.2.

Tagging uncertainty: the tagging uncertainty is taken into account by repeating the procedure to obtain the yields in the signal region but replacing the response of b-tagged and true light jets with responses constructed using true $b-$jet and light jet, instead. The difference in the yields is used as a systematic uncertainty on the number of expected multi-jet events in the signal region, and it is summarized in

Table 8.2.

Gaussian uncertainty: to estimate an uncertainty on the Gaussian component of the response function the smearing procedure is repeated using a wider response. The extent of this extra width is provided by the JER tool which is used to apply extra smearing, in the limit allowed for by the data. Since this effect is already corrected for, the resulting uncertainty is expected to be extremely conservative. The impact on the number of expected multi-jet events in the signal region is presented in Table 8.2.

Tail uncertainty: to evaluate the uncertainty on the tail the analysis is re-run after modifications to the low side tail of the response function. The tail is scaled up by a factor of 5 and a conservative estimate on the multi-jet yield in the signal region is obtained. Table 8.2 shows the resultant systematic uncertainty.

Selection	Nominal	JES	BTAG	GAUSS	TAIL
Gbb-loose	0.82±0.36	±24%	±130%	±144%	±50%
Gbb-medium	0.49±0.19	±24%	±110%	±100%	±100%
Gbb-tight	0.77±0.36	±12%	±12%	±5%	±47%
Gtt-loose	0.15±0.10	±27%	±20%	±30%	±140%
Gtt-tight	0.02±0.01	±1%	±300%	±50%	±150%

Table 8.2 Estimate of the multi-jet background and its systematic uncertainties for each of the five signal regions.

8.1.5 Final multi-jet estimate

The different sources of systematic uncertainty on the multi-jet estimate with the jet smearing method have been investigated for very pessimistic scenarios. For the final estimate of the multi-jet background, an uncertainty of 100% is assumed. The multi-jet estimate in the various signal regions is summarized in Table 8.3, along with its relative contribution to the total background. Overall, the multi-jet estimate accounts for less than 6% of the total background in all signal regions.

8.2 Non multi-jet background estimate

The strategy implemented to estimate the dominant $t\bar{t}$ background is a semi data-driven method that essentially relies on control regions enriched in $t\bar{t}$ events, with

Selection	Nominal	% SR
Gbb-loose	0.8 ± 0.8	2%
Gbb-medium	0.5 ± 0.5	3%
Gbb-tight	0.8 ± 0.8	6%
Gtt-loose	0.2 ± 0.2	2%
Gtt-tight	< 0.1	$< 1\%$

Table 8.3 Estimate of the multi-jet background for 4.7 fb^{-1} from the jet smearing method and its relative contribution to the total background in the various signal regions.

low expected yields from the targeted SUSY signals, and chosen to be kinematically similar to the signal regions. The number of $t\bar{t}$ events in each signal region is then estimated by multiplying the event yield observed in data in the corresponding control region by a transfer factor, extracted from MC simulations, which is defined as the ratio of the simulated $t\bar{t}$ event yield in the signal region to that in the control region.

Previous analyses have relied on $t\bar{t}$-enriched control regions defined by requiring exactly one lepton in the final state and applying a kinematical selection similar to that of the signal regions [142]. The requirement of one lepton in the event selection allows a relatively pure top (single and pair produced) sample but decreases significantly the statistics in the control regions. This is especially accurate in the case of a 3 b-jets analysis. Thus the lack of statistics after the 1-lepton plus 3 b-jets requirement prevents the use of 1-lepton control regions. Furthermore, the results will be interpreted in the context of the gluino-mediated stop pair production (with four top quarks in the final state, see Section 9.2), which may lead to an important signal contamination in 1-lepton plus 3 b-jets control regions. Therefore, transfer factors from exclusive 2 b-jets control regions to inclusive 3 b-jets signal regions using the 0-lepton selection are implemented for the analysis presented in this thesis. In this approach both detector related (e.g., JES and b-tagging) and theory related (e.g. $t\bar{t}$ cross section) uncertainties are expected to cancel out to a large extent in the ratio.

8.2.1 Prediction of the $t\bar{t}$ background

The inclusive $t\bar{t}$ production is the main source of SM background in all signal regions. Since the transfer factors from the 2 b-jets control regions to the 3 b-jets signal region are different between $t\bar{t}$ production in association with light jets and $t\bar{t}$ production in association with a $b\bar{b}$ pair, only the former is estimated with the semi

data-driven approach, whereas the latter is extracted from Monte Carlo simulations (Section 8.2.2).

Four control regions have been defined, differing by the requirement on the number of jets and the b-tagging operating point. They are labelled as CR4-60, CR4-70, CR6-70 and CR6-75 (Table 8.4), and defined using the following selection:

- Cuts $\#1-8$ and $\#10-13$ as introduced in Table 7.11.
- $E_{\mathrm{T}}^{\mathrm{miss}} > 160$ GeV.
- Exactly 2 b-jets with $p_{\mathrm{T}} > 30$ GeVand $|\eta| < 2.5$, using the OP at 60%, 70% and 75% for the CR labelled with 60, 70 and 75, respectively.
- $\mathrm{m_{eff}}(N_j) > 500$ GeV, with $N_j = 4$ and 6, for the control regions labelled with CR4 and CR6, respectively.

Common criteria: lepton veto, $p_{\mathrm{T}}^{j_1} > 130$ GeV, $= 2$ $b-$jets, $E_{\mathrm{T}}^{\mathrm{miss}}/\mathrm{m_{eff}} > 0.2$, $\Delta\phi_{min} > 0.4$, $E_{\mathrm{T}}^{\mathrm{miss}} > 160$ GeV, $\mathrm{m_{eff}} > 500$ GeV			
CR	N_j	b-tagging OP	corresponding SR
CR4-60	$\geq$ 4j	60%	SR4-L, SR4-M
CR4-70	$\geq$ 4j	70%	SR4-T
CR6-70	$\geq$ 6j	70%	SR6-L
CR6-75	$\geq$ 6j	75%	SR6-T

Table 8.4 Definition of the four control regions used to estimate the $t\bar{t}$+jets background.

The distributions of many key observables for both data and MC simulation are compared at each stage of the selection introduced above. The jet multiplicity is presented in Figure 8.5, after applying the cuts $\#1-13$ for the 4-jet selection and $E_{\mathrm{T}}^{\mathrm{miss}} > 160$ GeV, as introduced in Table 7.11 (i.e., before the b-tagging requirement). The distributions for the first- and second-leading jet p_{T}, the leading jet MV1 b-tagger weight and $\mathrm{m_{eff}}$ are shown in Figure 8.6, whereas the $E_{\mathrm{T}}^{\mathrm{miss}}$ distributions (for both the 4-jet and 6-jet selections) are presented in Figure 8.7. The b-jet multiplicity after requiring at least 1 b-tagged jet, with $p_{\mathrm{T}} > 30$ GeV and $|\eta| < 2.5$, for the three MV1 b-tagger operating points used in this analysis, is shown in Figure 8.8. In addition, the $E_{\mathrm{T}}^{\mathrm{miss}}$ distribution after the b-tagging requirement, for the different operating points used in the analysis, is shown in Figures 8.9 and 8.10 (for the 4-jet and 6-jet selections, respectively). For all cases, the b-tagging scale factors are

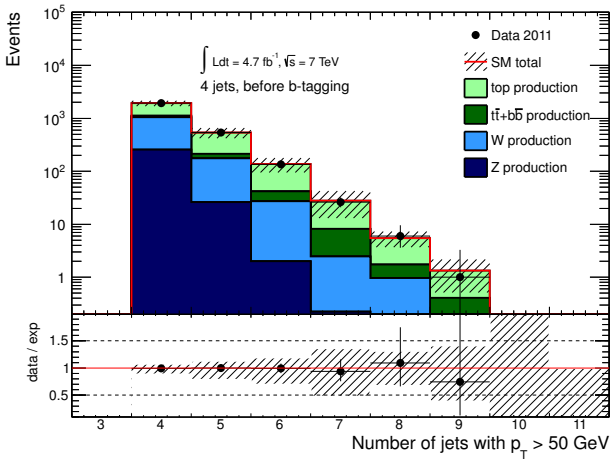

Figure 8.5 The jet multiplicity after applying the cuts #1 − 13 (for the 4-jet selection and $E_{\mathrm{T}}^{\mathrm{miss}} > 160$ GeV) as introduced in Table 7.11 (i.e., before the b-tagging requirement).

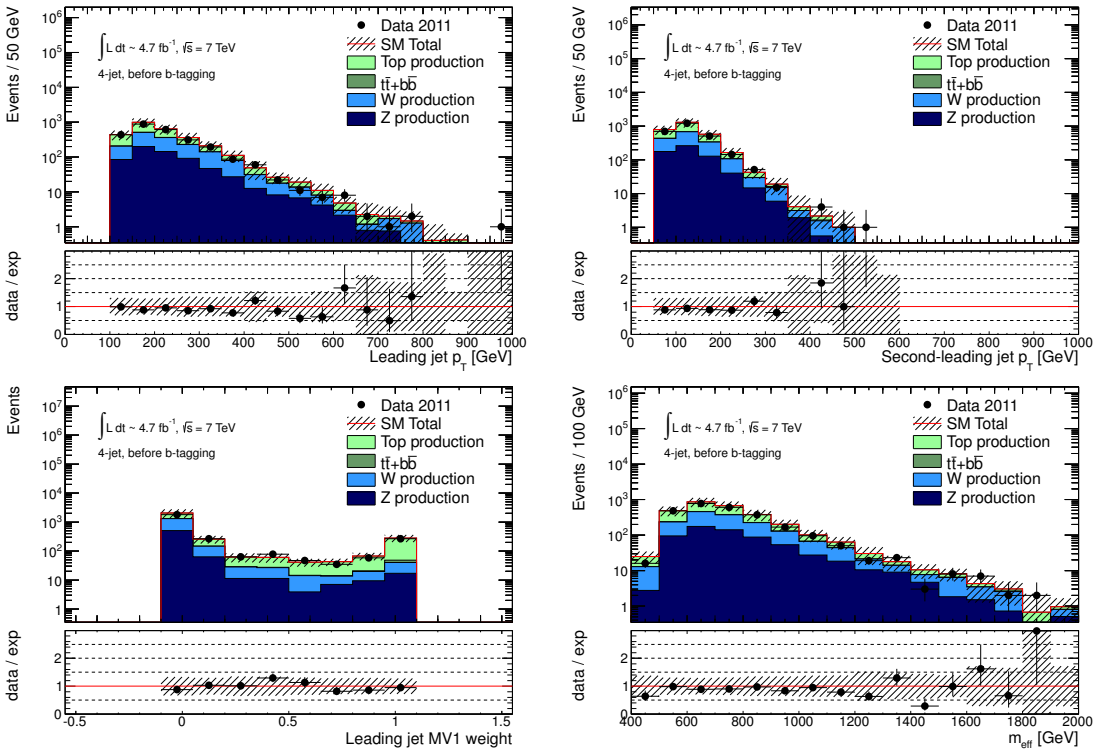

Figure 8.6 From top to bottom, left to right: the distributions of the leading jet p_{T}, the second leading jet p_{T}, the leading jet MV1 b-tagger weight and $\mathrm{m_{eff}}$ after applying the cuts #1−13 (for the 4-jet selection and $E_{\mathrm{T}}^{\mathrm{miss}} > 160$ GeV) as introduced in Table 7.11 (i.e., before the b-tagging requirement).

only applied after the b-tagging requirement. Overall, a good agreement is observed between data and MC simulation, well within uncertainties.

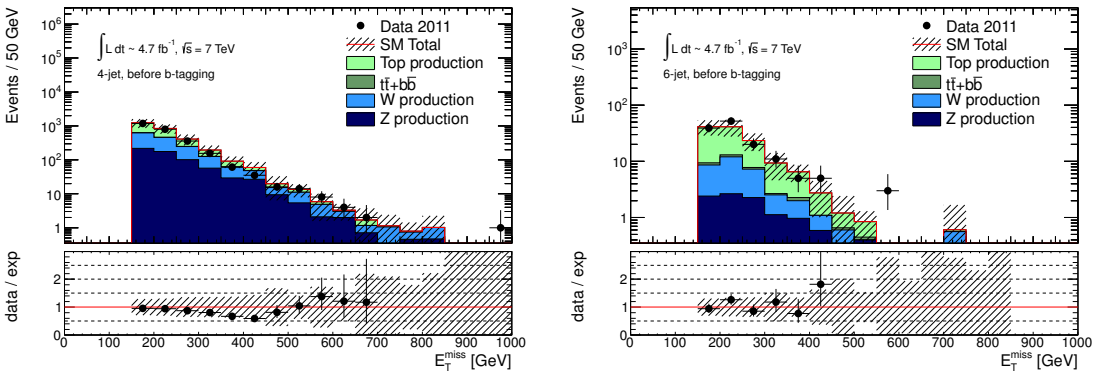

Figure 8.7 The $E_{\mathrm{T}}^{\mathrm{miss}}$ distribution for the 4-jet (left) and 6-jet (right) selections, after applying the cuts $\#1-13$ (for $E_{\mathrm{T}}^{\mathrm{miss}} > 160$ GeV) as introduced in Table 7.11 (i.e., before the b-tagging requirement).

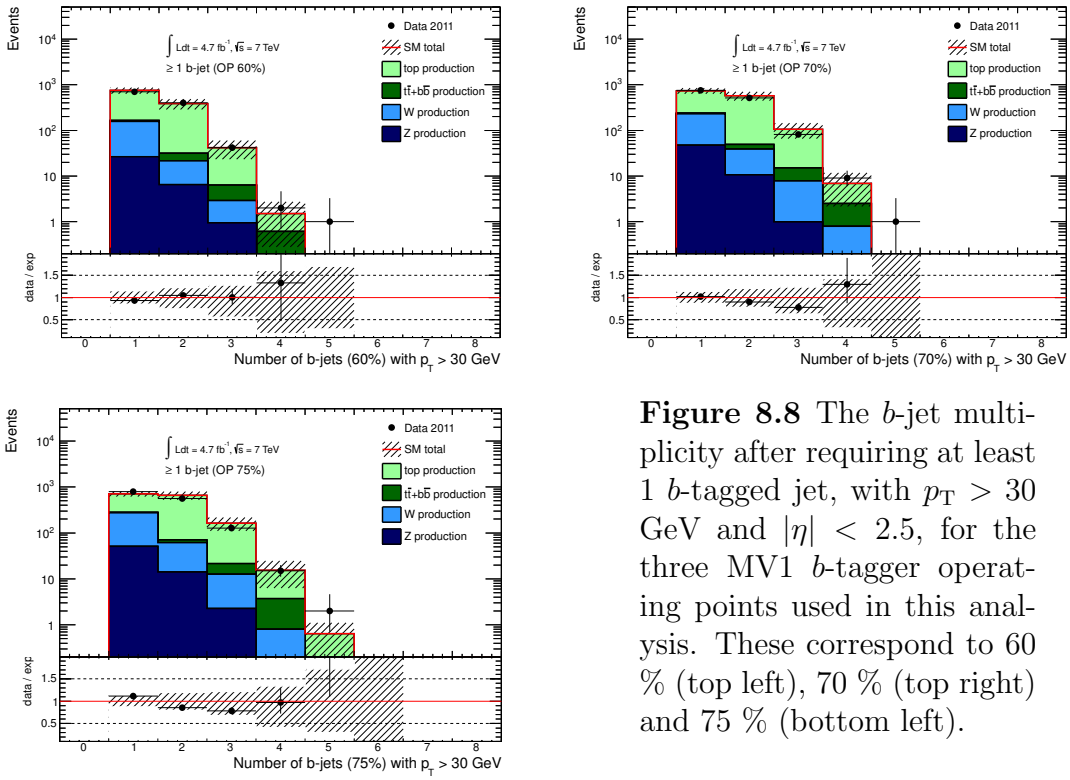

Figure 8.8 The b-jet multiplicity after requiring at least 1 b-tagged jet, with $p_{\mathrm{T}} > 30$ GeV and $|\eta| < 2.5$, for the three MV1 b-tagger operating points used in this analysis. These correspond to 60 % (top left), 70 % (top right) and 75 % (bottom left).

The distributions of the first-, second- and third-leading jet p_{T} and their corresponding MV1 b-tagger weights, $E_{\mathrm{T}}^{\mathrm{miss}}$ and $\mathrm{m_{eff}}$ are shown in Figures 8.11 and 8.12 for the CR4-60 and CR6-70, respectively. In addition, two signal points (with small and large mass splitting between the gluino and the LSP) for Gbb and Gtt topologies are also overlaid for each of the control regions with 4-jet and 6-jet selections, respectively, to illustrate possible signal contamination in the control regions. Overall, the agreement between data and the MC prediction is reasonable within the uncertainties in all cases. Similar results have been observed for CR4-70 and CR6-75.

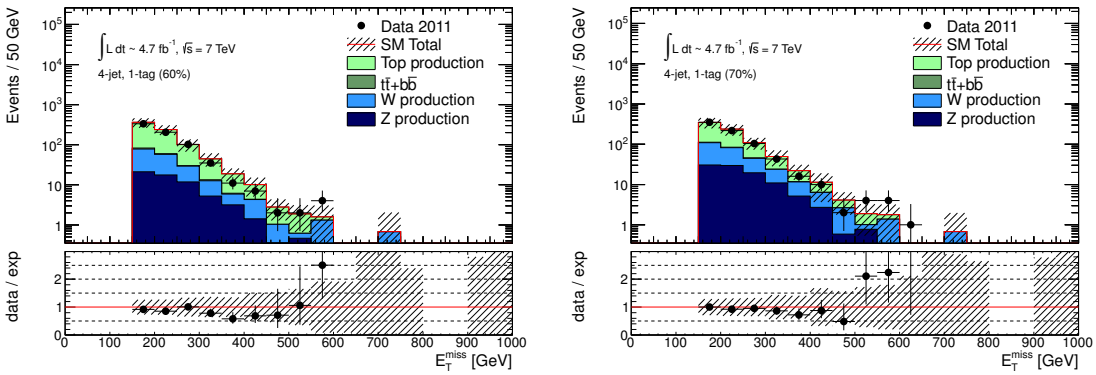

Figure 8.9 The $E_{\mathrm{T}}^{\mathrm{miss}}$ distribution after requiring at least 1 b-tagged jet, with $p_{\mathrm{T}} > 30$ GeV and $|\eta| < 2.5$, using the 60% (left) and 70% (right) MV1 b-tagger operating points (for the 4-jet selection). The b-tagging scale factor are only applied after the b-tagging requirement.

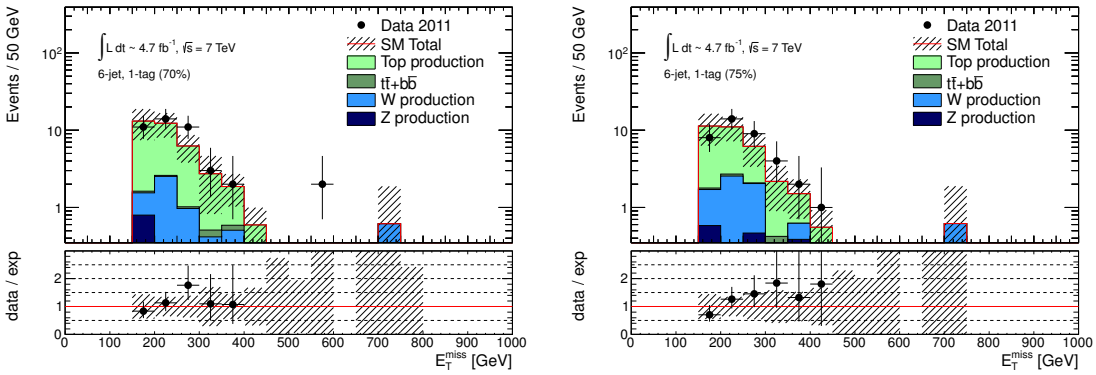

Figure 8.10 The $E_{\mathrm{T}}^{\mathrm{miss}}$ distribution after requiring at least 1 b-tagged jet, with $p_{\mathrm{T}} > 30$ GeV and $|\eta| < 2.5$, using the 70% (left) and 75% (right) MV1 b-tagger operating points (for the 6-jet selection). The b-tagging scale factor are only applied after the b-tagging requirement.

Table 8.5 shows the expected background composition of all control regions. The total number of expected SM events is also compared to the measured number of data events in 4.7 fb^{-1}, in the four $t\bar{t}$ control regions, where the contribution from $t\bar{t}$+jets events at this point is taken directly from MC simulation. The contributions from single top, $t\bar{t}$+$b\bar{b}$, $t\bar{t}$+W/Z and W/Z+jets processes are estimated from MC simulation (see Section 8.2.2), whereas the contribution from multi-jet events is estimated with the jet response smearing technique (see Section 8.1). Overall, the expected numbers of SM events and observed data events in the four control regions are found to be in agreement well within uncertainties.

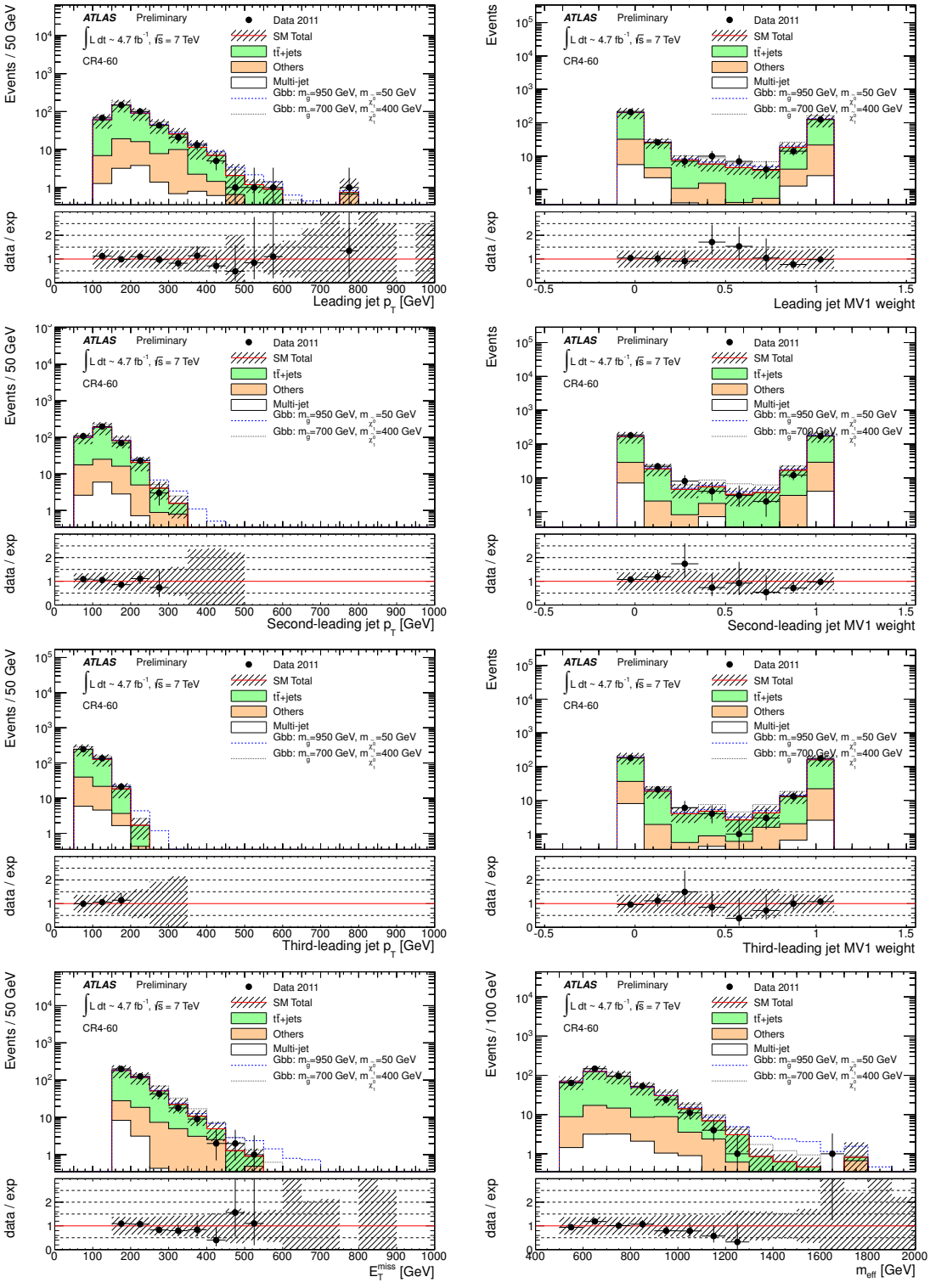

Figure 8.11 From top to bottom, left to right: the first-, second-, third-leading jet p_{T} and their MV1 b-tagger weights, $E_{\mathrm{T}}^{\mathrm{miss}}$ and $\mathrm{m_{eff}}$ distributions in CR4-60. Two signal points (with small and large mass splitting between the gluino and the LSP) for Gbb topologies are overlaid.

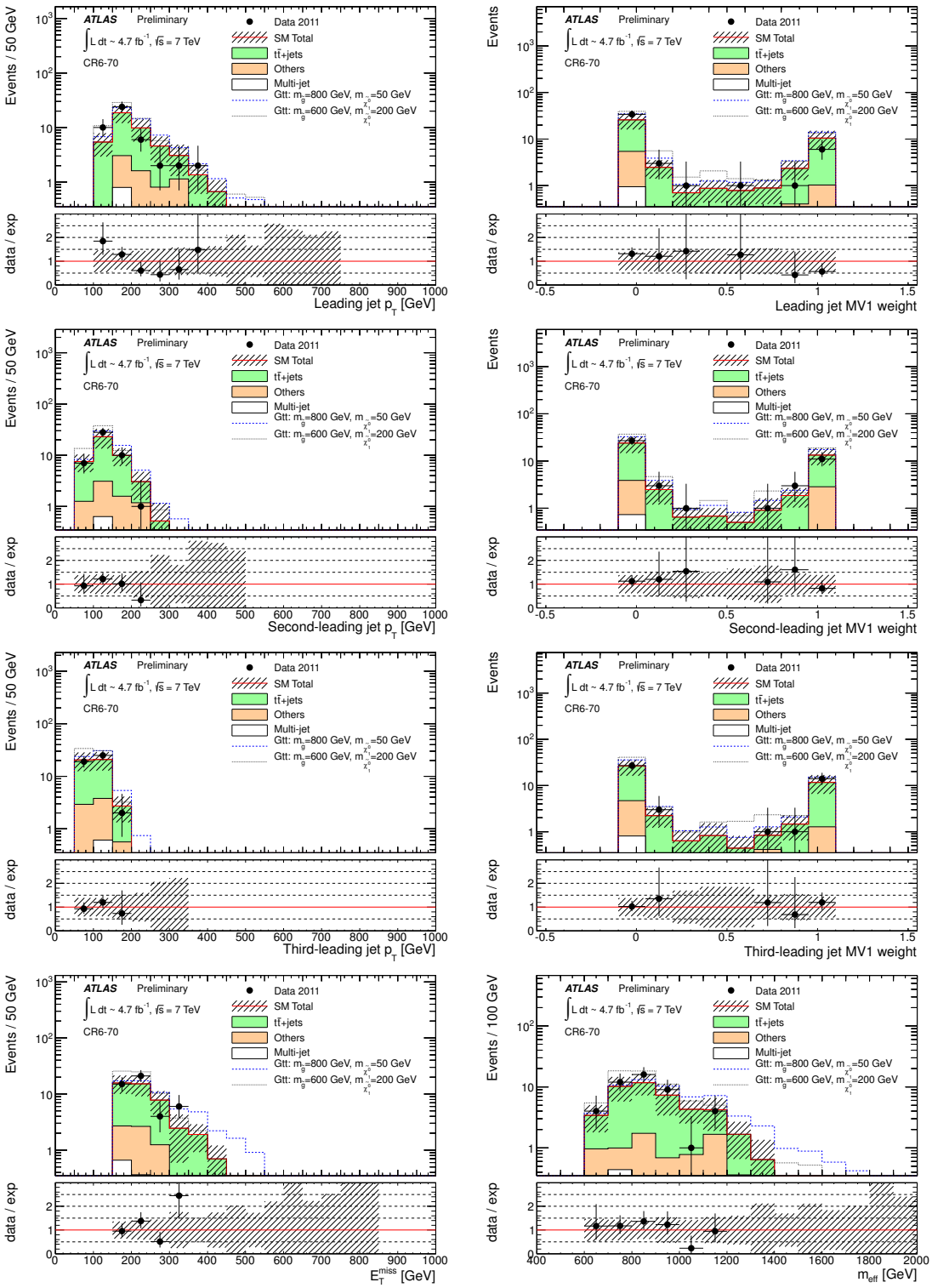

Figure 8.12 From top to bottom, left to right: the first-, second-, third-leading jet p_{T} and their MV1 b-tagger weights, $E_{\mathrm{T}}^{\mathrm{miss}}$ and $\mathrm{m_{eff}}$ distributions in CR6-70. Two signal points (with small and large mass splitting between the gluino and the LSP) for Gtt topologies are overlaid.

The detector-related systematic uncertainties are presented in Table 8.6. They are dominated by the jet energy scale (JES) and resolution (JER) uncertainties, and the uncertainty on the b-tagging efficiency and mistag rates. They have been evaluated as discussed in Section 7.4. The theoretical systematic uncertainties in the modelling of the $t\bar{t}$+jets background are presented in Table 8.7 and split in different sources, as introduced in Section 7.4.

CR	$t\bar{t}$+jets	others	SM	data
CR4-60	330 ± 90	65 ± 25	395 ± 115	402
CR4-70	490 ± 125	100 ± 35	590 ± 160	515
CR6-70	38 ± 11	7 ± 3	45 ± 13	46
CR6-75	40 ± 12	10 ± 4	50 ± 15	52

Table 8.5 Expected numbers of SM events and observed data events in the four $t\bar{t}$ control regions. The contribution from $t\bar{t}$+jets events is taken directly from MC simulation. The column "others" includes the contributions from single top, $t\bar{t}$+$b\bar{b}$, $t\bar{t}$+W/Z and W/Z+jets processes (also estimated from MC simulation), and the contribution from multi-jet events (as estimated by the jet smearing technique). The column "SM" shows the total expected background and is the sum of the columns "$t\bar{t}$+jets" and "others". The uncertainties presented include all detector-related systematic uncertainties.

CR	Events	MC Stat	JES	JER	cluster	b-tag	lumi	Total
CR4-60	330	2%	$^{+20}_{-18}$ %	4%	$^{+1}_{-0}$ %	$^{+18}_{-17}$ %	4%	27%
CR4-70	490	1%	$^{+20}_{-18}$ %	4%	$^{+1}_{-0}$ %	$^{+15}_{-14}$ %	4%	26%
CR6-70	38	4%	$^{+25}_{-24}$ %	6%	$^{+1}_{-1}$ %	$^{+13}_{-13}$ %	4%	29%
CR6-75	40	4%	$^{+27}_{-24}$ %	5%	$^{+0}_{-1}$ %	$^{+11}_{-10}$ %	4%	30%

Table 8.6 Monte Carlo based $t\bar{t}$ background estimation in the control regions and associated systematic uncertainties. The number of events corresponds to 4.7 fb^{-1}.

The predicted $t\bar{t}$ background in the 3 b-jets signal regions, $N^{Pred,t\bar{t}}_{SR^i(3b)}$, is estimated by normalising the MC event yield in the signal region to the extrapolated event yield observed in a $t\bar{t}$-dominated 2 b-jets control region, as follows:

$$N^{Pred,t\bar{t}}_{SR^i(3b)} = (N^{data}_{CR^i(2b)} - N^{MC,non-t\bar{t}}_{CR^i(2b)}) \times T_f^{2b\to 3b} \text{ , with } T_f^{2b\to 3b} \equiv \frac{N^{MC,t\bar{t}}_{SR^i(3b)}}{N^{MC,t\bar{t}}_{CR^i(2b)}} \text{ , } \quad (8.5)$$

where $N^{data}_{CR^i(2b)}$, $N^{MC,t\bar{t}}_{CR^i(2b)}$ and $N^{MC,non-t\bar{t}}_{CR^i(2b)}$ are the number of events obtained from data, $t\bar{t}$ Monte Carlo simulation and other background processes, respectively, in

Theory	# ME	Diff. MC	Scale uncertainties				PDF	Total
CR	partons	generator	ktfac↑	ktfac↓	qfac↑	qfac↓	MSTW	
CR4-60	4%	26%	-12%	+11%	-4%	-2%	$^{+2.9}_{-2.2}$ %	29%
CR4-70	3%	25%	-12%	+11%	-4%	-2%	$^{+2.9}_{-2.3}$ %	28%
CR6-70	6%	14%	-26%	+19%	-11%	-8%	$^{+3.7}_{-2.7}$ %	32%
CR6-75	5%	6%	-27%	+18%	-12%	-8%	$^{+3.6}_{-2.7}$ %	31%

Table 8.7 Theoretical uncertainties on the number of $t\bar{t}$ events in each control region as predicted by the Monte Carlo simulations.

each of the four control regions. The number of event obtained in each of the five signal regions from $t\bar{t}$ MC simulation is denoted as $N^{MC,t\bar{t}}_{SR^i(3b)}$. The index i refers to each SR and its corresponding CR, as introduced in Table 8.4.

Systematic uncertainties arise from detector related and theoretical uncertainties as explained above, affecting the T_f factors and $N^{MC,non-t\bar{t}}_{2b}$. However, in the procedure defined by Eq. 8.5 the systematic uncertainties that are correlated between the control and the signal regions are expected to largely cancel out in the T_f. Table 8.8 summarises the values of the T_f and their total uncertainty, which has been split into several detector and theory components. Table 8.9 disentangles the contribution from all the sources of theoretical uncertainty on the transfer factors. The pure MC estimate of the $t\bar{t}$ background for the five signal regions ($N^{MC,t\bar{t}}_{SR^i(3b)}$) is summarized in Table 8.10 together with its associated systematic uncertainties. The details of the theoretical uncertainties for $N^{MC,t\bar{t}}_{SR^i(3b)}$ are shown in Table 8.11.

SR	T_f	MC stat	JES	JER	cluster	pileup	b-tag	theory	total
SR4-L	0.099	2%	5%	6%	0%	1%	23%	8%	26%
SR4-M	0.049	2%	8%	11%	1%	2%	22%	11%	28%
SR4-T	0.023	2%	5%	4%	1%	1%	19%	12%	23%
SR6-L	0.267	7%	1%	9%	2%	1%	20%	13%	27%
SR6-T	0.195	7%	5%	8%	1%	0%	18%	14%	26%

Table 8.8 Estimation of the transfer factor T_f for the five signal regions of the 0-lepton analysis. The uncertainty is split into several detector and theory components.

T_f	Number of	Diff. MC	Scale uncertainties				PDF
SR	ME partons	generator	ktfac↑	ktfac↓	qfac↑	qfac↓	MSTW
SR4-L	1%	8%	-1.7%	+0.2%	-1.0%	-0.9%	$^{+0.5}_{-0.5}$ %
SR4-M	3%	8%	-6.4%	+2.3%	-3.0%	-2.5%	$^{+1.2}_{-1.0}$ %
SR4-T	1%	8%	-7.4%	+1.0%	-4.2%	-4.4%	$^{+2.2}_{-1.6}$ %
SR6-L	7%	8%	-3.3%	-1.8%	-2.8%	-3.4%	$^{+6.2}_{-5.1}$ %
SR6-T	10%	3%	-1.8%	-2.1%	-2.2%	-2.7%	$^{+8.0}_{-6.5}$ %

Table 8.9 Theoretical uncertainties on the $t\bar{t}$ transfer factors.

SR	Events	MC Stat	JES	JER	cluster	pileup	b-tag	lumi	theory
SR4-L	32.6	6%	$^{+17}_{-22}$ %	3%	$^{+1}_{-0}$ %	$^{+1}_{-0}$ %	$^{+32}_{-31}$ %	4%	26%
SR4-M	16.1	8%	$^{+18}_{-24}$ %	7%	$^{+2}_{-2}$ %	$^{+1}_{-2}$ %	$^{+33}_{-32}$ %	4%	31%
SR4-T	11.4	4%	$^{+26}_{-16}$ %	0%	0%	$^{+0}_{-1}$ %	$^{+28}_{-26}$ %	4%	30%
SR6-L	10.0	12%	$^{+27}_{-23}$ %	3%	$^{+1}_{-1}$ %	$^{+1}_{-1}$%	$^{+25}_{-24}$ %	4%	42%
SR6-T	7.9	11%	$^{+33}_{-24}$ %	4%	$^{+2}_{-0}$ %	0%	$^{+22}_{-21}$ %	4%	42%

Table 8.10 Monte Carlo based top background estimation in the signal regions and associated systematic uncertainties. The number of events corresponds to 4.7 fb^{-1}.

Theory	Number of	Diff. MC	Scale uncertainties				PDF
SR	ME partons	generator	ktfac↑	ktfac↓	qfac↑	qfac↓	MSTW
SR4-L	3%	18%	-14%	+11%	-5%	-3%	$^{+3.4}_{-2.8}$ %
SR4-M	7%	18%	-18%	+13%	-7%	-4%	$^{+4.1}_{-3.2}$ %
SR4-T	3%	17%	-19%	+12%	-8%	-6%	$^{+5.2}_{-3.8}$ %
SR6-L	13%	6%	-29%	+17%	-14%	-11%	$^{+10.0}_{-7.7}$ %
SR6-T	15%	9%	-28%	+16%	-14%	-11%	$^{+11.9}_{-9.0}$ %

Table 8.11 Theoretical uncertainties on the number of $t\bar{t}$ events in each signal region as predicted by the Monte Carlo simulations.

8.2.2 Estimation of other background processes

The other SM background production processes that have a small contribution to the data yield in the signal regions are W/Z boson and $t\bar{t}$ production in association with $b\bar{b}$ pairs, single top and the associated production of a $t\bar{t}$ pair with a vector boson ($t\bar{t}$+W/Z). The event yields for the relevant production processes are summarised in

Table 8.12, along with their corresponding uncertainties, as discussed in Section 7.4.

Process	Events	MC Stat	JES	JER	b-tagging	Lum	theory
			SR4-L				
W + HF	2.0	68%	17%	0%	34%	4%	80%
Z + HF	0.9	58%	4%	1%	29%	4%	100%
single top	2.0	23%	24%	8%	37%	4%	30%
$t\bar{t}$ + EW	1.4	6%	21%	0%	28%	4%	74%
$t\bar{t}$ + bb	4.0	13%	20%	7%	32%	4%	100%
			SR4-M				
W + HF	1.1	92%	15%	6%	32%	4%	80%
Z + HF	0.6	71%	3%	2%	32%	4%	100%
single top	1.3	29%	22%	3%	38%	4%	30%
$t\bar{t}$ + EW	0.8	8%	23%	1%	30%	4%	74%
$t\bar{t}$ + bb	2.3	17%	19%	7%	34%	4%	100%
			SR4-T				
single top	1.3	32%	24%	14%	26%	4%	30%
$t\bar{t}$ + EW	0.6	11%	30%	11%	23%	4%	74%
$t\bar{t}$ + bb	1.0	27%	35%	12%	29%	4%	100%
			SR6-L				
W + HF	0.1	100%	30%	100%	30%	4%	80%
Z + HF	0.1	100%	100%	100%	100%	4%	100%
single top	0.2	67%	2%	4%	48%	4%	30%
$t\bar{t}$ + EW	0.8	9%	21%	9%	20%	4%	74%
$t\bar{t}$ + bb	1.1	25%	22%	19%	19%	4%	100%
			SR6-T				
W + HF	0.1	100%	30%	100%	28%	4%	80%
Z + HF	0.1	100%	100%	100%	100%	4%	100%
$t\bar{t}$ + EW	0.6	11%	26%	11%	17%	4%	74%
$t\bar{t}$ + bb	0.8	32%	33%	14%	22%	4%	100%

Table 8.12 Monte Carlo based backgrounds estimation and associated systematic uncertainties for W/Z boson and $t\bar{t}$ production in association with heavy flavour jets, single top, associate production of a $t\bar{t}$ pair with a vector boson ($t\bar{t}$+W/Z), for each of the five signal regions. The number of events corresponds to 4.7 fb^{-1}.

In summary, a 100% uncertainty is assumed for the cross-section of $t\bar{t}$ and W/Z production in association with a $b\bar{b}$ pair. The yields for W production in association with heavy flavour jets are scaled by a factor of 1.63 (Wbb and Wcc) and 1.11 (Wc), with an uncertainty of 50% as part of the theory uncertainty. The associate production of a $t\bar{t}$ pair with a vector boson ($t\bar{t}$+W/Z) has been estimated with an uncertainty of 74% [264]. Overall, the reducible background contribution from

single top, $t\bar{t}$+W/Z and W/Z+heavy-flavour jets accounts for 10% to 20% of the total background depending on the signal region, whereas the irreducible $t\bar{t}$+$b\bar{b}$ background accounts for about 10% of the total background in all signal regions.

8.2.3 Semi data-driven $t\bar{t}$ background results

The $t\bar{t}$+jets yield in each signal region is obtained from the measured number of events in the corresponding control region (see Table 8.4) using the semi data-driven strategy (Eq. 8.5). The results are presented in Table 8.13, and they are compared to those obtained by performing a pure MC estimate of the $t\bar{t}$ background. Overall, a good agreement is observed. The main impact of the semi data-driven estimate is a reduction in the uncertainty by approximately a factor of two. Finally, the total expected background for the five signal regions is summarized in the last column of Table 8.13, and includes the final estimates of $t\bar{t}$+jets and the contributions from W/Z+jets, single top, $t\bar{t}$+$b\bar{b}$, $t\bar{t}$+W/Z and multi-jet processes.

SR	$t\bar{t}$+jets		others	SM
	MC	semi-DD		
SR4-L	32.6 ± 15.4	33.3 ± 7.9	11.1 ± 4.9	44.4 ± 10.0
SR4-M	16.1 ± 8.4	16.4 ± 4.1	6.6 ± 2.9	23.0 ± 5.4
SR4-T	11.4 ± 5.4	9.6 ± 2.1	3.7 ± 1.6	13.3 ± 2.6
SR6-L	10.0 ± 6.2	10.3 ± 3.3	2.4 ± 1.4	12.7 ± 3.6
SR6-T	7.9 ± 5.3	8.3 ± 2.4	1.6 ± 1.1	9.9 ± 2.6

Table 8.13 Estimation of the $t\bar{t}$ background for the five signal regions (for 4.7 fb^{-1}) as determined by a pure Monte Carlo estimate and the semi data-driven method. The column "others" includes the contributions from W/Z+jets, single top, $t\bar{t}$+$b\bar{b}$, $t\bar{t}$+W/Z and multi-jet processes. The column "SM" shows the total expected background and is the sum of the columns "$t\bar{t}$+jets" (semi-DD) and "others".

8.3 Validation of the transfer factors in the 1-lepton channel

The reliability of the MC extrapolation of the $t\bar{t}$ background to larger b-jet multiplicities has been checked in validation regions defined with kinematic cuts similar to those used in the control and signal regions, except that exactly one isolated electron or muon is required. Thus, the validation of the Monte Carlo simulation in predicting the extrapolation from the 2 b-jets region to the 3 b-jets region is done

by applying the semi-data driven method in the 1-lepton channel. Two validation regions (VR) enriched in $t\bar{t}$ events, labelled VR1-2b and VR1-3b, are defined from the following selection:

- Single lepton trigger.
- Preselection cuts.
- Exactly 1 signal lepton (e,μ).
- $\geqslant$ 4 jets with $p_{\mathrm{T}} > 30$ GeV and $|\eta| < 2.8$.
- $E_{\mathrm{T}}^{\mathrm{miss}} > 160$ GeV.
- 40 GeV $< \mathrm{m_T} <$ 100 GeV.
- $\mathrm{m_{eff}} > 500$ GeV.
- VR1-2b: exactly 2 b-jets, with $p_{\mathrm{T}} > 30$ GeV and $|\eta| < 2.5$, using the OP at 60%, 70% and 75% for the VR labelled with 60, 70 and 75, respectively.
- VR1-3b: $\geqslant$ 3 b-jets, with $p_{\mathrm{T}} > 30$ GeV and $|\eta| < 2.5$, using the OP at 60%, 70% and 75% for the VR labelled with 60, 70 and 75, respectively.

The cut on $\mathrm{m_T}$ is implemented to minimize the possible signal contamination from gluino-mediated stop pair production in the validation regions. The number of observed events in VR1-3b is estimated by multiplying the number of observed events in VR1-2b by the ratio of the number of simulated events in VR1-3b and VR1-2b:

$$N_{\mathrm{VR1-3}b}^{Pred} = N_{\mathrm{VR1-2}b}^{data} \times \frac{N_{\mathrm{VR1-3}b}^{MC}}{N_{\mathrm{VR1-2}b}^{MC}} \,. \tag{8.6}$$

Thus, the transfer factors are validated by comparing the predicted number of events in the 3 b-jets region to the observed event yield in the data. This validation is performed separately for the 3 b-tagging operating points used in the analysis (i.e., 60%, 70% and 75%). Figures 8.13 and 8.14 present the $E_{\mathrm{T}}^{\mathrm{miss}}$ and $\mathrm{m_{eff}}$ distributions for the electron and muon channel, respectively, in VR1-2b-OP60 (left) and VR1-3b-OP60 (right). Similar performance has been observed for the other regions.

The results of the validation are summarised in Table 8.14. The extrapolated event yield in the validation regions with at least three b-jets from the validation regions with exactly two b-jets is found to be consistent with the number of observed events for all b-tagging operating points.

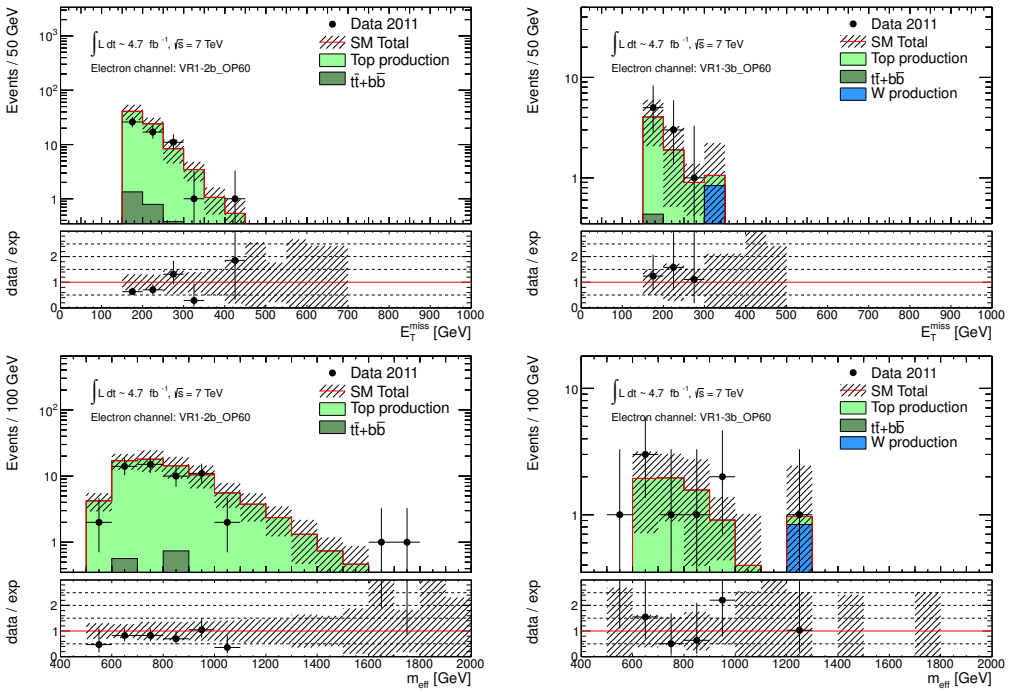

Figure 8.13 The $E_{\mathrm{T}}^{\mathrm{miss}}$ (top) and $\mathrm{m_{eff}}$ (bottom) distributions in VR1-2b-OP60 (left) and VR1-3b-OP60 (right) for the electron channel.

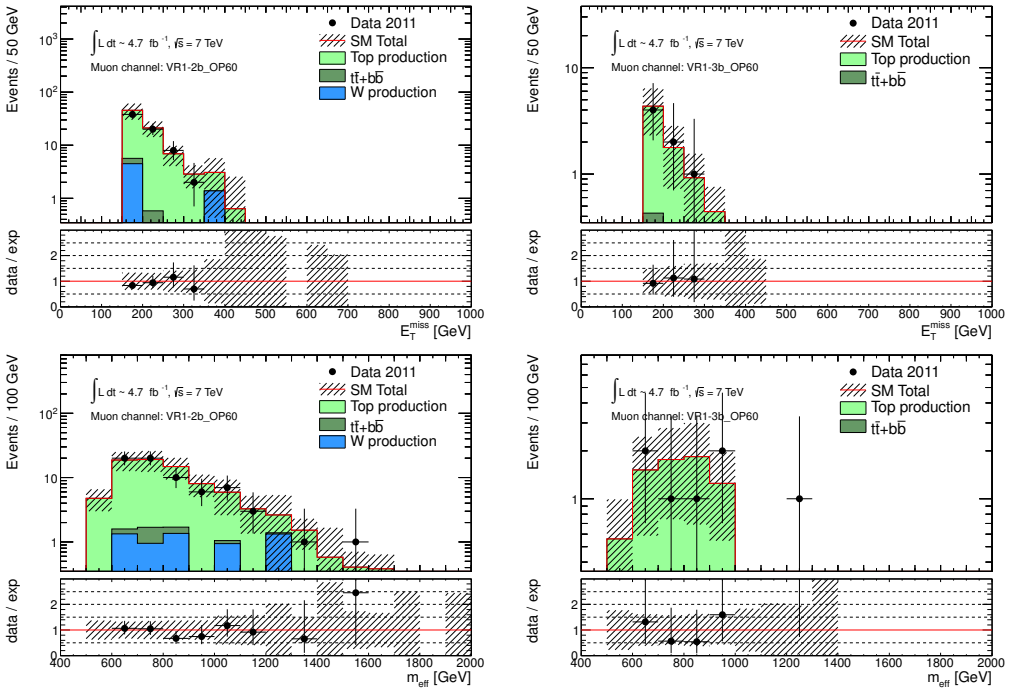

Figure 8.14 The $E_{\mathrm{T}}^{\mathrm{miss}}$ (top) and $\mathrm{m_{eff}}$ (bottom) distributions in VR1-2b-OP60 (left) and VR1-3b-OP60 (right) for the muon channel.

channel	VR1-2b MC	VR1-3b MC	VR1-2b Data	VR1-3b Prediction	VR1-3b Data
			b-tagging operating point at 60%		
1 electron	78.4 ± 24.8	7.4 ± 3.3	56	5.3 ± 3.0	9
1 muon	81.2 ± 25.6	8.0 ± 3.6	68	6.7 ± 3.8	7
			b-tagging operating point at 70%		
1 electron	117.9 ± 33.2	20.6 ± 8.1	77	13.5 ± 5.8	17
1 muon	114.5 ± 34.2	19.4 ± 8.0	90	15.3 ± 6.6	16
			b-tagging operating point at 75%		
1 electron	130.5 ± 36.7	32.7 ± 12.7	77	19.3 ± 6.7	26
1 muon	126.2 ± 36.1	30.0 ± 11.4	92	21.9 ± 7.6	26

Table 8.14 Validation of the transfer factors and associated systematic uncertainties using the 1-lepton selection. The results are found to be consistent with the number of observed events for all *b*-tagging operating points.

9

Results and interpretation

This chapter presents the final results of the search, obtained using the data collected during 2011 corresponding to a total integrated luminosity of 4.7 fb^{-1}. Section 9.1 presents the experimental results, and compares the observed event yield to the SM background prediction for each of the signal regions, as determined in Chapter 8. Section 9.2 discusses the interpretation of the results in terms of a variety of models. Finally, Section 9.3 summarizes the results obtained in this thesis and compare them to different searches performed within ATLAS and other experiments.

9.1 Experimental results

The SM background prediction as determined in Chapter 8 and the observed event yields for each signal region are summarized in Table 9.1. Overall, the SM estimate is found to be in good agreement with the observed data in all signal regions.

The distributions for the first- and second-leading jet p_{T}, the b-jet multiplicity, the leading jet MV1 b-tagger weight, the $E_{\mathrm{T}}^{\mathrm{miss}}$ and the $\mathrm{m_{eff}}$ obtained using 4.7 fb^{-1} of data are compared in Figures 9.1 and 9.2 to the Monte Carlo estimates for SR4-L and SR6-T, respectively. Two signal points (with small and large mass splitting between the gluino and the LSP) for the Gbb and Gtt models described in Section 2.7 are overlaid for SR with 4 and 6 jets selection, respectively. Similar results have been observed for SR4-M, SR4-T and SR6-L.

Signal Region	SM prediction	data (4.7 fb^{-1})
SR4-L	44.4 ± 10.0	45
SR4-M	23.0 ± 5.4	14
SR4-T	13.3 ± 2.6	10
SR6-L	12.7 ± 3.6	12
SR6-T	9.9 ± 2.6	8

Table 9.1 Comparison between the results for the SM prediction and the numbers of observed events in the five signal regions.

9.2 Interpretation of the results

Since no excess with respect to the SM predictions is observed in the data, limits for non-SM signal yield at 95% confidence level (CL) are derived by testing the signal plus background hypothesis in each signal region with the CL_s prescription (see Chapter 3). These limits are obtained by implementing a fitting procedure [265], where the number of observed events in data and the signal and background expectation values along with their corresponding uncertainties are inputs to the fit. In addition, a free parameter for the non-SM signal strength is used. This is constrained to be non-negative, and adjusted in the profile likelihood maximisation, ensuring thus a proper treatment of the expected signal contamination in the control regions when the results are interpreted in the framework of specific SUSY scenarios.

The observed upper limit on the signal strength parameter ($\mu_{up}^{\rm obs}$) is obtained in the following way. Firstly, the observed profile likelihood ratio $q_\mu^{\rm obs}$ is determined using Eq. 3.13 from the observed data ($\vec{x}$), an assumed value of the signal strength (μ), and the knowledge of the systematics embodied in the analysis (θ). Secondly, the $CL_s^{\rm obs}(\mu)$ function is calculated from $q_\mu^{\rm obs}$ according to Eq. 3.25. Finally, the observed upper limit is the value of μ which satisfies $CL_s^{\rm obs}(\mu_{up}^{\rm obs}) = 0.05$. The $CL_s^{\rm obs}(\mu)$ function is illustrated for an exclusion and a non-exclusion case in Figure 9.3.

The expected upper limit on the signal strength parameter ($\mu_{up}^{\rm exp}$) is obtained independently of the data yields in the signal regions. For a given value of μ, the distribution of q_μ under the background-only hypothesis, $f(q_\mu|0,\hat{\theta}_0)$, is built. Let's call q_μ^{50} the median of this distribution (i.e., the point at which the cumulative probability distribution crosses the 50% quantile). The function $CL_s^{50}(\mu)$ is then calculated from q_μ^{50} (again, Eq. 3.25), and the expected upper limit is the value of μ which satisfies $CL_s^{50}(\mu_{up}^{\rm exp}) = 0.05$. The plot of CL_s^{50} as a function of μ is shown in Figure 9.3, and denoted CL_s − median.

Since the upper limits are subject to the effect of statistical fluctuations, it is

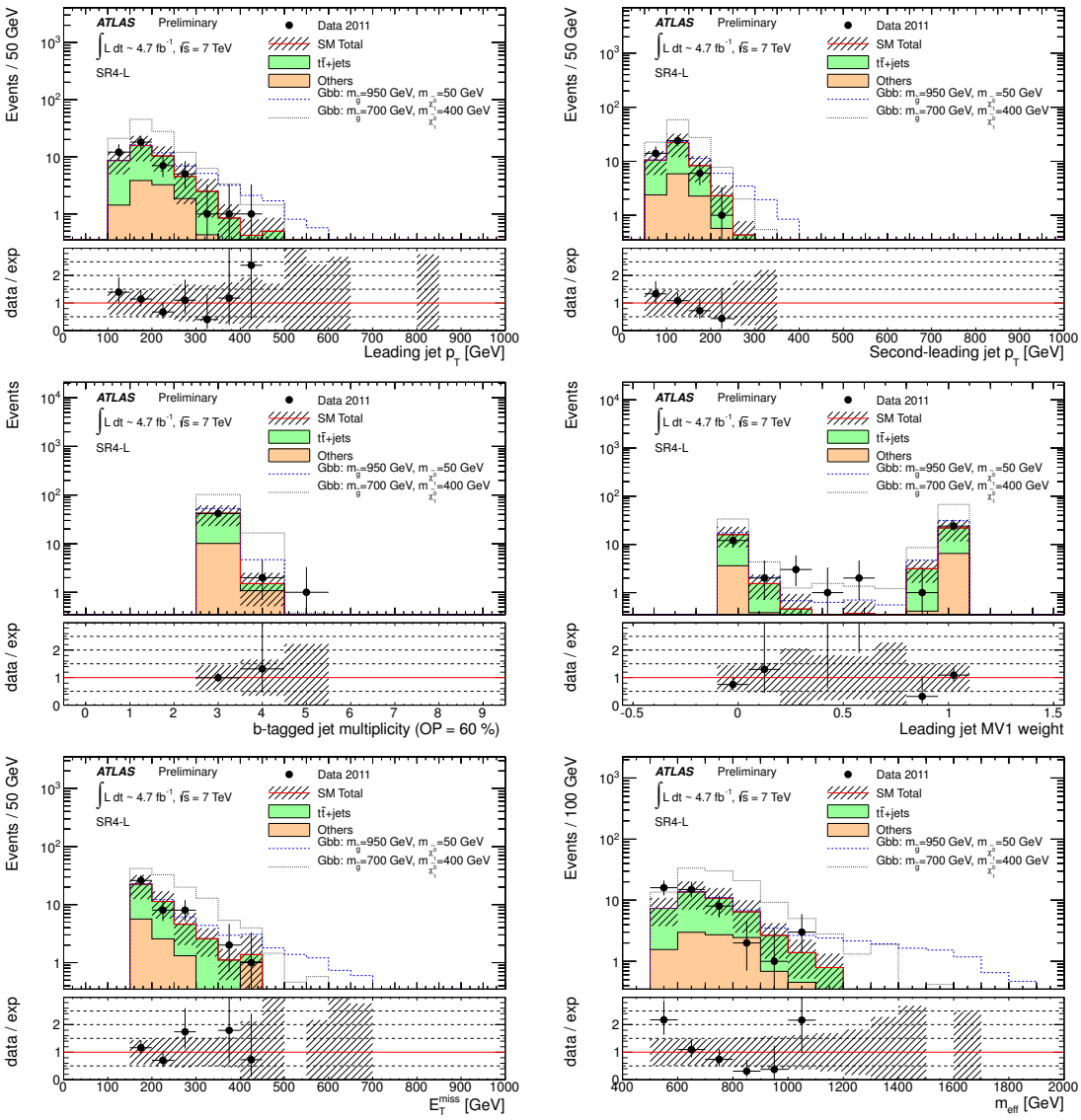

Figure 9.1 From top to bottom, left to right: the first- and second-leading jet p_{T}, the b-jet multiplicity, the leading jet MV1 b-tagger weight, the $E_{\mathrm{T}}^{\mathrm{miss}}$ and the $\mathrm{m_{eff}}$ distributions in the SR4-L signal region. The hatched band shows the systematic uncertainty on the MC prediction, which includes both experimental uncertainties (among which JES and b-tagging uncertainties are dominant) and theoretical uncertainties on the background normalisation and shape. The label "others" includes the contributions from single top, $t\bar{t}+b\bar{b}$, $t\bar{t}+W/Z$, W/Z+jets and multi-jet processes. The lower plot in each figure shows the ratio of the observed distribution to that expected for the SM background. Two signal points (with small and large mass splitting between the gluino and the LSP) for the Gbb models described in the text are overlaid.

customary to quantify this effect with error bands on the expected limit. The $\pm 1\sigma$ is calculated as above but replacing the 50% quantile by 16% and 84% quantiles,

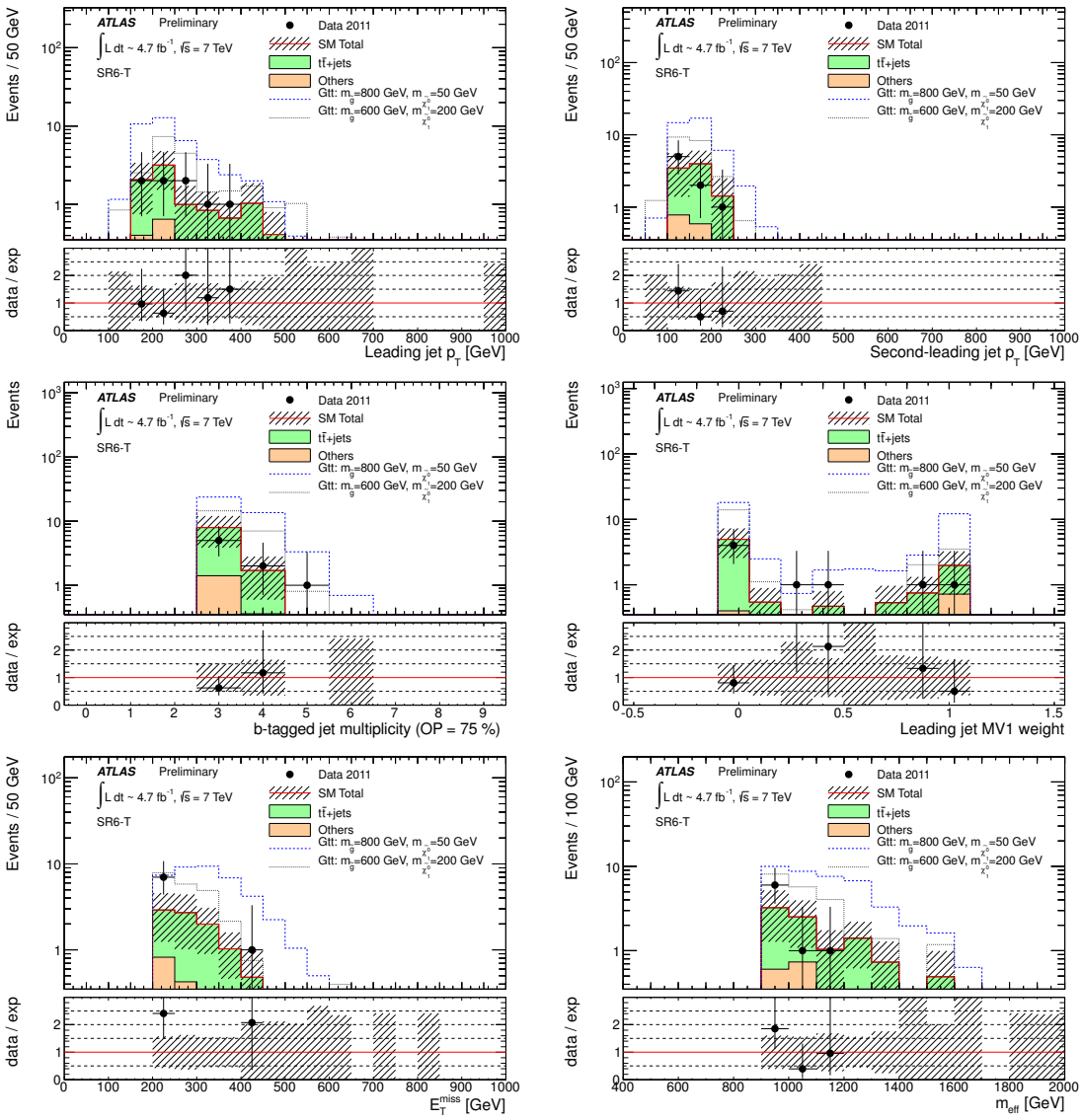

Figure 9.2 From top to bottom, left to right: the first- and second-leading jet p_{T}, the b-jet multiplicity, the leading jet MV1 b-tagger weight, the $E_{\mathrm{T}}^{\mathrm{miss}}$ and the $\mathrm{m_{eff}}$ distributions in the SR6-T signal region. The hatched band shows the systematic uncertainty on the MC prediction, which includes both experimental uncertainties (among which JES and b-tagging uncertainties are dominant) and theoretical uncertainties on the background normalisation and shape. The label "others" includes the contributions from single top, $t\bar{t}$+$b\bar{b}$, $t\bar{t}$+W/Z, W/Z+jets and multi-jet processes. The lower plot in each figure shows the ratio of the observed distribution to that expected for the SM background. Two signal points (with small and large mass splitting between the gluino and the LSP) for the Gtt models described in the text are overlaid.

q_μ^{16} and q_μ^{84}, and deriving the corresponding $CL_s^{16}(\mu)$ and $CL_s^{84}(\mu)$ functions, also plotted in Figure 9.3 and denoted as $CL_s \pm 1\sigma$. The $\pm 1\sigma$ error range of μ_{up}^{exp} is

obtained by solving the implicit equations $CL_s^{16}(\mu) = 0.05$ and $CL_s^{84}(\mu) = 0.05$. Likewise, the $\pm 2\sigma$ error range of μ_{up}^{exp} is obtained from the corresponding equations $CL_s^{2.5}(\mu) = 0.05$ and $CL_s^{97.5}(\mu) = 0.05$, also plotted in Figure 9.3 and denoted as $CL_s \pm 2\sigma$.

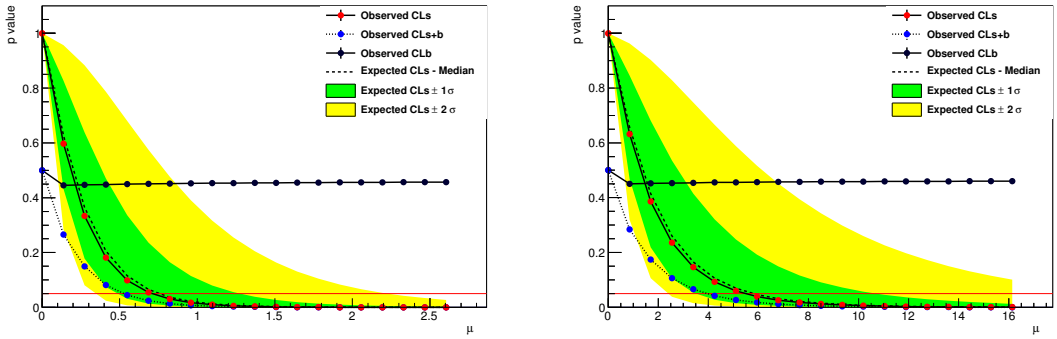

Figure 9.3 Plots of CL_s^{obs} and CL_s^{exp} as a function of the signal strength μ for an excluded (left) and a non-excluded (right) simplified model. The green and yellow bands show the ± 1 and ± 2 σ variations around the background-only CL_s^{exp} values. The 95% observed (expected) upper limit on the signal model is defined at the point where the CL_s^{obs} (CL_s^{exp}) curve crosses the horizontal 5% line in red. The number of hypothesis tests done to determine the upper limit (i.e., the number of points along the signal strength axis) has been set to 20.

The model independent upper limit on the number of signal events is determined by setting a signal expectation of 1 event without uncertainties. In this way, any upper limit determined on the signal strength parameter is exactly the upper limit on a possible number of signal events. Model-independent upper limits at 95% CL on the number of signal events (N_{signal}) and on the visible cross-section (σ_{vis}) for non-SM contributions derived for each signal region are presented in Table 9.2, where

$$\sigma_{\text{vis}} = (\sigma \times \text{BR})_{\text{signal}} \times (\mathcal{A} \times \mathcal{E})_{\text{signal}} = \frac{N_{\text{signal}}}{\int Ldt} \,. \tag{9.1}$$

The kinematic acceptance $\mathcal{A}$ accounts for the physics selection, and it is defined as

$$\mathcal{A} = \frac{N_{\text{fiducial}}}{N_{\text{total}}} \,, \tag{9.2}$$

where N_{total} is the initial number of events, and N_{fiducial} corresponds to the number of events passing the fiducial cuts (i.e., the analysis cuts on p_{T} and η, object overlap-removal in $\eta - \phi$ space, among others) based on the following objects: truth electrons/muons/$E_{\text{T}}^{\text{miss}}$, particle jets and b-quark matched to a jet (at parton level).

The experimental efficiency $\mathcal{E}$ accounts for the detector effects, and it is defined as

$$\mathcal{E} = \frac{N^{\text{reco}}_{\text{fiducial}}}{N_{\text{fiducial}}} \ , \tag{9.3}$$

where $N^{\text{reco}}_{\text{fiducial}}$ is the final event yield after the nominal analysis cuts applied to detector level objects/variables. It includes trigger and reconstruction inefficiencies, full particle identification cuts, resolution effects, among others. Thus, $\mathcal{A} \times \mathcal{E}$ is the full event selection efficiency at detector level.

	Obs (exp) 95% CL upper limit	
SR	N_{signal}	σ_{vis}(fb)
SR4-L	23.8 (23.4)	5.1 (5.0)
SR4-M	8.6 (12.8)	1.8 (2.7)
SR4-T	7.1 (9.2)	1.5 (2.0)
SR6-L	9.6 (10.1)	2.0 (2.1)
SR6-T	7.1 (8.3)	1.5 (1.8)

Table 9.2 Observed (expected) 95% CL upper limits on the non-SM contributions to all signal regions. Limits are given on numbers of events and in terms of visible cross-sections defined as cross-section times kinematic acceptance times experimental efficiency. Systematic uncertainties on the SM background estimation are included in the limits.

Finally, data are used to derive limits in the parameter space of several SUSY models. The signal region with the best expected sensitivity at each point in the parameter space in a given SUSY model is used to derive the limits at 95% CL. Signal cross-sections are calculated to next-to-leading order in the strong coupling constant, including the resummation of soft gluon emission at next-to-leading-logarithmic accuracy (NLO+NLL) [266–270]. The nominal cross-section, σ^{best}, and the total theoretical uncertainty, denoted $\sigma^{\text{SUSY}}_{\text{Theory}} \equiv \frac{\Delta\sigma^{\text{best}}}{\sigma^{\text{best}}}$, are taken from an envelope of cross-section predictions using different PDF sets and factorisation and renormalisation scales, as described in [271] (see Section 7.5). All detector-related systematic uncertainties are treated as fully correlated between signal and backgrounds.

The results are interpreted in the context of the Simplified Models and the phenomenological Minimal Supersymmetric Standard Model (pMSSM). The cross-sections as a function of the gluino mass together with the total theoretical uncertainty for the gluino-mediated stop and sbottom production processes are summarized in Table 9.3. The exclusion limits imposed on the different SUSY models characterised by off-shell or on-shell stop and sbottom production are discussed next.

$m_{\tilde{g}}$ (GeV)	$\sigma^{\text{best}}_{pp\to\tilde{g}\tilde{g}}$ (fb)	$\frac{\Delta\sigma^{\text{best}}}{\sigma^{\text{best}}}$ (%)	$m_{\tilde{g}}$ (GeV)	$\sigma^{\text{best}}_{pp\to\tilde{g}\tilde{g}}$ (fb)	$\frac{\Delta\sigma^{\text{best}}}{\sigma^{\text{best}}}$ (%)	$m_{\tilde{g}}$ (GeV)	$\sigma^{\text{best}}_{pp\to\tilde{g}\tilde{g}}$ (fb)	$\frac{\Delta\sigma^{\text{best}}}{\sigma^{\text{best}}}$ (%)
200	686710	14	550	1328	18	900	27	27
250	197147	14	600	708	19	950	16	28
300	67773	15	650	389	20	1000	10	30
350	26381	15	700	221	20	1050	6.2	32
400	11312	15	750	127	22	1100	3.9	34
450	5236	16	800	74	23	1150	2.5	36
500	2575	17	850	44	25	1200	1.6	39

Table 9.3 Gluino pair production cross-section and its theoretical uncertainty as a function of the gluino mass.

9.2.1 Exclusion limits for the Gbb simplified model

Results are interpreted in the context of simplified models for gluino mediated sbottom pair production (Gbb). For this simplified scenario, the $\tilde{b}_1$ is the lightest squark but $m_{\tilde{g}} < m_{\tilde{b}_1}$. Pair production of gluinos is the only process taken into account since the masses of all other sparticles apart from the $\tilde{\chi}^0_1$ are set above the TeV scale. A three-body decay via an off-shell sbottom is assumed for the gluino, yielding a 100% BR for the decay $\tilde{g} \to b\bar{b}\tilde{\chi}^0_1$. The sbottom mass has no impact on the kinematics of the decay and the exclusion limits are presented in the $(m_{\tilde{g}}, m_{\tilde{\chi}^0_1})$ plane.

Within this scenario, the impact of initial-state radiation (ISR) is expected to be large in the region with low $m_{\tilde{g}} - m_{\tilde{\chi}^0_1}$ due to the small signal acceptance. Therefore, an uncertainty on the modelling of ISR is assessed by comparing the signal acceptance obtained with the `HERWIG++` samples to the one obtained with dedicated `MADGRAPH+PYTHIA` samples generated with additional jets. This uncertainty varies from 4% to 35% as a function of $m_{\tilde{g}} - m_{\tilde{\chi}^0_1}$ and it is included in the total theoretical uncertainty for Gbb models, as shown in Figure 9.4.

The acceptance for the Gbb model in the SR4-T signal region is presented in Figure 9.5. For the region close to the forbidden region ($m_{\tilde{g}} - m_{\tilde{\chi}^0} \approx 0$), the values are found to be the lowest, and range $0.1 - 0.5\%$, since the b-jets have very little phase space available to them and thus the p_{T} of the leading b-jets from sbottom decays is generally softer than 30 GeV (hence those mass points may favor the 1 and 2 b-tag analyses). The acceptance follows a noticeable increasing tendency from low and middle $\Delta m(\tilde{g}, \tilde{\chi}^0_1)$ regions (1-5% and 5-35%, respectively) to high gluino and soft LSP masses, where it reaches 55%. The acceptance grows the fastest in the middle region due to the 30 GeV p_{T} threshold for b-jets. In effect, when moving

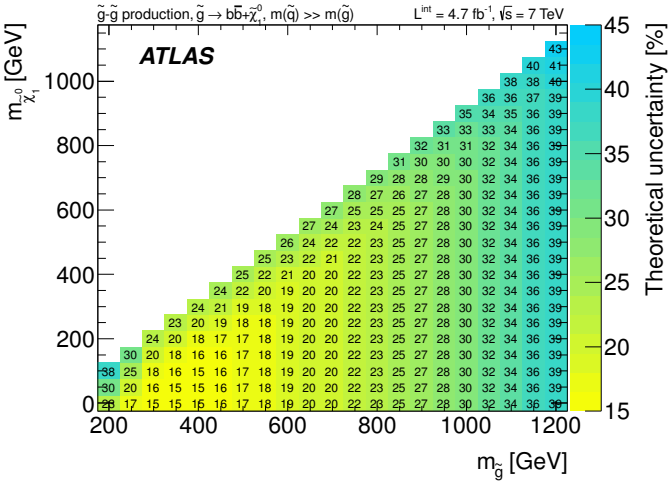

Figure 9.4 Total theoretical uncertainty for the Gbb model. An additional uncertainty on the modeling of the initial state radiation, derived as a function of $(m_{\tilde{g}} - m_{\tilde{\chi}_1^0})$ has been included for the Gbb model.

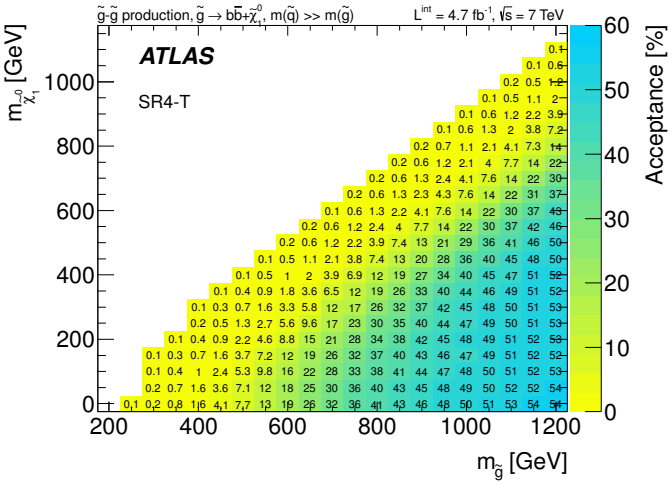

Figure 9.5 Acceptance for the Gbb model in the SR4-T signal region. The results for SR4-L and SR4-M can be found at [272].

away from the forbidden line, where the phase space available to b-jets is limited, the acceptance increases as more jets satisfy the condition as expected from the sbottom decays in the middle $\Delta m(\tilde{g}, \tilde{\chi}_1^0)$ regions. For high mass splitting values, the acceptance is the largest, but the growth is not so pronounced since there is a relatively large b-jet phase space available and therefore most of the b-jets are anyways hard.

The detector efficiency for the Gbb model in the SR4-T signal region is presented in Figure 9.6. Overall, the values are found to be quite homogeneous throughout the entire mass plane, and range 50-80%. This reflects the outstanding performance of the ATLAS detector and the sub-systems involved within the different kinematic

regimes covered by the analysis.

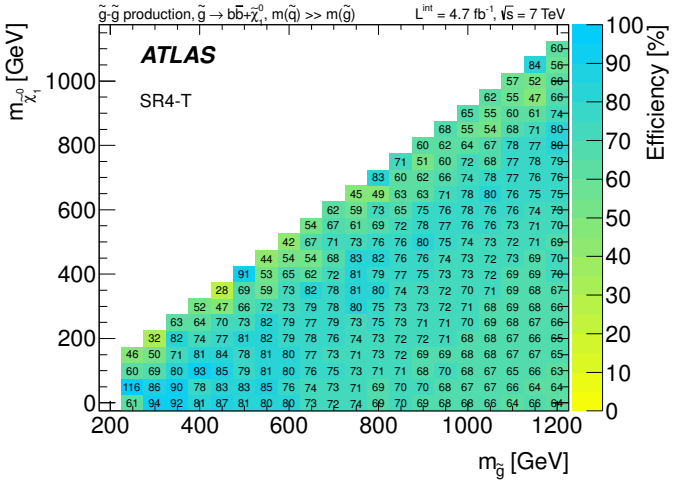

Figure 9.6 Detector efficiency for the Gbb model in the SR4-T signal region. The results for SR4-L and SR4-M can be found at [272].

The impact of the experimental uncertainty for the Gbb model (taking into account the jet energy scale and resolution, the b-tagging efficiency and the object identification efficiency, among others) in the SR4-T signal region is summarized in Figure 9.7. The values are found to increase from regions with high $\Delta m(\tilde{g}, \tilde{\chi}_1^0)$ (17-22%) to those with middle and low mass-splitting (22-35% and above 35%, respectively). The JES, the JER and the b-tagging efficiency have been found to be the main sources of experimental uncertainty. Since the first two sources have the highest uncertainties in the low p_{T} regime (see Section 5.5 and Chapter 6, respectively), the region close to the diagonal, where soft objects are produced, is expected to have the largest uncertainties. Overall, a similar behaviour has been found for SR4-L and SR4-M, for the three features discussed above (i.e, acceptance, efficiency and experimental uncertainty), and the results can be found in public web page [272].

The exclusion limits in the $(m_{\tilde{g}}, m_{\tilde{\chi}_1^0})$ plane for the Gbb model are shown in Figure 9.8. The dashed black and solid bold red lines show the 95% CL expected and observed limits respectively, including all uncertainties except the theoretical signal cross-section uncertainty. The shaded (yellow) band around the expected limit shows the impact of the experimental uncertainties while the dotted red lines show the impact on the observed limit of the variation of the nominal signal cross-section by $\pm 1\sigma^{\mathrm{SUSY}}_{\mathrm{Theory}}$. Also shown for reference is the previous ATLAS analysis [142]. Gluino masses below 1020 GeV are excluded for neutralino masses up to about 400 GeV while neutralino masses below 500 GeV are excluded for $m_{\tilde{g}} \leq 940$ GeV.

For the region close to the diagonal ($\Delta m(\tilde{g}, \tilde{\chi}_1^0) < 50$ GeV) the sensitivity of the search is deteriorated, since the energy available to be distributed among the

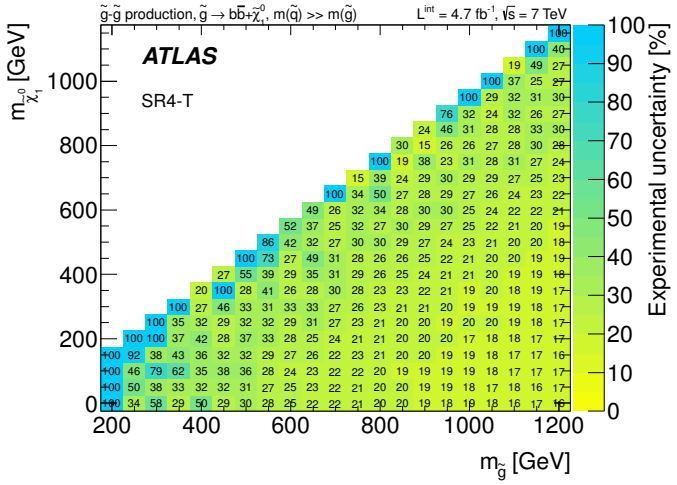

Figure 9.7 Impact of the experimental uncertainty (jet energy scale and resolution, b-tagging efficiency, object identification efficiency, among others) for the Gbb model in the SR4-T signal region. The results for SR4-L and SR4-M can be found at [272].

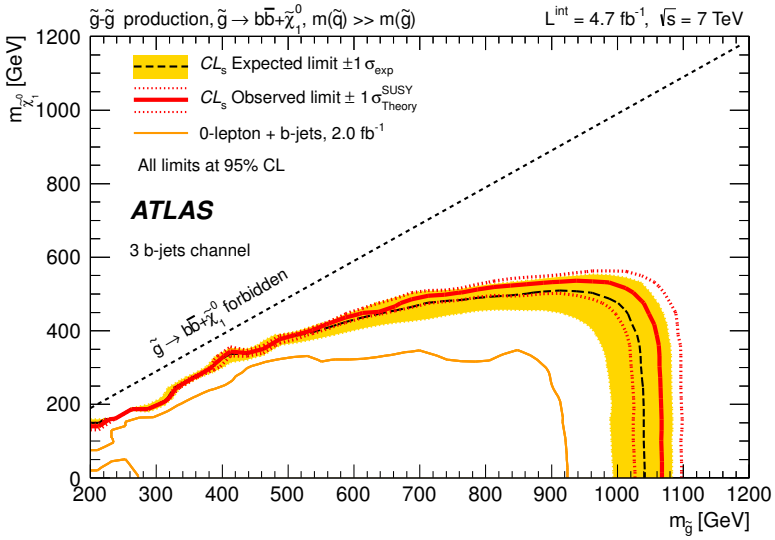

Figure 9.8 Exclusion limits in the $(m_{\tilde{g}}, m_{\tilde{\chi}_1^0})$ plane for the Gbb model. The dashed black and solid bold red lines show the 95% CL expected and observed limits respectively, including all uncertainties except the theoretical signal cross-section uncertainty. The shaded (yellow) band around the expected limit shows the impact of the experimental uncertainties while the dotted red lines show the impact on the observed limit of the variation of the nominal signal cross-section by $\pm 1\sigma^{\text{SUSY}}_{\text{Theory}}$ theoretical uncertainty. Also shown for reference is the previous ATLAS analysis [142].

resulting b-jets from the sbottom decay is close to zero ($m_{\tilde{g}} \simeq 2m_b + m_{\tilde{\chi}_1^0}$). However, the implementation of a looser b-jet p_{T} threshold (30 GeV) with respect to that used in previous searches with 1 and 2 b-tagged jets (50 GeV) results in an improvement of sensitivity (even under the evolving harsh conditions imposed by the LHC during

2011) when approaching the forbidden region, as it can be observed in the new excluded region presented in Figure 9.8. The more stringent limit for increasing values of $m_{\tilde{g}}$ and $m_{\tilde{\chi}^0}$ is achieved by requiring a higher total jet multiplicity in combination with looser b-tagging operating points, and enhanced $\mathrm{m_{eff}}$ and $E_{\mathrm{T}}^{\mathrm{miss}}$ cuts.

Figure 9.9 presents the 95% CL excluded signal model cross-section (left) and the signal region which leads to the best expected upper limit on the visible cross-section (right) for the Gbb model. The SR4-T has the best sensitivity at high gluino masses, whereas the looser signal regions (SR4-L and SR4-M) have a better sensitivity at low gluino masses and near the forbidden region because of the softer kinematic cuts applied.

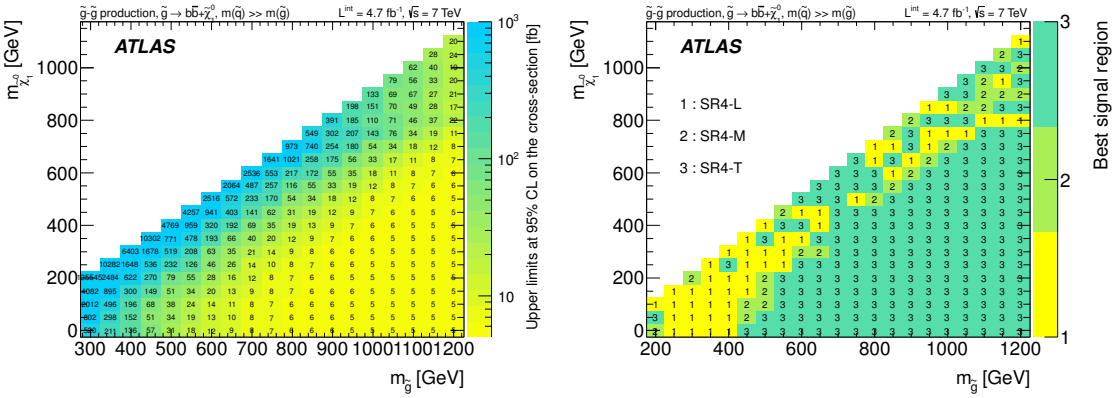

Figure 9.9 Left: 95 % CL excluded signal model cross-section for the Gbb model. Right: signal region which leads to the best expected upper limit on the visible cross-section for the Gbb model.

9.2.2 Exclusion limits for the Gtt simplified model

Results are interpreted in the context of simplified models for gluino mediated stop pair production (Gtt). For this simplified scenario, the $\tilde{t}_1$ is the lightest squark but $m_{\tilde{g}} < m_{\tilde{t}_1}$. Pair production of gluinos is the only process taken into account since the mass of all other sparticles apart from the $\tilde{\chi}_1^0$ are above the TeV scale. A three-body decay via off-shell stop is assumed for the gluino, yielding a 100% BR for the decay $\tilde{g} \to t\bar{t}\tilde{\chi}_1^0$. The stop mass has no impact on the kinematics of the decay and the exclusion limits are presented in the $(m_{\tilde{g}}, m_{\tilde{\chi}_1^0})$ plane.

The acceptance for the Gtt model in the SR6-L signal region is presented in Figure 9.10. For the Gtt topology, even on the forbidden line the 3rd-leading b-jet is reasonably energetic since there is always a minimum b-jet phase space available due to the large top mass. The acceptance follows the same tendency as for the Gbb case, from 1-5% in the low $\Delta m(\tilde{g}, \tilde{\chi}_1^0)$ regions to 40% at high gluino and soft LSP masses.

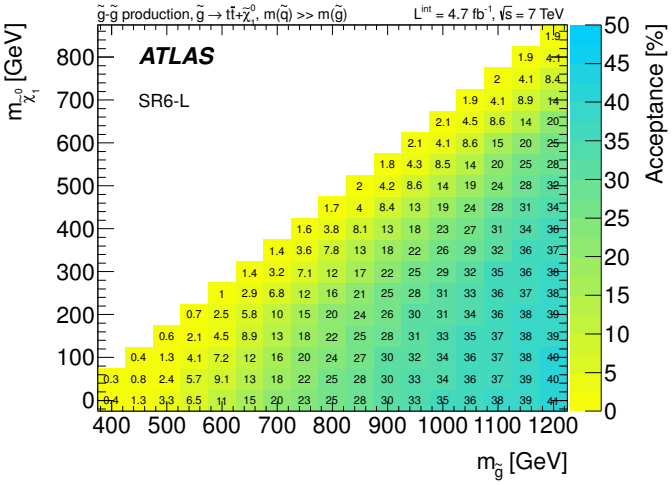

Figure 9.10 Acceptance for the Gtt model in the SR6-L signal region.

The detector efficiency for the Gtt model in the SR6-L signal region is presented in Figure 9.11. Overall, the values are found to be quite homogeneous throughout the entire mass plane, and range 30-50%.

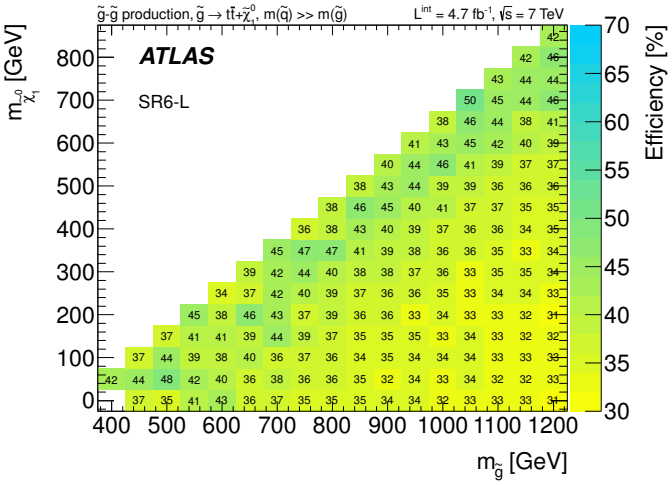

Figure 9.11 Detector efficiency for the Gtt model in the SR6-L signal region.

The impact of the experimental uncertainty for the Gtt model (taking into account the jet energy scale and resolution, the b-tagging efficiency and the object identification efficiency, among others) in the SR6-L signal region is summarized in Figure 9.12. The values observed are found to increase from regions with high $\Delta m(\tilde{g}, \tilde{\chi}_1^0)$ (10-13%) to those with middle and low mass-splitting (14-20% and above 20%, respectively). Given the minimum imposed in phase space by the top mass for the Gtt topology, the objects in the final state are generally harder than those in the Gbb topology, and therefore the uncertainties obtained from the JES, the JER and the b-tagging efficiency are expected to be small for this signal region. Overall, a

similar behaviour has been found for SR6-T, for the three features discussed above (i.e, acceptance, efficiency and experimental uncertainty), and the results can be found in public web page [272].

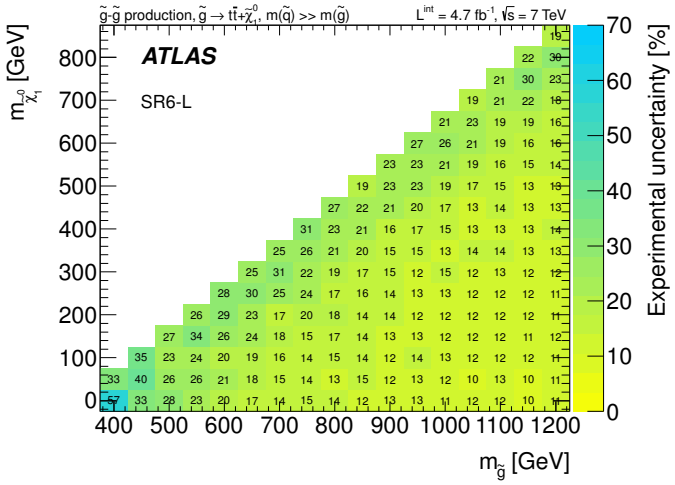

Figure 9.12 Relative experimental uncertainty (jet energy scale and resolution, b-tagging efficiency, object identification efficiency, among others) for the Gtt model in the SR6-L signal region.

The exclusion limits in the $(m_{\tilde{g}}, m_{\tilde{\chi}_1^0})$ plane for the Gtt model are shown in Figure 9.13. Also shown for reference are the previous ATLAS analyses [144, 273, 274]. In this scenario, gluino masses below 940 GeV are excluded for $m_{\tilde{\chi}_1^0} < 50$ GeV while neutralino masses below 320 GeV are excluded for $m_{\tilde{g}} \leq 800$ GeV.

For the region close to the diagonal the sensitivity of the search is reasonable, as there is a relatively large b-jet phase space imposed by the top mass. Interestingly, the implementation of a looser b-jet p_{T} threshold (30 GeV) with respect to that used in previous searches with 1 and 2 b-tagged jets (50 GeV) results in a new excluded region that almost reaches the forbidden region limit, as it can be observed in Figure 9.13. The more stringent limit for increasing values of $m_{\tilde{g}}$ and $m_{\tilde{\chi}^0}$ is achieved by requiring a higher total jet multiplicity in combination with looser b-tagging operating points, and enhanced $\mathrm{m_{eff}}$ and $E_{\mathrm{T}}^{\mathrm{miss}}$ cuts.

Figure 9.14 presents the 95% CL excluded signal model cross-section (left) and the signal region which leads to the best expected upper limit on the visible cross-section (right) for the Gtt model. The SR6-T has the best sensitivity at high gluino masses, whereas the looser signal region SR6-L have a better sensitivity at low gluino masses and near the forbidden region because of the softer kinematic cuts applied.

9.2.3 Exclusion limits for the Gtb simplified model

Results are interpreted in the context of simplified models for gluino mediated sbottom and stop pair production (Gtb). For this simplified scenario, the sbottom

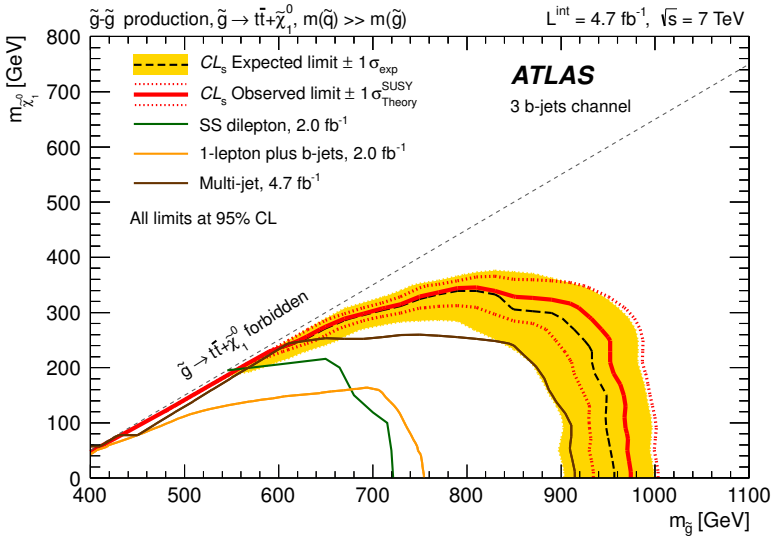

Figure 9.13 Exclusion limits in the $(m_{\tilde{g}}, m_{\tilde{\chi}_1^0})$ plane for the Gtt model. The dashed black and solid bold red lines show the 95% CL expected and observed limits respectively, including all uncertainties except the theoretical signal cross-section uncertainty. The shaded (yellow) band around the expected limit shows the impact of the experimental uncertainties while the dotted red lines show the impact on the observed limit of the variation of the nominal signal cross-section by $\pm 1\sigma^{\text{SUSY}}_{\text{Theory}}$ theoretical uncertainty. Also shown for reference are the previous ATLAS analyses [144, 273, 274].

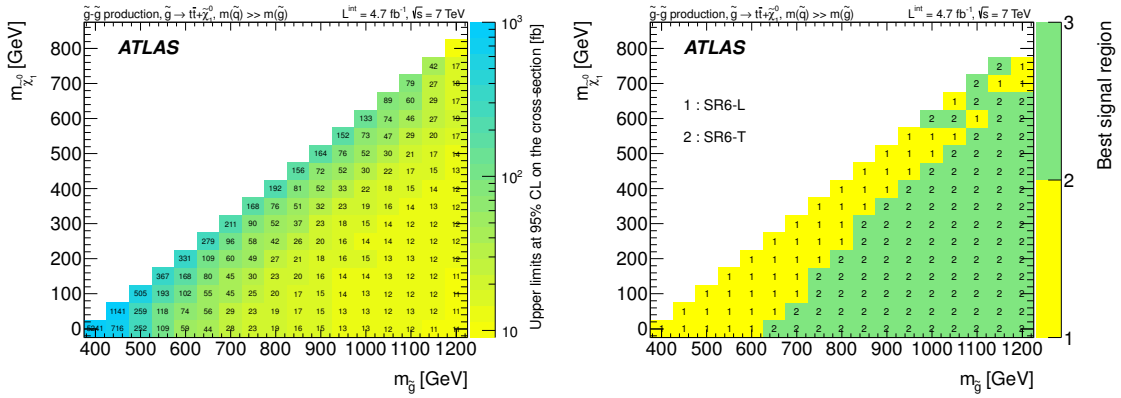

Figure 9.14 Left: 95 % CL excluded signal model cross-section for the Gtt model. Right: signal region which leads to the best expected upper limit on the visible cross-section for the Gtt model.

and stop are the lightest squarks but $m_{\tilde{g}} < m_{\tilde{b}}$ and $m_{\tilde{g}} < m_{\tilde{t}}$. Pair production of gluinos is the only process taken into account, with gluinos decaying via virtual stops or sbottoms with a branching ratio of 50 % assumed for $\tilde{t} \to b + \tilde{\chi}_1^+$ and $\tilde{b} \to t + \tilde{\chi}_1^-$, respectively. The mass difference between charginos and neutralinos is set to 2 GeV, such that the fermions produced in $\tilde{\chi}^\pm \to \tilde{\chi}^0 + ff'$ are invisible to

the event selection, and gluino decays result in three-body final states: $b + \bar{t} + \tilde{\chi}_1^0$ or $t + \bar{b} + \tilde{\chi}_1^0$.

In this scenario, $\mathcal{A} \times \mathcal{E}$ is found to be between 0.1-3%, 3-15% and 15-25% for low, medium and high mass-spliting regions, respectively, depending on the signal region considered. The impact of the b-tagging uncertainty for SR4-L and SR4-M ranges 10-20%, 20-24% and 24-26% for low, medium and high mass-spliting regions, respectively, whereas for SR4-T, SR6-L, and SR6-T the effect is observed to be within 8-15% overall. Moreover, the impact of the JES uncertainty in the five signal regions is observed to be 15-30%, 7-15% and 3-7% for low, medium and high mass-spliting regions, respectively.

Figure 9.15 presents the exclusion limits in the $(m_{\tilde{g}}, m_{\tilde{\chi}_1^0})$ plane for the Gtb model. Also shown for reference is the previous ATLAS analysis [142]. Overall, gluino masses below 980 GeV are excluded for neutralino masses up to about 300 GeV while neutralino masses below 400 GeV are excluded for $m_{\tilde{g}} \leq 820$ GeV.

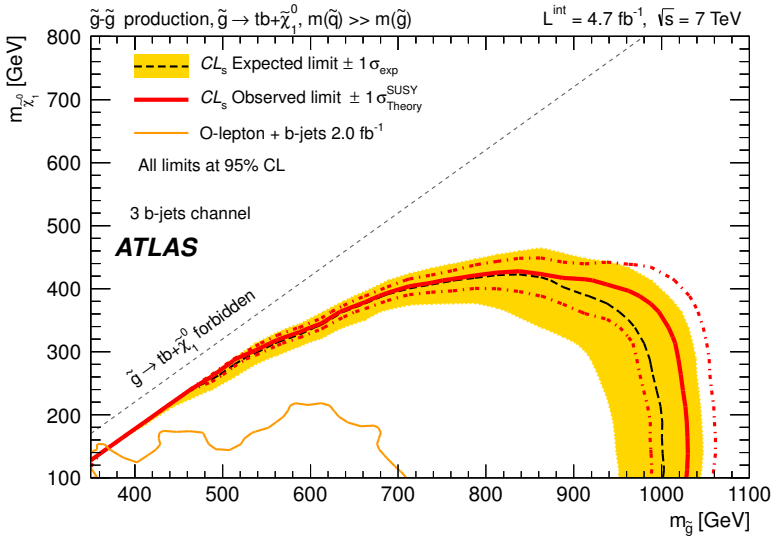

Figure 9.15 Exclusion limits in the $(m_{\tilde{g}}, m_{\tilde{\chi}_1^0})$ plane for the Gtb model. The dashed black and solid bold red lines show the 95% CL expected and observed limits respectively, including all uncertainties except the theoretical signal cross-section uncertainty. The shaded (yellow) band around the expected limit shows the impact of the experimental uncertainties while the dotted red lines show the impact on the observed limit of the variation of the nominal signal cross-section by $\pm 1\sigma_{\text{Theory}}^{\text{SUSY}}$ theoretical uncertainty. Also shown for reference is the previous ATLAS analysis [142].

For the region close to the diagonal the sensitivity of the search is deteriorated, since although there is a relatively large b-jet phase space imposed by the top mass (usually the 1st and 2nd b-jets) in the Gtb topology, those originated from the sbottom decay (generally the 3rd and 4th b-jets) have very little phase space available to them and thus they are soft. However, the implementation of a loose b-jet

p_{T} threshold (30 GeV) results in an improvement of sensitivity when approaching the forbidden region, as it can be observed in the new excluded region presented in Figure 9.15. The set of five signal regions (despite being primarily targeted at the Gbb and Gtt topologies) has been found to be sufficient to maintain close to within 30-50% of optimal sensitivity for the Gtb topologies as well (see Section 7.6). This results in a more stringent limit with respect to the previous analysis with 1 and 2 b-tagged jets for increasing values of $m_{\tilde{g}}$ and $m_{\tilde{\chi}^0}$. The signal regions SR4-T and SR6-T are found to lead to the best expected upper limit on the visible cross-section for the Gtb models.

9.2.4 Exclusion limits for the gluino-stop pMSSM model

Results are interpreted in the context of the so-called gluino-stop MSSM scenarios. The phenomenological constraints imposed are summarized next. The $\tilde{t}_1$ is the lightest squark, all other squarks are heavier than the gluino, and $m_{\tilde{g}} > m_{\tilde{t}_1} + m_t$, so the branching ratio for $\tilde{g} \to \tilde{t}_1 t$ decays is 100%. Stops are produced via $\tilde{g}\tilde{g}$ and $\tilde{t}_1\tilde{t}_1$[1], and are assumed to decay exclusively via $\tilde{t}_1 \to b\tilde{\chi}^{\pm}$. The neutralino mass is set to 60 GeV and the chargino mass to 120 GeV (according to previous limits imposed on supersymmetric particle searches [28]), where the latter is assumed to decay through a virtual W boson.

The full signal efficiency for the gluino-stop pMSSM model in the $(m_{\tilde{g}}, m_{\tilde{t}_1})$ plane is shown in Figure 9.16 for the signal region SR6-T. In this scenario, the values are found to be between 0.4-3%, 4-6% and 6-7.5% for low, medium and high values of both $m_{\tilde{t}_1}$ and $m_{\tilde{g}}$, respectively. This tendency results from the gluino-mediated on-shell stop production, with the neutralino and chargino masses set to 60 GeV and 120 GeV, respectively. Thus, the higher the gluino and stop masses (with small $\Delta m(\tilde{g}, \tilde{t}_1)$), the larger the phase space available for producing reasonably energetic b-jets from the subsequent decays in the final state.

The impact of the b-tagging and JES uncertainties are shown in Figure 9.17 (left and right, respectively) for the signal region SR6-T. The former (latter) is found to decrease from 16% (35.5%) to 3.5% (2%) for low and high values of ($m_{\tilde{g}}$,$m_{\tilde{t}_1}$), respectively.

The SR6-T is found to have a best sensitivity at high gluino masses, whereas the SR6-L has a better sensitivity at low gluino masses because of the softer kinematic cuts. Figure 9.18 presents the exclusion limits in the $(m_{\tilde{g}}, m_{\tilde{t}_1})$ plane for the gluino-stop model. Also shown for reference are the previous ATLAS analyses [142, 273]. Overall, gluino masses below 820 GeV are excluded for stop masses up to 640 GeV in this scenario.

[1]Direct stop pair production is also included but its contribution to the signal regions is negligible, as it results in only two b-jets in the final state.

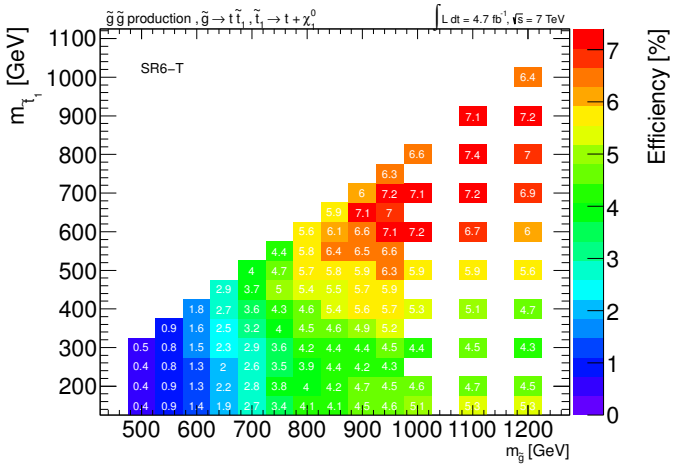

Figure 9.16 The signal efficiency for gluino mediated stop pair production in the $(m_{\tilde{g}}, m_{\tilde{t}_1})$ plane for the pMSSM gluino-stop model, for the signal region SR6-T.

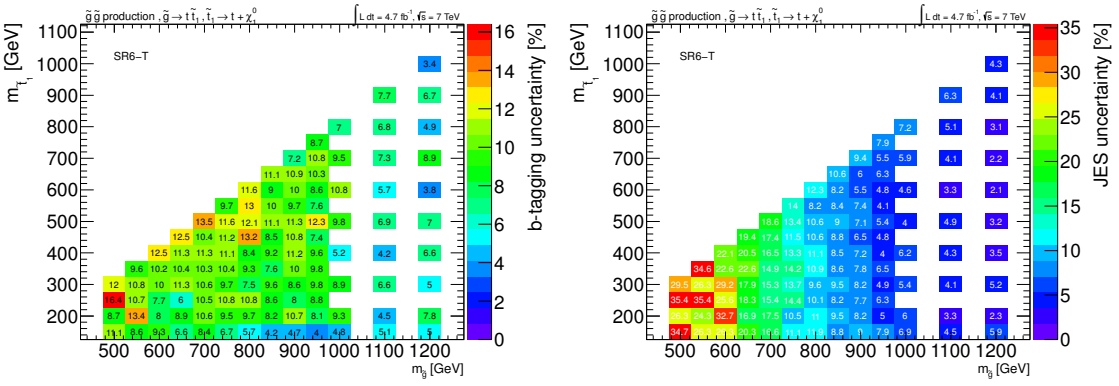

Figure 9.17 Impact of the b-tagging (left) and JES (right) uncertainties for gluino mediated stop pair production in the $(m_{\tilde{g}}, m_{\tilde{t}_1})$ plane in the pMSSM gluino-stop model, for the signal region SR6-T.

9.2.5 Exclusion limits for the gluino-sbottom pMSSM model

Results are interpreted in the context of the so-called gluino-sbottom MSSM scenarios. The phenomenological constraints imposed are summarized next. The $\tilde{b}_1$ is the lightest squark, all other squarks are heavier than the gluino, and $m_{\tilde{g}} > m_{\tilde{b}_1} > m_{\tilde{\chi}_1^0}$, so the branching ratio for $\tilde{g} \to \tilde{b}_1 b$ decays is 100%. Sbottoms are produced via $\tilde{g}\tilde{g}$ and $\tilde{b}_1\tilde{b}_1$[2], and are assumed to decay exclusively via $\tilde{b}_1 \to b\tilde{\chi}_1^0$, where $m_{\tilde{\chi}_1^0}$ is set to 60 GeV.

The efficiencies for gluino mediated on-shell sbottom pair production are found to increase from low to high values of both $m_{\tilde{b}_1}$ and $m_{\tilde{g}}$. The largest values are obtained

[2]Direct sbottom pair production is also included but its contribution to the signal regions is negligible, as it results in only two b-jets in the final state.

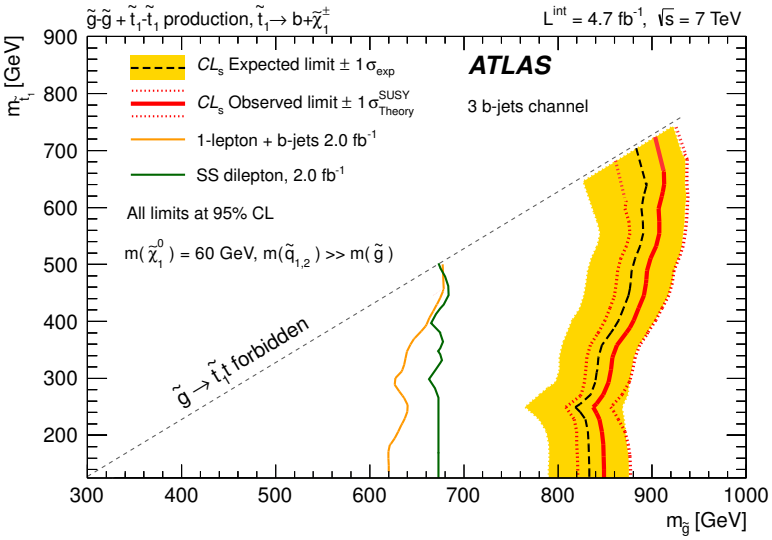

Figure 9.18 The exclusion limits in the $(m_{\tilde{g}}, m_{\tilde{t}_1})$ plane for the gluino-stop model. The dashed black and solid bold red lines show the 95% CL expected and observed limits respectively, including all uncertainties except the theoretical signal cross-section uncertainty. The shaded (yellow) band around the expected limit shows the impact of the experimental uncertainties while the dotted red lines show the impact on the observed limit of the variation of the nominal signal cross-section by $\pm 1\sigma_{\text{Theory}}^{\text{SUSY}}$ theoretical uncertainty. Also shown for reference are the previous ATLAS analyses [142, 273].

for SR4-T, within the range 15-38%. The other two regions (SR4-L and SR4-M) reach values of approximately 20% for both cases. The impact of the b-tagging uncertainty is found to be 23-32% for SR4-L and SR4-M, whereas values between 10-25% are observed for SR4-T. In addition, the effect of the JES uncertainty for the three signal regions above is found to range between 2-15%. The impact of these uncertainties decreases from low to high values of $(m_{\tilde{g}}, m_{\tilde{b}_1})$. The SR4-T has the best sensitivity at high gluino masses, whereas SR4-L and SR4-M have a better sensitivity at low gluino masses because of the softer kinematic cuts. Figure 9.19 presents the exclusion limits in the $(m_{\tilde{g}}, m_{\tilde{b}_1})$ plane for the gluino-sbottom model. Also shown for reference are previous CDF [275, 276], DØ [277] and ATLAS [142] results. Overall, gluino masses below 1020 GeV are excluded for sbottom masses up to 820 GeV in this scenario.

9.3 Discussion

The expected and observed 95% CL exclusion limits for Gbb, Gtt and Gtb simplified models and the gluino-stop and gluino-sbottom MSSM models considered above have been presented in Figures 9.8, 9.13 and 9.15, and in Figures 9.18

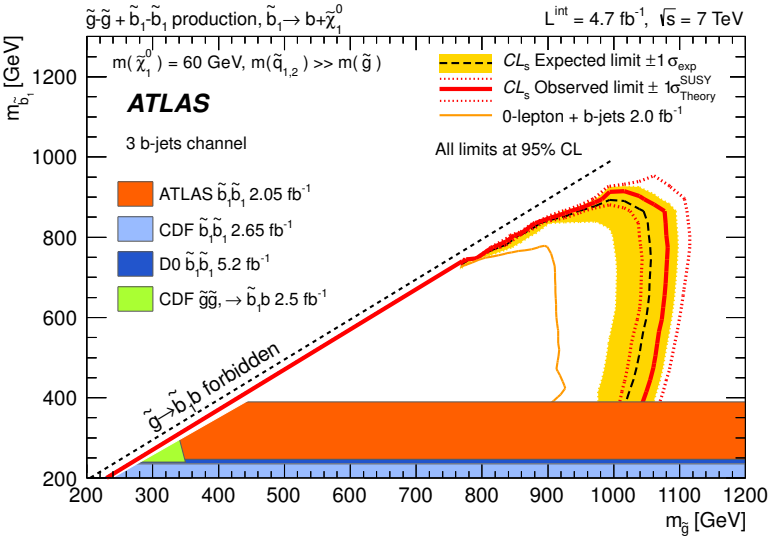

Figure 9.19 The exclusion limits in the $(m_{\tilde{g}}, m_{\tilde{b}_1})$ plane for the gluino-sbottom model. The dashed black and solid bold red lines show the 95% CL expected and observed limits respectively, including all uncertainties except the theoretical signal cross-section uncertainty. The shaded (yellow) band around the expected limit shows the impact of the experimental uncertainties while the dotted red lines show the impact on the observed limit of the variation of the nominal signal cross-section by $\pm 1\sigma^{\text{SUSY}}_{\text{Theory}}$ theoretical uncertainty. Also shown for reference are the previous CDF [275, 276], DZero [277] and ATLAS [142] analyses.

and 9.19, respectively. In the gluino-sbottom model, gluino masses below 1000 GeV are excluded for sbottom masses up to about 870 GeV using the most conservative $-1\sigma^{\text{SUSY}}_{\text{Theory}}$ hypothesis. This extends by approximatively 100 GeV the limits derived in the same scenario by the previous ATLAS analysis performed with 2 fb^{-1} [142] and is complementary to the ATLAS search for direct sbottom pair production, also carried out with 2 fb^{-1} [144]. The exclusion is less stringent in the region with low $m_{\tilde{g}} - m_{\tilde{b}_1}$, where softer jets are expected. Because of the kinematic cuts applied, the limits depend on the neutralino mass assumption for low mass splitting between the sbottom and the neutralino as shown for the Gbb model where gluino masses below 1020 GeV are excluded for neutralino masses up to about 400 GeV, improving the previous ATLAS limits [142] by approximatively 100 GeV. In the gluino-stop model, gluino masses below 820 GeV are excluded for stop masses up to 640 GeV, extending the previous ATLAS limits [142, 273] by approximatively 150 GeV. In the Gtt model, gluino masses below 940 GeV are excluded for $m_{\tilde{\chi}^0_1} < 50$ GeV while neutralino masses below 320 GeV are excluded for $m_{\tilde{g}} = 800$ GeV. This search extends the exclusion limits on the gluino mass from the ATLAS multi-jet analysis carried out with the same data set [274] and from the CMS same-sign dilepton analysis performed with 5 fb^{-1} [278] by approximatively 60 GeV and 130 GeV, respectively, for neutralino masses below 100 GeV. In the region with low $m_{\tilde{g}} - m_{\tilde{\chi}^0_1}$, the lim-

its obtained with the CMS analysis are most stringent due to the softer kinematic cuts. Finally, Gtb simplified models where gluinos can decay in either stop-top or sbottom-bottom (thus leading to final states including two tops and two bottom quarks) have been also considered. In this scenario, gluino masses below 980 GeV are excluded for neutralino masses up to about 300 GeV while neutralino masses below 400 GeV are excluded for $m_{\tilde{g}} \leq 820$ GeV, improving the previous ATLAS limit [142] by approximatively 300 GeV.

10

Conclusions

The Large Hadron Collider has steadily run colliding bunches of protons at $\sqrt{s} = 7$ TeV since 2010, and the experiments therein are taking the first steps toward resolving many long-standing puzzles about fundamental physics at the weak scale.

The outstanding performance of the ATLAS detector with all its sub-detectors running in optimal conditions allowed the rediscovery of the Standard Model in this new energy regime. This successful achievement is based on a complete and exhaustive understanding of the experimental objects resulting from particles produced in a pp collision that are reconstructed from the enormous variety of signals that the detector systems of the ATLAS experiment provide. Within this framework, this thesis presents two original contributions: the measurement of the jet energy resolution (JER) and the search for top and bottom scalar quarks from gluino pair production in events with large missing transverse momentum and at least three jets identified as originating from a b-quark.

The contribution of the calorimeter information to the data analysis in ATLAS is of key importance to provide solid and common foundations for understanding jet physics and missing transverse energy. Thus, the precise determination of the jet energy scale (JES) and the jet energy resolution (JER) are the two major tasks of the ATLAS jet calibration program. Chapter 6 has presented the first determination of the jet energy resolution and its uncertainty with the `ATLAS` detector in proton-proton collisions at a centre-of-mass energy of $\sqrt{s} = 7$ TeV. The jet energy resolution for various JES calibration schemes has been estimated using two in situ methods with a data sample corresponding to an integrated luminosity of 35 pb^{-1} collected by the `ATLAS` experiment at $\sqrt{s} = 7$ TeV. The Monte Carlo simulation describes the jet energy resolution measured in data within 10% for jets with p_{T} values between 30 GeV and 500 GeV in the rapidity range $|y| < 2.8$. The resolutions obtained

applying the in situ techniques to Monte Carlo simulation are in agreement within 10% with the resolutions determined by comparing jets at calorimeter and particle level. The total uncertainties on these measurements range from 20% to 10% for jets within $|y| < 2.8$ and with transverse momenta increasing from 30 GeV to 500 GeV. Overall, the results measured with the two in situ methods have been found to be consistent within the determined systematic uncertainties. A degradation of the jet energy resolution performance with a data sample collected during 2011 that corresponds to 950 pb^{-1} of integrated luminosity has been observed, due to the increasing amount of pile-up given the evolving conditions of the LHC towards its nominal parameters. Thus, the understanding of the jet energy resolution in very high pile-up environment is one of the main challenges for 2012 data. It is of key importance to establish the impact of higher pile-up conditions and harsh noise thresholds on the jet energy resolution in order to help provide the best performance for topo-clustering and local hadron calibration for future physics analysis.

Final states with high transverse momentum $b-$jets, large $E_{\mathrm{T}}^{\mathrm{miss}}$ with or without leptons are sensitive to SUSY signal production involving third generation squarks. The main results presented in this thesis correspond to the first search for top and bottom squarks from gluino pair production in events with large missing transverse momentum and at least three jets identified as originating from a b-quark. The analysis has been performed with the full 2011 data sample corresponding to a total integrated luminosity of 4.7 fb^{-1} of proton-proton collisions at center-of-mass energy $\sqrt{s} = 7$ TeV using the ATLAS detector at the LHC [279]. The results of searches for supersymmetry in events with large missing transverse momentum and heavy flavour jets using at least one or two b-jets had been reported by the initial publications of ATLAS within this area. These corresponded to analysis done with 35 pb^{-1} of data collected in 2010 [139], two analysis done with 0.83 fb^{-1} [140] and 1.03 fb^{-1} [141] of data collected during early 2011, and their corresponding updates using a data sample of 2 fb^{-1} [142, 144].

For the search presented in this thesis, a new strategy to characterize the first robust evidence for new physics likely to be seen at the LHC has been implemented, by means of the so-called *simplified models*, which allow to present the results of the search in a manner that is as model-independent as possible. An exhaustive optimization has been done targeting different topologies involving SUSY particles using the simplified models, from which five enriched signal regions (SR) have been chosen to identify possible SUSY-like event candidates with at least three b-jets and missing transverse energy. The results obtained for each of the five SR have been found to be in good agreement with the SM predictions, and therefore, exclusion limits at 95% CL are presented for a variety of gluino-mediated models:

- Phenomenological MSSM gluino-sbottom model: MSSM scenarios where a scalar bottom $\tilde{b}_1$ is the lightest squark and all other squarks are heavier than

the gluino (with $m_{\tilde{g}} > m_{\tilde{b}_1} > m_{\tilde{\chi}_1^0}$). In this case, the results are presented in the $m_{\tilde{g}}, m_{\tilde{b}_1}$ mass plane at fixed $\tilde{\chi}_1^0$ mass. The sbottom is assumed to decay exclusively via $\tilde{b}_1 \to b + \tilde{\chi}_1^0$, where the neutralino mass is assumed to be 60 GeV. In this scenario, gluino masses below 1020 GeV are excluded for sbottom masses up to 820 GeV.

- Gbb simplified model: gluinos decay into three-body final states ($b\bar{b}\tilde{\chi}_1^0$) via an off-shell sbottom ($m_{\tilde{b}_1} > m_{\tilde{g}} > m_{\tilde{\chi}_1^0}$). In this scenario, the results are presented in the $m_{\tilde{g}}, m_{\tilde{\chi}_1^0}$ mass plane at fixed (large) sbottom mass. Gluino masses below 1020 GeV are excluded for neutralino masses up to about 400 GeV while neutralino masses below 500 GeV are excluded for $m_{\tilde{g}} \leq 940$ GeV.

- Phenomenological MSSM gluino-stop model: MSSM scenarios where instead the scalar top $\tilde{t}_1$ is the lightest squark ($m_{\tilde{g}} > m_{\tilde{t}_1} > m_{\tilde{\chi}^\pm} > m_{\tilde{\chi}_1^0}$), with $BR(\tilde{g} \to \tilde{t}t)$=100%. In this case, the results are presented in the $m_{\tilde{g}}, m_{\tilde{t}_1}$ mass plane at fixed $\tilde{\chi}_1^0$ and $\tilde{\chi}^\pm$ masses. The stop decays as $\tilde{t}_1 \to b + \tilde{\chi}^\pm$, and chargino masses are assumed to be around 120 GeV, i.e. twice the neutralino mass. In this scenario, gluino masses below 820 GeV are excluded for stop masses up to 640 GeV.

- Gtt simplified model: Results were also interpreted in the context of simplified models assuming $\tilde{g} \to t\bar{t}\tilde{\chi}_1^0$ decays ($m_{\tilde{t}_1} > m_{\tilde{g}} > m_{\tilde{\chi}^\pm} > m_{\tilde{\chi}_1^0}$). The results are presented in the $m_{\tilde{g}}, m_{\tilde{\chi}_1^0}$ mass plane at fixed (large) stop mass. In this scenario, gluino masses below 940 GeV are excluded for $m_{\tilde{\chi}_1^0} < 50$ GeV while neutralino masses below 320 GeV are excluded for $m_{\tilde{g}} \leq 800$ GeV.

- Gtb simplified model: This analysis was also used to derive exclusion limits for a simplified model where gluinos are assumed to decay via off-shell stops or sbottoms in $tb\tilde{\chi}_1^0\tilde{\chi}_1^0$ final states ($m_{\tilde{b}_1}, m_{\tilde{t}_1} > m_{\tilde{g}} > m_{\tilde{\chi}^\pm} > m_{\tilde{\chi}_1^0}$). In these simplified models, virtual stops and sbottoms decay with BR=50% in $b + \tilde{\chi}_1^\pm$ and $t + \tilde{\chi}_1^\pm$, respectively. A small mass difference between charginos and neutralinos is assumed ($\Delta M(\tilde{\chi}^\pm, \tilde{\chi}_1^0) = 2$ GeV). The results are presented in the $m_{\tilde{g}}, m_{\tilde{\chi}_1^0}$ mass plane at fixed (large) sbottom and stop masses. Gluino masses below 980 GeV are excluded for neutralino masses up to about 300 GeV while neutralino masses below 400 GeV are excluded for $m_{\tilde{g}} \leq 820$ GeV.

The key motivation for searching third generation squarks at the LHC is the naturalness criterion in which the masses of the particles, whose existence strongly influence the evolution of the Higgs mass parameters, are severely constrained. The minimal requirements to naturally solve the hierarchy problem are light stops, sbottoms and gauginos, and as a consequence, the gluino is required not to be heavier than about 1.5 TeV due to its contribution to the radiative correction to the stop

mass. The results presented in this thesis have contributed to the search of third generation squarks, where impressive limits have been set with the ATLAS detector using proton-proton collisions at $\sqrt{s} = 7$, excluding already a significant amount of the parameter space. Overall, these results are the most stringent limits obtained up to now by collider experiments, where gluino-mediated models with gluino masses up to 1.02 TeV are excluded, extending significantly all previous results, and imposing harsh constraints in the natural spectrum motivated by the supersymmetric models.

Bibliografy

[1] L. Evans and P. Bryant, *LHC Machine*, Journal of Instrumentation **3** (2008) no. 08, S08001.

[2] ATLAS Collaboration, *The ATLAS Experiment at the CERN Large Hadron Collider*, Journal of Instrumentation **3** (2008) no. 08, S08003.

[3] S. L. Glashow, *Partial-symmetries of weak interactions*, Nuclear Physics **22** (1961) no. 4, 579 – 588.

[4] S. Weinberg, *A Model of Leptons*, Phys. Rev. Lett. **19** (Nov, 1967) 1264–1266.

[5] A. Salam, *Elementary Particle Physics: Relativistic Groups and Analyticity*, in Eighth Nobel Symposium (1968) 367.

[6] H. Fritzsch, M. Gell-Mann, and H. Leutwyler, *Advantages of the Color Octet Gluon Picture*, Phys.Lett. **B47** (1973) 365–368.

[7] D. J. Gross and F. Wilczek, *Asymptotically Free Gauge Theories. I*, Phys. Rev. D **8, 10** (Nov, 1973) 3633–3652.

[8] S. Weinberg, *Non-Abelian Gauge Theories of the Strong Interactions*, Phys. Rev. Lett. **31, 7** (Aug, 1973) 494–497.

[9] A. S. Kronfeld and C. Quigg, *Resource Letter: Quantum Chromodynamics*, Am.J.Phys. **78** (2010) 1081–1116, arXiv:1002.5032 [hep-ph] (2010).

[10] Yu.A. Golfand and E.P. Likhtman, JETP Lett. **13** (1971) 323; A. Neveu and J.H. Schwartz, Nucl. Phys. **B31** (1971) 86; A. Neveu and J.H. Schwartz, Phys. Rev. **D4** (1971) 1109; P. Ramond, Phys. Rev. **D3** (1971) 2415; D.V. Volkov and V.P. Akulov, Phys. Lett. **B46** (1973) 109; J. Wess and B. Zumino, Phys. Lett. **B49** (1974) 52; J. Wess and B. Zumino, Nucl. Phys. **B70** (1974) 39 .

[11] U. Amaldi, W. de Boer, and H. Fürstenau, *Comparison of grand unified theories with electroweak and strong coupling constants measured at LEP*, Phys. Lett. B **260** (1991) 447.

[12] W. Beenakker, R. Hopker, and M. Spira, *PROSPINO: A Program for the production of supersymmetric particles in next-to-leading order QCD*, arXiv:hep-ph/9611232 [hep-ph] (1996).

[13] S. P. Martin A Supersymmetry Primer (1997) , arXiv:hep-ph/9709356 [hep-ph] (1997).

[14] S. Dimopoulos and H. Georgi, *Softly broken Supersymmetry and SU(5)*, Nucl. Phys. **B193** (1981) 150.

[15] M. E. Peskin, *Summary of Lepton Photon 2011*, arXiv:1110.3805 [hep-ph] (2011).

[16] P. A. M. Dirac, *The Quantum Theory of the Emission and Absorption of Radiation*, Proc. R. Soc. Lond **A114** (1927) 243–265.

[17] S. Tomonaga, *On a Relativistically Invariant Formulation of the Quantum Theory of Wave Fields*, Progress of Theoretical Physics **1** (1946) no. 2, 27–42.

[18] J. Schwinger, *Quantum Electrodynamics. I. A Covariant Formulation*, Phys. Rev. **74, 10** (1948) 1439–1461.

[19] R. P. Feynman, *Mathematical Formulation of the Quantum Theory of Electromagnetic Interaction*, Phys. Rev. **80, 3** (1950) 440–457.

[20] E. Fermi, *Towards the Theory of β-Rays*, Nuovo Cim. **11** (1934) 1–19.

[21] E. Noether, *Invariante Varlationsprobleme*, Math-phys. Klasee (1918) 235–257.

[22] K. Nishijima, *Charge Independence Theory of V Particles*, Progress of Theoretical Physics **13** (1955) no. 3, 285–304.

[23] M. Gell-Mann, *The interpretation of the new particles as displaced charge multiplets*, Il Nuovo Cimento (1955-1965) **4** (1956) 848–866.

[24] F. Halzen and A. Martin, *Quarks and Leptons: An Introductory Course in Modern Particle Physics*. Wiley Text Books, USA, 1984.

[25] M. Peskin and D. Schroeder, *Quantum field theory*. Addison-Wesley Advanced Book Program, 1996.

[26] N. Cabibbo, *Unitary Symmetry and Leptonic Decays*, Phys. Rev. Lett. **10** (Jun, 1963) 531–533.

[27] M. Kobayashi and T. Maskawa, *CP-Violation in the Renormalizable Theory of Weak Interaction*, Progress of Theoretical Physics **49** (1973) no. 2, 652–657.

[28] J. Beringer and others (Particle Data Group), *The Review of Particle Physics*, Phys. Rev. D **86** (2012) 1528.

[29] Y. Nambu, *Quasi-Particles and Gauge Invariance in the Theory of Superconductivity*, Phys. Rev. **117, 3** (Feb, 1960) 648–663.

[30] J. Goldstone, *Field Theories with Superconductor Solutions*, Nuovo Cimento **19** (1961) 154–164.

[31] P. W. Anderson, *Plasmons, Gauge Invariance, and Mass*, Phys. Rev. **130, 1** (Apr, 1963) 439–442.

[32] P. W. Higgs, *Broken Symmetries and the Masses of Gauge Bosons*, Phys. Rev. Lett. **13, 16** (Oct, 1964) 508–509.

[33] P. Higgs, *Broken symmetries, massless particles and gauge fields*, Physics Letters **12** (1964) no. 2, 132 – 133.

[34] Englert, F. and Brout, R. , *Broken Symmetry and the Mass of Gauge Vector Mesons*, Phys. Rev. Lett. **13, 9** (Aug, 1964) 321–323.

[35] G. S. Guralnik, C. R. Hagen, and T. W. B. Kibble, *Global Conservation Laws and Massless Particles*, Phys. Rev. Lett. **13, 20** (Nov, 1964) 585–587.

[36] P. W. Higgs, *Spontaneous Symmetry Breakdown without Massless Bosons*, Phys. Rev. **145, 4** (May, 1966) 1156–1163.

[37] UA1 Collaboration, G. Arnison et al., *Experimental observation of isolated large transverse energy electrons with associated missing energy at* $\sqrt{s} = 540$ *GeV*, Phys. Lett. **B122** (1983) 103–116.

[38] UA1 Collaboration, G. Arnison et al., *Experimental observation of lepton pairs of invariant mass around 95* GeV/c^2 *at the CERN SPS collider*, Phys. Lett. **B126** (1983) 398–410.

[39] CDF Collaboration Collaboration, *Observation of Top Quark Production in* $\overline{p}p$ *Collisions with the Collider Detector at Fermilab*, Phys. Rev. Lett. **74, 14** (Apr, 1995) 2626–2631.

[40] D0 Collaboration Collaboration, *Search for High Mass Top Quark Production in $p\bar{p}$ Collisions at $\sqrt{s} = 1.8$ TeV*, Phys. Rev. Lett. **74, 13** (Mar, 1995) 2422–2426.

[41] CMS Collaboration, *The CMS experiment at the CERN LHC*, Journal of Instrumentation **3** (2008) no. 08, S08004.

[42] ATLAS Collaboration, *Observation of a new particle in the search for the Standard Model Higgs boson with the ATLAS detector at the LHC*, Phys.Lett. **B716** (2012) 1–29, arXiv:1207.7214 [hep-ex] (2012).

[43] CMS Collaboration, *Observation of a new boson at a mass of 125 GeV with the CMS experiment at the LHC*, Phys.Lett. **B716** (2012) 30–61, arXiv:1207.7235 [hep-ex] (2012).

[44] M. Gell-Mann, *A schematic model of baryons and mesons*, Physics Letters **8** (1964) no. 3, 214 – 215.

[45] G. Zweig, *A schematic model of baryons and mesons*, CERN preprints No. 8182/TH. 401 and No. 8419/TH. 412, unpublished. (1964) .

[46] J. J. J. Kokkedee, *The Quark Model*. Benjamin, New York, USA, 1969.

[47] B. V. Struminsky, *Magnetic moments of barions in the quark model*, JINR-Preprint (January, 1965) 1939.

[48] O. W. Greenberg, *Spin and Unitary-Spin Independence in a Paraquark Model of Baryons and Mesons*, Phys. Rev. Lett. **13, 20** (Nov, 1964) 598–602.

[49] M. Y. Han and Y. Nambu, *Three-Triplet Model with Double* SU(3) *Symmetry*, Phys. Rev. **139, 4B** (Aug, 1965) B1006–B1010.

[50] E. D. Bloom, D. H. Coward, H. DeStaebler, J. Drees, G. Miller, L. W. Mo, R. E. Taylor, M. Breidenbach, J. I. Friedman, G. C. Hartmann, and H. W. Kendall, *High-Energy Inelastic $e-p$ Scattering at 6° and 10°*, Phys. Rev. Lett. **23, 16** (Oct, 1969) 930–934.

[51] J. Friedman and H. Kendall Ann. Rev. Nucl. Sci. **22** (1972) 203.

[52] J. D. Bjorken and E. A. Paschos, *Inelastic Electron-Proton and γ-Proton Scattering and the Structure of the Nucleon*, Phys. Rev. **185, 5** (Sep, 1969) 1975–1982.

[53] R. P. Feynman, *Very High-Energy Collisions of Hadrons*, Phys. Rev. Lett. **23, 24** (Dec, 1969) 1415–1417.

[54] C. N. Yang and R. L. Mills, *Conservation of Isotopic Spin and Isotopic Gauge Invariance*, Phys. Rev. **96, 1** (Oct, 1954) 191–195.

[55] R. Ellis, W. Stirling, and B. Webber, *QCD and Collider Physics*. Cambridge, 1996.

[56] G. 't Hooft, *Dimensional regularization and the renormalization group*, Nuclear Physics B **61** (1973) no. 0, 455 – 468.

[57] S. Bethke, *The 2009 World Average of alpha(s)*, Eur.Phys.J. **C64** (2009) 689–703, arXiv:0908.1135 [hep-ph] (2009).

[58] D. J. Gross and F. Wilczek, *Ultraviolet Behavior of Non-Abelian Gauge Theories*, Phys. Rev. Lett. **30, 26** (Jun, 1973) 1343–1346.

[59] H. D. Politzer, *Reliable Perturbative Results for Strong Interactions?*, Phys. Rev. Lett. **30, 26** (Jun, 1973) 1346–1349.

[60] H. Georgi and S. Glashow, *Unity of all elementary-particle forces*, Phys. Rev. Lett. **32** (1974) 438–441.

[61] G. Hanson et al., *Evidence for Jet Structure in Hadron Production by e^+e^- Annihilation*, Phys. Rev. Lett. **35, 24** (Dec, 1975) 1609–1612.

[62] L. DiLlela, *Jet Production in Hadronic Collisions*, Annual Review of Nuclear and Particle Science **35** (1985) 107–134.

[63] M. Dobbs, S. Frixione, E. Laenen, K. Tollefson, H. Baer, et al., *Les Houches guidebook to Monte Carlo generators for hadron collider physics*, arXiv:hep-ph/0403045 [hep-ph] (2004).

[64] T. Sjostrand, *Monte Carlo Generators*, arXiv:hep-ph/0611247 [hep-ph] (2006).

[65] M. Mangano et al., *ALPGEN, a generator for hard multiparton processes in hadronic collisions*, JHEP **0307** (2003) 001, arXiv:hep-ph/0206293 [hep-ph] (2003).

[66] J. Alwall, M. Herquet, F. Maltoni, O. Mattelaer, and T. Stelzer, *MadGraph 5 : Going Beyond*, JHEP **06** (2011) 128.

[67] S. Frixione and B. R. Webber, *The MC@NLO 3.2 event generator*, arXiv:hep-ph/0601192 [hep-ph] (2006).

[68] T. Sjostrand, S. Mrenna, and P. Z. Skands, *PYTHIA 6.4 Physics and Manual*, JHEP **0605** (2006) 026, arXiv:hep-ph/0603175 [hep-ph] (2006).

[69] G. Corcella et al., *HERWIG 6: An event generator for hadron emission reactions with interfering gluons (including supersymmetric processes)*, JHEP **01** (2001) 010.

[70] M. Bahr et al., *Herwig++ Physics and Manual*, Eur. Phys. J. **C58** (2008) 639–707, arXiv:0803.0883 [hep-ph] (2008).

[71] M. Bahr et al., *Herwig++ 2.3 Release Note*, arXiv:0812.0529 [hep-ph] (2008).

[72] M. Bengtsson and T. Sjostrand, *Parton Showers In Leptoproduction Events*, Z.Phys. C **37** (1988) 465.

[73] S. Hoeche et al., *Matching parton showers and matrix elements*, arXiv:hep-ph/0602031 [hep-ph] (2006).

[74] S. Catani et al., *QCD matrix elements + parton showers*, JHEP **0111** (2001) 063, arXiv:hep-ph/0109231 [hep-ph] (2001).

[75] F. Krauss, *Matrix elements and parton showers in hadronic interactions*, JHEP **0208** (2002) 015, arXiv:hep-ph/0205283 [hep-ph] (2002).

[76] J. C. Collins and D. E. Soper, *The Theorems of Perturbative QCD*, Annual Review of Nuclear and Particle Science **37** (1987) no. 1, 383–409.

[77] G. Altarelli and G. Parisi, *Asymptotic freedom in parton language*, Nuclear Physics B **126** (1977) no. 2, 298 – 318.

[78] J. Pumplin et al., *New generation of parton distributions with uncertainties from global QCD analysis*, JHEP **07** (2002) 012.

[79] P. Nadolsky et al., *Implications of CTEQ global analysis for collider observables*, Phys. Rev. **D78** (2008) 013004.

[80] MSTW PDFs : PDF benchmarking for LHC processes, http://mstwpdf.hepforge.org/pdf4lhc/. .

[81] A. Sherstnev and R. Thorne Eur. Phys. J. **C55** (2008) 553–575, arXiv:0711.2473 [hep-ph] (2008).

[82] B. Andersson, G. Gustafson, and B. Soderberg, *A General Model for Jet Fragmentation*, Z. Phys. **C20** (1983) 317.

[83] B. Andersson, G. Gustafson, and B. Soderberg, *A Probability Measure on Parton and String States*, Nucl. Phys. **B264** (1986) 29.

[84] B. Webber, *A QCD Model for Jet Fragmentation Including Soft Gluon Interference*, Nucl.Phys. **B238** (1984) 492.

[85] ATLAS Collaboration, ATL-PHYS-PUB-2010-014 (2010).

[86] ATLAS Collaboration, ATLAS-CONF-2010-031 (2010).

[87] A. Y. Smirnov, *Neutrino physics: Open theoretical questions*, Int.J.Mod.Phys. **A19** (2004) 1180–1200, arXiv:hep-ph/0311259 [hep-ph] (2004).

[88] B. Paczynski, *Gravitational Microlensing by the Galactic Halo*, AstroPhys. J. **304** (1986) 1–5.

[89] K. Griest, *Galactic microlensing as a method of detecting massive compact halo objects*, AstroPhys. J. **366** (1991) 412–421.

[90] F. D. Paolis, G. Ingrosso, P. Jetzer, and M. Roncadelli, *A Case for a Baryonic Dark Halo*, Phys. Rev. Lett. **74** (1995) 14–47.

[91] J. Dunkley et al., *Five-Year Wilkinson Microwave Anisotropy Probe (WMAP) Observations: Likelihoods and Parameters from the WMAP data*, Astrophys. J. Supp **180** (2009) 306.

[92] H. E. Haber, *The Supersymmetric top ten lists*, arXiv:hep-ph/9308209 [hep-ph] (1993).

[93] M. Veltman, *Second threshold in weak interactions*, Acta Phys. Pol. B **8** (1977) 475.

[94] E. Gildener, *Gauge-symmetry hierarchies*, Phys. Rev. D **14 (16)** (1976) 1667–1672.

[95] S. Weinberg, *Gauge hierarchies*, Phys. Letter B **82 (3-4)** (1979) 387–391.

[96] L. Susskind, *The Gauge Hierarchy Problem, Technicolor, Supersymmetry, and all that*, Phys. Rep. **104** (1984) 181–193.

[97] H. Haber and G. Kane, *The search for supersymmetry: probing physics beyond the Standard Model*, Phys. Rep. **117** (1985) 75–263.

[98] S. Weinberg, *Implications of dynamical symmetry breaking*, Phys. Rev. D **13 (4)** (1976) 974–996.

[99] L. Susskind, *Dynamics of spontaneous symmetry breaking in the Weinberg-Salam theory*, Phys. Rev. D **20 (10)** (1979) 2619–2625.

[100] S. Dimopoulos and S. Raby, *Supercolor*, Nucl. Phys. B **192** (1981) 353.

[101] E. Witten, *Dynamical breaking of Supersymmetry*, Nucl. Phys. B **188** (1981) 513–554.

[102] P. Fayet, Nucl. Phys. **B90** (1975) 104; P. Fayet, Phys. Lett. **B69** (1977) 489; G.R. Farrar and P. Fayet, Phys. Lett. **B76** (1978) 575 .

[103] R. Haag, J. T. Lopuszanski, and M. Sohnius, *All possible generators of supersymmetries of the S-Matrix*, Nucl. Phys. B **88** (1975) 257–274.

[104] L. S. J. Polchinski, *Breaking Of Supersymmetry At Intermediate-Energy*, Phys. Rev. D **26** (1982) 3661.

[105] T. Grisaru, W. Siegel, and M. Rocek, *Improved methods for Supergraphs*, Nucl. Phys. B **159** (1979) 429.

[106] H. Georgi, H. Quinn, and S. Weinberg, *Hierarchy of interactions in Unified Gauge Theories*, Phys. Rev. Lett. **33** (1974) 451.

[107] P. Nath and R. Arnowitt, *Generalized Supergauge Symmetry As A New Framework For Unified Gauge Theories*, Phys. Lett. B **56** (1975) 177.

[108] D. Gross and R. Jackiw, Phys.Rev. **D6** (1972) 477; L. Alvarez-Gaume and E. Witten, Nucl. Phys. B234 (1983) 269 .

[109] J. Gunion, H. E. Haber, G. Kane, and S. Dawson, *in The Higgs hunter's guide, Chapter 4*.

[110] S. Dawson, *The MSSM and why it works*, arXiv:hep-ph/9712464 [hep-ph] (1997).

[111] Super-Kamiokande Collaboration Collaboration, H. Nishino et al., *Search for Proton Decay via $p \to e^+\pi^0$ and $p \to \mu^+\pi^0$ in a Large Water Cherenkov Detector*, Phys. Rev. Lett. **102, 14** (Apr, 2009) 141801.

[112] H. Goldberg, *Constraint on the Photino Mass from Cosmology*, Phys. Rev. Lett. **50** (May, 1983) 1419–1422.

[113] S. Dimopoulos and D. W. Sutter, *The Supersymmetric flavor problem*, Nucl.Phys. **B452** (1995) 496–512, arXiv:hep-ph/9504415 [hep-ph] (1995).

[114] A. Djouadi, *The Anatomy of electro-weak symmetry breaking. II. The Higgs bosons in the minimal supersymmetric model*, Phys.Rept. **459** (2008) 1–241, arXiv:hep-ph/0503173 [hep-ph] (2008).

[115] A. H. Chamseddine, R. Arnowitt, and P. Nath, *Locally Supersymmetric Grand Unification*, Phys. Rev. Lett. **49, 14** (Oct, 1982) 970–974.

[116] G.L. Kane and C. Kolda and J.D. Wells, Phys. Rev. Lett. **70**, 2686 (1993) [hep-ph/9210242]; J.R. Espinosa and M. Quiros, Phys. Lett. **B302**, 51 (1993) [hep-ph/9212305] .

[117] M. Dine and W. Fishler, *Phenomenological model of particle physics based on supersymmetry*, Phys. Lett. B **110** (1982) 227.

[118] M. Dine and A. E. Nelson, *Dynamical Supersymmetry Breaking at Low Energies*, Phys. Rev. D **48** (1993) 1277–1287.

[119] V. Rubakov and M. Shaposhnikov, *Do We Live Inside a Domain Wall?*, Phys.Lett. **B125** (1983) 136–138.

[120] L. Randall and R. Sundrum, *A Large mass hierarchy from a small extra dimension*, Phys.Rev.Lett. **83** (1999) 3370–3373, arXiv:hep-ph/9905221 [hep-ph] (1999).

[121] G. F. Giudice, M. A. Luty, H. Murayama, and R. Rattazzi, *Gaugino mass without singlets*, JHEP **9812** (1998) 027, arXiv:hep-ph/9810442 [hep-ph] (1998).

[122] A. Djouadi, J.-L. Kneur, and G. Moultaka, *SuSpect: A Fortran code for the supersymmetric and Higgs particle spectrum in the MSSM*, Comput.Phys.Commun. **176** (2007) 426–455, arXiv:hep-ph/0211331 [hep-ph] (2007).

[123] C. Berger, J. Gainer, J. Hewett, and T. Rizzo, *Supersymmetry without prejudice*, JHEP 0902:023 (2009) .

[124] G. D'Ambrosio, G. Giudice, G. Isidori, and A. Strumia, *Minimal flavor violation: An Effective field theory approach*, Nucl.Phys. **B645** (2002) 155–187, arXiv:hep-ph/0207036 [hep-ph] (2002).

[125] N. Arkani-Hamed et al., *MARMOSET: The Path from LHC Data to the New Standard Model via On-Shell Effective Theories*, arXiv:hep-ph/0703088 [HEP-PH] (2007).

[126] J. Alwall, P. Schuster, and N. Toro, *Simplified Models for a First Characterization of New Physics at the LHC*, Phys. Rev. **D79** (2009) , arXiv:hep-ph/0810.3921 (2009).

[127] J.Alwall, M.P.Le, M.Lisanti, and J.G.Wacker, *Model-independent jets plus missing energy searches.*, Phys. Rev. **D79** (2009) , arXiv:hep-ph/0809.3264 (2009).

[128] E. Izaguirre, M. Manhart, J. G. Wacker, [hep-ph/1003.3886]; D. S. M. Alves, E. Izaguirre, J. G. Wacker, [hep-ph/1008.0407] .

[129] A. Martin, R. Roberts, W. Stirling, and R. Thorne, *Uncertainties of predictions from parton distributions. 1: Experimental errors*, Eur.Phys.J. **C28** (2003) 455–473, arXiv:hep-ph/0211080 [hep-ph] (2003).

[130] S. Dawson, E. Eichten, and C. Quigg, *Search for Supersymmetric Particles in Hadron - Hadron Collisions*, Phys.Rev. **D31** (1985) 1581.

[131] A. Sherstnev and R. Thorne, *Parton Distributions for LO Generators*, Eur.Phys.J. **C55** (2008) 553–575, arXiv:0711.2473 [hep-ph] (2008).

[132] C. Quigg, *LHC Physics Potential versus Energy*, arXiv:0908.3660 [hep-ph] (2009).

[133] LHC New Physics Working Group Collaboration, D. Alves et al., *Simplified Models for LHC New Physics Searches*, J.Phys. **G39** (2012) 105005, arXiv:1105.2838 [hep-ph] (2012).

[134] D. S. Alves, E. Izaguirre, and J. G. Wacker, *Where the Sidewalk Ends: Jets and Missing Energy Search Strategies for the 7 TeV LHC*, JHEP **1110** (2011) 012, arXiv:1102.5338 [hep-ph] (2011).

[135] Characterization of New Physics at the LHC – I (ATLAS/CMS/LPCC Workshop at CERN) (2010), http://indico.cern.ch/conferenceDisplay.py?confId=94910 .

[136] Characterization of New Physics at the LHC – II (ATLAS/CMS/LPCC Workshop at CERN) (2010), http://indico.cern.ch/conferenceDisplay.py?confId=107769 .

[137] Signatures of new physics at the LHC (2010), http://LHCNewPhysics.org/ .

[138] PROSPINO2, http://www.thphys.uni-heidelberg.de/~plehn/index.php?show=prospino&visible=tools .

[139] ATLAS Collaboration, *Search for supersymmetry in pp collisions at* $\sqrt{s} = 7$ *TeV in final states with missing transverse momentum and b-jets*, arXiv:1103.4344 [hep-ex] (2011).

[140] *Search for supersymmetry in pp collisions at $\sqrt{s} = 7$ TeV in final states with missing transverse momentum, b-jets and no leptons with the ATLAS detector*, Tech. Rep. ATLAS-CONF-2011-098, CERN, Geneva, Jul, 2011. http://cdsweb.cern.ch/record/1369212.

[141] *Search for supersymmetry in pp collisions at $\sqrt{s} = 7$ TeV in final states with missing transverse momentum, b-jets and one lepton with the ATLAS detector*, Tech. Rep. ATLAS-CONF-2011-130, CERN, Geneva, Sep, 2011. http://cdsweb.cern.ch/record/1383833.

[142] ATLAS Collaboration, *Search for supersymmetry in pp collisions at $\sqrt{s} = 7$ TeV in final states with missing transverse momentum and b-jets with the ATLAS detector*, Phys.Rev. **D85** (2012) 112006, arXiv:1203.6193 [hep-ex] (2012).

[143] CMS Collaboration, *Search for new physics with jets and missing transverse momentum in pp collisions at $\sqrt{s} = 7$" TeV*, Journal of High Energy Physics **2011** (2011) 1–46. 10.1007/JHEP08(2011)155.

[144] ATLAS Collaboration, *Search for scalar bottom pair production with the ATLAS detector in pp Collisions at $\sqrt{s} = 7$ TeV*, Phys.Rev.Lett. **108** (2012) 181802, arXiv:1112.3832 [hep-ex] (2012).

[145] A. Frodesen, O. Skeggestad, and H. TØfte, *Probability and Statistics in Particle Physics*. Reklametrykk A.s, Bergen, Norway, 1979, ISBN 82-00-01906-3.

[146] M. G. Kendall and A. Stuart, *The Advanced Theory of Statistics, Vol 2, 2^{nd} edition*. Charles Griffen & Company Limited, London, 1967, ISBN 0 7204 02395.

[147] S. A. A. Stuart, J.K. Ord, *Kendall's Advanced Theory of Statistics, Classical Inference and the Linear Model, Vol. 2A, 6^{th} edition*. Oxford University Press, London, 1999.

[148] ATLAS and CMS Collaborations and LHC Higgs Combination Group, ATL-PHYS-PUB-2011-11, CMS NOTE-2011/005 (2011).

[149] Cowan, G. and others, *Asymptotic formulae for likelihood-based tests of new physics*, Eur. Phys. J. **C71** (2011) 1554.

[150] S. Wilks, *The large-sample distribution of the likelihood ratio for testing composite hypotheses*, Ann. Math. Stat. **9** (1938) 60–62.

[151] A. Wald, *Tests of statistical hypotheses concerning several parameters when the number of observations is large*, Trans. Am. Math. Soc. **54(3)** (1943) 426–482.

[152] T. Junk, *Confidence Level Computation for Combining Searches with Small Statistics*, Nucl. Instrum. Meth. **A 434** (1999) 435–443.

[153] A. L. Read, *Presentation of search results: The CL(s) technique*, J. Phys. **G28** (2002) 2693–2704.

[154] D. Casadei Statistical methods used in ATLAS for exclusion and discovery (2011) 063, arXiv:1108.2288 [physics] (2011).

[155] L. Lyons, *Open statistical issues in particle physics*, ArXiv e-prints (2008) , arXiv:0811.1663 [stat.AP] (2008).

[156] ALICE Collaboration, *The ALICE experiment at the CERN LHC*, Journal of Instrumentation **3** (2008) no. 08, S08002.

[157] LHCb Collaboration, *The LHCb Detector at the LHC*, Journal of Instrumentation **3** (2008) no. 08, S08005.

[158] ATLAS Collaboration, *Luminosity Determination in pp Collisions at sqrt(s)=7 TeV Using the ATLAS Detector at the LHC*, Eur.Phys.J. **C71** (2011) 1630, arXiv:1101.2185 [hep-ex] (2011).

[159] D. Fournier, *Performance of the LHC, ATLAS and CMS in 2011*, arXiv:1201.4681 [hep-ex] (2012).

[160] ATLAS Luminosity Public Results, https://twiki.cern.ch/twiki/bin/view/AtlasPublic/LuminosityPublicResults .

[161] S. van der Meer, *Calibration of the effective beam height in the ISR*, Tech. Rep. CERN-ISR-PO-68-31. ISR-PO-68-31, CERN, Geneva, 1968.

[162] D. Belohrad et al., *Commissioning and First Performance of the LHC Beam Current Measurement Systems, in Proceedings of the 1st International Particle Accelerator Conference*. Kyoto, Japan, 23–28 May 2010, 1110–1112 (2010), ISBN: 9789290833529.

[163] ATLAS Collaboration, *Luminosity Determination in pp Collisions at* $\sqrt{s} = 7$ *TeV using the ATLAS Detector in 2011*, tech. rep., CERN, Geneva, 2011.

[164] G. Anders et al., *LHC Bunch Current Normalisation for the April-May 2010 Luminosity Calibration Measurements*, .

[165] ATLAS Collaboration, *The ATLAS Simulation Infrastructure*, Eur.Phys.J. **C70** (2010) 823–874, arXiv:1005.4568 [physics.ins-det] (2010).

[166] GEANT4 Collaboration, S. Agostinelli et al. Nucl. Instrum. Meth. **A506** (2003) 250–303.

[167] G. Folger and J. P. Wellisch, *String parton models in Geant4*, arXiv:0306007 [nucl-th] (2003).

[168] H. W. Bertini, *Intranuclear-cascade calculation of the secondary nucleon spectra from nucleon-nucleus interactions in the energy range 340 to 2900 MeV and comparisons with experiment*, Phys. Rev. **188** (1969) 1711–1730.

[169] J. Butterworth, J. R. Forshaw, and M. Seymour, *Multiparton interactions in photoproduction at HERA*, Z. Phys. **C72** (1996) 637–646.

[170] R. Hamberg, W. van Neerven, and T. Matsuura, *A Complete calculation of the order $\alpha - s^2$ correction to the Drell-Yan K factor*, Nucl.Phys. **B359** (1991) 343–405.

[171] K. Melnikov and F. Petriello Phys. Rev. **D74** (2006) 114017.

[172] K. Melnikov and F. Petriello Phys. Rev. Lett. **96** (2006) 231803, arXiv:hep-ph/0603182 [hep-ph] (2006).

[173] Top Systematic Uncertainties. https://twiki.cern.ch/twiki/bin/view/AtlasProtected/TopSystematicUncertainties .

[174] R. Bonciani, S. Catani, M. L. Mangano, and P. Nason, *NLL resummation of the heavy-quark hadroproduction cross-section*, Nucl. Phys. **B529** (1998) 424–450.

[175] S. Moch and P. Uwer, *Theoretical status and prospects for top-quark pair production at hadron colliders*, Phys. Rev. D **78, 3** (Aug, 2008) 034003.

[176] M. Beneke, M. Czakon, P. Falgari, A. Mitov, and C. Schwinn, *Threshold expansion of the $gg(q\bar{q}) \to Q\bar{Q} + X$ cross section at $O(\alpha(s)^4)$*, Phys.Lett. **B690** (2010) 483–490, arXiv:0911.5166 [hep-ph] (2010).

[177] N. Kidonakis, *NNLL resummation for s-channel single top quark production*, Phys.Rev. **D81** (2010) 054028, arXiv:1001.5034 [hep-ph] (2010).

[178] J. M. Campbell and R. K. Ellis, *An Update on vector boson pair production at hadron colliders*, Phys.Rev. **D60** (1999) 113006, arXiv:hep-ph/9905386 [hep-ph] (1999).

[179] J. M. Campbell, R. K. Ellis, and C. Williams, *Vector boson pair production at the LHC*, JHEP **1107** (2011) 018, arXiv:1105.0020 [hep-ph] (2011).

[180] P. Z. Skands, B. Allanach, H. Baer, C. Balazs, G. Belanger, et al., *SUSY Les Houches accord: Interfacing SUSY spectrum calculators, decay packages, and event generators*, JHEP **0407** (2004) 036, arXiv:hep-ph/0311123 [hep-ph] (2004).

[181] B. Allanach, C. Balazs, G. Belanger, M. Bernhardt, F. Boudjema, et al., *SUSY Les Houches Accord 2*, Comput.Phys.Commun. **180** (2009) 8–25, arXiv:0801.0045 [hep-ph] (2009).

[182] Supersymmetry Les Houches Accord, Tools: http://home.fnal.gov/~skands/slha/ .

[183] A. Djouadi, M. M. Muhlleitner, and M. Spira Acta Phys. Polon. **B38** (2007) 635–644, arXiv:hep-ph/0609292 (2007).

[184] ATLAS Collaboration, *Expected Performance of the ATLAS Experiment - Detector, Trigger and Physics*, arXiv:0901.0512 [hep-ex] (2009).

[185] T. Cornelissen, M. Elsing, S. Fleischmann, W. Liebig, E. Moyse, and A. Salzburger, *Concepts, Design and Implementation of the ATLAS New Tracking (NEWT)*, Tech. Rep. ATL-SOFT-PUB-2007-007. ATL-COM-SOFT-2007-002, CERN, Geneva, Mar, 2007. http://cdsweb.cern.ch/record/1020106.

[186] *Tracking Results and Comparison to Monte Carlo simulation at* $\sqrt{s} = 900\ GeV$, Tech. Rep. ATLAS-CONF-2010-011, CERN, Geneva, Jul, 2010. http://cdsweb.cern.ch/record/1276323.

[187] *Performance of the ATLAS Silicon Pattern Recognition Algorithm in Data and Simulation at* $\sqrt{s} = 7\ TeV$, Tech. Rep. ATLAS-CONF-2010-072, CERN, Geneva, Jul, 2010. https://cdsweb.cern.ch/record/1281363.

[188] *Performance of primary vertex reconstruction in proton-proton collisions at* $\sqrt{s} = 7\ TeV$ *in the ATLAS experiment*, Tech. Rep. ATLAS-CONF-2010-069, CERN, Geneva, Jul, 2010. https://cdsweb.cern.ch/record/1281344.

[189] *Characterization of Interaction-Point Beam Parameters Using the pp Event-Vertex Distribution Reconstructed in the ATLAS Detector at the LHC*, Tech. Rep. ATLAS-CONF-2010-027, CERN, Geneva, May, 2010. http://cdsweb.cern.ch/record/1277659.

[190] *Expected electron performance in the ATLAS experiment*, Tech. Rep. ATL-PHYS-PUB-2011-006, CERN, Geneva, Apr, 2011. http://cdsweb.cern.ch/record/1345327.

[191] W. Lampl et al., *Calorimeter Clustering Algorithms: Description and Performance*, Tech. Rep. ATL-LARG-PUB-2008-002, CERN, April, 2008. http://cdsweb.cern.ch/record/1099735.

[192] P. Speckmayer, A. Höcker, J. Stelzer, and H. Voss, *The toolkit for multivariate data analysis, TMVA 4*, Journal of Physics: Conference Series **219** (2010) no. 3, 032057.

[193] ATLAS Collaboration Collaboration, *Electron performance measurements with the ATLAS detector using the 2010 LHC proton-proton collision data*, Eur.Phys.J. **C72** (2012) 1909, arXiv:1110.3174 [hep-ex] (2012).

[194] S. H. et al., *A muon identification and combined reconstruction procedure for the ATLAS detector at the LHC using the (MUONBOY, STACO, MuTag) reconstruction packages*, Nucl. Instrum. Meth. **A572** (2007) 77–79.

[195] *Muon reconstruction efficiency in reprocessed 2010 LHC proton-proton collision data recorded with the ATLAS detector*, Tech. Rep. ATLAS-CONF-2011-063, CERN, Geneva, Apr, 2011. http://cdsweb.cern.ch/record/1345743.

[196] *Muon Momentum Resolution in First Pass Reconstruction of pp Collision Data Recorded by ATLAS in 2010*, Tech. Rep. ATLAS-CONF-2011-046, CERN, Geneva, Mar, 2011. http://cdsweb.cern.ch/record/1338575.

[197] C. Buttar, J. D'Hondt, M. Kramer, G. Salam, M. Wobisch, et al., *Standard Model Handles and Candles Working Group: Tools and Jets Summary Report*, arXiv:0803.0678 [hep-ph] (2008).

[198] *Properties of Jets and Inputs to Jet Reconstruction and Calibration with the ATLAS Detector Using Proton-Proton Collisions at* $\sqrt{s} = 7$ *TeV*, Tech. Rep. ATLAS-CONF-2010-053, CERN, Geneva, Jul, 2010. http://cdsweb.cern.ch/record/1281310/.

[199] G. S. M. Cacciari and G. Soyez, *The anti-k_t jet clustering algorithm*, JHEP **04** (2008) 063, arXiv:0802.1189 [hep-ph] (2008).

[200] L. Asquith et al., *Performance of Jet Algorithms in the ATLAS Detector*, Tech. Rep. ATL-PHYS-INT-2010-129, CERN, Geneva, Dec, 2010.

[201] S. D. Ellis and D. E. Soper, *Successive combination jet algorithm for hadron collisions*, Phys. Rev. D **48, 7** (Oct, 1993) 3160–3166.

[202] Y. Dokshitzer, G. Leder, S. Moretti, and B. Webber, *Better jet clustering algorithms*, Journal of High Energy Physics **1997** (1997) no. 08, 001.

[203] S. Catani, Y. Dokshitzer, and B. Webber, *The k_t-clustering algorithm for jets in deep inelastic scattering and hadron collisions*, Physics Letters B **285** (1992) no. 3, 291 – 299.

[204] M. Cacciari, G. P. Salam, and G. Soyez, *The Catchment Area of Jets*, JHEP **0804** (2008) 005, arXiv:0802.1188 [hep-ph] (2008).

[205] M. Aleksa et al., *ATLAS Combined Testbeam: Computation and Validation of the Electronic Calibration Constants for the Electromagnetic Calorimeter*, Tech. Rep. ATL-LARG-PUB-2006-003, CERN, Geneva, Apr, 2006. http://cdsweb.cern.ch/record/942528.

[206] ATLAS Collaboration Collaboration, *Jet energy measurement with the ATLAS detector in proton-proton collisions at sqrt(s) = 7 TeV*, arXiv:1112.6426 [hep-ex] (2011).

[207] *In-situ jet energy scale and jet shape corrections for multiple interactions in the first ATLAS data at the LHC*, Tech. Rep. ATLAS-CONF-2011-030, CERN, Geneva, Mar, 2011. http://cdsweb.cern.ch/record/1337780.

[208] *Close-by Jet Effects on Jet Energy Scale Calibration in pp Collisions at sqrt(s)=7 TeV with the ATLAS Detector*, Tech. Rep. ATLAS-CONF-2011-062, CERN, Geneva, Apr, 2011. http://cdsweb.cern.ch/record/1345091.

[209] *Light-quark and Gluon Jets in ATLAS*, Tech. Rep. ATLAS-CONF-2011-053, CERN, Geneva, Apr, 2011. http://cdsweb.cern.ch/record/1342550.

[210] *Calibrating the b-Tag Efficiency and Mistag Rate in 35 pb^{-1} of Data with the ATLAS Detector*, Tech. Rep. ATLAS-CONF-2011-089, CERN, Geneva, Jun, 2011. http://cdsweb.cern.ch/record/1356198.

[211] *Commissioning of the ATLAS high-performance b-tagging algorithms in the 7 TeV collision data*, Tech. Rep. ATLAS-CONF-2011-102, CERN, Geneva, Jul, 2011. http://cdsweb.cern.ch/record/1369219.

[212] G. Piacquadio and C. Weiser, *A new inclusive secondary vertex algorithm for b-jet tagging in ATLAS*, Journal of Physics: Conference Series **119** (2008) no. 3, 032032.

[213] *Measurement of the b-tag Efficiency in a Sample of Jets Containing Muons with 5 fb^{-1} of Data from the ATLAS Detector*, Tech. Rep.

ATLAS-CONF-2012-043, CERN, Geneva, Mar, 2012. http://cdsweb.cern.ch/record/1435197.

[214] *b-jet tagging calibration on c-jets containing D^{*+} mesons*, Tech. Rep. ATLAS-CONF-2012-039, CERN, Geneva, Mar, 2012. http://cdsweb.cern.ch/record/1435193.

[215] ATLAS Collaboration Collaboration, *Performance of Missing Transverse Momentum Reconstruction in Proton-Proton Collisions at 7 TeV with ATLAS*, Eur.Phys.J. **C72** (2012) 1844, arXiv:1108.5602 [hep-ex] (2012).

[216] ATLAS Collaboration, *Measurement of inclusive jet and dijet cross sections in proton-proton collisions at 7 TeV centre-of-mass energy with the ATLAS detector*, Eur.Phys.J. **C71** (2011) 1512, arXiv:1009.5908 [hep-ex] (2011).

[217] ATLAS Collaboration, *Measurement of multi-jet cross sections in proton-proton collisions at a 7 TeV center-of-mass energy*, Eur.Phys.J. **C71** (2011) 1763, arXiv:1107.2092 [hep-ex] (2011).

[218] ATLAS Collaboration, *Measurement of Dijet Azimuthal Decorrelations in pp Collisions at $\sqrt{s}$=7 TeV*, Phys. Rev. Lett. **106** (2011) 172002, arXiv:1102.2696 [hep-ex] (2011).

[219] ATLAS Collaboration, *Measurement of the production cross section for W-bosons in association with jets in pp collisions at $\sqrt{s}$ = 7 TeV with the ATLAS detector*, Phys. Lett. **B 698** (2011) 325–345, arXiv:1012.5382 [hep-ex] (2011).

[220] ATLAS Collaboration, *Measurement of the top quark-pair production cross section with ATLAS in pp collisions at $\sqrt{s} = 7$ TeV*, Eur.Phys.J. **C71** (2011) 1, arXiv:1012.1792 [hep-ex] (2011).

[221] ATLAS Collaboration, *Search for Quark Contact Interactions in Dijet Angular Distributions in pp Collisions at $\sqrt{s}$ = 7 TeV Measured with the ATLAS Detector*, Phys. Lett. B **694** (2011) 327–345, arXiv:1009.5069 [hep-ex] (2011).

[222] ATLAS Collaboration, *Search for New Particles in Two-Jet Final States in 7 TeV Proton-Proton Collisions with the ATLAS Detector at the LHC*, Phys. Rev. Lett. **105** (2010) 161801, arXiv:1008.2461 [hep-ex] (2010).

[223] ATLAS Collaboration, *Search for supersymmetry using final states with one lepton, jets, and missing transverse momentum with the ATLAS detector in*

$\sqrt{s}$ = 7 *TeV pp collisions*, Phys. Rev. Lett. **106** (2011) 131802, arXiv:1102.2357 [hep-ex] (2011).

[224] ATLAS Collaboration, *Search for squarks and gluinos using final states with jets and missing transverse momentum with the ATLAS detector in* $\sqrt{s} = 7$ *TeV proton-proton collisions*, Phys.Lett. **B701** (2011) 186–203, arXiv:1102.5290 [hep-ex] (2011).

[225] ATLAS Collaboration, *Jet energy resolution in proton-proton collisions at* $\sqrt{s} = 7$ *TeV recorded in 2010 with the ATLAS detector*, arXiv:1210.6210 [hep-ex] (2012).

[226] DØ Collaboration, B. Abbott et al., *High-*p_T *jets in* $p\bar{p}$ *collisions at* $\sqrt{s} = 630$ *GeV and 1800 GeV*, Phys. Rev. **D64** (2001) 032003, arXiv:0012046 [hep-ex] (2001).

[227] UA2 Collaboration, P. Bagnaina et al., *Measurement of jet production properties at the CERN* $p\bar{p}$ *collider*, Phys. Lett. **B 144** (1984) 283.

[228] R. Corke and T. Sjostrand, *Improved Parton Showers at Large Transverse Momenta*, Eur.Phys.J. **C69** (2010) 1–18, arXiv:1003.2384 [hep-ph] (2010).

[229] T. Sjostrand and P. Z. Skands, *Transverse-momentum-ordered showers and interleaved multiple interactions*, Eur.Phys.J. **C39** (2005) 129–154, arXiv:0408302 [hep-ph] (2005).

[230] B. Andersson et al., *Parton Fragmentation and String Dynamics*, Phys. Rep. **97** (1983) 31–145.

[231] ATLAS Collaboration, *Charged-particle multiplicities in pp interactions measured with the ATLAS detector at the LHC*, New J.Phys. **13** (2011) 053033, arXiv:1012.5104 [hep-ex] (2011).

[232] P. Z. Skands, *Tuning Monte Carlo Generators: The Perugia Tunes*, Phys. Rev. D **82** (2010) 074018, arXiv:1005.3457 [hep-ph] (2010).

[233] ATLAS Collaboration, *Study of Jet Shapes in Inclusive Jet Production in pp Collisions at* $\sqrt{s} = 7$ *TeV using the ATLAS Detector*, Phys.Rev. **D83** (2011) 052003, arXiv:1101.0070 [hep-ex] (2011).

[234] ATLAS Collaboration, *ATLAS Monte Carlo tunes for MC09*, tech. rep. http://cdsweb.cern.ch/record/1247375.

[235] T. Sjostrand, *PYTHIA 8 Status Report*, arXiv:0809.0303 [hep-ph] (2008).

[236] M. Bahr et al., *Herwig++ Physics and Manual*, Eur.Phys.J. **C58** (2008) 639–707, arXiv:0803.0883 [hep-ph] (2008).

[237] G. Marchesini et al., *A Monte Carlo Event Generator For Simulating Hadron Emission Reactions With Interfering Gluons*, Comput. Phys. Commun. **67** (1991) 465–508.

[238] G. Marchesini et al., *Monte Carlo Simulation of General Hard Processes with Coherent QCD Radiation*, Nucl. Phys. **B 310** (1988) 461.

[239] B. R. Webber, *A QCD model for jet fragmentation including soft gluon interference*, Nucl. Phys. **B 238** (1984) 492.

[240] M. Bahr, S. Gieseke, and M. H. Seymour, *Simulation of multiple partonic interactions in Herwig++*, JHEP **07** (2008) 076, arXiv:0803.3633 [hep-ph] (2008).

[241] M. L. Mangano, M. Moretti, and R. Pittau, *Multijet matrix elements and shower evolution in hadronic collisions: $Wb\bar{b}$ + n jets as a case study*, Nucl. Phys. B **632** (2002) 343–362, arXiv:0108069 [hep-ph] (2002).

[242] J. Pumplin et al., *New generation of parton distributions with uncertainties from global QCD analysis*, JHEP **07** (2002) 012, arXiv:0201195 [hep-ph] (2002).

[243] R. Achenbach et al., *The ATLAS Level-1 Calorimeter Trigger*, tech. rep. "http://cdsweb.cern.ch/record/1080560".

[244] Atlas Collaboration, *Performance of the ATLAS Trigger System in 2010*, Eur.Phys.J. **C72** (2012) 1849, arXiv:1110.1530 [hep-ex] (2012).

[245] M. Cacciari and G. P. Salam, *Dispelling the N^3 myth for the k_t jet-finder*, Phys. Lett. B **641** (2006) no. 1, 57 – 61.

[246] M. Cacciari, G. P. Salam, G. Soyez, *FastJet*, http://fastjet.fr/.

[247] G. Romeo et al., *Track-Based Jet Corrections in ATLAS*, Tech. Rep. ATL-PHYS-INT-2009-075, CERN, Geneva, Aug, 2009.

[248] CMS Collaboration, *Jet Energy Resolution in CMS at $\sqrt{s} = 7$ TeV*, Tech. Rep. CMS-PAS-JME-10-014, CERN, 2011. http://cds.cern.ch/record/1339945.

[249] The BOOST 2012 workshop, http://ific.uv.es/boost2012/ .

[250] D. W. Miller, S. Dong, and A. Schwartzman, *Measurement of Hadronic Event Shapes and Jet Substructure in Proton-Proton Collisions at 7.0 TeV Center-of-Mass Energy with the ATLAS Detector at the Large Hadron Collider. oai:cds.cern.ch:1393742.* PhD thesis, Stanford U., Menlo Park, CA, 2011. Presented 03 Jun 2011.

[251] ATLAS Collaboration, Unprescaled Triggers during 2011, https://twiki.cern.ch/twiki/bin/viewauth/Atlas/LowestUnprescaled2011 .

[252] How to Clean Jets in ATLAS, https://twiki.cern.ch/twiki/bin/view/AtlasProtected/HowToCleanJets .

[253] ATLAS Multijet JES Uncertainty Provider, https://twiki.cern.ch/twiki/bin/view/AtlasProtected/MultijetJESUncertaintyProvider .

[254] A. Ahmed et al., *Supporting Document: Measurement of the W cross section and asymmetry in the electron and muon decay channels at* $\sqrt{s} = 7$ *TeV*, Tech. Rep. ATL-COM-PHYS-2010-447, 2010.

[255] B. P. Kersevan and E. Richter-Was, *The Monte Carlo event generator AcerMC version 2.0 with interfaces to PYTHIA 6.2 and HERWIG 6.5*, arXiv:hep-ph/0405247 [hep-ph] (2004).

[256] ATLAS Collaboration, *Measurement of the cross section for the production of a W boson in association with b-jets in pp collisions at* $\sqrt{s} = 7$ *TeV with the ATLAS detector*, Phys.Lett. **B707** (2012) 418–437, arXiv:1109.1470 [hep-ex] (2012).

[257] ATLAS Collaboration, *Measurement of the cross-section for b-jets produced in association with a Z boson at* $\sqrt{s} = 7$ *TeV with the ATLAS detector*, Phys.Lett. **B706** (2012) 295–313, arXiv:1109.1403 [hep-ex] (2012).

[258] PDF4LHC Recommendations, http://www.hep.ucl.ac.uk/pdf4lhc/PDF4LHCrecom.pdf. .

[259] ATLAS Collaboration, Trigger Public Results, https://twiki.cern.ch/twiki/bin/view/AtlasPublic/TriggerPublicResults .

[260] V. Cavaliere, *b-jet triggering in ATLAS*, Tech. Rep. ATL-DAQ-PROC-2012-038, CERN, Geneva, Jun, 2012.

[261] ALEPH Collaboration, *A precise measurement of* $\Gamma_{Z\to b\bar{b}}/\Gamma_{Z\to hadrons}$, Physics Letters B **313, 3-4** (1993) 535–548.

[262] ATLAS Collaboration, Public b-jet Trigger Plots for Collision Data, https://twiki.cern.ch/twiki/bin/view/AtlasPublic/BJetTriggerPublicResults .

[263] ATLAS Collaboration, *Search for squarks and gluinos with the ATLAS detector in final states with jets and missing transverse momentum using 4.7 fb^{-1} of $\sqrt{s} = 7$ TeV proton-proton collision data*, arXiv:1208.0949 [hep-ex] (2012).

[264] ATLAS Collaboration, *Search for gluinos in events with two same-sign leptons, jets and missing transverse momentum with the ATLAS detector in pp collisions at $\sqrt{s} = 7$ TeV*, Phys.Rev.Lett. **108** (2012) 241802, arXiv:1203.5763 [hep-ex] (2012).

[265] K. Cranmer, A. Shibata, and D. Tardif, *HistFactory User Guide (ROOT 5.32) Draft 5* (2012).

[266] W. Beenakker, R. Hopker, M. Spira, and P. Zerwas, *Squark and gluino production at hadron colliders*, Nucl.Phys. **B492** (1997) 51–103, arXiv:hep-ph/9610490 [hep-ph] (1997).

[267] A. Kulesza and L. Motyka, *Threshold resummation for squark-antisquark and gluino-pair production at the LHC*, Phys.Rev.Lett. **102** (2009) 111802, arXiv:0807.2405 [hep-ph] (2009).

[268] A. Kulesza and L. Motyka, *Soft gluon resummation for the production of gluino-gluino and squark-antisquark pairs at the LHC*, Phys.Rev. **D80** (2009) 095004, arXiv:0905.4749 [hep-ph] (2009).

[269] W. Beenakker, S. Brensing, M. Kramer, A. Kulesza, E. Laenen, et al., *Soft-gluon resummation for squark and gluino hadroproduction*, JHEP **0912** (2009) 041, arXiv:0909.4418 [hep-ph] (2009).

[270] W. Beenakker, S. Brensing, M. Kramer, A. Kulesza, E. Laenen, et al., *Squark and Gluino Hadroproduction*, Int.J.Mod.Phys. **A26** (2011) 2637–2664, arXiv:1105.1110 [hep-ph] (2011).

[271] M. Kramer, A. Kulesza, R. van der Leeuw, M. Mangano, S. Padhi, et al., *Supersymmetry production cross sections in pp collisions at sqrts = 7 TeV*, arXiv:1206.2892 [hep-ph] (2012).

[272] The ATLAS Collaboration, Search for gluino-mediated scalar top and bottom quark production in final states with missing transverse energy and at least three b-jets with the ATLAS Detector. Additional material: https://atlas.web.cern.ch/Atlas/GROUPS/PHYSICS/PAPERS/SUSY-2012-02/ .

[273] ATLAS Collaboration, *Search for Gluinos in Events with Two Same-Sign Leptons, Jets, and Missing Transverse Momentum with the ATLAS Detector in pp Collisions at $\sqrt{s} = 7$ TeV*, Phys. Rev. Lett. **108, 24** (Jun,2012) 241802.

[274] ATLAS Collaboration, *Hunt for new phenomena using large jet multiplicities and missing transverse momentum with ATLAS in 4.7 fb^{-1} of $\sqrt{s} = 7$ TeV" proton-proton collisions*, Journal of High Energy Physics **2012, 7** (2012) 1–40.

[275] CDF Collaboration, *Search for Gluino-Mediated Bottom Squark Production in $p\bar{p}$ Collisions at $\sqrt{s} = 1.96$ TeV*, Phys. Rev. Lett. **102, 22** (Jun, 2009) 221801.

[276] CDF Collaboration, *Search for the Production of Scalar Bottom Quarks in $p\bar{p}$ Collisions at $\sqrt{s} = 1.96$ TeV*, Phys. Rev. Lett. **105, 8** (Aug, 2010) 081802.

[277] D0 Collaboration, *Search for scalar bottom quarks and third-generation leptoquarks in $p\bar{p}$ collisions at $\sqrt{s} = 1.96$ TeV.*, Physics Letters B **693** (2010) no. 2, 95 – 101.

[278] CMS Collaboration, *Search for new physics in events with same-sign dileptons and b-tagged jets in pp collisions at $\sqrt{s} = 7$ TeV*, JHEP **1208** (2012) 110, arXiv:1205.3933 [hep-ex] (2012).

[279] ATLAS Collaboration, *Search for top and bottom squarks from gluino pair production in final states with missing transverse energy and at least three b-jets with the ATLAS detector*, arXiv:1207.4686 [hep-ex] (2012).